Particle Size and Microstructure Control of Ni-Rich Layered Oxide Cathodes for Next Generation Li-Ion Batteries

Narayan Simrit Kaur

Doctoral Thesis

Department of Materials Science and Engineering

Registration No.: 200207386

October 2024



Abstract

Ni-rich layered oxides are very promising candidates for cathode active materials in Li-ion batteries. Especially LiNiO₂ (LNO) with its theoretical capacity of 275 mAh/g could be designated to replace state of the art layered oxide materials containing unethically mined cobalt. Yet, the synthesis of LNO is providing some difficulties due to cation mixing, the occupation of Li sites with Ni²⁺, and the structural instability during cycling due to occurring phase transitions, which results in irreversible capacity loss and capacity fading during cycling, as well as a decreased capacity retention. Emerging oxygen from the structure during cycling enacts as an additional safety risk.

Optimising the synthesis of the LiNiO₂ precursor Ni(OH)₂ via a precipitation reaction in a stirred tank reactor as well as the high temperature solid-state reaction to lithiate the precursor to form the final LiNiO₂ is suggested to mitigate some of these issues from the start by carefully controlling the particle size and morphology to prevent internal mechanical strain during the phase transitions, improve Li diffusion within the structure and reduce potential cation mixing. Analytical techniques like X-ray diffraction (XRD) and refinements of the resulting diffraction pattern, scanning electron microscopy (SEM), laser diffraction. tap density, Brunauer-Emmett-Teller (BET) analysis and magnetic measurements were used to examine the crystal structure and the materials properties, as well as electrochemical cycling to study morphological influences on the cycling behaviour of the as-prepared materials. Advanced methods like thermogravimetric analysis (TGA), in situ X-ray absorption spectroscopy (XAS) and X-ray photoelectron spectroscopy (XPS), operando muon spin relaxation spectroscopy and in situ X-ray diffraction combined with computer tomography (XRD-CT), help understand internal processes and mechanisms during operation.

Ni(OH)₂, the precursor for LNO, was successfully synthesised with a quasispherical morphology of secondary particles and a seemingly dense packing of primary particles. Different particle sizes can be produced on demand by tweaking the reaction conditions. LiNiO₂ was produced with improved annealing conditions, yielding a reliably repeatable low cation mixing of below 2% while maintaining spherical-like secondary particles with randomly aligned cuboid primary particles in the core and radially aligned primary particles towards the surface of the secondary particle assembly. These improved materials show enhanced cycling

behaviour with initial capacities above $250\,\text{mAh/g}$ while sustaining a capacity retention over $100\,\text{cycles}$ above $80\,\%$.

Additionally, doping of the optimised LNO gives an overview of the properties enhanced or mitigated through the dopant and will give new insights and opportunities to combine specific targeted dopants to improve battery performance and life even more.

Acknowledgements

My sincerest gratitude to ਅਕਾਲ ਪੁਰਖ, ਵਾਹਿਗੁਰੂ and ਅੰਤਰਜਾਮੀ. I would not be here without you! May all living beings be healthy, happy and blessed.

ਨਾਨਕ ਨਾਮ ਚੜ੍ਹਦੀ ਕਲਾ ॥ ਤੇਰੇ ਭਾਣੇ ਸਰਬੱਤ ਦਾ ਭਲਾ

ਵਾਹਿਗੁਰੂ ਜੀ ਕਾ ਖਾਲਸਾ ਵਾਹਿਗੁਰੂ ਜੀ ਕੀ ਫ਼ਤਿਹ

Table of Contents

Abstract	I
Acknowledgements	III
Table of Contents	IV
Abbreviations	VIII
List of Tables	XI
List of Figures	XII
1. Introduction	
2. Literature Review	
2.1. Cathode Materials for LIBs	4
2.2. High Nickel Content Layered Cathodes	6
2.2.1. Crystal Structure	7
2.2.1.1. TM(OH) ₂ Precursor for Layered Oxide Materials	7
2.2.1.2. Cathode Active Layered Oxide LiNiO ₂	8
2.2.2. Electrochemistry of LiNiO ₂	10
2.2.3. Physical Properties of LiNiO ₂	11
2.2.4. Instabilities of LiNiO ₂	12
2.2.4.1. Moisture Instability	12
2.2.4.2. Thermal Instability and Oxygen Evolution	13
2.2.4.3. Mechanical Instability	14
2.3. Synthesis Methods	16
2.3.1. Solid-State Synthesis	16
2.3.2. Co-Precipitation Synthesis	17
2.3.3. Other Synthetic Methods	19
2.4. Doping of Cathode Active Materials	20
3. Experimental Methods	29
3.1. X-Ray Diffraction XRD	29
3.2. Rietveld Refinement	31

3.3.	Scanning Electron Microscopy SEM	32
3.4.	Thermal Analysis	33
3.5.	Laser Diffraction	33
3.6.	Tap Density	35
3.7.	Brunauer-Emmett-Teller (BET) Surface Area Analysis	35
3.8.	Galvanostatic Cycling	37
3.9.	X-Ray Absorption Spectroscopy XAS	39
3.9.	X-Ray Absorption Near-Edge Structure XANES	41
3.9.	2. Extended X-Ray Absorption Fine Structure EXAFS	41
3.9.	3. Soft X-Ray Absorption Spectroscopy sXAS	41
3.10.	X-ray Photoelectron Spectroscopy XPS	43
3.11.	Hard X-ray Photoelectron Spectroscopy (HAXPES)	43
3.12.	Magnetometry SQUID	43
3.13.	Muon-Spin Relaxation Spectroscopy μSR	44
3.14.	X-Ray Diffraction Computed Tomography	46
	imisation of the Annealing Process for the Layered Oxide Cathode Mate	
	Introduction	48
4.2.	Experimental Synthesis Optimisation	48
4.2.	Intermediate Grinding Evaluation	49
4.2.	2. Characterisation of LiNiO ₂	52
4	.2.2.1. Structural Characterisation	53
4	.2.2.2. Morphological Characterisation	57
4	.2.2.3. Electrochemical cycling	61
4.3.	Conclusion	74
	rphology Control of the Ni(OH) ₂ Precursor Particles for the Layered Ox LiNiO ₂	
5.1.	Introduction	

5.2. E	xperimental Precursor Synthesis Optimisation	78
5.2.1.	Reaction Time	81
5.2.2.	Reaction Temperature	84
5.2.3.	Ni:NH ₄ OH Ratio	87
5.2.4.	pH	90
	haracterisation and Electrochemical Cycling of LiNiO ₂ using different N Precursor Synthesis	
5.4. A	dvanced Methods of Characterisation of LiNiO ₂	106
5.4.1.	Hard XAS	106
5.4.2.	Soft XAS	108
5.4.3.	HAXPES	111
5.4.4.	Magnetometry	113
5.4.5.	Muon Spin Relaxation Spectroscopy	116
5.4.6.	in-situ XRD-CT	120
5.5. St	ummary and Conclusion	122
6. Doped	LiNiO ₂	127
6.1. In	troduction	127
6.2. S	ynthesis	127
6.3. C	haracterisation	128
6.3.1.	Cobalt-doped LNO	136
6.3.2.	Manganese-doped LNO	140
6.3.3.	Copper-doped LNO	143
6.3.4.	Zinc-doped LNO	146
6.3.5.	Tin-doped LNO	149
6.3.6.	Zirconium-doped LNO	152
6.3.7.	Titanium-doped LNO	155
6.3.8.	Tungsten-doped LNO	158

6.	.4. Summary and Conclusion	162
	Conclusion	
8.	Outlook	165
9.	References	166
10.	Appendix	191

Abbreviations

EV Electric Vehicle

LIB Lithium-Ion Battery

PVDF PolyVinylidene DiFluoride

CMC CarboxyMethyl Cellulose

SBR Styrene-Butadiene Rubber

EC Ethylene Carbonate

DMC DiMethyl Carbonate

PE PolyEthylene

PP PolyPropylene

XRD X-Ray Diffraction

SEM Scanning Electron Microscope

XANES X-ray Absorption Near-Edge Structure

EXAFS Extended X-ray Absorption Fine Structure

XRD-CT X-ray Diffraction-Computer Tomography

TM Transition Metal

CEI Cathode Electrolyte Interface

TPD-MS Temperature-Programmed Desorption - Mass Spectroscopy

SEI Solid Electrolyte Interface

ICP-OES Induced Coupled Plasma – Optical Emission Spectroscopy

NMR Nuclear Magnetic Resonance

XAS	X-ray Absorption Spectroscopy
TGA	ThermoGravimetric Analysis
DTG	Differential ThermoGravimetry
MS	Mass Spectrometry
DSC	Differential Scanning Calorimetry
JT	Jahn-Teller
STR	Stirred Tank Reactor
PSD	Particle Size Distribution
SOC	State Of Charge
EIS	Electrochemical Impedance Spectroscopy
STEM-EELS	Scanning Transition Electron Microscopy – Electron Energy Loss Spectroscopy
GNC	Glycine Nitrate Combustion
HRTEM	High Resolution Transition Electron Microscopy
SAED	Selected Area Electron Diffraction
DFT	Density Functional Theory
ICSD	Inorganic Crystal Structure Database
SE	Secondary Electrons
BE	Backscattered Electrons
DI	DeIonised
BET	Brunauer-Emmett-Teller
GCPL	Galvanostatic Cycling with Potential Limitation

NMP N-Methyl-2-Pyrrolidone

TEY Total Electron Yield

FY Fluorescence Yield

IPFY Inverse Partial Fluorescent Yield

XPS X-ray Photoelectron Spectroscopy

HAXPES Hard X-ray PhotoElectron Spectroscopy

SQUID Superconducting QUantum Interference Device

ZFC Zero-Field Cooling

FC Field Cooling

KT Kubo-Toyabe

LF Longitudinal Field

HT High Temperature

GOF Goodness Of Fit

OCV Open-Circuit Voltage

μSR Muon Spin Relaxation

EDX Energy-Dispersive X-ray Spectroscopy

LED Light Emitting Diode

LNO $\text{Li}_{1-x}\text{Ni}_{1+x}\text{O}_2$

 $NMC \quad Li(Ni_{1-x-y}Co_xMn_y)O_2$

 $NCA Li(Ni_{1-x-y}Co_xAl_y)O_2$

List of Tables

Table 4.1: Experimental design parameters for the calcination procedure for LiNiO ₂ 53
Table 4.2: Lattice parameters, unit cell volumes and Ni ²⁺ occupancies derived from Rietveld refinements for as-prepared LiNiO ₂ samples. Standard deviations in brackets. Green shading depicts down selection of samples for further examination in the next chapters
Table 4.3: Ratio of lattice parameter and Bragg peak ratios from X-ray diffraction patterns of as-prepared samples of LiNiO ₂ . Standard deviations in brackets. Green shading depicts down selection of samples for further examination in the next chapters
Table 4.4: Electrochemical values derived from the cycling data of the nine selected samples of as-prepared LiNiO ₂ and Ni occupancy in Li layer derived from Rietveld refinements72
Table 5.1: Reaction conditions for the optimisation of synthesis of Ni(OH) ₂ 79
Table 5.2: Particle size of precipitated Ni(OH) ₂ at different reaction times
Table 5.3: Particle size of precipitated Ni(OH) ₂ at different reaction temperatures85
Table 5.4: Particle size and tap density of precipitated Ni(OH) ₂ at different Ni:NH ₄ OH ratios
Table 5.5: Particle size of precipitated Ni(OH) ₂ at different pHs92
Table 5.6: Peak analysis of XRD patterns (Cu source, higher resolution) of annealed asprepared precursor Ni(OH) ₂ at different Ni:NH ₄ OH ratios
Table 5.7: Particle size and tap density of annealed as-prepared precursor Ni(OH) ₂ at different Ni:NH ₄ OH ratios
Table 5.8: Multi point BET surface analysis data of annealed as-prepared precursor Ni(OH) ₂ at different Ni:NH ₄ OH ratios
Table 5.9: Lattice parameters and Ni occupancy in Li layer (higher resolution Mo source) of annealed as-prepared precursor Ni(OH) ₂ at different Ni:NH ₄ OH ratios. Standard deviation in brackets.
Table 5.10: Electrochemical values derived from the cycling data of the as-prepared LiNiO ₂ using Ni(OH) ₂ precursor synthesised with different Ni:NH ₄ OH ratios

Table 5.11: Magnetic moments and constants obtained from SQUID measurements of LiNiO ₂ synthesised with different Ni:NH ₄ OH ratios during the precursor synthesis. Ni ²⁺ occupancy in Li layer from Rietveld refinements of Mo XRD patterns included
Table 6.1: Ratio of lattice parameter and Bragg peak ratios of as-prepared samples of doped LiNiO ₂ . Standard deviations in brackets
Table 6.2: Lattice parameters, volume and Ni ²⁺ and dopant occupancies derived from XRD patterns and its refinements for as-prepared LiNiO ₂ samples. Standard deviations in brackets.
Table 6.3: Electrochemical values derived from the cycling data of the as-prepared LiNiO ₂ using doped Ni(OH) ₂ precursor
List of Figures
Figure 1.1: Schematic design of a LIB (left) [206] and visualisation of a LIB during charge and discharge (right). Reproduced from [207] with permission from the Royal Society of Chemistry.
Figure 2.1: Positions of redox energies relative to the top of the anion: p bands (left), reproduced from [14] with permission from Springer Nature. Schematic energy diagram in a battery cell (right). Reproduced from [13] with permission from the American Chemical Society4
Figure 2.2: Li <i>TMO</i> ₂ structure for (a) the idealized unit cell close packing containing O (white) Li (grey) and <i>TM</i> (black) and (b) a layered cation structure viewed along the (1 1 1) plane. Reproduced from [46] with permission from Elsevier
Figure 2.3: Crystal structure of β -Ni(OH) ₂ (left) and α -Ni(OH) ₂ (right), showing layered structure with changing interslab spacing (Ni-Ni and O-O distances) depending on intercalated anions or H ₂ O molecules in the α -type. NiO ₆ octahedra depicted in green and blue spheres represent oxygen. Reproduced from [35] with permission from the Royal Society of Chemistry.
Figure 2.4: Changes in oxidation state of nickel ions during the first electrochemical cycle. Reproduced from [61] with permission from Elsevier

Figure 2.5: Li ion diffusion in layered oxides. Reproduced from [67] with permission from the
American Physical Society11
Figure 2.6: Charge-discharge cycle of a Li/LiNiO ₂ cell (left) and corresponding derivative curve (right). Reproduced from [81] with permission of Elsevier
Figure 2.7: Change in interlayer distance of Li _{1-x} NiO ₂ . Reproduced from [49] with permission from the Electrochemical Society
Figure 2.8: Hexagonal and monoclinic setting. Reproduced from [49] with permission from the Electrochemical Society.
Figure 2.9: Gap of O-2p and TM-3d band centers of doped Li _{0.5} NiO ₂ . Preferred site occupation of dopants labelled in different colours. Reproduced from [98] with permission from the American Chemical Society.
Figure 3.1: Reflections of X-rays (Bragg equation). Reproduced from [151] with permission from Springer Nature
Figure 3.2: Schematic of image formation in a scanning electron microscope. Reproduced from [158] with permission from Springer Nature
Figure 3.3: Illustration of laser diffraction in a particle size analyser. The red arrow represents the laser beam. The blue arrow contains the sample dispersion. [160]
Figure 3.4: Adsorption processes during BET measurements; formation of monolayer, multilayer and complete filling with increasing applied pressure. [165]
Figure 3.5: Diagram of coin cell
Figure 3.6: Photoelectric effect showing the ejection of electrons from the core level and its resulting interactions with neighbouring atoms. [171]
Figure 3.7: Absorption spectra showing the different regions like XANES and EXAFS. [171]
Figure 3.8: Auger effect when core electron is ejected, creating a hole. An electron from a higher energy shell will fill that hole and an Auger electron will be released to balance the energy difference. Reproduced from [173] with permission from Springer Nature
Finden Ltd

Figure 4.1: SEM images of the Ni(OH) ₂ sample precipitated in a stirred tank reactor (Chapter
5) and used for further investigations in this chapter
Figure 4.2: Thermogravimetric analysis of a stoichiometric mixture of Ni(OH) ₂ prepared in the STR and 3% excess of LiOH•H ₂ O heated up to 800°C under oxygen flow. TG curve in black and its derivative DTG curve in blue.
Figure 4.3: High temperature operando X-ray diffraction patterns of a mixture of Ni(OH) ₂ and LiOH•H ₂ O in air between 35 and 500°C. Calculated patterns of LiOH•H ₂ O (red, collection code 9138 [183]) and Ni(OH) ₂ (black, collection code 169978 [36]) at the bottom, calculated patterns from the ICSD of NiO (pink, collection code 9866 [186]), Li ₂ CO ₃ (turquoise, collection code 100324 [185]) and LiOH (blue, collection code 27543 [184]) at the top. Measured patterns between 35 and 300°C in orange and between 350 and 500°C in green
Figure 4.4: Powder X-ray diffraction patterns of selected as prepared LiNiO ₂ samples. These samples are all pre-calcined for 5 h at 500°C and calcined for 15 h at 670°C (purple), 710°C (green) and 750°C (blue). Calculated LiNiO ₂ pattern from ICSD (black, collection code 78687 [187]) as comparison including Bragg peak labels. Remaining XRD patterns can be found in the supplementary information.
Figure 4.5: Refinement of measured Cu source XRD pattern of LiNiO ₂ pre-calcined for 5 h at 500°C and calcined for 5 h at 710°C. Measured pattern (black), calculated pattern of LiNiO ₂ (orange, collection code 78687 [187]) and the difference between observed and calculated patterns (grey). Peak positions of LiNiO ₂ in green.
Figure 4.6: SEM images of LiNiO ₂ samples calcined for 15 h. a) sample 15/670, b) sample 5/350-15/710, c) sample 5/500-15/750. Lower magnification images (left) and higher magnification (right)
Figure 4.7: SEM images of LiNiO ₂ samples calcined for 10 h. d) sample 10/750, e) sample 5/350-10/750, f) sample 5/500-10/710. Lower magnification images (left) and higher magnification (right)
Figure 4.8: SEM images of LiNiO ₂ samples calcined for 5 h. g) sample 5/750, h) sample 5/350-5/750, i) sample 5/500-5/710. Lower magnification images (left) and higher magnification (right)
Figure 4.9: Charge/discharge plot for LiNiO ₂ synthesised via a solid-state route, sample 15/670 (blue), sample 5/350-15/710 (orange) and sample 5/500-15/750 (green). Cycled between 3 –

4.3 V vs. Li/Li ⁺ at a rate of C/20 for two cycles and C/2 for the third cycle. Solid line shows 1 ^s
cycle, dashed line depicts 2 nd cycle and dotted line represents the 3 rd cycle
Figure 4.10: Discharge capacity retention plot including coulombic efficiencies over 100 cycles for LiNiO ₂ synthesised via a solid-state route, sample 15/670 (blue), sample 5/350-15/710 (orange) and sample 5/500-15/750 (green). Cycled between 3 – 4.3 V vs. Li/Li ⁺ at a rate of C/20
for two cycles and C/2 for the third cycle.
Figure 4.11: Differential Capacity plots obtained for LiNiO ₂ synthesised via a solid-state route a) sample 15/670, b) sample 5/350-15/710 and c) 5/500-15/750. Coin half cells cycled between 3 – 4.3 V vs. Li/Li ⁺ at a rate of C/20 for two cycles and C/2 for the third cycle. 2 nd cycle depicted in blue, 3 rd cycle in orange and 100 th cycle in green.
Figure 4.12: Charge/discharge plot for LiNiO ₂ synthesised via a solid-state route, sample 10/750 (yellow), sample 5/350-10/750 (turquoise) and sample 5/500-10/710 (pink). Cycled between 3 – 4.3 V vs. Li/Li ⁺ at a rate of C/20 for two cycles and C/2 for the third cycle. Solid line shows 1 st cycle, dashed line depicts 2 nd cycle and dotted line represents the 3 rd cycle66
Figure 4.13: Discharge capacity retention plot including coulombic efficiencies over 100 cycles for LiNiO ₂ synthesised via a solid-state route, sample 10/750 (yellow), sample 5/350-10/750 (turquoise) and sample 5/500-15/710 (pink). Cycled between 3 – 4.3 V vs. Li/Li ⁺ at a rate of C/20 for two cycles and C/2 for the third cycle
Figure 4.14: Differential Capacity plots obtained for LiNiO ₂ synthesised via a solid-state route a) sample 10/750, b) sample 5/350-10/750 and c) 5/500-10/710. Coin half cells cycled betweer 3 – 4.3 V vs. Li/Li ⁺ at a rate of C/20 for two cycles and C/2 for the third cycle. 2 nd cycle depicted in blue, 3 rd cycle in orange and 100 th cycle in green.
Figure 4.15: Charge/discharge plot for LiNiO ₂ synthesised via a solid-state route, sample 5/750 (green), sample 5/350-5/750 (purple) and sample 5/500-5/710 (red). Cycled between 3 – 4.3 V vs. Li/Li ⁺ at a rate of C/20 for two cycles and C/2 for the third cycle. Solid line shows 1 st cycle dashed line depicts 2 nd cycle and dotted line represents the 3 rd cycle
Figure 4.16: Discharge capacity retention plot including coulombic efficiencies over 100 cycles for LiNiO ₂ synthesised via a solid-state route, sample 5/750 (green), sample 5/350-5/750 (purple) and sample 5/500-5/710 (red). Cycled between 3 – 4.3 V vs. Li/Li ⁺ at a rate of C/20 for two cycles and C/2 for the third cycle
DWD CYCLES ADOLE / / TOT THE INITO CYCLE

Figure 4.17: Differential Capacity plots obtained for LiNiO ₂ synthesised via a solid-state route,
a) sample 5/750, b) sample 5/350-5/750 and c) 5/500-5/710. Coin half cells cycled between 3
-4.3 V vs. Li/Li ⁺ at a rate of C/20 for two cycles and C/2 for the third cycle. 2 nd cycle depicted
in blue, 3 rd cycle in orange and 100 th cycle in green
Figure 4.18: Overview and comparison of 1 st cycle capacity plot (left) and discharge capacity retention plot (right) of the pre-selected nine samples of LiNiO ₂ , calcined under different conditions.
Figure 5.1: STR set-up containing a precursor solution of nickel sulphate, ammonia and sodium hydroxide
Figure 5.2: Schematic of stirred tank reactor. [212]80
Figure 5.3: XRD patterns of precipitated Ni(OH) ₂ precursor material synthesised at different feeding and dwelling times (blue: feeding time of 5 h and dwelling time of 14 h; purple: feeding time of 9 h and dwelling time of 10 h; pink: feeding time of 17 h and dwelling time of 20 h). Calculated Ni(OH) ₂ pattern from ICSD (black, collection code 169978 [36]) as comparison including Bragg peak labels.
Figure 5.4: Particle size distribution derived from laser diffraction of precipitated Ni(OH) ₂ precursor material synthesised at different feeding and dwelling times (blue: feeding time of 5 h and dwelling time of 14h; purple: feeding time of 9 h and dwelling time of 10 h; pink: feeding time of 17 h and dwelling time of 20 h). 82 Figure 5.5: SEM images of precipitated Ni(OH) ₂ at different reaction times (short to long time from left to right).
Figure 5.6: XRD patterns of precipitated Ni(OH) ₂ precursor material synthesised at different reaction temperatures (blue: 40°C; purple: 50°C; pink: 60°C). Calculated Ni(OH) ₂ pattern from ICSD (black, collection code 169978 [36]) as comparison including Bragg peak labels85
Figure 5.7: Particle size distribution derived from laser diffraction of precipitated Ni(OH) ₂ precursor material synthesised at different reaction temperatures (blue: 40°C; purple: 50°C; pink: 60°C).
Figure 5.8: SEM images of precipitated Ni(OH) ₂ at different reaction temperatures (low to high temperature from left to right)

Figure 5.9: XRD patterns of precipitated Ni(OH) ₂ precursor material synthesised at different
Ni:NH ₄ OH ratios (orange: ratio 1:1.2; blue: ratio 1:2.5; green: ratio 1:3.75; red: ratio 1:5).
Calculated Ni(OH) ₂ pattern from ICSD (black, collection code 169978 [36]) as comparison
including Bragg peak labels
Figure 5.10: Particle size distribution derived from laser diffraction of precipitated Ni(OH) ₂
precursor material synthesised at different Ni:NH ₄ OH ratios; (orange: ratio 1:1.2; blue: ratio
1:2.5; green: ratio 1:3.75; red: ratio 1:5))
Figure 5.11: SEM images of the precursor material Ni(OH) ₂ using different Ni:NH ₄ OH ratios
(low to high ratio from left to right)89
Figure 5.12: SEM images of cross-sections of as-prepared precursor material Ni(OH) ₂ using
different Ni:NH ₄ OH ratios (low to high ratio from left to right)
unicient ivi.ivii4011 fatios (low to ingli fatio from left to fight).
Figure 5.13: XRD patterns of precipitated β-Ni(OH) ₂ precursor material synthesised at different
pH (blue: 10.6; purple: 11; pink: 11.4). Calculated Ni(OH) ₂ pattern from ICSD (black,
collection code 169978 [36]) as comparison including Bragg peak labels91
Figure 5.14: Particle size distribution derived from laser diffraction of precipitated Ni(OH) ₂
precursor material synthesised at different pH (purple: pH 11; pink: pH 11.4)91
Figure 5.15: SEM images of precipitated Ni(OH) ₂ at different pHs (low to high pH from left to
right)92
Figure 5.16: XRD patterns of LiNiO ₂ material synthesised using different Ni:NH ₄ OH ratios
during precursor synthesis (orange: ratio 1:1.2; blue: ratio 1:2.5; green: ratio 1:3.75; red: ratio
1:5). Calculated LiNiO ₂ pattern from ICSD (black, collection code 78687 [187]) as comparison
including Bragg peak labels. Zoomed-in sections of split Bragg peaks 006/102 at 38°20 and
008/110 at 64.5° 2θ on the right95
000/110 at 04.5 20 on the right
Figure 5.17: Particle size distribution derived from laser diffraction of LiNiO ₂ material
synthesised using different Ni:NH ₄ OH ratios during precursor synthesis (orange: ratio 1:1.2;
blue: ratio 1:2.5; green: ratio 1:3.75; red: ratio 1:5)
Figure 5.18: SEM images of annealed as-prepared precursor Ni(OH) ₂ using different
Ni:NH ₄ OH ratios (low to high ratio from left to right)

Figure 5.19: SEM images of cross-sections of as-prepared precursor material Ni(OH) ₂ (top) and lithiated LiNiO ₂ (bottom) using different Ni:NH ₄ OH ratios (low to high ratio from left to right)
Figure 5.20: Multi point BET surface analysis and linear fits of annealed as-prepared precursor Ni(OH) ₂ at different Ni:NH ₄ OH ratios (orange: ratio 1:1.2; blue: ratio 1:2.5; green: ratio 1:3.75; red: ratio 1:5)).
Figure 5.21: Mo source XRD patterns of LiNiO ₂ material synthesised using different Ni:NH ₄ OH ratios during precursor synthesis (orange: ratio 1:1.2; blue: ratio 1:2.5; green: ratio 1:3.75; red: ratio 1:5). Calculated LiNiO ₂ pattern from ICSD (black, collection code 78687 [187]) as comparison. [187]
Figure 5.22: Refinement of measured Mo source XRD pattern of LiNiO ₂ pre-calcined for 5 h at 350°C and calcined for 15 h at 710°C. Measured pattern (black), calculated pattern of LiNiO ₂ (orange, collection code 78687 [187]) and the difference between observed and calculated patterns (grey). Peak positions of LiNiO ₂ in green
Figure 5.23: Electrochemical data obtained for LiNiO ₂ synthesised using as-prepared Ni(OH) ₂ precursor with different Ni:NH ₄ OH ratios. Precursors pre-calcined for 5 h at 350°C and calcined for 10 h at 710°C. Charge/discharge plot between 3 – 4.3 V vs. Li/Li ⁺ at a rate of C/20 for two cycles and C/2 for the third cycle. Solid line shows 1 st cycle, dashed line depicts 2 nd cycle and dotted line represents the 3 rd cycle. Ni:NH ₄ OH ratio of 1:1.2 (orange), 1:2.5 (blue), 1:3.75 (green) and 1:5 (red).
Figure 5.24: Discharge capacity retention and coulombic efficiencies obtained for LiNiO ₂ synthesised using as-prepared Ni(OH) ₂ precursor with different Ni:NH ₄ OH ratios. Precursors pre-calcined for 5 h at 350°C and calcined for 10 h at 710°C. Solid line shows 1 st cycle, dashed line depicts 2 nd cycle and dotted line represents the 3 rd cycle. Ni:NH ₄ OH ratio of 1:1.2 (orange), 1:2.5 (blue), 1:3.75 (green) and 1:5 (red).
Figure 5.25: Differential capacity plots obtained for LiNiO ₂ synthesised using as-prepared Ni(OH) ₂ precursor with a Ni:NH ₄ OH ratio of a) 1:1.2 (orange), b) 1:2.5 (blue), c) 1:3.75 (green) and d) 1:5(red). Precursors were pre-calcined for 5 h at 350°C and calcined for 10 h at 710°C. Potential window between 3 – 4.3 V vs. Li/Li ⁺ at a rate of C/20. Comparison between second cycle (after conditioning), third cycle and 100 th cycle
Figure 5.26: Magnified XANES spectra collected on the Ni K-edge of LiNiO ₂ cycled in half cells to different states of charge. OCV (blue), 3.8 V (yellow), 4.2 V (green), 4.5 V (red), 4.7 V

(purple) and charged to 4.3 V and discharged to 3 V (black). Inset shows a magnified view of the absorption edge at half height (E _{0.5}) of the normalised spectra
Figure 5.27: Full range of hard XAS spectra collected on the Ni K-edge of LiNiO ₂ cycled in half cells to 3.8 V (yellow), 4.2 V (green), 4.5 V (red) and 4.7 V (purple)
Figure 5.28: Magnified Fourier transformed EXAFS spectra collected on the Ni K-edge of LiNiO ₂ cycled in half cells to 3.8 V (yellow), 4.2 V (green), 4.5 V (red) and 4.7 V (purple) Dashed lines highlight the Ni-O and Ni-Ni distances
Figure 5.29: sXAS spectra of the Ni L-edge of cycled LiNiO ₂ cathodes probed in TEY mode at OCV (blue), 3.8 V (yellow), 4.2 V (green), 4.4 V (red) and 4.7 V (purple). Optimised LNC was used made with a precursor synthesised at a Ni:NH ₄ OH ratio of 1:5. The cathode contains 90% of LNO, 5% of carbon black and 5% of PVDF
Figure 5.30: sXAS spectra of the O K-edge of cycled LiNiO ₂ cathodes probed in TEY mode at OCV (blue), 3.8 V (yellow), 4.2 V (green), 4.4 V (red) and 4.7 V (purple). Optimised LNO was used made with a precursor synthesised at a Ni:NH ₄ OH ratio of 1:5. The cathode contains 90 % of LNO, 5 % of carbon black and 5 % of PVDF
Figure 5.31: HAXPES data from the C 1s (left) and O 1s (right) regions of cycled LNO electrodes using an incident X-ray energy of 2.2 keV. OCV data is shown in yellow, 3.8 V in light green, 4.2 V in dark green, 4.4 V in light blue and 4.7 V in dark blue
Figure 5.32: HAXPES data from the Ni 3p region of cycled LNO electrodes using an incident X-ray energy of 2.2 keV. OCV data is shown in yellow, 3.8 V in light green, 4.2 V in dark green 4.4 V in light blue and 4.7 V in dark blue
Figure 5.33: Curie-Weiss plot showing linear behaviour above 50 K for LiNiO ₂ synthesised with different Ni:NH ₄ OH ratios during the precursor synthesis
Figure 5.34: Susceptibility curve for LiNiO ₂ synthesised with different Ni:NH ₄ OH ratios during the precursor synthesis
Figure 5.35: Decay positron asymmetry obtained from μSR measurements at 300 K for a powder sample of LiNiO ₂ synthesised using a precursor with a Ni:NH ₄ OH rate of 1:5. Data from zero field (black), applied longitudinal fields at 5 Gauss (orange) and 10 Gauss (yellow) and corresponding fits using a dynamic Kubo-Toyabe function. Plot by Innes McClelland. 117

Figure 5.36: Temperature dependency of the static field distribution at the muon stopping site
Δ (blue) and the fluctuation rate ν (orange) for μSR data collected for a powder sample of
LiNiO ₂ synthesised using a precursor with a Ni:NH ₄ OH rate of 1:5118
Figure 5.37: Muon relaxation rates during operando μSR measurements of LiNiO ₂ cell during
1 st cycle charge (left) and discharge (right). Plot by Innes McClelland119
Figure 5.38: 1st cycle charge/discharge curve (left) and dQ/dV plot (right) of muon operando
cell with Li anode and LiNiO ₂ cathode. Plot by Innes McClelland
Figure 5.39: Field fluctuation rate v of 1st cycle charge (left) and discharge (right) during
operando μSR measurements of LiNiO ₂ cell. Plot by Innes McClelland
Figure 5.40: Crystallite alignment from XRD-CT corrected and reconstructed 3D volumetric
images. Bragg reflections (003) in red, (101) in green and (104) in dark blue. Image by Finden
Ltd (left). Secondary pristine LiNiO ₂ particle cross-section SEM (right)120
Figure 5.41: Comparison of global XRD patterns of LiNiO2 (black) and local XRD patterns
(red, green and dark blue) showing localised differences in peak intensities. Graph by Finden
Ltd
Figure 6.1: XRD patterns of as prepared doped Ni(OH) ₂ samples. Co-doped (blue), Mn-doped
(red), Cu-doped (green), Zn-doped (orange), Sn-doped (pink), Zr-doped (purple), Ti-doped
(yellow) and W-doped (turquoise). Calculated Ni(OH)2 pattern from ICSD (black) as
comparison including Bragg peak labels128
Figure 6.2: XRD patterns of as prepared doped LiNiO ₂ samples. These samples are all pre-
calcined for 5 h at 350°C and calcined for 15 h at 710°C. Co-doped (blue), Mn-doped (red), Cu-
doped (green), Zn-doped (orange), Sn-doped (pink), Zr-doped (purple), Ti-doped (yellow) and
W-doped (turquoise). Calculated LiNiO2 pattern from ICSD (black) as comparison including
Bragg peak labels
Figure 6.3: Electrochemical data obtained for doped LiNiO ₂ synthesised via a solid-state route,
pre-calcined for 5 h at 350°C and calcined for 15 h at 710°C. Charge/discharge plot between 3
– 4.3 V vs. Li/Li ⁺ at a rate of C/20 for two cycles and C/2 for the third cycle. Solid line shows
1st cycle, dashed line depicts 2nd cycle and dotted line represents the 3rd cycle. Co-doped
(blue), Mn-doped (red), Cu-doped (green), Zn-doped (orange), Sn-doped (pink), Zr-doped
(purple), Ti-doped (yellow) and W-doped (turquoise)

Figure 6.4: Electrochemical data obtained for doped LiNiO ₂ synthesised via a solid-state route.
pre-calcined for 5 h at 350°C and calcined for 15 h at 710°C. Differential capacity plot dQ/dV
for the second cycle. Potential window between 3 – 4.3 V vs. Li/Li ⁺ at a rate of C/20. Co-doped
(blue), Mn-doped (red), Cu-doped (green), Zn-doped (orange), Sn-doped (pink), Zr-doped
(purple), Ti-doped (yellow) and W-doped (turquoise)
Figure 6.5: Electrochemical data obtained for doped LiNiO ₂ synthesised via a solid-state route pre-calcined for 5 h at 350°C and calcined for 15 h at 710°C. Discharge capacity retention and
coulombic efficiencies over 100 cycles. Co-doped (blue), Mn-doped (red), Cu-doped (green),
Zn-doped (orange), Sn-doped (pink), Zr-doped (purple), Ti-doped (yellow) and W-doped
(turquoise)
Figure 6.6: XRD pattern of Co-doped LiNiO ₂ , pre-calcined for 5 h at 350°C and calcined for
15h at 710°C. Calculated LiNiO ₂ (black, collection code 78687 [187])) and LiNi _{0.96} Co _{0.04} O ₂
(grey, collection code 83303 [103]) patterns from ICSD for comparison
Figure 6.7: SEM images of Co-doped Ni(OH) ₂ (left) and Co-doped LiNiO ₂ (right). Particle size
distribution of secondary particle assemblies using smaller magnification in the top row and
primary particles at higher magnification in the bottom row
Figure 6.8: SEM image of a particles cross-section (left) and EDX analysis of the cross-section
of as-prepared Co-doped Ni(OH)2 precursor (top row) and Co-doped LiNiO2 (bottom row).
Elemental mapping of nickel (turquoise), oxygen (green) and cobalt (pink)138
Figure 6.9: Electrochemical data obtained for Co-doped LiNiO2 synthesised via a solid-state
route, pre-calcined for 5 h at 350°C and calcined for 15 h at 710°C. Differential capacity plot
dQ/dV comparing cycle 3 and 100. Potential window between 3 – 4.3 V vs. Li/Li ⁺ at a rate of
C/20
Figure 6.10: XRD pattern of Mn-doped LiNiO ₂ , pre-calcined for 5 h at 350°C and calcined for
15h at 710°C. Calculated LiNiO ₂ (black, collection code 78687 [187])) and LiNi _{0.5} Mn _{0.5} O ₂
(grey, collection code 152273 [208]) patterns from ICSD for comparison140
Figure 6.11: SEM images of Mn-doped Ni(OH) ₂ (left) and Mn-doped LiNiO ₂ (right). Particle
size distribution of secondary particle assemblies using smaller magnification in the top row
and primary particles at higher magnification in the bottom row

Figure 6.12: SEM image of a particles cross-section (left) and EDX analysis of the cross-section	on
of as-prepared Mn-doped Ni(OH) ₂ precursor (top row) and Mn-doped LiNiO ₂ (bottom row	v).
Elemental mapping of nickel (turquoise), oxygen (green) and manganese (pink)14	42
Figure 6.13: Electrochemical data obtained for Mn-doped LiNiO ₂ synthesised via a solid-sta	ıte
route, pre-calcined for 5h at 350°C and calcined for 15h at 710°C. Differential capacity pl	lot
dQ/dV comparing cycle 3 and 100. Potential window between 3 – 4.3 V vs. Li/Li ⁺ at a rate	of
C/20	42
Figure 6.14: XRD pattern of Cu-doped LiNiO ₂ , pre-calcined for 5 h at 350°C and calcined f	
15 h at 710°C. Calculated LiNiO ₂ (black, collection code 78687 [187])) and Li ₂ CO ₃ (turquois	
collection code 100324 [185]) patterns from ICSD for comparison. Asterisks ma	
corresponding Bragg peaks	43
Figure 6.15: SEM images of Cu-doped Ni(OH) ₂ (left) and Cu-doped LiNiO ₂ (right). Partic	ele
size distribution of secondary particle assemblies using smaller magnification in the top ro)W
and primary particles at higher magnification in the bottom row	44
Figure 6.16: SEM image of a particles cross-section (left) and EDX analysis of the cross-section	
of as-prepared Cu-doped Ni(OH) ₂ precursor (top row) and Cu-doped LiNiO ₂ (bottom row	
Elemental mapping of nickel (turquoise), oxygen (green) and copper (pink)14	45
Figure 6.17: Electrochemical data obtained for Cu-doped LiNiO ₂ synthesised via a solid-sta	ıte
route, pre-calcined for 5 h at 350°C and calcined for 15 h at 710°C. Differential capacity pl	lot
dQ/dV comparing cycle 3 and 100. Potential window between 3 – 4.3 V vs. Li/Li ⁺ at a rate	of
C/2014	45
E	c
Figure 6.18: XRD pattern of Zn-doped LiNiO ₂ , pre-calcined for 5 h at 350°C and calcined f	
15h at 710°C. Calculated LiNiO ₂ (black, collection code 78687 [187])) pattern from ICSD f	
comparison	46
Figure 6.19: SEM images of Zn-doped Ni(OH) ₂ (left) and Zn-doped LiNiO ₂ (right). Partic	ele
size distribution of secondary particle assemblies using smaller magnification in the top ro	w
and primary particles at higher magnification in the bottom row.	47
Figure 6.20: SEM image of a particles cross-section (left) and EDX analysis of the cross-section	on
of as-prepared Zn-doped Ni(OH) ₂ precursor (top row) and Zn-doped LiNiO ₂ (bottom row	
	47

Figure 6.21: Electrochemical data obtained for Zn-doped LiNiO ₂ synthesised via a solid-state
route, pre-calcined for 5 h at 350°C and calcined for 15 h at 710°C. Differential capacity plo
dQ/dV comparing cycle 3 and 100. Potential window between $3-4.3V$ vs. Li/Li ⁺ at a rate of
C/20
Figure 6.22: XRD pattern of Sn-doped LiNiO ₂ , pre-calcined for 5h at 350°C and calcined for 15h at 710°C. Calculated LiNiO ₂ (black, collection code 78687 [187])) and Li ₂ CO ₃ (red collection code 100324 [185]) patterns from ICSD for comparison. Asterisks mark corresponding Bragg peaks.
Figure 6.23: SEM images of Sn-doped Ni(OH) ₂ (left) and Sn-doped LiNiO ₂ (right). Particle size distribution of secondary particle assemblies using smaller magnification in the top row and primary particles at higher magnification in the bottom row
Figure 6.24: SEM image of a particles cross-section (left) and EDX analysis of the cross-section of as-prepared Sn-doped Ni(OH) ₂ precursor (top row) and Sn-doped LiNiO ₂ (bottom row) Elemental mapping of nickel (turquoise), oxygen (green) and tin (pink)
Figure 6.25: Electrochemical data obtained for Sn-doped LiNiO $_2$ synthesised via a solid-state route, pre-calcined for 5 h at 350°C and calcined for 15 h at 710°C. Differential capacity plot dQ/dV for the first, second and third cycle. Potential window between 3 – 4.3 V vs. Li/Li ⁺ at a rate of C/20.
Figure 6.26: XRD pattern of Zr-doped LiNiO ₂ , pre-calcined for 5h at 350°C and calcined for 15h at 710°C. Calculated LiNiO ₂ (black, collection code 78687 [187]) and Li ₂ ZrO ₃ (pink collection code 94893 [209]) patterns from ICSD for comparison. Asterisks mark corresponding Bragg peaks.
Figure 6.27: SEM images of Zr-doped Ni(OH) ₂ (left) and Zr-doped LiNiO ₂ (right). Particle size distribution of secondary particle assemblies using smaller magnification in the top row and primary particles at higher magnification in the bottom row.
Figure 6.28: SEM image of a particles cross-section (left) and EDX analysis of the cross-section of as-prepared Zr-doped Ni(OH) ₂ precursor (top row) and Zr-doped LiNiO ₂ (bottom row) Elemental mapping of nickel (turquoise), oxygen (green) and zirconium (pink)
Figure 6.29: Electrochemical data obtained for Zr-doped LiNiO ₂ synthesised via a solid-state route, pre-calcined for 5h at 350°C and calcined for 15h at 710°C. Differential capacity plo

rate of C/20
Figure 6.30: XRD pattern of Ti-doped LiNiO ₂ , pre-calcined for 5 h at 350°C and calcined for 15 h at 710°C. Calculated LiNiO ₂ (black, collection code 78687 [187])) and LiNi _{0.7} Ti _{0.3} O ₂ (grey, collection code 83283 [210]) patterns from ICSD for comparison
Figure 6.31: SEM images of Ti-doped Ni(OH) ₂ (left) and Ti-doped LiNiO ₂ (right). Particle size distribution of secondary particle assemblies using smaller magnification in the top row and primary particles at higher magnification in the bottom row
Figure 6.32: SEM image of a particles cross-section (left) and EDX analysis of the cross-section of as-prepared Ti-doped Ni(OH) ₂ precursor (top row) and Ti-doped LiNiO ₂ (bottom row) Elemental mapping of nickel (turquoise), oxygen (green) and titanium (pink)
Figure 6.33: Electrochemical data obtained for Ti-doped LiNiO ₂ synthesised via a solid-state route, pre-calcined for 5 h at 350°C and calcined for 15 h at 710°C. Differential capacity plot dQ/dV comparing cycle 3 and 100. Potential window between 3 – 4.3 V vs. Li/Li ⁺ at a rate of C/20.
Figure 6.34: XRD pattern of W-doped LiNiO ₂ , pre-calcined for 5 h at 350°C and calcined for 15 h at 710°C. Calculated LiNiO ₂ (black, collection code 78687 [187])) and LiNi _{0.99} W _{0.01} O ₂ (grey, collection code 47982 [211]) patterns from ICSD for comparison
Figure 6.35: Refinement of measured Cu source XRD pattern of W-doped LiNiO ₂ Measured pattern (black), calculated pattern of LiNiO ₂ (orange, collection code 78687 [187]) and the difference between observed and calculated patterns (grey). Peak positions of LiNiO ₂ in green
Figure 6.36: SEM images of W-doped Ni(OH) ₂ (left) and W-doped LiNiO ₂ (right). Particle size distribution of secondary particle assemblies using smaller magnification in the top row and primary particles at higher magnification in the bottom row
Figure 6.37: SEM image of a particles cross-section (left) and EDX analysis of the cross-section of as-prepared Ti-doped Ni(OH) ₂ precursor (top row) and Ti-doped LiNiO ₂ (bottom row) Elemental mapping of nickel (turquoise), oxygen (green) and titanium (pink)
Figure 6.38: Electrochemical data obtained for W-doped LiNiO ₂ synthesised via a solid-state route, pre-calcined for 5 h at 350°C and calcined for 15 h at 710°C. Differential capacity plot

dQ/dV comparing cycle 3 and 100. Potential window between 3 – 4.3 V vs. Li/Li ⁺ at a rate of C/20
Figure 10.1: XRD pattern of LiNiO ₂ samples calcined for 15 h at 670°C (purple), 710°C (green) and 750°C (blue) without any pre-calcination procedure. Calculated LiNiO ₂ pattern from ICSD (black, collection code 78687 [187]) as comparison
Figure 10.2: XRD pattern of LiNiO ₂ samples calcined for 10 h at 670°C (purple), 710°C (green) and 750°C (blue) without any pre-calcination procedure. Calculated LiNiO ₂ pattern from ICSD (black, collection code 78687 [187]) as comparison
Figure 10.3: XRD pattern of LiNiO ₂ samples calcined for 5 h at 670°C (purple), 710°C (green) and 750°C (blue) without any pre-calcination procedure. Calculated LiNiO ₂ pattern from ICSD (black, collection code 78687 [187]) as comparison
Figure 10.4: XRD pattern of selected as prepared LiNiO ₂ samples. These samples are all precalcined for 5 h at 350°C and calcined for 15 h at 670°C (purple), 710°C (green) and 750°C (blue). Calculated LiNiO ₂ pattern from ICSD (black, collection code 78687 [187]) as comparison including Bragg peak labels.
Figure 10.5: XRD pattern of selected as prepared LiNiO ₂ samples. These samples are all precalcined for 5 h at 350°C and calcined for 10 h at 670°C (purple), 710°C (green) and 750°C (blue). Calculated LiNiO ₂ pattern from ICSD (black, collection code 78687 [187]) as comparison including Bragg peak labels.
Figure 10.6: XRD pattern of selected as prepared LiNiO ₂ samples. These samples are all precalcined for 5 h at 350°C and calcined for 5 h at 670°C (purple), 710°C (green) and 750°C (blue). Calculated LiNiO ₂ pattern from ICSD (black, collection code 78687 [187]) as comparison including Bragg peak labels.
Figure 10.7: XRD pattern of selected as prepared LiNiO ₂ samples. These samples are all precalcined for 5 h at 500°C and calcined for 10 h at 670°C (purple), 710°C (green) and 750°C (blue). Calculated LiNiO ₂ pattern from ICSD (black, collection code 78687 [187]) as comparison including Bragg peak labels.
Figure 10.8: XRD pattern of selected as prepared LiNiO ₂ samples. These samples are all precalcined for 5 h at 500°C and calcined for 10 h at 670°C (purple), 710°C (green) and 750°C (blue). Calculated LiNiO ₂ pattern from ICSD (black, collection code 78687 [187]) as comparison including Bragg peak labels.

Figure 10.9: Refinement of measured Cu source XRD pattern of LiNiO ₂ calcined for 15 h at
670°C without pre-calcination. Measured pattern (black), calculated LiNiO2 pattern (orange
collection code 78687 [187]) and the difference between observed and calculated pattern (grey)
Peak positions of LiNiO ₂ in green195
Figure 10.10: Refinement of measured Cu source XRD pattern of LiNiO ₂ pre-calcined for 5 h at 350°C and calcined for 15 h at 710°C. Measured pattern (black), calculated LiNiO ₂ pattern (orange, collection code 78687 [187]) and the difference between observed and calculated pattern (grey). Peak positions of LiNiO ₂ in green.
Figure 10.11: Refinement of measured Cu source XRD pattern of LiNiO ₂ pre-calcined for 5 hat 500°C and calcined for 15 h at 750°. Measured pattern (black), calculated LiNiO ₂ pattern (orange, collection code 78687 [187]) and the difference between observed and calculated pattern (grey). Peak positions of LiNiO ₂ in green
Figure 10.12: Refinement of measured Cu source XRD pattern of LiNiO ₂ calcined for 10 h at 750°C with no pre-calcination. Measured pattern (black), calculated LiNiO ₂ pattern (orange collection code 78687 [187]) and the difference between observed and calculated pattern (grey) Peak positions of LiNiO ₂ in green
Figure 10.13: Refinement of measured Cu source XRD pattern of LiNiO ₂ pre-calcined for 5 hat 350°C and calcined for 10 h at 750°C. Measured pattern (black), calculated LiNiO ₂ pattern (orange, collection code 78687 [187]) and the difference between observed and calculated pattern (grey). Peak positions of LiNiO ₂ in green.
Figure 10.14: Refinement of measured Cu source XRD pattern of LiNiO ₂ pre-calcined for 5 hat 500°C and calcined for 10 h at 710°C. Measured pattern (black), calculated LiNiO ₂ pattern (orange, collection code 78687 [187]) and the difference between observed and calculated pattern (grey). Peak positions of LiNiO ₂ in green
Figure 10.15: Refinement of measured Cu source XRD pattern of LiNiO ₂ calcined for 5 h a 750°C without pre-calcination step. Measured pattern (black), calculated LiNiO ₂ pattern (orange, collection code 78687 [187]) and the difference between observed and calculated pattern (grey). Peak positions of LiNiO ₂ in green
Figure 10.16: Refinement of measured Cu source XRD pattern of LiNiO ₂ pre-calcined for 5 h at 350°C and calcined for 5 h at 750°C. Measured pattern (black), calculated LiNiO ₂ pattern (orange, collection code 78687 [187]) and the difference between observed and calculated pattern (grey). Peak positions of LiNiO ₂ in green.
DAND THE EVEN ALL FOR THE STREET HE

Figure 10.17: Refinement of measured Cu source XRD pattern of LiNiO ₂ pre-calcined for 5 h
at 500°C and calcined for 5 h at 710°. Measured pattern (black), calculated LiNiO $_2$ pattern
(orange, collection code 78687 [187]) and the difference between observed and calculated
pattern (grey). Peak positions of LiNiO ₂ in green
Figure 10.18: Refinement of measured Cu source XRD pattern of LiNiO ₂ pre-calcined for 5 h
at 350°C and calcined for 15 h at 710°C using a Ni(OH) $_2$ precursor synthesised at a Ni:NH $_4$ OH
ratio of 1:1.2. Measured pattern (black), calculated LiNiO2 pattern (orange, collection code
78687 [187]) and the difference between observed and calculated pattern (grey). Peak positions
of LiNiO ₂ in green
Figure 10.19: Refinement of measured Cu source XRD pattern of LiNiO ₂ pre-calcined for 5 h
at 350°C and calcined for 15 h at 710°C using a Ni(OH) ₂ precursor synthesised at a Ni:NH ₄ OH
ratio of 1:2.5. Measured pattern (black), calculated LiNiO ₂ pattern (orange, collection code
78687 [187]) and the difference between observed and calculated pattern (grey). Peak positions
of LiNiO ₂ in green
Figure 10.20: Refinement of measured Cu source XRD pattern of LiNiO $_2$ pre-calcined for 5 h
at 350°C and calcined for 15 h at 710°C using a Ni(OH) $_2$ precursor synthesised at a Ni:NH $_4$ OH
ratio of 1:3.75. Measured pattern (black), calculated LiNiO2 pattern (orange, collection code
$78687\ [187]$) and the difference between observed and calculated pattern (grey). Peak positions
of LiNiO ₂ in green
Figure 10.21: Refinement of measured Cu source XRD pattern of LiNiO ₂ pre-calcined for 5 h
at 350°C and calcined for 15 h at 710°C using a Ni(OH) ₂ precursor synthesised at a Ni:NH ₄ OH
ratio of 1:5. Measured pattern (black), calculated LiNiO $_2$ pattern (orange, collection code 78687
[187]) and the difference between observed and calculated pattern (grey). Peak positions of
LiNiO ₂ in green
Figure 10.22: Refinement of measured Mo source XRD pattern of LiNiO ₂ pre-calcined for 5 h
at 350°C and calcined for 15 h at 710°C using a Ni(OH) ₂ precursor synthesised at a Ni:NH ₄ OH
ratio of 1:1.2. Measured pattern (black), calculated LiNiO ₂ pattern (orange, collection code
78687 [187]) and the difference between observed and calculated pattern (grey). Peak positions
of LiNiO ₂ in green
Figure 10.23: Refinement of measured Mo source XRD pattern of LiNiO ₂ pre-calcined for 5 h
at 350°C and calcined for 15 h at 710°C using a Ni(OH) ₂ precursor synthesised at a Ni:NH ₄ OH ratio of 1:2.5. Measured pattern (black), calculated LiNiO ₂ pattern (orange, collection code
TALLO DE 177 A IMPASTITUO DALLUTO EDIACKE CALCITIATUO E INNELA DATTUTO LOTADO COLLOCTION COMO

78687 [187]) and the difference between observed and calculated pattern (grey). Peak positions of LiNiO ₂ in green
Figure 10.24: Refinement of measured Mo source XRD pattern of LiNiO ₂ pre-calcined for 5 h at 350°C and calcined for 15 h at 710°C using a Ni(OH) ₂ precursor synthesised at a Ni:NH ₄ OH ratio of 1:3.75. Measured pattern (black), calculated LiNiO ₂ pattern (orange, collection code 78687 [187]) and the difference between observed and calculated pattern (grey). Peak positions of LiNiO ₂ in green.
Figure 10.25: Refinement of measured Mo source XRD pattern of LiNiO ₂ pre-calcined for 5 h at 350°C and calcined for 15 h at 710°C using a Ni(OH) ₂ precursor synthesised at a Ni:NH ₄ OH ratio of 1:5. Measured pattern (black), calculated LiNiO ₂ pattern (orange, collection code 78687 [187]) and the difference between observed and calculated pattern (grey). Peak positions of LiNiO ₂ in green.
Figure 10.26: Electrochemical data obtained for LiNiO ₂ using a precursor synthesised at a Ni:NH ₄ OH ratio of 1:5. LNO cathodes cycled to 3.8 V (yellow), 4.2 V (green), 4.4 V (red) and 4.7 V (purple), decrimped and used for sXAS measurements
Figure 10.27: Electrochemical data obtained for LiNiO ₂ using a precursor synthesised at a Ni:NH ₄ OH ratio of 1:5. LNO cathodes cycled to 3.8 V (yellow), 4.2 V (green), 4.4 V (red), 4.7 V (purple) and charged and discharged (4.7 V – 3 V, black), decrimped and used for HAXPES measurements.
Figure 10.28: Electrochemical data obtained for Co-doped LiNiO ₂ synthesised via a solid-state route, pre-calcined for 5 h at 350°C and calcined for 15 h at 710°C. Charge/discharge plot between 3 – 4.3 V vs. Li/Li ⁺ at a rate of C/20 for two cycles and C/2 for the third cycle. Solid line shows 1st cycle, dashed line depicts 2nd cycle and dotted line represents the 3rd cycle.
Figure 10.29: Electrochemical data obtained for Mn-doped LiNiO ₂ synthesised via a solid-state route, pre-calcined for 5 h at 350°C and calcined for 15 h at 710°C. Charge/discharge plot between 3 – 4.3 V vs. Li/Li ⁺ at a rate of C/20 for two cycles and C/2 for the third cycle. Solid line shows 1st cycle, dashed line depicts 2nd cycle and dotted line represents the 3rd cycle.
Figure 10.30: Electrochemical data obtained for Cu-doped LiNiO ₂ synthesised via a solid-state route, pre-calcined for 5 h at 350°C and calcined for 15 h at 710°C. Charge/discharge plot

between $3-4.3\,V$ vs. Li/Li $^+$ at a rate of C/20 for two cycles and C/2 for the third cycle. Solid

line shows 1st cycle, dashed line depicts 2nd cycle and dotted line represents the 3rd cycle
Figure 10.31: Electrochemical data obtained for Zn-doped LiNiO ₂ synthesised via a solid-state route, pre-calcined for 5 h at 350°C and calcined for 15 h at 710°C. Charge/discharge plot between 3 – 4.3 V vs. Li/Li ⁺ at a rate of C/20 for two cycles and C/2 for the third cycle. Solid line shows 1st cycle, dashed line depicts 2nd cycle and dotted line represents the 3rd cycle.
Figure 10.32: Electrochemical data obtained for Sn-doped LiNiO ₂ synthesised via a solid-state route, pre-calcined for 5 h at 350°C and calcined for 15 h at 710°C. Charge/discharge plot between 3 – 4.3 V vs. Li/Li ⁺ at a rate of C/20 for two cycles and C/2 for the third cycle. Solid line shows 1st cycle, dashed line depicts 2nd cycle and dotted line represents the 3rd cycle.
Figure 10.33: Electrochemical data obtained for Zr-doped LiNiO ₂ synthesised via a solid-state route, pre-calcined for 5 h at 350°C and calcined for 15 h at 710°C. Charge/discharge plot between 3 – 4.3 V vs. Li/Li ⁺ at a rate of C/20 for two cycles and C/2 for the third cycle. Solid line shows 1st cycle, dashed line depicts 2nd cycle and dotted line represents the 3rd cycle.
Figure 10.34: Electrochemical data obtained for Ti-doped LiNiO ₂ synthesised via a solid-state route, pre-calcined for 5 h at 350°C and calcined for 15 h at 710°C. Charge/discharge plot between 3 – 4.3 V vs. Li/Li ⁺ at a rate of C/20 for two cycles and C/2 for the third cycle. Solid line shows 1st cycle, dashed line depicts 2nd cycle and dotted line represents the 3rd cycle.
Figure 10.35: Electrochemical data obtained for W-doped LiNiO ₂ synthesised via a solid-state route, pre-calcined for 5 h at 350°C and calcined for 15 h at 710°C. Charge/discharge plot between 3 – 4.3 V vs. Li/Li ⁺ at a rate of C/20 for two cycles and C/2 for the third cycle. Solid line shows 1st cycle, dashed line depicts 2nd cycle and dotted line represents the 3rd cycle.
Figure 10.36: Refinement of measured Cu source XRD pattern of Co-doped LiNiO ₂ calcined for 5 h at 350°C and calcined for 15 h at 710°C using a 3% Co-doped Ni(OH) ₂ precursor synthesised at a Ni:NH ₄ OH ratio of 1:5. Measured pattern (black), calculated LiNiO ₂ pattern (orange, collection code 78687 [187]) and the difference between observed and calculated pattern (grey). Peak positions of LiNiO ₂ in green

Figure 10.37: Refinement of measured Cu source XRD pattern of Mn-doped LiNiO ₂ calcined
for 5 h at 350 $^{\circ}\text{C}$ and calcined for 15 h at 710 $^{\circ}\text{C}$ using a 3 $\%$ Mn-doped Ni(OH) ₂ precursor
$synthesised \ at \ a \ Ni:NH_4OH \ ratio \ of \ 1:5. \ Measured \ pattern \ (black), \ calculated \ LiNiO_2 \ pattern$
(orange, collection code 78687 [187]) and the difference between observed and calculated
pattern (grey). Peak positions of LiNiO ₂ in green209
Figure 10.38: Refinement of measured Cu source XRD pattern of Cu-doped LiNiO ₂ calcined
for $5h$ at $350^{\circ}\mathrm{C}$ and calcined for $15h$ at $710^{\circ}\mathrm{C}$ using a 3% Cu-doped $Ni(OH)_2$ precursor
$synthesised \ at \ a \ Ni:NH_4OH \ ratio \ of \ 1:5. \ Measured \ pattern \ (black), \ calculated \ LiNiO_2 \ pattern$
(orange, collection code 78687 [187]) and the difference between observed and calculated
pattern (grey). Peak positions of LiNiO ₂ in green210
Figure 10.39: Refinement of measured Cu source XRD pattern of Zn-doped LiNiO2 calcined
for $5h$ at $350^{\circ}\mathrm{C}$ and calcined for $15h$ at $710^{\circ}\mathrm{C}$ using a 3% Zn-doped $Ni(OH)_2$ precursor
$synthesised \ at \ a \ Ni:NH_4OH \ ratio \ of \ 1:5. \ Measured \ pattern \ (black), \ calculated \ LiNiO_2 \ pattern$
(orange, collection code 78687 [187]) and the difference between observed and calculated
pattern (grey). Peak positions of LiNiO ₂ in green210
Figure 10.40: Refinement of measured Cu source XRD pattern of Sn-doped LiNiO ₂ calcined
for 5 h at 350 $^{\circ}\text{C}$ and calcined for 15 h at 710 $^{\circ}\text{C}$ using a 3 $\%$ Sn-doped Ni(OH) ₂ precursor
synthesised at a Ni:NH ₄ OH ratio of 1:5. Measured pattern (black), calculated LiNiO ₂ pattern
(orange, collection code 78687 [187]) and the difference between observed and calculated
pattern (grey). Peak positions of LiNiO ₂ in green
Figure 10.41: Refinement of measured Cu source XRD pattern of Zr-doped LiNiO ₂ calcined
for $5h$ at $350^{\circ}\mathrm{C}$ and calcined for $15h$ at $710^{\circ}\mathrm{C}$ using a 3% Zr-doped Ni(OH) $_2$ precursor
synthesised at a Ni:NH ₄ OH ratio of 1:5. Measured pattern (black), calculated LiNiO ₂ pattern
(orange, collection code 78687 [187]) and the difference between observed and calculated
pattern (grey). Peak positions of LiNiO ₂ in green and of the Li ₂ ZrO ₃ side phase in blue211
Figure 10.42: Refinement of measured Cu source XRD pattern of Ti-doped LiNiO ₂ calcined
for $5h$ at $350^{\circ}\mathrm{C}$ and calcined for $15h$ at $710^{\circ}\mathrm{C}$ using a 3% Ti-doped $Ni(OH)_2$ precursor
synthesised at a Ni:NH ₄ OH ratio of 1:5. Measured pattern (black), calculated LiNiO ₂ pattern
(orange, collection code 78687 [187]) and the difference between observed and calculated
(orange, concerton code 76667 [167]) and the difference between observed and calculated

1. Introduction

In 2015 a binding global climate change agreement was drawn up in Paris to which almost 190 states committed themselves. It included the adjustment to climate change, long-term reduction of emission of greenhouse gases – also by saving energy – and the support of developing countries to adapt to climate change. Important cornerstones are the availability of clean energy, a sustainable industry, an environmentally friendly building sector, interventions for the safety of the ecosystem and the valid combat against environmental pollution. [1] To reduce the emission of greenhouse gases, a shift to a low-carbon economy and a low- or zero-emission mobility is required. A very promising technology to reduce the impacts of road transport are electric vehicles (EVs), whose main component for energy storage lithium-ion battery (LIB). These batteries are already in use in laptops and smaller devices, but there are still significant developments to be made. The reduction of cost, the increase of lifetime and energy density as well as the sustainability, responsible mining and the recyclability of the energy storage system are important tasks to consider. [2] [3] [4]

The development of batteries began in 1800, when Alessandro Volta invented the voltaic pile. A continuous current was produced by the contact of different kinds of metals in a salty solution. This discovery paved the way for the development of electrical storage based on chemical reactions. Since then, the link between electricity and chemistry was drawn by Sir Humphry Davy and between electricity and magnetism by Michael Faraday. The first rechargeable batteries were invented by Gaston Planté in 1866 (lead-acid battery) and later in 1901 the nickel-cadmium battery by Waldemar Jungner and Thomas Edison, independently. [5] [6] As new technologies demand higher capacity and more compact and safer batteries, research into lithium batteries began in the 1950s when the stability of Li in non-aqueous solutions was noticed. [7] After the commercialisation of the lithium-ion battery by Sony in 1991, the Nobel prize in chemistry was awarded to Goodenough, Whittingham and Yoshino in 2019 for their contributions to a lightweight, rechargeable and powerful battery and making a step towards a fossil fuel-free society. [8] Today, rechargeable LIBs are the dominant power source for portable electronic devices and have become suitable for EVs as the battery capacity and capacity retention has been improved. Further development is needed to increase the driving range or reduce the charging time of EVs, substitute scarce elements like cobalt, which is mined under inhuman conditions and develop new materials for the cell chemistry.

Rechargeable batteries consist of electrochemical cells that derive electrical energy from spontaneous redox reactions. In a closed system, two electrodes with different chemical potentials (anode and cathode) are immersed in a conductive fluid (electrolyte) and divided by a porous membrane (separator) as can be seen in Figure 1.1. During discharge, electrons are released at the anode and move through an external circuit to the cathode while metal ions are released into the internal solution and move through the separator to intercalate into the cathode structure. This process is reversed during charge (Figure 1.1 right).

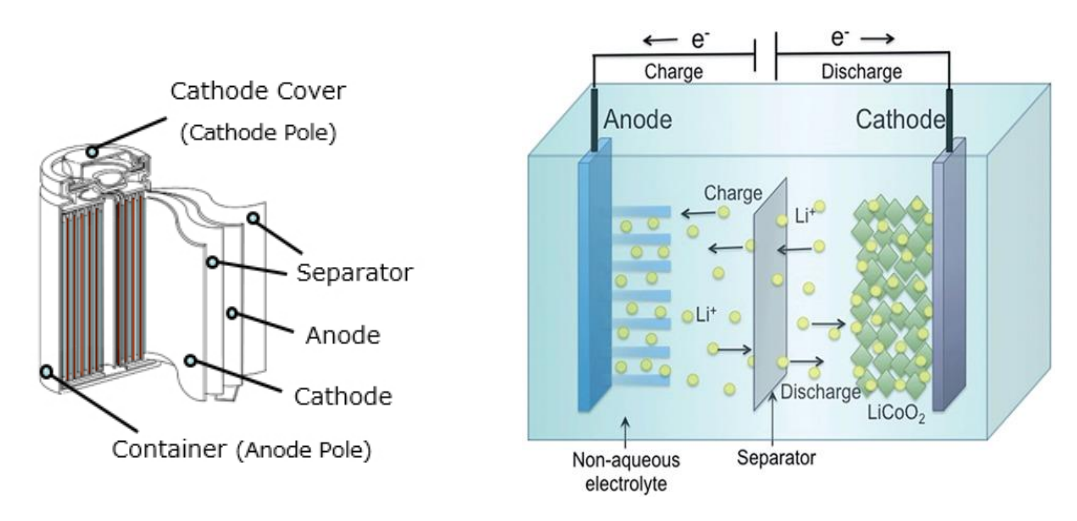


Figure 1.1: Schematic design of a LIB (left) [206] and visualisation of a LIB during charge and discharge (right). Reproduced from [207] with permission from the Royal Society of Chemistry.

To ensure long term reversibility, the (de-) intercalation of lithium ions must cause minimal volume expansion/contraction in the host structure and minimal side reactions on the electrode surface. To work properly, the battery system must be a good ionic and electronic conductor, to ensure good ion and electron transport. Thus, the positive electrode consists of the ionic conducting active material, carbon particles to increase electronic conductivity and a binder, like polyvinylidene difluoride (PVDF) or *carboxymethyl* cellulose (CMC) styrene-butadiene rubber (SBR) to act as a binder. The anode consists of graphitic carbon and is the source of lithium ions and electrons in LIBs. It is consumed during discharge and restored during charge. The electrolyte solution comprises a mixture of lithium salt, like LiPF₆ and organic solvents such as ethylene carbonate (EC) or dimethyl carbonate (DMC) and acts as an electronic insulator and ionic conductor. To prevent an electronic short circuit, the anode and cathode must be physically separated by a microporous membrane, like polyethylene (PE) or polypropylene (PP) which is permeable to Li-ions.

The focus of this PhD lies on cathode materials as these limit the overall energy density of the battery cell. There are several key requirements for cathode material development and improvement. In EVs, a high energy storage enhances the driving range and implements a high capacity and a high voltage. Also, a high-power density is essential for the use of regenerative braking in EVs as they display the fast reaction of the material with the Li-ions during intercalation and removal. Furthermore, a structure that is chemical and mechanical stable during charge and discharge, low cost and an environmental benignity are desirable improvements. [9] The aim of this PhD is to work on nickel-rich layered oxides as high-capacity material for lithium-ion batteries. To achieve a high capacity, the challenge lies in the stabilisation of the structure. The goal of this thesis is the optimisation of the co-precipitation synthesis of the precursor material Ni(OH)₂ regarding morphology, particle size and shape of the secondary particles as well as the high temperature lithiation process to synthesise LiNiO₂. Furthermore, doping of this optimised material to further increase the electrochemical performance and the structural stability will be attempted. The synthesised materials will be characterised using X-ray diffraction (XRD) for phase-purity, Rietveld refinement of XRD patterns for crystal structure analysis, scanning electron microscopy (SEM) for imaging, topographic analysis and morphology characterisation and galvanostatic cycling to examine the cycle performance, the capacity and the charge/discharge rates as well as some advanced methods like X-ray absorption near-edge structure (XANES), extended X-ray absorption fine structure (EXAFS), in-situ X-ray diffraction computer tomography (XRD-CT), magnetic measurements and muon relaxation spectroscopy, to just name a few.

2. Literature Review

2.1. Cathode Materials for LIBs

The conceptual framework behind commercial cathode materials in rechargeable lithium-ion batteries is the intercalation chemistry. Guest ions are implemented in and removed from the crystal lattice of a host material without destroying the structure. Under this consideration, TiS₂ was discovered to be a semiconductive metal with high electronic and also ionic conductivity, a good structural stability and complete reversibility, suitable as a cathode material. The LiTiS₂ battery was patented by Whittingham in 1975. [10] [11] To further improve the cell, Goodenough started to investigate oxide cathodes and patented LiCoO₂ in 1979. [12]

The voltage of an electrochemical cell is determined by the difference in chemical potentials of cathode and anode. The redox energy of the cathode should be in a low-energy state while the redox energy of the anode should be in a high-energy state with an electrolyte that is stable within the working potential window as can be seen on the right side of Figure 2.1. [13] To stabilise a high oxidation state with low energy in the active cathode material and further improve the cell voltage of the LiTiS₂ cell, O^{2-} seems very suitable as it is situated at a lower energy compared to S^{2-} as depicted on the left in Figure 2.1.

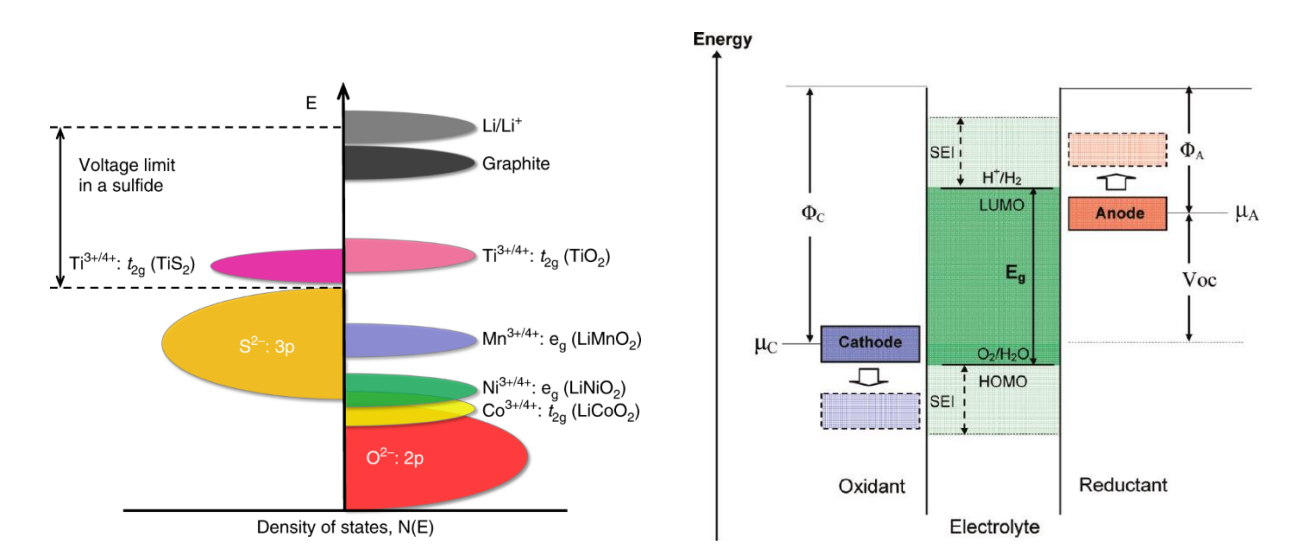


Figure 2.1: Positions of redox energies relative to the top of the anion: p bands (left), reproduced from [14] with permission from Springer Nature. Schematic energy diagram in a battery cell (right). Reproduced from [13] with permission from the American Chemical Society.

Thus, three classes of oxide cathodes were discovered by Goodenough in the 1980s, including polyanionic cathodes processed by Manthiram and Arumugam, spinel oxide cathodes developed by Thackeray and layered oxides cathodes, such as LiCoO₂, elaborated by Mizushima. [14] In layered oxides, the Li⁺ and *transition metal* (TM)³⁺ occupy octahedral sites in alternate layers in the α -NaFeO₂ structure with a $R\overline{3}m$ symmetry (Figure 2.2). Containing fast charge-discharge characteristics, a good reversibility, easy preparation and Sony commercialising it in 1991 [15], LiCoO₂ remains one of the best cathodes to date.

To further improve fast lithium-ion diffusion, enhance the limited capacity due to oxygen release and phase changes, the high cost and toxicity and most important the inhumane, perilous mining of Co, alternative compounds are investigated and developed. Many different 3d-transition metals are suitable for substitution on the cobalt site, like manganese and nickel, even mixed systems are developed as cathode materials. Each transition metal has its unique advantages and disadvantages on the structure and the electrochemical behaviour of the cathode. LiMnO₂ and LiNiO₂, operating using the redox couples Mn^{3+/4+} and Ni^{3+/4+}, are both less expensive, less toxic and show improved chemical stability compared to LiCoO₂. There is less or no overlap between the bands of Ni^{3+/4+} and O²⁻ and Mn^{3+/4+} and O²⁻, respectively, as depicted in Figure 2.1 (left), compared to Co^{3+/4+} and O²⁻. Both compounds show structural and thermal instability due to the mixed site occupation of Li⁺ and Ni²⁺ in LiNiO₂ and the low octahedral-site stabilisation energy of Mn³⁺ which leads to a phase transition from layered to spinel in LiMnO₂.

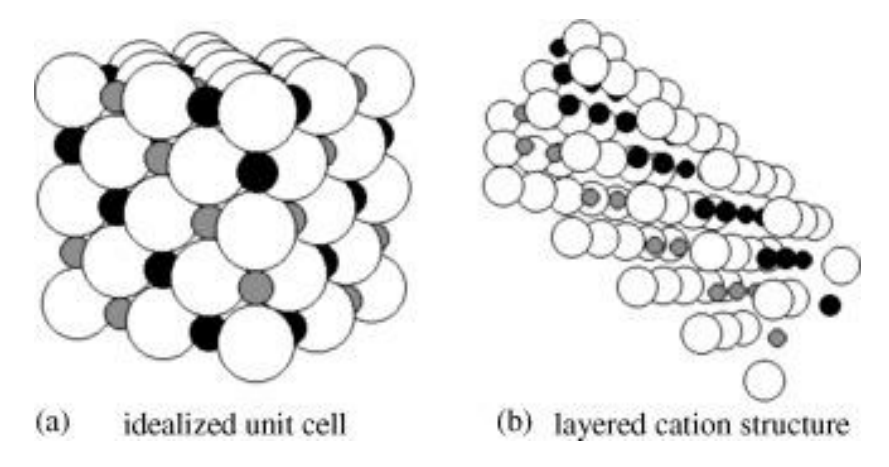


Figure 2.2: Li TMO_2 structure for (a) the idealized unit cell close packing containing O (white) Li (grey) and TM (black) and (b) a layered cation structure viewed along the (1 1 1) plane. Reproduced from [46] with permission from Elsevier.

Using ternary systems like LiNi_{1-y-z}Mn_yCo_zO₂ (NMC), the high discharge capacities of Ni, the structural stabilisation of Mn and the cycling stability of Co are combined. Mn⁴⁺ stabilises Ni²⁺

in the NMC structure but does not take part in charge-discharge processes. The main redox couple utilised during Li⁺ intercalation and removal is Ni^{2+/4+}, while Co^{3+/4+} is harnessed at higher potentials. Still, the optimum chemical composition for a combination of energy storage, power capability and cost needs to be determined. [9] [14] [16]

The increase of the Ni content and decrease of the Co content increases the capacity and lowers the costs in \$/kWh as it provides a better performance. However, for high-nickel content cathodes, the chemically unstable Ni³⁺ and Ni⁴⁺ ions cause the formation of a *cathode-electrolyte interphase* (CEI), or more generally a *surface-electrolyte interface* (SEI) and thus limits the cyclability of the cell. Phase transitions at high state of charge introduce cracks due to volume changes and further increase CEI formation leading to a rapid capacity fade. Like LiNiO₂, Ni-rich layered oxides are difficult to synthesise as an ordered layered material due to cation mixing between Li⁺ and Ni²⁺. Both have similar ionic radii (0.76 Å and 0.69 Å, respectively) [17] and thus are able to occupy the same site in the crystal structure in a random arrangement. This effect is called anti-site mixing, resulting in Li within the TM layer and TM ions hindering the motion of Li⁺ diffusion within the lithium layer. Common synthesis methods are solid-state, sol-gel and co-precipitation reactions, with the latter being the current standard procedure in the battery industry due to the scalability of the process. Those methods require a final calcination step at high temperatures (750 – 1000°C). [9] [14] [16]

To overcome the various degradation processes, electrochemically stable cations are introduced into the transition metal layers like aluminium, sodium, tungsten or magnesium to increase the structural and thermal stability. Another approach is the coating of the secondary particles to form a passivating layer and thus improve the electrochemical properties and structural stability of the cathode materials. [9] [16]

2.2. High Nickel Content Layered Cathodes

Many doped materials like LiNi_{1-y-z}Mn_yCo_zO₂ (NMC) [18] [19] [20] or LiNi_{1-x-y}Co_xAl_yO₂ (NCA) [21] [22] [23] have been extensively studied to reduce Co and other transition metal contents from the cathode. But to eliminate cobalt completely from the cathode materials, it is important to study and understand the chemistry of the prototypical LiNiO₂, its advantages like the high theoretical capacity and good reversibility at low cost, but also the challenges like the capacity loss during the first cycle and the structural and thermal instabilities.

The first publications on the layered oxide with the highest nickel content, LiNiO₂, date back to the 1950s, when Dyer et al. isolated the lithium nickelate(III) for the first time, "by bubbling oxygen through sodium hydroxide and lithium hydroxide, respectively, contained in nickel tubes at 800°C". [24] They investigated higher oxidation states of metals following Verwey et al. and their study on controlled-valency semiconductors. Verwey showed that the electronic conductivity can be varied by introducing a fraction of foreign ions into a material, which contains ions of the same element but of different oxidation states occupying the same lattice site, to fill the vacancies and balance the extra charge. [25] Goodenough et al. and a few years later also Bronger et al. developed a method to synthesis the solid solution series Li_xNi_{2-x}O₂ and study their magnetic properties. [26] [27] [28]

2.2.1. Crystal Structure

2.2.1.1. TM(OH)₂ Precursor for Layered Oxide Materials

Ni(OH)₂ is used as a precursor for the solid-state synthesis of LiNiO₂. Ni(OH)₂ is mixed with a lithium source to form the layered oxide LiNiO₂. Ni(OH)₂ and its structural, physical and electrochemical properties are extensively studied [29] [30] [31] [32] and it is also used as a positive electrode in Ni-based alkaline secondary batteries [33] [34].

Ni(OH)₂ exists as two polymorphs, the alpha and beta form. Both compounds are layered materials, whereas α -Ni(OH)₂ consists of intercalated water molecules or anions between the weakly bonded stacked β -Ni(OH)₂ layers. These impurities can rotate and translate within the plane and are not fixed at a specific crystallographic site within the structure but weakly associated with the Ni-site [35]. The crystal structures of both polymorphs can be seen in Figure 2.3. For battery application, the beta form is further used to synthesise LiNiO₂ or other layered Ni-rich oxides as cathode materials for lithium-ion batteries. β -Ni(OH)₂, isomorphous to brucite (Mg(OH)₂), crystallises in the space group $P\overline{3}m1$ ($a = 3.126\,\text{Å}$, $c = 4.605\,\text{Å}$, Z = 1) with hexagonal close-packed oxygen, edge-sharing NiO₆ octahedra with a Ni oxidation state of 2+, and hydrogen sitting in the tetrahedral spaces in the interslab [36] [37] [38]. Possible stacking faults along the c-axis cause fcc blocks to form within the lattice, increase the intersheet distances and corresponding Bragg peaks in XRD pattern to be broadened. Potential stacking faults are the rotation of the adjacent layers around the c-plane, the translation within the ab-plane or both, rotation and translation. Other structural disorders are turbostraticity and interstratification, which translates to random layer orientation due to H₂O incorporation

 $(\alpha\text{-Ni}(OH)_2)$ and phases consisting of α - and β -type structural motifs within one crystal, respectively. [39] [40] [33]

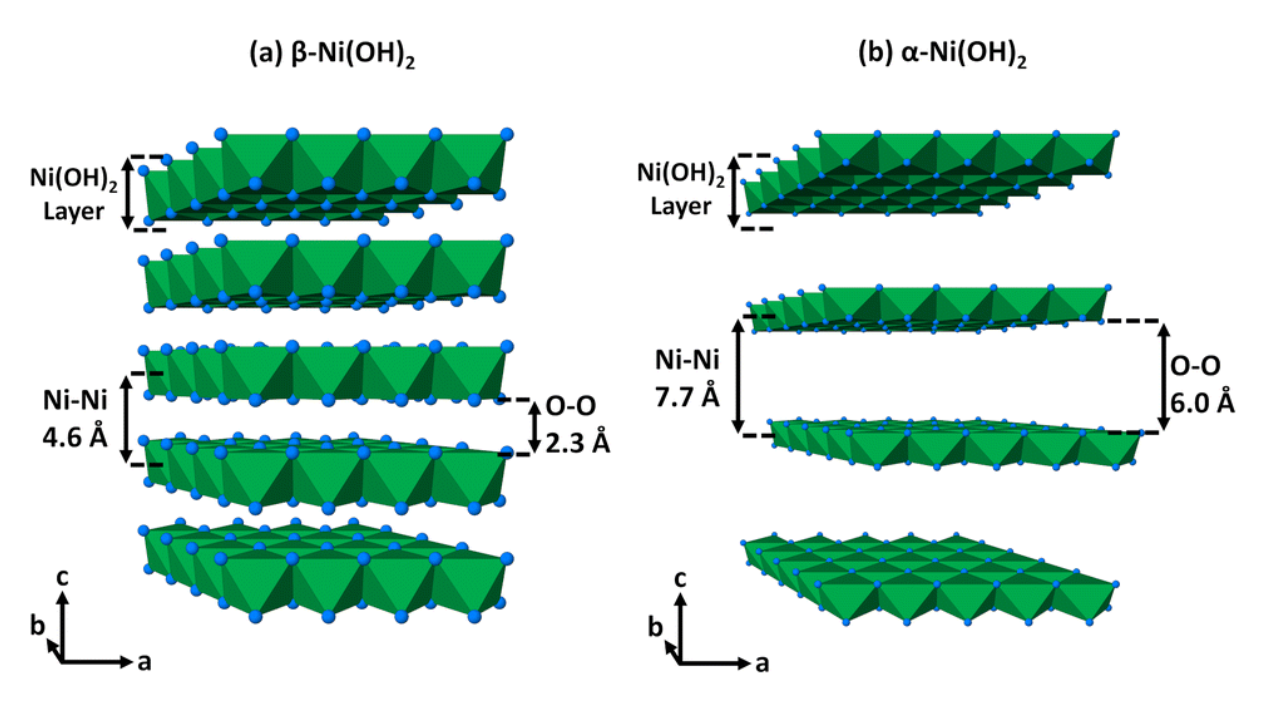


Figure 2.3: Crystal structure of β -Ni(OH)₂ (left) and α -Ni(OH)₂ (right), showing layered structure with changing interslab spacing (Ni-Ni and O-O distances) depending on intercalated anions or H₂O molecules in the α -type. NiO₆ octahedra depicted in green and blue spheres represent oxygen. Reproduced from [35] with permission from the Royal Society of Chemistry.

During precipitation from aqueous solutions, α -Ni(OH)₂ is formed and through ageing, transformed into the β -type. Using ammonia as a gelating agent in this reaction, tends to be a more effective way to gain pure β -Ni hydroxide without any intercalated water or anion molecules in the structure. [41] β -Ni(OH)₂ loses absorbed water and dehydrates above 200°C. The alpha type exhibits a weight loss of 30% below 150°C. [38]

2.2.1.2. Cathode Active Layered Oxide LiNiO₂

β-LiNiO₂ crystallises in the rhombohedral space group $R\overline{3}m$ with a trigonal symmetry and the cell parameters $a=2.88\,\text{Å}$ and $c=14.18\,\text{Å}$, isostructural to α-NaFeO₂. Two close-packed sublattices, one containing O anions and the other containing Li and Ni cations on alternating layers along the c axis, interpenetrate each other. The oxygen ions are situated in a cubic close-packed array at Wyckoff 6c sites, while Li ions are located at 3a and Ni at 3b sites. The Ni and Li octahedra are connected via edges and the Li diffusion takes place via the tetrahedral pathways formed by these octahedra. [24] [42] [43]

LNO is synthesised via a high temperature solid-state reaction of Ni(OH)₂ and LiOH•H₂O. After the initial dehydration of the reactants, the solid solution of LNO starts to form from the

electrochemically inactive rock-salt structure of NiO with a c/a ratio of 4.90. Ni²⁺ is exchanged for Li⁺ in this structure, leading to the oxidation of the remaining Ni²⁺ to Ni³⁺, to compensate the occurring charge imbalance. This is more favourable than the formation of cation vacancies in the lattice. The increasing size difference between Ni³⁺ (0.56 Å) < Ni²⁺ (0.69 Å) < Li⁺ (0.76 Å) [17] facilitates the layering by reducing steric effects, building Ni³⁺ slabs and larger Li⁺ interslabs with oxygen octahedrally surrounded. An increased c/a ratio of 4.93 due to a hexagonal distortion of the cubic lattice can be observed. These *Jahn-Teller* (JT) distortions of the NiO₆ octahedra are locally only and do not affect long range ordering of the rhombohedral structure. [24] [44]

LNO tends to lose Li⁺ from the structure during high temperature calcination due to its high vapour pressure. This and the instability of Ni³⁺ at high synthesis temperatures lead to the reduction of Ni³⁺ to Ni²⁺, which is then able to migrate from 3b sites to the octahedral vacancies (3a) in the Li layers, giving the non-stoichiometric formula [Li⁺_{1-z}Ni²⁺_z]_{3a}[Ni³⁺_{1-z}Ni²⁺_z]_{3b}[O₂]_{6c}. The occurring lattice contraction, due to smaller ions in the Li layer and the elongation of the c axis, affect the Li⁺ diffusion and thus the electrochemical properties. [43] [45] [46] [47] [48] Upon 25% cation mixing, the structure changes to a spinel structure and the electrochemically inactive rock-salt type with space group $Fm\overline{3}m$ is formed when 50% displacement is reached. This structure contains immobile Li ions and is electrochemically inactive. [49]

Various structural studies using X-ray diffraction, *inductively coupled plasma optical emission spectroscopy* (ICP-OES) [50] [51] [52] or neutron diffraction [53] [54] [55] [56] have investigated the cation mixing and the lithium content in the structures. Bianchini et al. observed features in X-ray diffraction patterns of LNO via *in situ* synchrotron X-ray diffraction studies during the synthesis. The I(003) reflection indicates a layered structure as well as the splitting of the cubic (220) and (111) peaks to the rhombohedral (018)/(110) and (006)/(012) reflections, respectively. [42] Ohzuku et al. investigated the relationship between the integrated intensity ratio I(003)/I(104) and the cation mixing – as the (003) peak belongs to the rhombohedral structure and the (104) peak also belongs to the cubic structure. [49] According to Dahn et al., the relative intensity ratio of the combined (102, 006) peak to the (101) peak can be utilised to measure the amount of Li in the compound. [57] This relationship was verified by Reimers et al., who used synchrotron X-ray data for their calculations [58] and Moshtev et al., who compare the calculated values with experimental values from chemical analysis and found a linear dependency. [59] Also, Li et al. confirmed the ratio of the Bragg intensities R = (I(006)/I(102))/I(101) by determining the nickel(III) content by a titration method. [60]

2.2.2. Electrochemistry of LiNiO₂

The electrochemical capability depends on the Li ions in the structure. Lithium de-/intercalates from and into the structure along the Li occupied planes. Good cycling characteristics require repeated de- and repopulation with minimal structural changes and damage to the structure.

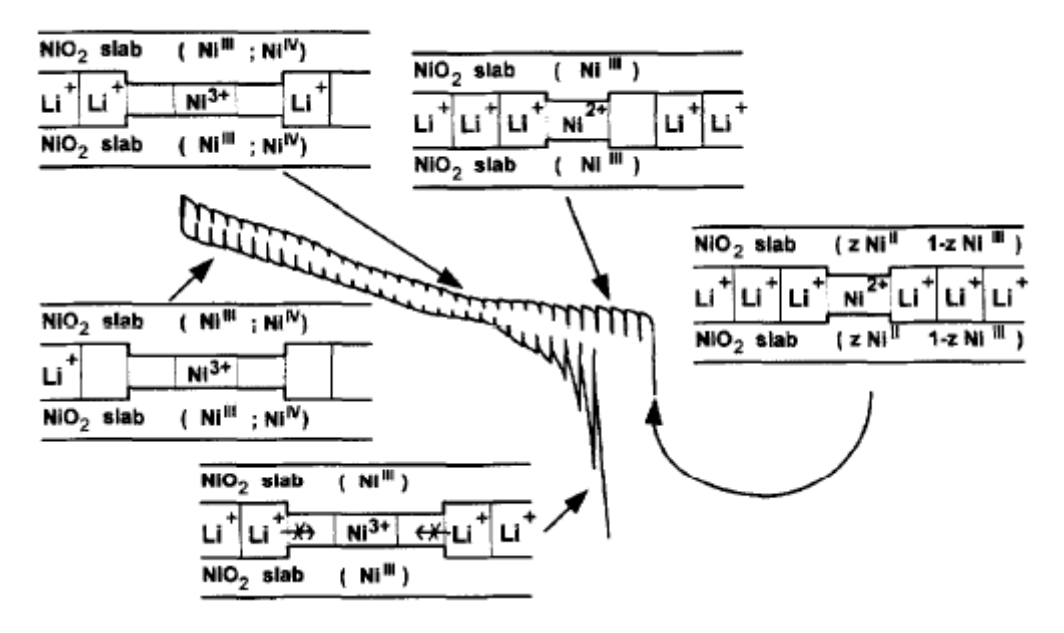


Figure 2.4: Changes in oxidation state of nickel ions during the first electrochemical cycle. Reproduced from [61] with permission from Elsevier.

LNO has a theoretical capacity of 274 mAh/g [49] [50] but a capacity drop is observed during the first cycle. Upon charging, the Ni ions are oxidised, starting with Ni²⁺ in the TM layers followed by Ni²⁺ in the Li layer upon further removal of Li⁺ ions. This leads to a decrease of the interslab space, as the ionic radius decreases, making it harder for the Li to reintercalate into the structure, and an amount of Li is irreversibly lost, as shown in Figure 2.4. Total reversibility of the first cycle indicates negligible Ni²⁺ in the Li layer. [43] [46] [61] Upon further delithiation, Ni³⁺ is oxidised according to the following reaction equation:

$$LiNi^{3+}O_2 \to Ni^{4+}O_2 + Li^+ + e^-$$
 (2.1)

During the deintercalation reaction, the cell parameters change, a is decreasing and c is expanding due to the increasing repulsion of the NiO₂ slabs. At this very low Li content, the interlayer starts to collapse as both a and c further decrease, leading to electrochemically inactive rock-salt structures at the surface, as Ni⁴⁺ is again reduced to Ni²⁺, releasing oxygen and affecting the cycling performance. [52] [62] [63] [62] Arai et al. showed, that upon

excessive extraction of 90% of Li from $[\text{Li}_{0.99}\text{Ni}_{0.01}]_{3a}[\text{Ni}]_{3b}[\text{O}_2]_{6c}$, inactive domains are generated. This can be avoided by limiting the extraction to only 80%. [64]

Due to the phase transitions occurring during Li^+ intercalation and deintercalation, severe capacity fading is observed due to the increased activation barrier for Li diffusion and kinetic hindrance. This is due to the decreased space in the interslab as Ni^{2+} is oxidised when Li is deintercalated. The two-dimensional diffusion of Li is mainly along the Li layer via tetrahedral sites as can be seen in Figure 2.5. [52] [65] [66] Kang et al. investigated factors that affect the Li diffusion using first-principle calculations. They found a relation between the diffusion activation barrier and the size of the tetrahedral sites, determined by the c lattice parameter but also the electrostatic interactions between Li and the TM. [67] Following this, it is crucial to control the synthesis conditions to produce stoichiometric LNO with as little Ni^{2+} in the Li layer and Li residuals on the surface as possible.

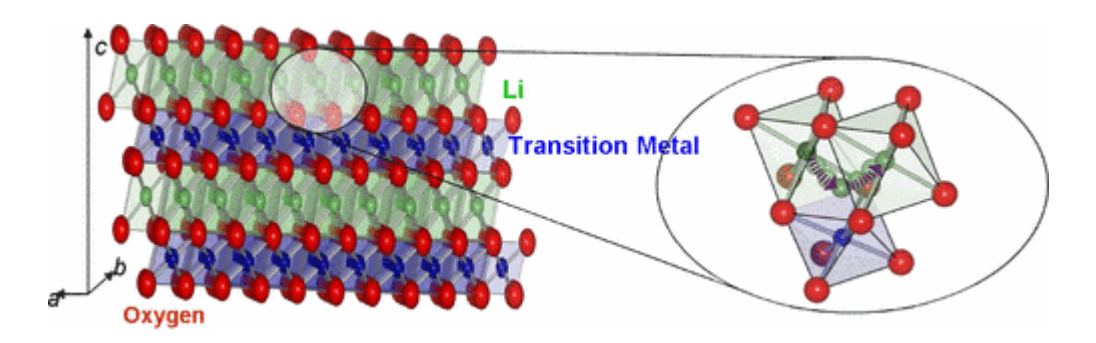


Figure 2.5: Li ion diffusion in layered oxides. Reproduced from [67] with permission from the American Physical Society.

2.2.3. Physical Properties of LiNiO₂

LNO shows semiconducting behaviour with a small activation energy of $0.2 \, \text{eV}$. [56] Electrons from the low-spin trivalent state $t_{2g}{}^6 e_g{}^1$ of nickel take part in the conduction due to a strong covalent Ni-O-Ni overlap. The increase in divalent Ni ions migrating to the Li layers, promote structural changes as described in Chapter 2.2.1.2, leading to a decrease in electron mobility and conduction. [43] [68]

In a stoichiometric compound, the magnetic nickel in its low-spin state is separated by three non-magnetic layers (O-Li-O) and the material behaves as an anti-ferromagnet. [45] At lower temperatures, the electron spin of Ni³⁺ in the Li layer dominates the magnetic relaxation, while the relaxation is based on the motion of Li⁺ at higher temperatures. [43] Due to an excess of

Ni²⁺ in the Li layer, the Ni²⁺ in the interslab can interact with the Ni³⁺ in the adjacent slabs with different magnetic moments and ferromagnetism is observed. As the magnetic properties are very sensitive to any deviations from the stoichiometry, the real composition of the material and the amount of Ni²⁺ present in the Li layer, can be determined via *nuclear magnetic resonance* (NMR) measurements. [26] [27] [44] [68] [69] [70]

2.2.4. Instabilities of LiNiO₂

2.2.4.1. Moisture Instability

Due to the Li loss during high temperature calcination, an excess of Li precursor is used. Unreacted Li reacts quickly with moisture or CO₂ in air leading to lithium salts like LiOH or Li₂CO₃ on the surface. These side phases will deteriorate the electrochemical performance if the amount is high enough. A smaller concentration can be tolerated as the alternative is a washing step followed by a heat treatment. The use of water during the washing step may lead to an extraction of Li and thus, an expansion along the *c* axis. [43] [45] [50] Shkrob et al. investigated and evidenced the proton – lithium exchange in the layered LNO structure due to exposure to moisture. [71] Moshtev et al. found that ethanol is more suitable for the washing process without causing delithiation and deteriorating the cycling behaviour. Additionally, the as-prepared samples are more resistant to moisture in air than samples containing a side phase.

Also handling or storing the final compound is affected by its moisture sensitivity, leading to a capacity decrease and the growth of Li₂CO₃, LiHCO₃ and LiOH on the surface. In addition, a NiO layer forms at the interface between the bulk material and the residual Li layer due to the loss of Li and oxygen from the lattice. [73] Liu et al. investigated the deterioration of LNO after storage in air over time by Rietveld analysis of X-ray diffraction patterns, *X-ray photoelectron spectroscopy* (XPS) and *temperature programmed desorption - mass spectroscopy* (TPD-MS) measurements. They found electrochemically inactive Li₂CO₃ and active oxygen species on the surface, a weakening of the layered structure, and transformation of Ni³⁺ to Ni²⁺. [74] Handling in a dry atmosphere is crucial but even here, the material is prone to degradation over time. [50] Mu et al. investigated the surface chemistry and especially long-term sample storage in an Ar glove box by soft *X-ray absorption spectroscopy* (XAS) and SEM. They found that even in a dry atmosphere, lithium residuals and carbonate species form at the surface after two weeks resulting in lower initial discharge capacities and coulombic efficiencies but also in similar capacity retentions. After three months of storage, the surface species can be seen in SEM

images. Washing or high temperature annealing under oxygen is recommended and decreasing the time between synthesis and processing. [75]

2.2.4.2. Thermal Instability and Oxygen Evolution

Upon heating, electrochemically delithiated Li_xNiO₂ releases oxygen, as Ni⁴⁺ is rather reduced to Ni²⁺ than Ni³⁺. Ni²⁺ then migrates to the Li layer and induces structural changes due to the disorder in the crystal structure, especially for x < 0.5. Li_{0.5}NiO₂ forms a stable spinel phase LiNi₂O₄ above 150°C [76], but all other phases are metastable. The temperature and the amount of O_2 released, depends on the amount of lithium still present in the material as smaller x shows a larger amount of oxygen released at lower temperatures. [77] The thermal behaviour was studied by Dahn et al. via thermogravimetric analysis (TGA), mass spectrometry (MS) of the evolved gases and X-ray diffraction of the decomposed material. They found numerous steps, starting at 160°C in the TGA, indicating a decomposition and various phase changes. [77] Arai et al. investigated the thermal behaviour using TGA combined with differential scanning calorimetry (DSC) up until 300°C. They confirmed the structural change to a spinel phase by the observation of exothermic peaks at around 180°C for x < 0.5. The oxygen release depicted by a weight loss in the TG and endothermic behaviour at around 200°C in the DSC indicates the start of the next transition. Using XRD, the structural transition product at 300°C was identified as a rock-salt structure. [78] These mechanisms cause huge safety issues due to heat release and the possible reaction of oxygen with the electrolyte in the battery as Zhang et al. observed during their DSC study of Li_xNiO_2 in the presence of electrolyte. With decreasing x values, the reactivity increased, showing significantly increased exothermic energy around 200°C compared to samples without electrolyte which show only the decomposition of the LNO. [79] Li et al. address the relation between the thermal stability and the crystal size of the particles for the first time in 1996. They found that larger crystals are more stable than smaller crystals and agglomerated particles. [60]

2.2.4.3. Mechanical Instability

Phase transitions during charge/discharge induce a volume expansion and shrinkage, respectively, affecting the primary and secondary particles of the cathode. The formation of cracks along the particles and internal microcracks, lead to a loss of electrical contact, electrochemical performance and structural degradation. Additionally, the electrolyte is able to infiltrate these cracks, forming SEI layers at the grain boundaries. [52] [80] Cracking can be minimised by avoiding the region above 4.1 V, where the H2 \rightarrow H3 transition takes place and induces mechanical stress to the crystal structure, as shown by Yoon et al. [52] and Broussely et al [65].

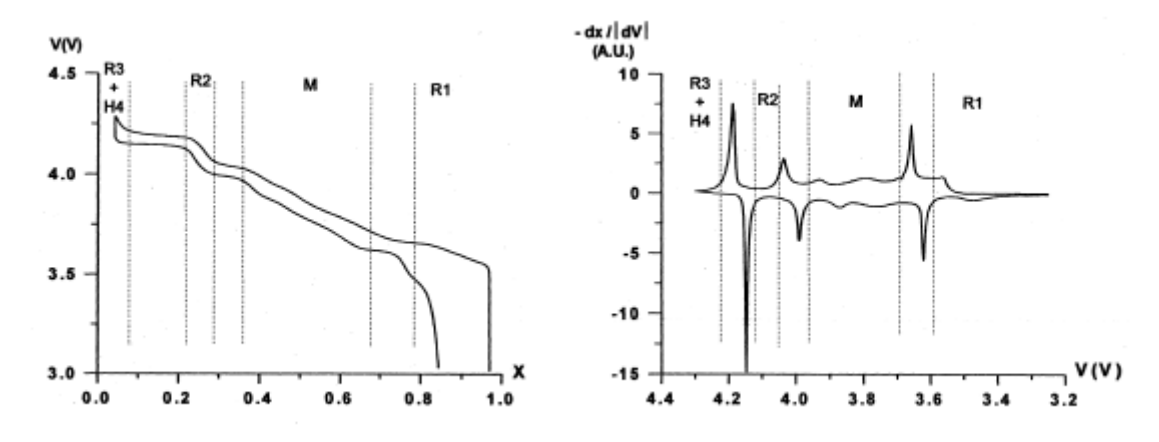


Figure 2.6: Charge-discharge cycle of a Li/LiNiO_2 cell (left) and corresponding derivative curve (right). Reproduced from [81] with permission of Elsevier.

The phase transitions of $\text{Li}_x \text{NiO}_2$ (Figure 2.6) consists of three single phase and two-phase regions. For x > 0.85 a rhombohedral H1 phase, for 0.75 > x > 0.5 a monoclinic M and for 0.5 > x > 0.25 again a rhombohedral H2 phase is observed with a great rechargeability in these regions. [81] The transitions are abbreviated either by R for rhombohedral or by H for hexagonal. For x > 0.9 the H3 phase occurs. Due to different preparation methods and different stoichiometry, there is a slight difference in x values reported by different groups. [45] [49] [50] [66] Arai et al. investigated the electrochemical properties of $\text{Li}_{1-x} \text{Ni}_{1+x} \text{O}_2$ with various x values and found a nearly stoichiometric sample with a large reversible capacity of 200 mAh/g between 3.0 V and 4.5 V. They also showed that 0.8 mol of Li can be extracted without drastic changes in the interlayer distance. [50] Ohzuku et al. studied the electrochemical behaviour dependant on the synthesis method and the structural disorder. They achieved a rechargeable capacity of 150 mAh/g between 2.5 V and 4.2 V and the change of interlayer distance during the different phase changes can be seen in Figure 2.7.

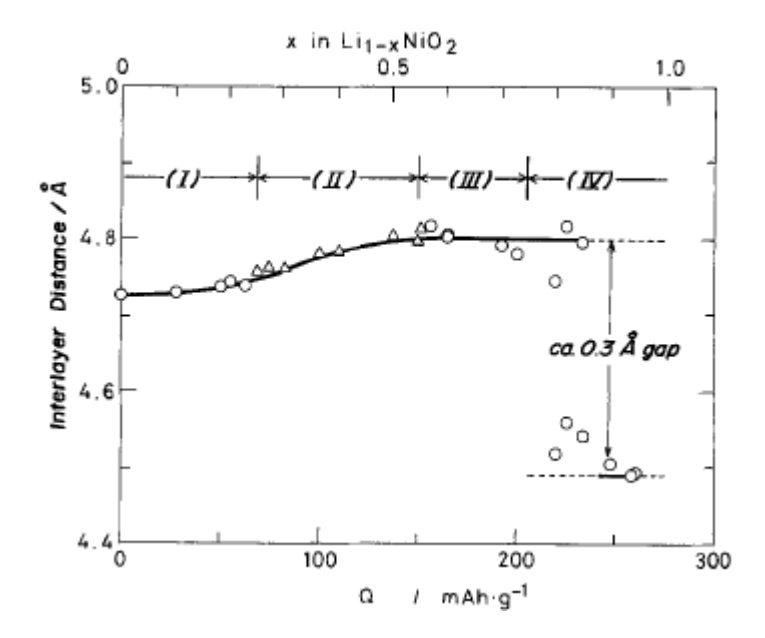


Figure 2.7: Change in interlayer distance of Li_{1-x}NiO₂. Reproduced from [49] with permission from the Electrochemical Society.

The H1 phase is the pristine LNO, as the original hexagonal structure is maintained. In between the single phases, a smooth transition takes place where a solid solution of both single phases exists. The monoclinic phase can be detected via X-ray diffraction by the splitting of (101) and (104) peaks. The structural relationship between the hexagonal and the monoclinic setting can be seen in Figure 2.8. Due to off-stoichiometric samples, this region is sometimes suppressed, as Ni²⁺ disrupts the Li vacancy ordering in the Li layer. [49] Peres et al. investigated the monoclinic phase using XRD, *extended X-ray absorption fine structure* (EXAFS) and electron diffraction. They observed that the vacancy ordering in the Li layer causing the monoclinic phase, is not driven by Jahn-Teller distortions but by a four times bigger superstructure which results from the ordering of Li and vacancies during the charging process. [82] [83]

The second hexagonal phase H2 is formed again via a transition period accompanied by an increase of the *c*-lattice parameter. The H2 phase is stable up to highly delithiated states, but as soon as the transformation is finished, the *c* parameter starts to decrease again while *a* continuously decreases. De Biasi et al. observed oxygen evolution and an electrochemical instability due to a significant change in *c*-lattice parameter in the H3 single phase region leading to a huge amount of mechanical stress at 4.15 V. The results are in good agreement with [84], Rietveld refinements and gas analysis. [62] Upon total delithiation, a rhombohedral H4 phase forms, which is an irreversible transition as nickel migration causes the deformation of the lattice, leaving the material inactive [45] [85] [86] This phase is difficult to isolate from the

H3 phase but Tarascon et al. found the distorted CdI₂ structure with the C2/m space group and the cell parameters a=4.88 Å, b=2.81 Å, c=5.58 Å and $\beta=125.84^{\circ}$. [86]

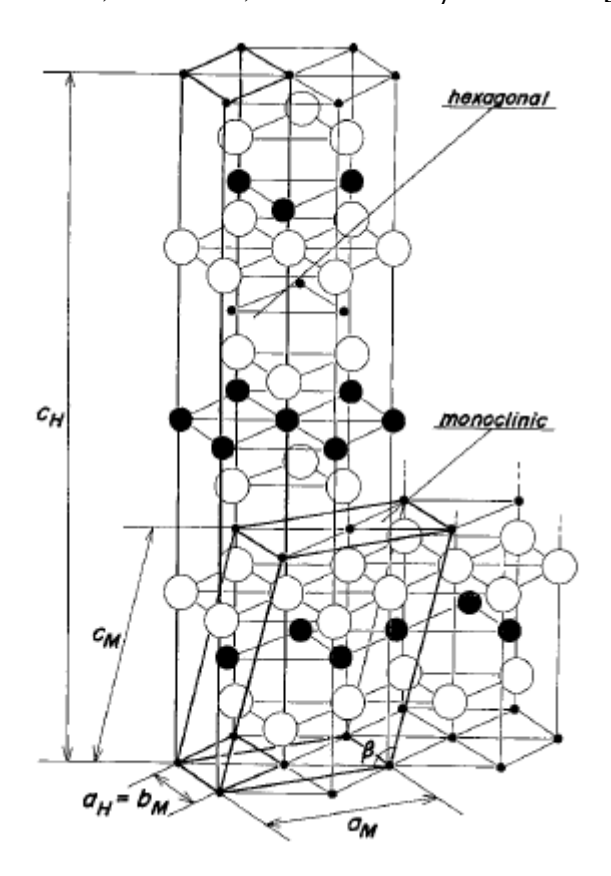


Figure 2.8: Hexagonal and monoclinic setting. Reproduced from [49] with permission from the Electrochemical Society.

2.3. Synthesis Methods

2.3.1. Solid-State Synthesis

The simplest and most direct, but not fastest way to obtain a material, is by thoroughly mixing the powder precursors with a mortar and pestle or ball mill for a varying amount of time to ensure homogeneity. The mixture is then heated at high temperatures for a long time. Often, regrinding is required during heating periods. The process is easily scalable but often yields side phases. It is very time-consuming, and the structure and morphology cannot be controlled, thus, the selection and synthesis of the precursors is very important. For the synthesis of LNO, many different precursors are possible, such as oxides, hydroxides, carbonates, acetates, etc. High temperatures during the synthesis may cause Li to evaporate due to its high vapour pressure. The resulting vacancies in the Li layer of the layered structure can be prevented by utilising an oxidising atmosphere as well as hindering the evaporated Li from reacting with

moisture or CO₂ from air to build side phases on the surface of the material. Additionally, the oxidising atmosphere can minimise cation mixing in the Li layer, producing Ni³⁺ rather than Ni²⁺. Many different studies have been reported to find the best calcination temperature to minimize cation mixing and the formation of the side phase.

To obtain near-stoichiometric samples, Ohzuku et al. prepared LNO using different nickel and lithium precursor powders such as Ni(NO₃)₂, Ni(OH)₂, NiCO₃, NiOOH and LiOH, LiNO₃ and Li₂CO₃. They worked under oxygen and under air and calcined the samples between 500 and 1000°C. [49] Rougier et al. used stoichiometric mixtures of NiO with Li₂O, Li₂O₂ and Li₂CO₃ to obtain the lowest reaction temperature and the most reactive starting material. The samples were prepared in a dry box and heated between 600 – 800°C under oxygen. [44] Kanno et al. synthesised LNO using Li₂O₂ and NiO in different atmospheres like oxygen, nitrogen or air at temperatures between 450 – 850°C for 48 h. To compensate for Li loss during synthesis above 700°C, an excess of several percentage of Li starting material is used. [50] [84] [62] To remove remaining Li salts from the sample, washing is recommended after calcination. Due to the moisture sensitivity of LNO, as explained previously, an additional heating step may be required which might again lead to formation of side phases, more gas evolution and a higher initial capacity loss. [87] According to Xu et al., a small amount of surface carbonates does not affect the bulk material and even samples with only a small excess of Li source showed Li₂CO₃ on the surface. [88]

2.3.2. Co-Precipitation Synthesis

During this solution-based synthesis, solid products are generated by adding a precipitating agent to a solution containing the desired cation and anion, such as a Ni salt and NaOH, respectively. Precipitation synthesis can produce a well-mixed hydroxide precursor species which can then be lithiated in a subsequent solid-state reaction. The solubility of nickel hydroxide is low, which readily enables controlled precipitation from the nickel salt solution. By exceeding its solubility limit and using a chelating agent, a solid crystal product is precipitated from the liquid phase following the reaction Equations 2.2 and 2.3. Important parameters of the synthesis to control are the temperature, the pH value, the feeding rate and concentration of the chelating agent, an inert atmosphere (nitrogen), the stirring speed and the precipitate dwell time in the supernatant solution. [89]

$$Ni^{2+} + n NH_3 \rightarrow [Ni(NH_3)_n]^{2+}$$
 (2.2)

$$[Ni(NH_3)_n]^{2+} + 2 OH^- \rightarrow Ni(OH)_2 + n NH_3$$
 (2.3)

Due to cation mixing and the difficulties synthesising stoichiometric LiNiO₂, it is important to ensure that all the reaction variables are strictly controlled and modified carefully to ensure optimised starting conditions. Thus, the optimisation and control of the Ni(OH)₂ precursor is one of the main tasks to produce a stable and electrochemically high performing cathode material.

Using a stirred tank reactor (STR), the control mechanism for critical factors like the temperature, pH, the atmosphere in the reactor, feeding rate of starting materials to control the reactions taking place during formation of the precipitate is simplified. Particle size and morphology can be easily controlled and adjusted with changes to the feedstock solution during the course of the reaction, enabling finely tuned core-shell and concentration gradient particles to be produced. By changing the concentration and feeding rate of the chelating agent NH₄OH, nucleation and growth processes can be adjusted as they are competing reactions in the solution and determine the resulting particle size and morphology. Nickel sulphate is fed into a basic solution of NH₄OH. Once the supersaturation of Ni²⁺ in the solution is reached, a Ni-ammonia complex is formed with the help of the chelating agent, reducing the supersaturation and the formation of new particles. The addition of NaOH to control the pH, is essential for the crystal growth as NH₃ is slowly exchanged with OH⁻ to form the Ni(OH)₂. There is a constant struggle between nucleation and crystal growth in the solution – therefore manipulations of the reaction rate can shift the equilibrium one way or the other to obtain a desired particle size. It is important to maintain a homogeneous nucleation to achieve a narrow particle size distribution. Later, after the feeding time and during the dwelling time in the supernatant, Ostwald ripening occurs. Here, smaller particles are dissolved and re-crystallise as larger particles. [90] [91]

Many research groups investigated the optimum parameters for Ni-rich layered oxides in a STR, like Välikangas et al., who performed this highly sensitive reaction at different temperatures between $40 - 70^{\circ}$ C and investigated the particle growth during the reaction by analysing the particle size distribution and the electrochemical behaviour after lithiation of the precursor material. A more narrow *particle size distribution* (PSD) is shown for a longer precipitation time and a higher tap density for a higher reaction temperature. [92] In 2015, Weiwei et al. investigated the influence of the operating conditions like the impeller type and speed $(300 - 500 \, \text{rpm})$ and the feeding height on the particle size and distribution in a STR. They found a huge effect of impeller diameter and speed, as a larger diameter leads to a larger particle size distribution. Increasing the stirring speed results in smaller particles, with the smallest

particles (12<d₄₃<15 μm) produced at 500 rpm. [91] A large study was undertaken by Ramesh et al., as they investigated the reaction in a continuous stirred tank reactor (STR) and varied the pH, the temperature, different starting materials and also studied the effect of digestion using powder XRD and IR. During the digestion of the precipitate in the supernatant, its longand short-range ordering and its crystallinity is changed for the better, transforming stepwise from α-Ni(OH)₂ to the more stable and highly crystalline β-Ni(OH)₂. [93] Peng et al. investigated the microstructure and growth characteristics of Ni(OH)₂ via precipitation in a STR to produce spherical particles and understand the reaction mechanism. They reacted NiSO₄ with NaOH and NH₄OH at temperatures of $50 - 55^{\circ}$ C and pH values of 11.0 - 11.5, sampling the precipitate during the reaction to verify the reaction mechanism. During nucleation, crystallisation and Ostwald ripening, they found that the particles grow radially in all directions very quickly. [90] Acharya et al. synthesised nickel hydroxide by the use of different precipitation agents like urea, NaOH or ammonia and investigated the ageing time as well. Their findings showed that the morphology of the particles are greatly influenced by the chelating agent as urea formed poorly crystalline material, while the combination of NaOH and ammonia showed an improved crystallinity of the β-Ni(OH)₂. [41] Finally, van Bommel et al. studied LNO as well as NMC and showed, that the pH has a huge influence on the tap density and the morphology of the particles. Their findings suggest that the minimum suitable pH for Ni(OH)₂ synthesis is 11.4. [94] Most work is done for NMC cathode material, so the optimisation of spherical, dense Ni(OH)₂ particles of 10 µm size and a narrow size distribution for the combined parameter set used with the STR is yet to be completed.

2.3.3. Other Synthetic Methods

Other methods for Ni-rich cathode synthesis include sol-gel synthesis, microwave-assisted synthesis, combustion synthesis, hydrothermal methods, chemical vapour deposition or laser ablation.

During a sol gel synthesis, a suspension of reactive inorganic precursors is heated to remove the solvent phase, forming a viscous sol containing colloid particles and upon further heating, a gel-like network. The precursors condense in the heated suspension into cross-linked polymers and later polymerise to form a three-dimensional network. The gel is then fired to remove volatile components left in the pores which leads to either an aerogel or a xerogel. The use of a complexing agent like citric acid, can further improve the condensation reaction by driving the formation of the complex in the solution and preventing premature precipitation.

[95] The good homogeneity in the gel precursor and the low temperature and fast reaction time are some advantages compared to solid-state synthesis.

Microwave-assisted synthesis uses microwave radiation to heat the sample. During conventional heating, the sample starts to heat up on the walls of the vessel more quickly, while the core takes much longer to achieve the desired temperature. Internal heating is applied by microwave radiation, generating heat in materials containing electric charges. This leads to an evenly distributed heating rate all over and within the sample. Kalyani et al. used microwave radiation to synthesise phase pure LiNiO₂ by studying possible precursors, radiation times and the electrochemical characteristics. They gained samples with discharge capacities of about $150 - 160 \, \text{mAh/g}$ after 30 cycles. As this method is cost-effective and energy efficient, it might be a suitable replacement for long heat treatment methods. [43]

Using the combustion synthesis, highly uniform particles with controlled stoichiometry can be achieved. Usually, metal nitrates are mixed with fuels, like urea or glycine with a high combustion enthalpy to provide the necessary energy. An initial heating is required to ignite the process and enable a self-sustained exothermic reaction. [43] [45] Within seconds or minutes, the reaction takes place but the process is challenging to scale up, as a large volume is needed to produce a small amount of sample. This method has been very popular recently for preparation of nanomaterials. [96] [97]

2.4. Doping of Cathode Active Materials

Introducing dopants into LiNiO₂ is an efficient strategy to access the strong redox active Ni ions but at the same time cope with the structural and thermal instabilities and electrochemical performance issues of the layered oxide material, especially the poor capacity retention. To understand how the dopants influence the structure, properties and the electrochemical performance, dopants are substituted into the precursor structure of Ni(OH)₂ during co-precipitation or added during the solid-state synthesis of Ni(OH)₂ and LiOH•H₂O. It is crucial to understand which sites different dopants will occupy to predict beneficial or detrimental changes in the structure and the electrochemical cycling behaviour of the new compounds as well as the interference of substituting several dopants in one host structure. First-principles calculations by Guo et al., to investigate the suppression of oxygen evolution within LiNiO₂ through dopants, resulted in a helpful overview of preferred site occupancies as well as O-2p – Ni-3d gaps in doped Li_{0.5}NiO₂. The graph (Figure 2.9) reveals that Co, Mn, Sn,

Zr, Ti and W all occupy the octahedral site in the TM layer whereas Cu and Zn prefer the tetrahedral site in the Li layer. [98]

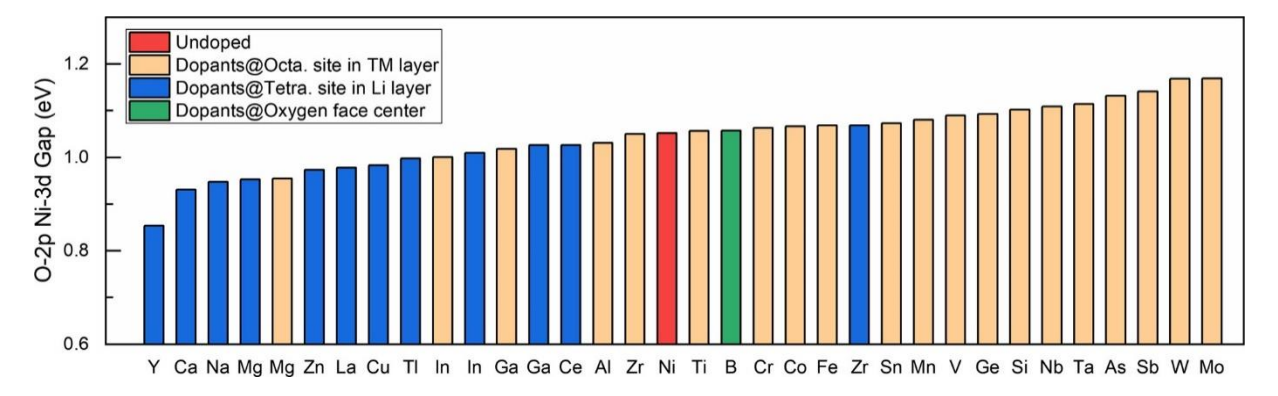


Figure 2.9: Gap of O-2p and TM-3d band centers of doped Li_{0.5}NiO₂. Preferred site occupation of dopants labelled in different colours. Reproduced from [98] with permission from the American Chemical Society.

Numerous studies were undertaken for Co and Mn as well as examination of co-doping of these elements. Mixed Co-Mn-doping in Ni-rich layered oxides has been extensively reported and NMC materials are already commercialised [99] [100] [101]. Distinguishing which of the improving contributions can be attributed to which dopant in co-doped materials, is pivotal to be able to tailor materials for specific needs. Therefore, it is important to investigate the influence of single dopants on a material, their site occupancy in the lattice, the influence that has on physical properties and the electrochemical behaviour during cycling before starting to combine dopants in a compound.

Co decreases the likelihood of cation mixing during solid-state synthesis and mitigates phase transitions during cycling which stabilises the electrochemical performance of the doped material. Ni³⁺ is replaced by certain amounts of Co³⁺, which doesn't affect the electronic charge balance within the material. [102] Rougier et al. as well as Zhecheva et al., were able to successfully show that Co-substitution of 3 % can form a stoichiometric compound without any Ni²⁺ in the structure and thus an increase cell performance. [103] [104] Yang et al. synthesised LiNi_{0.88}Co_{0.12}O₂ and examined a more ordered structure with an initial discharge capacity of 215 mAh/g. [105] Amine et al., synthesised Co-rich LiNi_{0.6}Co_{0.4}O₂ with a near-perfect layered structure and almost no cation disorder. They state that Co³⁺ reduces cation mixing by supresses the magnetic frustration in the structure. On the other hand, the Co³⁺/Co⁴⁺ band overlaps strongly with the oxygen 2p band (Figure 2.1), increasing the oxygen release at high *state of charge* (SOC). [106] Hausbrand et al., highlighted the significance of oxygen loss in layered cathode materials. The removal of electrons during delithiation from covalent TM-O bonds leads to the formation of oxygen vacancies for compensation. [107]

As Cobalt is rather toxic and increases safety concerns within batteries as well as its high cost and environmental and ethical issues of the mining processes lead to increased research interest to replace Co in Ni-rich layered oxide cathodes. [106] Other dopants like Manganese are favoured, as Mn⁴⁺ ions have a structural and chemical stabilising effect on the LiNiO₂ and lead to improved capacity retention [108]. The low cost and thermal stability at high SOC, like the stabilisation of lattice oxygen and suppressing phase transitions, are a big benefit when developing new or optimising current cathode materials. [47] [106] Drawbacks of pure LiMnO₂ forming a spinel structure [109] during electrochemical cycling, could be mitigated by co-doping Ni and Mn, as Ohzuku and Makimura showed. [110] On the other hand, substituting some Ni³⁺ with Mn⁴⁺, will likely reduce Ni³⁺ to Ni²⁺ for charge balance, leading to increased cation mixing in the structure and its detrimental influence on the structure of the layered oxide during cycling [111]. Studies also showed the decreased cell capacity with an increased amount of Mn substitution which point out, how careful systems need to be optimised regarding the dopant level to improve the host structure instabilities. [112] [110] [113] Bach et al. showed that with a higher manganese content, multiphase materials were obtained with deteriorating electrochemical behaviour. [114] Ceder et al., found Li(Ni_{0.5}Mn_{0.5})O₂ by using an ion exchange synthesis where Na⁺ is replaced by Li⁺. A combination of high rate and high capacity could be attested, while the well-layered stoichiometric structure stayed intact. [115]

The element copper is said to improve conductivity and take part in charge transport processes, it is cheaper than nickel and cobalt, and very abundant and thus is a suitable dopant to investigate in LiNiO₂. Several studies have been undertaken before and show that doping Cu ions into the layered host structure is beneficial for stabilising the structure, reducing cation mixing and improving the reversibility of phase transitions. As Cu²⁺ is substituted on the Ni site, the Ni is prone to stay in a 3+ oxidation state to maintain charge balance, reducing the possibility of Li/Ni cation mixing in the structure. This improves Li diffusion during cycling and thus resulting capacity retention, as shown by Kong et al. [116] Ramos-Sanchez et al although, show that doping of Cu²⁺ can potentially be detrimental to the electrochemical cycling as it occupies Li sites like Ni²⁺ and further decreases Li diffusion and mobility. They found that doping of Cu³⁺ in the structure yields a highly ordered structure with a high degree of cationic ordering as well but is not easy to synthesise and rather develops as a two-phase material with a Cu²⁺-rich phase and a Cu³⁺-rich phase. [117] [118] Kin et al. confirmed, that doping LiNiO₂ with copper leads to an implementation of Cu²⁺ rather than Cu³⁺, leading to poor structural stability and electrochemical behaviour. [119]

Additionally, studies of Cu-doped NMC materials with the same structure as LNO, can be examined as well, to determine the effect of the copper doping. Fan et al. doped LiNi_{1/3}Co_{1/3}Mn_{1/3}O₂ with up to 1% Cu on the Ni site and exhibited improved charge/discharge cycling performance with an initial discharge capacity of 180 mAh/g and a coulombic efficiency of 90.3%. Due to an enlarged Li spacing and a reduced degree of cation mixing, Li diffusion improves during cycling. [120] Milewska et al. substituted 2% of Ni with Cu and showed increased lithium diffusion and electronic transport properties and thus increased rate capability and capacity retention. [121]

Substituting Ni with Zn ions seems to be advantageous with regards to stabilising the structure during cycling and thus improving capacity retention as well as superior lithium-ion diffusion during cycling. With a slightly increased ionic radius $(Zn^{2+} (0.88 \text{ Å}) > Ni^{2+} (0.69 \text{ Å}))$ [17], Zn-doping in the Ni layer, leads to an elongation of the c-axis as well as the unit cell volume by increasing the electrostatic repulsion between the Ni layers. This increases the LiO₂ interslab which facilitates the Li ion transport during cycling. This effect was shown in a study by Jie-Bin et al. who synthesised the doped material via a solid-state route and cycled the corresponding cells between 2.8 – 4.6 V vs Li/Li⁺ at 0.3 C [122] as well as Du et al., who synthesised their material via sol-gel method and cycled the corresponding cells at 0.1 C between 2.8 – 4.4 V. [123] No signs of Zn containing side phases are detected in the XRD pattern and the morphology of the secondary particles are very similar compared to the undoped material. Based on refinements and unit cell parameters, the Zn-doping was correlated to the improved capacity retention in Zn-doped LiNi_{1/3}Co_{1/3}Mn_{1/3}O₂ materials. Jie-Bin et al. measured the Li diffusion coefficient via cyclic voltammetry measurements and strengthened the assumption of increased interslab space in the structure. Both studies show very similar results independent from the different synthesis methods of the doped materials. [122] Fey et al. studies the effect of Zn doping in the host structure LiNi_{0.8}Co_{0.2}O₂ (LNCO) and exhibited improved electrochemical properties, especially an increased capacity retention over 100 cycles from 61.4% for undoped LNCO to 81% for Zn-doped LNCO. Based on studies of Mg-doped layered oxides, they suggest that due to the size of Zn²⁺, some of the dopant will occupy lithium sites in the interslab, stabilising the structure during cycling. [124]

Several research publications can be found by Delmas et al. that use Zn as a dopant in the $Ni(OH)_2$ structure via co-precipitation method. They use XANES and EXAFS to confirm that Zn ions occupy the octahedral sites, substituting nickel ions in the structure when adding less than 10% of Zn. Above this value, the desired β -Ni(OH)₂ structure transitions into the hydrated α -Ni(OH)₂ structure, involving Zn ions on the tetrahedral sites of the lattice. [125] [126] [127]

Other research groups like Chen et al., confirm the phase change with increasing Zn levels in the precursor material Ni(OH)₂ used for LiNiO₂ solid-state synthesis. [128]

A rather less investigated element to dope into layered oxide structures is tin. Sn⁴⁺ will preferably substitute the nickel position in the structure, with an ionic radius of 0.69 Å [17], but not participate in electrochemical reactions. It is very abundant in nature, non-toxic and of low cost. Its oxygen bond energy (548 kJ/mol) is very strong compared to other transition metals (Ni-O 392kJ/mol) and will thus stabilise the layered structure of its host. The high electronegativity of Sn⁴⁺ will improve Li⁺ diffusion and inhibit oxygen release from the structure by decreasing covalency of the TM-O. So far, several studies were published where Sn was substituted in NMC materials, showing enhanced electrochemical performance. Eilers-Rethwisch et al. synthesised Li(Ni_{0.6}Mn_{0.2}Co_{0.2-x}Sn_x)O₂ via co-precipitation, implementing 0.5 % dopant into the hydroxide precursor synthesis, showing a lattice expansion due to the size difference of Sn⁴⁺ > Co³⁺. An additional Li₂SnO₃ phase was detected which has no influence on the electrochemical performance. The improved structural stability due to the increased bond dissociation energy of Sn-O, lead to lower c lattice contractions when delithiated and thus a longer cycle life and better thermal stability. [129] Zhu et al. gained similar results from the synthesis of Sn-doped LiNi_{0.5}Co_{0.2}Mn_{0.3}O₂, exhibiting Li₂SnO₃ as a surface layer for higher dopant concentrations > 3 %, which acts as Li⁺-conductive layer on the surface and further improves physical and electrochemical properties. A high coulombic efficiency of 84.9%, discharge capacity retention over 100 cycles of 88.4% and an increased Li⁺ diffusion coefficient of 2.11•10⁻¹⁰ for the 3% Sn-doped material, is in accordance with the low cation mixing and thus less pronounced structural transitions during cycling lead to an improved electrochemical performance. [130] Sn-doped NMC90 (Li($N_{i0.9-x}Co_{0.05}Mn_{0.05}Sn_x$)O₂ synthesised via solid-state reaction by Nguyen et al., exhibited an improved microstructure, with radially aligned primary particles, improving Li⁺ diffusion during cycling. No side phase was detected nor a big difference in lattice parameters compared to the undoped material, as 0.3 % Sn was substituted for Ni in the structure. Electrochemical cycling showed similar initial discharge capacities but improved capacity retention over 100 cycles when cycled between 2.7 and 4.4 V at a C-rate of 0.5 C. Structural degradation via microcrack formation is inhibited by the microstructure of Sn-doped NMC90 leading to stable electrochemical performance. [131] Improved conductivity and reduced resistivity leading to improved reversible capacity and cycling performance due to 3% Sn doping of LiNi_{0.8}Co_{0.2}O₂ was also confirmed by Ma et al. They synthesised the material via a rheological phase reaction and exhibited a crystal lattice expansion due to the larger ionic radius of Sn⁴⁺ smaller particle size, further improving the overall conductivity. Sn⁴⁺ doping also entails charge compensation, which is achieved by hindering Ni²⁺ to oxidise to form Ni defects in the structure, leading to more structural stability and an increased electronic conductivity. The strength of the Sn-O bonding stabilises the hexagonal structure. [132] Recently, Sn-doping was implemented via solid-state reaction into LiNiO₂ by Wu et al., leading to an enlarged crystal lattice and exhibiting an additional Li₂SnO₃ surface layer. The stronger Sn-O bonding energy confines the Ni²⁺ movement in the structure. The size reduction of primary particles leads to shorter diffusion length and with the increased diffusion pathways due to the lattice expansion caused by the larger Sn-ions, the electrochemical performance improves. A reduction of the phase changes causes less volume changes during cycling and involves enhanced capacity retention. [133]

Tetravalent ions like Sn^{4+} , Ti^{4+} and Zr^{4+} prefer to sit on the 3b Wyckoff site of the hexagonal layered α-NaFeO₂ structure of NMC or LNO materials. They act as pillars due to their slightly larger ionic size $(r(Zr^{4+}) = 0.72 \text{ Å} [17])$ and its bond dissociation energy of 760 kJ/mol, influencing cation mixing and suggesting improved structural stability and thus enhanced Li⁺ diffusion during cycling. Few studies exist that use Zr as dopant in layered oxide materials. Chen et al., synthesised Zr-doped Li(Ni_{0.4}Co_{0.2}Mn_{0.4})_{1-x}Zr_xO₂ (x = 0.01) via a sol-gel method. They show slightly increased lattice parameters for the doped material compared to the undoped equivalent. Improved Li⁺ transportation processes as well as decreased charge transfer resistivity, evaluated using Electrochemical Impedance Spectroscopy EIS measurements, is advantageous to the rate performance and cycle reversibility. The doped material shows slightly lower initial capacity, but the capacity retention over 50 cycles of 80.5 % is superior compared to the undoped material. [134] Shangguan et al., examined the effect of Zr⁴⁺ doping and Li₂ZrO₃ coating on LiNi_{0.5}Mn_{0.5}O₂ via solvothermal and solid-state synthesis. The XRD pattern indicates a well layered α -NaFeO₂-type structure with a $R\overline{3}m$ space group with Zr^{4+} enlarging the d-spacing to enhance Li⁺ migration. An increased amount of coating suggests a smaller degree of Li/Ni mixing according to Rietveld refinements. The electrochemical performance of the 3 mol%-doped sample shows the highest initial capacities as well as the best capacity retention over 120 cycles. The synergistic effect of both doping and coating improves the structural stability and cycling performance of the cathode and reduces side reactions between the cathode and the electrolyte. [135] Li et al., showed enhanced capacity retention of Zr-doped $LiNi_{0.83}Co_{0.12}Mn_{0.05}O_2$ synthesised by co-precipitation, of 79.5 % after 200 cycles (2.8 -4.5 V vs Li/Li⁺ at 1C) and increased initial discharge capacities of 189.4 mAh/g compared to the undoped sample (178.3 mAh/g). [136] For LiNi_{0.5}Co_{0.2}Mn_{0.3}O₂, Wang et al., exhibited that Zrdoping decreases initial discharge capacities compared to the undoped sample, but the capacity

retention was improved significantly as well as the structural stability and cation mixing in the structure. [137] Finally, Yoon et al., prepared 0.4% Zr-doped LiNiO₂ via co-precipitation method followed by a high temperature solid-state synthesis. The unit cell of the doped material was slightly enlarged, which, in combination with elongated radially aligned primary particles, improved the Li⁺ diffusion during cycling. Initial discharge capacities of 246.5 mAh/g for the doped compared to the undoped equivalent (247.5 mAh/g) and coulombic efficiency of 97% for both compounds are observed during electrochemical cycling. The cycling stability although improves due to the Zr-doping with 81% after 100 cycles at 0.5 C. First-principles calculations in this study suggest that low-level Zr-doping promotes cation ordering in the structure. Enhanced electrochemical behaviour is more likely to be achieved by particle morphology rather than the suppression of antisite defect, as the here-synthesised material shows exceptional cycling behaviour with a small amount of antisite defects compared to literature so far. [138]

Ti⁴⁺ is used as a promising tetravalent ion to be doped into the layered structure of NMC or LNO materials and their electrochemical behaviour as well as structural and physical properties evaluated. Ti⁴⁺ can compensate the charge deficit that arises due to the formation of Ni²⁺ ions in the layered oxide materials and entail structural instabilities in the crystal lattice. Like Zr⁴⁺, Ti⁴⁺ increases the thermodynamic barrier for unfavourable Ni migration within the structure and also strengthens the O bond which suppresses oxygen loss during cycling. [139] Steiner et al., investigated 3 % Ti⁴⁺ doping into a LiNi_{0.8}Mn_{0.1}Co_{0.1}O₂ host via co-precipitation synthesis, followed by an annealing process. They exhibited an evenly dopant-enriched surface layer using Scanning Transition Electron Microscopy – Electron Energy Loss Spectroscopy STEM-EELS and XAS, which can inhibit electrolyte oxidation at the cathode surface. The electrochemical performance of this material showed increased discharge capacity and capacity retention from 69 % to 80 % over 300 cycles when cycled between 2.5 – 4.5 V vs Li/Li⁺ at 1 C for the doped cathodes. Other synthesis methods to achieve this material showed less improved cycling performance. [140] Kam et al., confirm that the electrochemical behaviour of Ti-doped NMC materials depend greatly on the synthesis method. They produced Ti-doped NMC333 as well as Ti-doped NMC442 via glycine-nitrate combustion (GNC) processes and coprecipitation synthesis. Apart from the expected increase in unit cell parameters due to the larger Ti⁴⁺ ions for lower dopant-levels, magnetic measurements and synchrotron X-ray diffraction indicate that the necessary charge compensation is accomplished via reduction of Mn⁴⁺ to Mn³⁺ and the decreased volume change during deintercalation leads to an improved cycling performance, respectively. [141] In particular, LiNi_{1/3}Co_{1/4}Ti_{1/12}Mn_{1/3}O₂ shows high-capacity, high-rate behaviour with a very low irreversible capacity loss when synthesised via GNC. [142]

In 2001, Kim and Amine synthesised LiNi_{1-x}Ti_xO₂ (0.025 $\le x \le 0.2$) via solid-state synthesis at 750°C for 30h under oxygen and observed superior electrochemical cycling behaviour with good initial capacities and remarkable capacity retention when cycled at C/5 rate between 2.8 and 4.3 V. They assume that the improved cycling behaviour is due to the mitigation of the Ni²⁺ impurity migration into the Li plane and the shift towards one-phase rather than the usual twophase oxidation/reduction reaction. A dopant content of 2.5 % Ti, shows the most promising electrochemical values. [119] [143] LiNi_{0.5}Ti_{0.5}O₂ obtained via ion exchange of a Na-Ti-Ni precursor, utilising a molten salt synthesis by Tsuda et al., exhibited better cycling behaviour at elevated temperatures of 55°C than at RT, that showed severe irreversible behaviour. Explanations for the inadequate electrode performance at RT could be the small amount of remaining Na lowering the overall Li content, the Ti⁴⁺ migration into the Li layer or the difficulty to oxidise nickel into its tetravalent state during cycling. [144] In contrast to that, Kwon et al., prepared LiNi_{0.99}Ti_{0.01}O₂ via combustion method and found an increased discharge capacity and better cycling performance for the doped sample in comparison to the pristine material. They suggest that compared to other synthesis methods like solid-state synthesis, the combustion method results in higher crystallinity and higher uniformity of the particle size. They also undermine the believe that Ti⁴⁺ is decreasing the cation mixing of LNO, leading to a larger discharge capacity of Ti-doped LNO. [145]

Doping layered oxides with high-valence elements such as Nb⁵⁺, Ta⁵⁺, Mo⁶⁺ and W⁶⁺ seem to boost the improvement of electrochemical behaviour even more. Degradation mechanisms like microcrack formation during constant de-/reintercalation of Li from and into the host structure are mitigated by the modification of the structure. Yet, the mechanisms as well as the occupied sites in the crystal lattice are not fully investigated yet. High-valence dopants seems to act differently than conventional dopants discussed so far and they seem to accumulate on the surface of the cathode materials rather than being integrated into the structure. [139] Kim et al., synthesised 1 % W-doped NMC via co-precipitation method and they demonstrate high specific capacities of > 220 mAh/g, an increased energy density and improved thermal and cycling stability in full cells over 1000 cycles. For the pristine material, a mixture of a layered, ordered $R\overline{3}m$ phase and a cation-disordered $Fm\overline{3}m$ rock-salt phase was detected via XRD, High Resolution Transition Electron Microscopy HRTEM and Selected Area Electron Diffraction SAED. Nuclear Magnetic Resonance Spectroscopy NMR and Density Functional Theory DFT

was used to confirm the rock-salt phase as well as to understand the increased formation of that phase due to the W-doping which suggests that W-doping has different effects on the layered and on the rock-salt phase. It promotes the segregation of a W-doped rock-salt phase to the surface as well as stabilising the layered structure by reducing Ni³⁺ to Ni²⁺ for charge compensation and lowering the Jahn-Teller effect and suppressing oxygen release during cycling. [146] Song et al., coated NMC622 with a WO₃ layer and noticed that some W⁶⁺ ions were doped into the structure. This was confirmed by X-ray diffraction, as the peak positions shift towards lower angles, indicating an enlargement of the unit cell due to the much bigger W⁶⁺ ions. This sample also showed the best cycling performance in the study, with discharge capacities of 166 and 141 mAh/g after 1 and 200 cycles, respectively and a capacity retention of 84.8%. It is unclear how much influence the doping or the coating has on the cycling performance and how far inside the particle, the W⁶⁺ ions penetrate. [147] Rye et al., investigated W-doped LNO materials, using 1-2% of tungsten in a co-precipitation reaction. Increasing W-doping seems to increase cation mixing in the layered structure and a secondary surface phase was found which is suspected to protect the cathode surface and improve cycling stability. Electrochemical data obtained between 2.7 and 4.3 V at 0.1 C shows decreased discharge capacities with increased doping-level, yet an improved capacity retention. Differential capacity plots reveal less pronounced phase changes throughout the cycling, especially the H2/H3 transition at higher voltages was delayed and suppressed and its reversibility improved, leading to improved structural durability and thus less microcrack formation. [148] Dahn et al., synthesised WO₃-coated and W-doped LiNiO₂ via dry particle fusion method and co-precipitation/solid-state synthesis, respectively, to investigate the underlying mechanism of action of W as well as the dopant location within the structure. They found increasing cation mixing with increasing W content using Rietveld refinements and W being incorporated in a Li_xW_yO_z (x/y > 1) primary particle grain boundary phase using DFT calculations, leading to Li deficiency in the material. EELS mapping confirms W concentrated at the grain boundaries rather than evenly distributed throughout the structure. They found that increasing high temperature (HT) treatment decreases primary particle size with tungsten incorporation, while the pristine materials primary particles grow with increasing temperature. Cycling between 3 – 4.3 V vs Li/Li⁺ at C/20 for two cycles, C/5 for 50 cycles and another two cycles at C/20, exhibits the suppression of the H2/H3 phase transition with W-doping, which is expected to be caused by the increased amount of Ni in the Li layer. [149] [150]

3. Experimental Methods

3.1. X-Ray Diffraction XRD

X-ray diffraction is used to reveal the crystal structure, the atomic composition of a material where light microscopy is not feasible any more due to smallest interatomic distances of 2-3 Å. As X-rays comprise a wavelength of 1-3 Å, which is nearly identical to interatomic distances, they get scattered elastically at the electron shells of the atoms in the translational crystal lattice (Thomson scattering), get refracted and the single waves interfere with each other (Figure 3.1).

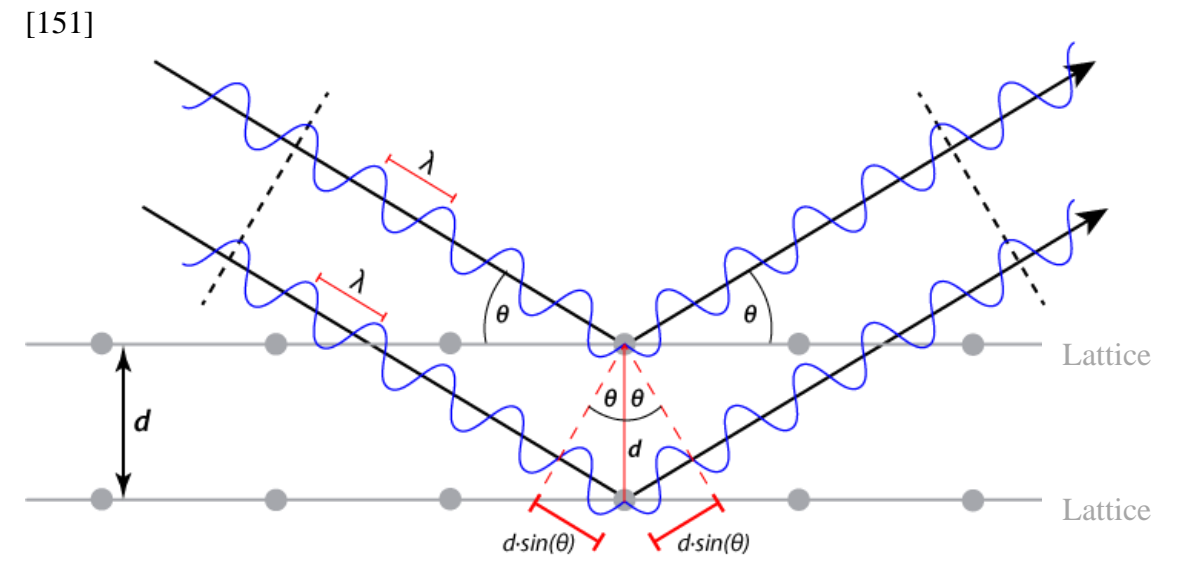


Figure 3.1: Reflections of X-rays (Bragg equation). Reproduced from [151] with permission from Springer Nature.

X-ray diffraction of a polycrystalline powder is used to identify and quantify substances by means of phase analysis. The scattered X-ray beam meets the planes of the crystal lattice of the powder sample under a certain angle and the measured intensities of the diffracted radiation are plotted as a function of the angle 2θ. If the X-rays interfere constructively after diffraction it will result in a detected intensity peak which is at angle dependent on the terms seen in the Bragg equation. Across all the interatomic distances in a crystalline material, this process can provide a diffraction pattern which is unique to the atomic composition of the material.

Mathematically, the Laue condition and Bragg equation are used to derive the geometrical interference conditions. According to Laue, the path difference consisting of the order number n and the wavelength λ of two waves being scattered at adjacent points in the reciprocal space is calculated via the angle of incidence μ and the angle of reflection ν along α -axis:

$$n_1 \lambda = a \cos \mu_a + a \cos \nu_a \tag{3.1}$$

In a three-dimensional lattice all three Laue equations, corresponding to the three crystallographic axes must be fulfilled at the same time and all scattering waves in the translational lattice must resonate in-phase which implies the crystal to move during the scattering experiment. Analogously, the Bragg equation (illustrated in Figure 3.1) indicates in real space at which angle of incidence θ , constructive interference takes place within scattering in a three-dimensional lattice (with d being the interlayer distance):

$$2dsin\theta = n\lambda \tag{3.2}$$

During a diffraction experiment the intensity of the scattered X-rays is measured as a function of the diffraction angle θ . The crystal structure is then deduced from the spatial arrangement and the intensity of the reflections. [152] [153] [154] A measured characteristic diffraction pattern consists of peaks at angles 2θ , where the X-rays get diffracted. The recorded peak positions are determined by the distance between the lattice planes. The peak intensities are influenced by the chemical composition of the material, the volume fraction of a phase, the atom location and the overlay of peaks due to the symmetry of the unit cell. Furthermore, the peak shape is affected by instrumental as well as sample-related factors like transparency, the crystallite size and microstrain. Peak broadening or shifting to higher or lower angles as well as the asymmetry of peaks at lower angles can be related to light elements in the structure, small crystallites or a strained lattice.

Diffraction can be measured in reflection or transmission geometry. For reflective geometry, the detector is on the same side of the sample and the incident beam is getting reflected on the flat sample surface with randomly oriented crystallites. Transmission geometry features the detector on the other side of the sample, measuring the beam going through the sample without being absorbed by it. This mode is advantageous for measuring reflections at low angles and minimises effects of preferred orientation in the sample.

To investigate phase purity of the samples in this thesis, the powders were finely ground to gain a higher amount of lattice plains and randomly oriented crystallites and applied on a flat stainless-steel sample carrier to be measured in a benchtop MiniFlex Rigaku diffractometer in reflection mode (Cu-K $_{\alpha}$ -radiation: $\lambda = 1.5406\,\text{Å}$) over a $10 \le 2\theta \le 80^{\circ}\,2\theta$ range at a step speed varying between $2.5-4^{\circ}$ /min and a step width of 0.02° . To analyse the phases and to assign the obtained Bragg reflections, the measured diffractogram is compared to diffractograms from

the *inorganic crystal structure database* (ICSD) To further examine the lattice parameters via refinements of the XRD patterns, a higher resolution STOE STADI P X-ray diffractometer with a pure Mo K_{α} source ($\lambda = 0.7107 \, \text{Å}$) was chosen for the samples to be measured again. They were measured in transmission mode with a step width of 0.02° and a speed of $200 \, \text{s/step}$.

3.2. Rietveld Refinement

Rietveld refinement [155] is a structural refinement from powder diffraction data and can accurately determine structural details of powdered samples. As a starting point reasonable values of refinable parameters like unit cell parameters, density and Wyckoff positions are required from a calculated powder pattern of a known structure type. This is compared and iteratively refined to the measured powder pattern of the unknown substance. The aim is to identify the intensities and peak positions in a powder pattern as this contains only one-dimensional summations of a 3D diffraction pattern, which can cause partially overlapping reflections or diverging peak shapes. To work with powder diffraction patterns, the background scattering must be known exactly. To circumvent the possibility of a false assumption due to a differing trial structure compared with the true structure, single parameters are refined at any time by least squares algorithms and the difference function determined between the calculated and the observed intensities of the Bragg peaks I^{calc} and I^{obs}, respectively. The refined resulting model is checked for reliability and satisfactory representation of the real structure by means of the *R*-factor as well as the *Rw*-factor consisting of intensity values:

$$Rw = \frac{\sum_{hkl} (I^{calc} - I^{obs})}{\sum_{hkl} I^{obs}} \bullet 100\%$$
 (3.3)

Here, I^{calc} is the refined diffraction pattern and I^{obs} is the measured diffraction pattern. The quality of the refinement is shown graphically by depicting the experimental and the calculated patterns and the difference of both including the Bragg positions. Structural analysis of powder XRD data for each sample was carried out using the GSAS-II program. [156] The background was refined using a polynomial function, followed by a scale factor. Lattice parameters, crystallite size and microstrain and sample displacement were added to the refinement. To obtain the fractional occupancies in the structure, Ni²⁺ was added to the 3*a* sites and the Wyckoff positions of the Li and Ni atoms as well as their displacement parameters U_{iso} refined with the help of constraints to keep the total nickel content in the structure equal to 1.

3.3. Scanning Electron Microscopy SEM

SEM can be used to either observe and image the micro and nano structural surface details and 3D characteristics of a material like morphology, grain size and shape, grain boundaries and defects by scanning the surface in a raster using a focused electron beam. An electron beam has high energy (20 – 100 kV) and small wavelength (0.859 – 0.037 Å) and can resolve details in a material in a magnification range of 10 and 10000 x, it can penetrate a few microns into the sample and generates *secondary electrons* (SE), *backscattered electrons* (BE) and X-rays. Secondary electrons are of low energy and derive from the surface of the sample, resulting in obtained surface images of the sample. Backscattered electrons on the other hand escape from deeper inside the material due to their higher energy and contribute to the distribution of elements in the sample. These signals are used to examine the surface topography, crystallography and chemical composition. [157] [158] [159] The schematic of a SEM is shown in Figure 3.2.

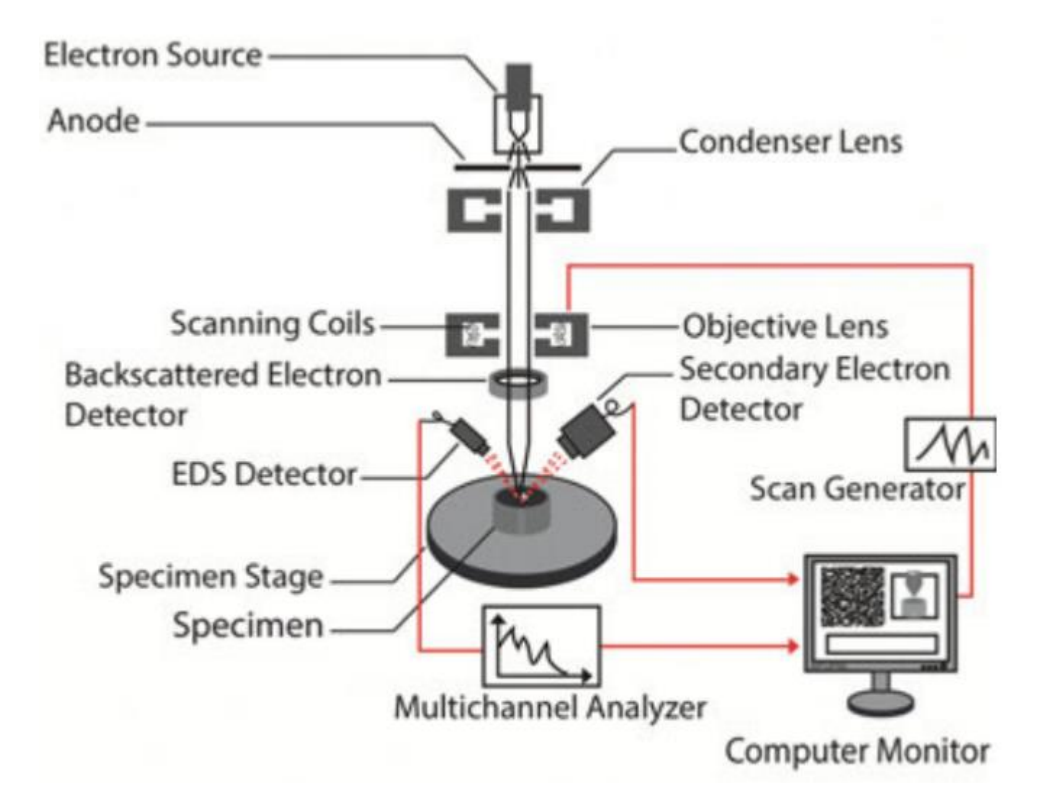


Figure 3.2: Schematic of image formation in a scanning electron microscope. Reproduced from [158] with permission from Springer Nature.

SEM images were obtained using an Inspect F50 SEM from FEI with SE and BE image detectors, operating voltages of 10 kV and a spot size of 3.5. The samples were dispersed onto adhesive conductive carbon tabs attached to an aluminium stub and gold coated under vacuum

for 20 seconds to improve the conduction of the surface of the samples to avoid charging during imaging. *Energy-dispersive X-ray spectroscopy* (EDX) analysis at SEM samples was performed on the same SEM equipment using the additional EDX detector. This detector will only gather chemical information from produced X-rays and produce elemental maps of the samples.

3.4. Thermal Analysis

In thermogravimetric analysis (TGA) a substance is exposed to a temperature program in a closed system where the mass change is recorded by a highly sensitive balance. The temperature program can include heating or cooling at fixed rates as well as constantly holding a temperature for a defined time. The furnace chamber can also be used with various gases to represent inert or reactive atmospheres, commonly nitrogen or oxygen. A TGA curve records the mass change that occurs as a function of the applied temperature and time parameters of the process. The curve reveals changes in the composition of the substance at a given onset temperature such as decomposition reaction, evaporation of crystal water from the structure or uptake of reaction partners from the environment. Another way of using the TGA data is by plotting the derivative of the thermogravimetric (TG) curve to depict the changes happening during heating and cooling even more clearly and deriving the exact temperatures from that. [89] [152] [160]

A Perkin Elmer Pyris 1 TGA is used to determine the mass loss during the measurement. The temperature programme used resembles the calcination condition of LiNiO₂. The sample is heated to 800°C with heating and cooling rates of 5 K/min and the experiment is done in an oxygen atmosphere.

3.5. Laser Diffraction

Laser diffraction uses a light source (He-Ne laser, red and blue laser diodes) to measure the angle of diffracted light when hitting a particle, to determine its size distribution. Specimen particles are dispersed in a liquid and passed through by a laser beam. The particles diffract the incoming light beam at various angles, with larger particles scattering light at smaller angles and vice versa, generating a pattern of concentric circles (Figure 3.3). These overlapping patterns are converted to a spatial intensity pattern via Fourier transformation. The intensity is dependent on the wavelength of the light, the diffraction angles and the number of particles in

the solution. If the solution is over saturated, the light will be diffracted multiple times before it is detected. The measured intensities are then converted into a particle size distribution.

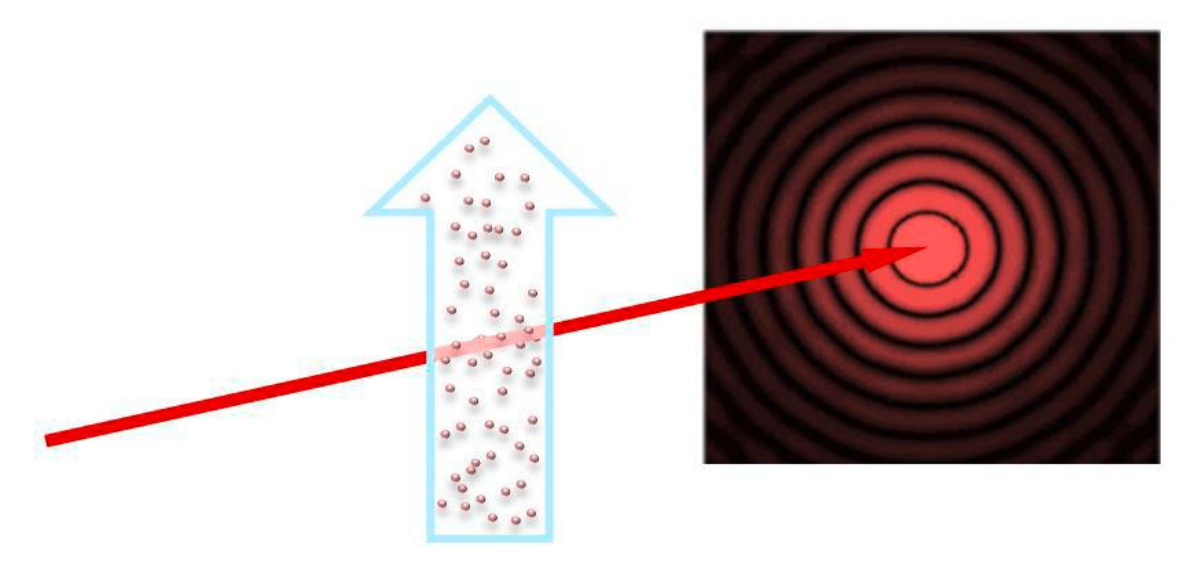


Figure 3.3: Illustration of laser diffraction in a particle size analyser. The red arrow represents the laser beam. The blue arrow contains the sample dispersion. [160]

Following the Fraunhofer diffraction theory, assuming a spherical particle shape, the laser beam will hit the sample and be scattered at its surface. It does not consider phenomena like absorption, refraction or reflection of the light. Experimentally measuring the particle size distribution only works when assuming the particles are uniform regarding sphericity, density and refractive index. So, the values gained from any particle sizing technology differ from reality as there is no guarantee that all the particles in the sample are perfectly spherical.

Particle sizes are being reported here as a volume distribution using three values on the x-axis, D10, D50 and D90, where D50 is the median. It is defined as the point where half of the particles are smaller, and the other half are bigger than this diameter. Similarly, 10 percent of the total particle population lies below the D10 and 90 percent of the population lies below the D90 value. [161] [162] [163]

Here the particle size distribution is measured using the Mastersizer 3000 from Malvern Panalytical. The particles are dispersed in *deionised* (DI) water and measured 10 times using both, a red (He-Ne, 632.8 nm) and blue (10 mW *light emitting diode* (LED), 470 nm) light source and a detector array with an angular range between 0.015 and 144 degrees.

3.6. Tap Density

Bulk density is the ratio of the mass of a sample to its volume. It includes voids between the particles as it is measured in an untapped state. It is dependent on the particle size and density and their spatial arrangement as well as the surface area, the moisture content and the cohesiveness of the material. Tap density on the other hand, is the increased bulk density after a certain amount of tapping of the sample. This removes the influence of the interparticular voids and gives an idea about the compressibility or flowability of a powder, when compared to the bulk density. This is usually done using the Hausner's ratio or the compressibility index. In battery cathode active material research, the tap density is often stated to give an idea about the packing density in the cathode sheet. [164] [165]

The measurements are conducted in 5 mL cylinders in a tapping density tester JV 200i by Copley. The powders are tapped for 10 min at a rate of 200 taps per minute. The initial and final volume is recorded and tap density, Hausner's ratio and the compressibility index calculated.

3.7. Brunauer-Emmett-Teller (BET) Surface Area Analysis

Measuring the specific surface area of a solid can help understand reaction processes happening during electrochemical cycling and reactivity of the surface. One very simple method to determine the specific surface area is the *Brunauer-Emmett-Teller* (BET) analysis technique which is an extended Langmuir theory to multilayer molecular adsorption. Here, the surface is exposed to a reactive gas (argon, nitrogen or krypton), while the sample is cooled with liquid nitrogen under vacuum. The gas molecules form an adsorption layer on the sample surface (see Figure 3.4). Once the saturation pressure is reached, the sample is heated, the adsorbed gas is released and quantified. To avoid any errors due to contaminants at the surface and to increase accuracy of the measurement, the sample will be degassed before measurement under vacuum at highest temperatures possible to not damage the sample. [166] [167] [168]

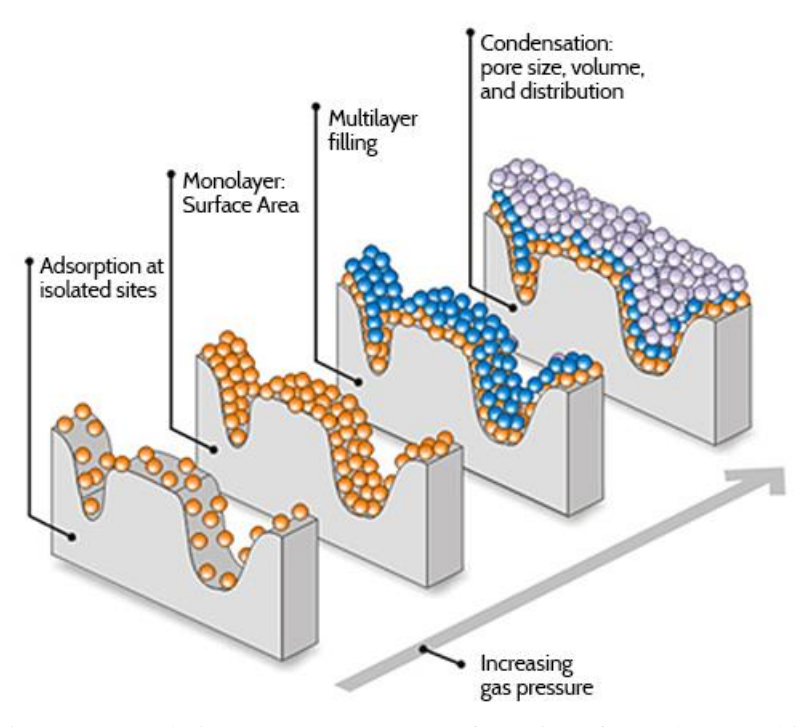


Figure 3.4: Adsorption processes during BET measurements; formation of monolayer, multilayer and complete filling with increasing applied pressure. [165]

The amount of adsorbed gas Q is displayed as a function of relative pressure. The linear part of the data between $0.05 \le P/P_0 \le 0.35$ is used to calculate the surface area using the BET Equation 3.4.

$$\frac{1}{Q\left[\frac{P}{P_0} - 1\right]} = \frac{1}{Q_m C} + \frac{C - 1}{Q_m C} \left(\frac{P}{P_0}\right) \tag{3.4}$$

With P/P_0 being the relative pressure, C the BET constant and Q and Q_m the adsorbed weight and adsorbed monolayer weight, respectively. The slope s and the intercept y of the BET plot can be derived from Equations 3.5 and 3.6.

$$s = \frac{C - 1}{Q_m C} \tag{3.5}$$

$$y = \frac{1}{Q_m C} \tag{3.6}$$

From there, Q_m and C can be obtained (Equations 3.7 and 3.8):

$$Q_m = \frac{1}{s+y} \tag{3.7}$$

$$C = \frac{s}{y} + 1 \tag{3.8}$$

Finally, the surface area can be calculated from Equations 3.9 and 3.10:

$$S_t = \frac{Q_m N A_m}{M_V} \tag{3.9}$$

$$S_{BET} = \frac{S_t}{m} \tag{3.10}$$

Where N is Avogadro's number, A_m is the cross-sectional adsorbate area $(0.162 \, \text{nm}^2 \, \text{for})$ nitrogen), M_v is the molar volume of the adsorbate gas and m is the mass of the adsorbant. [167]

BET analysis was performed by Abby J. Shipley in the department of Chemical and Biological Engineering at University of Sheffield on a Micromeritics 3Flex advanced gas adsorption tool. The samples were degassed at 150°C overnight for around 18 h in a separate vacuum degassing mantle before measuring the surface area using nitrogen gas.

3.8. Galvanostatic Cycling

To investigate the electrochemical performance of cathode materials in battery cells, a very common method to gain a deeper insight into the materials and processes is *galvanostatic cycling with potential limitation* (GCPL). Here, a constant current is applied to a cell and the potential as a function of charge is recorded within a defined potential window. The direction of the current is switched cyclically which corresponds to charge and discharge processes. The current used is denoted as *C* rate, where 1 C is the current needed to charge the electrode in 1 hour, relative to the capacity which depends on the mass of the electrode material inside the cell and the Li⁺ amount which can be de-/intercalated. It describes the electric charge a battery can deliver at a given voltage. Results of these techniques are the specific capacity of the cell. The capacity shows how much energy the cell can store and release during operating conditions. Every cathode active material has a theoretical capacity which is dependent on the amount of Li⁺ ions that can be extracted from the structure or intercalated into the structure during charge and discharge and can be calculated using the following equation:

$$Q = \frac{nF}{M_W} \tag{3.11}$$

Where Q is the capacity in C/kg. n is the number of Li⁺ ions per formula unit in the electrode material, F is the Faraday constant (~ 96485 C/mol), and MW is the molecular weight of the active electrode material. Another output of these experiments is the capacity rate change with respect to voltage during cycling in form of a dQ/dV plot. These plots show voltage regions with large capacity changes that can be associated with ionic (re)intercalation and the redox processes that take place in the cathode. They show phase transitions that occur during cycling and degradation processes can be quantified as well.

Galvanostatic cycling experiments are conducted in coin cells on a BioLogic VSP potentiostat. A coin cell was built as depicted in Figure 3.5 in an Argon filled glovebox. Dried cathode disks used in the coin cells were produced from a slurry containing 90 wt% of sample, 5 wt% carbon black and PVDF each and between 0.25 and 0.3 mL *N-Methyl-2-pyrrolidone* (NMP) as solvent. The dry ingredients were ground in a mortar and pestle for 10 min before adding the NMP until the slurry has a consistency of honey. It is then mixed in a Thinky mixer for 10 min and cast onto carbon-coated aluminium sheets with a thickness of 15 µm. The sheets were dried at 100°C

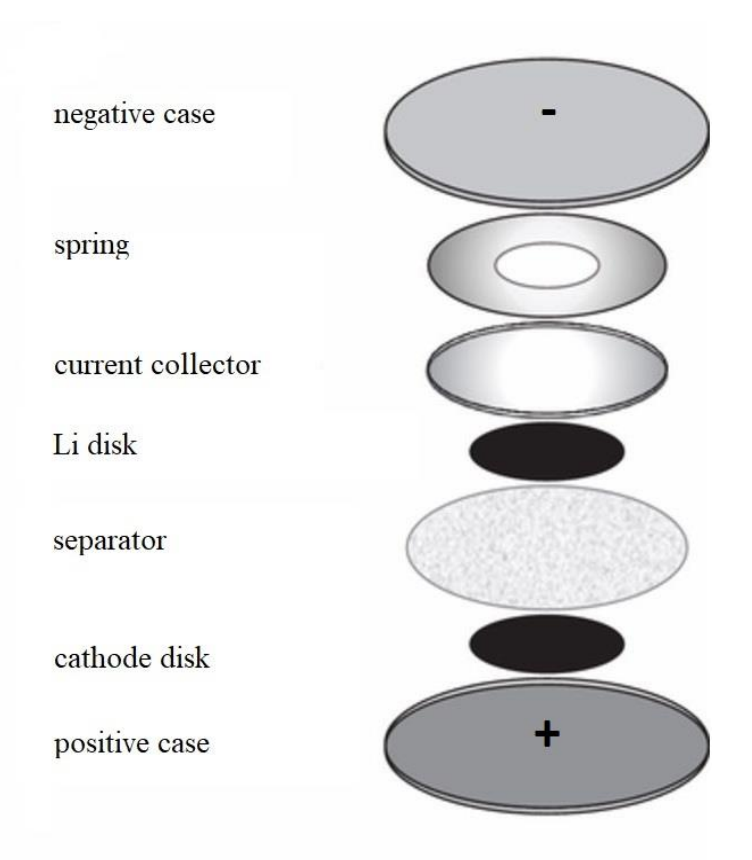


Figure 3.5: Diagram of coin cell.

to evaporate the NMP for 3 h and stored in a vacuum oven at 80°C. The following day, disks were punched from the sheets and stored in a glovebox.

From the assumed practical capacity of 220 mAh/g of LNO, the current was calculated using the mass of the dried cathode material. The coin cell is cycled at room temperature between 3 and 4.3 V vs. Li/Li⁺ after a resting period of 2 hours, at the current corresponding to a rate of C/20 for 2 cycles and then for another 98 cycles at C/2. Coin cells made from the synthesis optimisation samples of the precipitation synthesis of the Ni(OH)₂ precursor and the doped LNO samples were conducted in a controlled temperature chamber. For samples from solid-state optimisation experiments although, the temperature chambers were not yet available for use and so the electrochemical testing was carried out at room temperature, which fluctuated due to the heat produced by battery cyclers in the room.

3.9. X-Ray Absorption Spectroscopy XAS

X-ray absorption spectroscopy is used to probe the bonding state of an element and its local structure in a chemical structure. The incident X-ray is absorbed by an electron at or near the core-level of an atom. That electron is being ejected from its shell either to an unoccupied excited electronic state of higher energy or into continuum. A photoelectron is released at the same time and its energy detected. This process is called photoelectric effect and depicted in Figure 3.6. As the binding energies of the initial state of the core electrons of different elements are known, the intensity measured by the released photoelectron compared to the incoming intensity of the beam gives the absorption coefficient μ according to the Lambert-Beer law (Equation 3.12).

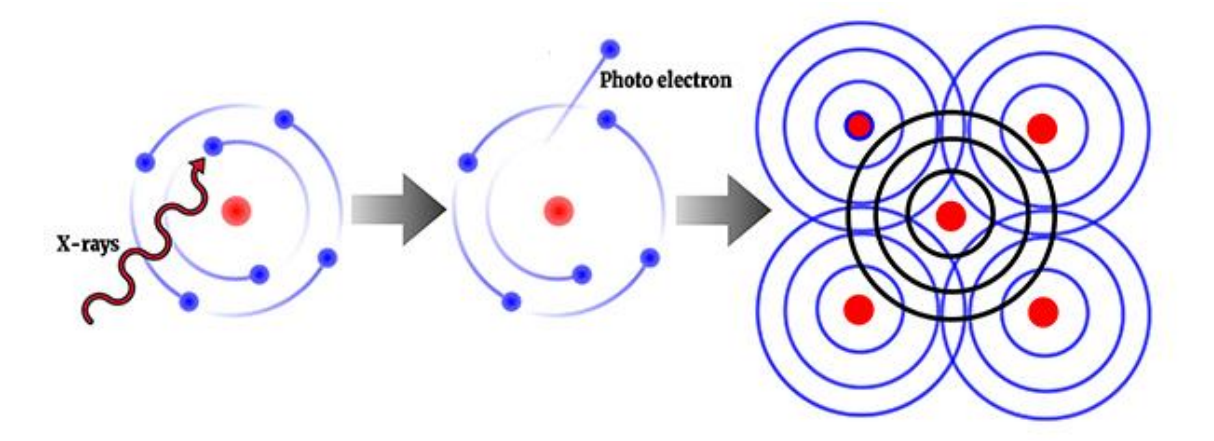
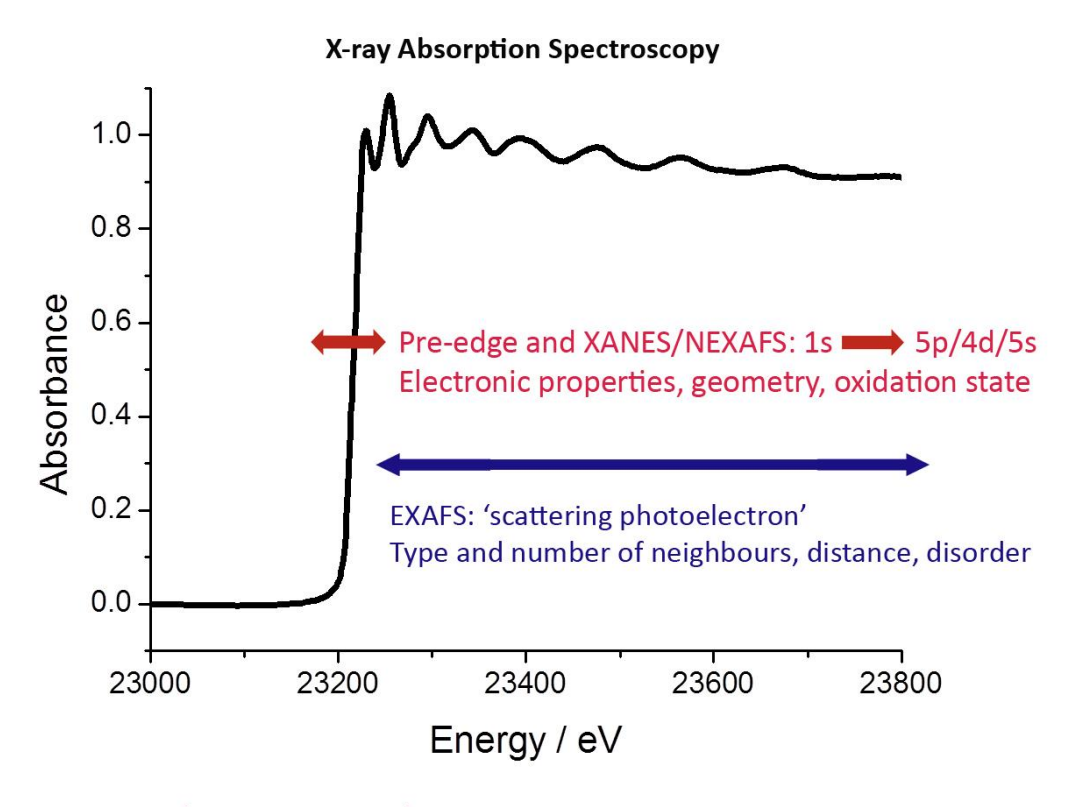


Figure 3.6: Photoelectric effect showing the ejection of electrons from the core level and its resulting interactions with neighbouring atoms. [171]

Photoelectrons ejected from the 1s core shell are related to the K absorption edge and those emitted from the 2s or 2p shell to the L absorption edge.

$$I = I_0 e^{-\mu t} (3.12)$$

Where I₀ is the intensity of the incident beam, t is the sample thickness, and I is the measured intensity. Using a synchrotron source, the X-ray energy can be tuned to any element desired, where the binding energy of a core electron needs to be less than the incident X-ray. Both, the use of soft (< 5 keV) and hard X-rays (> 5 eV) is common. Following the dipole selection rules, soft X-rays probe the surface, the metal L-edges (3d states) and oxygen K-edges (2p states), and hard X-rays investigate the coordination chemistry of metal atoms penetrating their K-edges.



XANES – X-ray Absorption Near Edge Structure NEXAFS – Near Edge X-ray Absorption Fine Structure EXAFS – Extended X-ray Absorption Fine Structure

Figure 3.7: Absorption spectra showing the different regions like XANES and EXAFS. [171]

The resulting spectra of hard X-ray absorption spectroscopy can be divided into XANES or near edge X-ray absorption fine structure (NEXAFS) and EXAFS regions (Figure 3.7) and gives information regarding the oxidation state of the probed element and its chemical

environment. The XANES region consists of the pre-edge feature, the edge itself and the white line, which is the absorption peak maximum. Everything beyond that are oscillations in the EXAFS region, where the neighbouring environment of the absorbing element can be examined. [169] [170] [171] [172]

3.9.1. X-Ray Absorption Near-Edge Structure XANES

This method probes the electronic structure and local coordination environment of the absorbing element. It allows for the oxidation number determination of the examined element It qualitatively describes the coordination chemistry, the molecular orbitals, the band structure and shows what electronic state the photoelectron occupies. In the resulting spectra, usually measured in transmission mode, the pre-edge is caused by electronic transitions to empty bound states, which are controlled by dipolar selection rules. The absorption edge defines the ionisation threshold to continuum states and shifts to higher energies with increasing oxidation state of the probed element. The XANES region beyond the white line is dominated by scattering resonances of ejected photoelectrons at low kinetic energies and gives atomic positions of neighbouring atoms, their distances and angles. [170]

3.9.2. Extended X-Ray Absorption Fine Structure EXAFS

EXAFS describes the higher energy regions of the absorption spectrum. Atom numbers, types and distances of neighbouring atoms from the absorbing atom are determined. The spectra show oscillations which can be understood as waves, scattered at neighbouring atoms, as the photoelectron propagates outwards. For easier quantification, the X-ray energies are converted into wavenumbers k. To make interpretation of the frequencies at higher wavenumbers easier, a weighting factor is used. The weighting factor amplifies the oscillations at higher wavenumbers relative to the size of the oscillations at low wavenumbers. [170]

3.9.3. Soft X-Ray Absorption Spectroscopy sXAS

Soft X-rays of lower photon energy and longer wavelength are used to probe the electronic structure of an element at the surface of a material, usually in a surface-sensitive *total electron yield* mode (TEY) with a depth of < 10 nm or by using the sub-surface sensitive *fluorescence yield* mode (FY) up to a depth of around 100 nm. This method can help understand the evolution of the surface structure, like side phases or unoccupied states near the Fermi level. [173] These

states, occupied or unoccupied, are of special interest in the battery application processes, as electrons are removed or added from or to these levels during the electrochemical charge and discharge processes. Here, core electrons get excited by the incident beam into empty states above the Fermi level or into the vacuum. The resulting hole is filled by an electron from a higher shell while transferring the difference in energy to an electron in the outermost shell, which is then released and called Auger electron (Figure 3.8). [174]

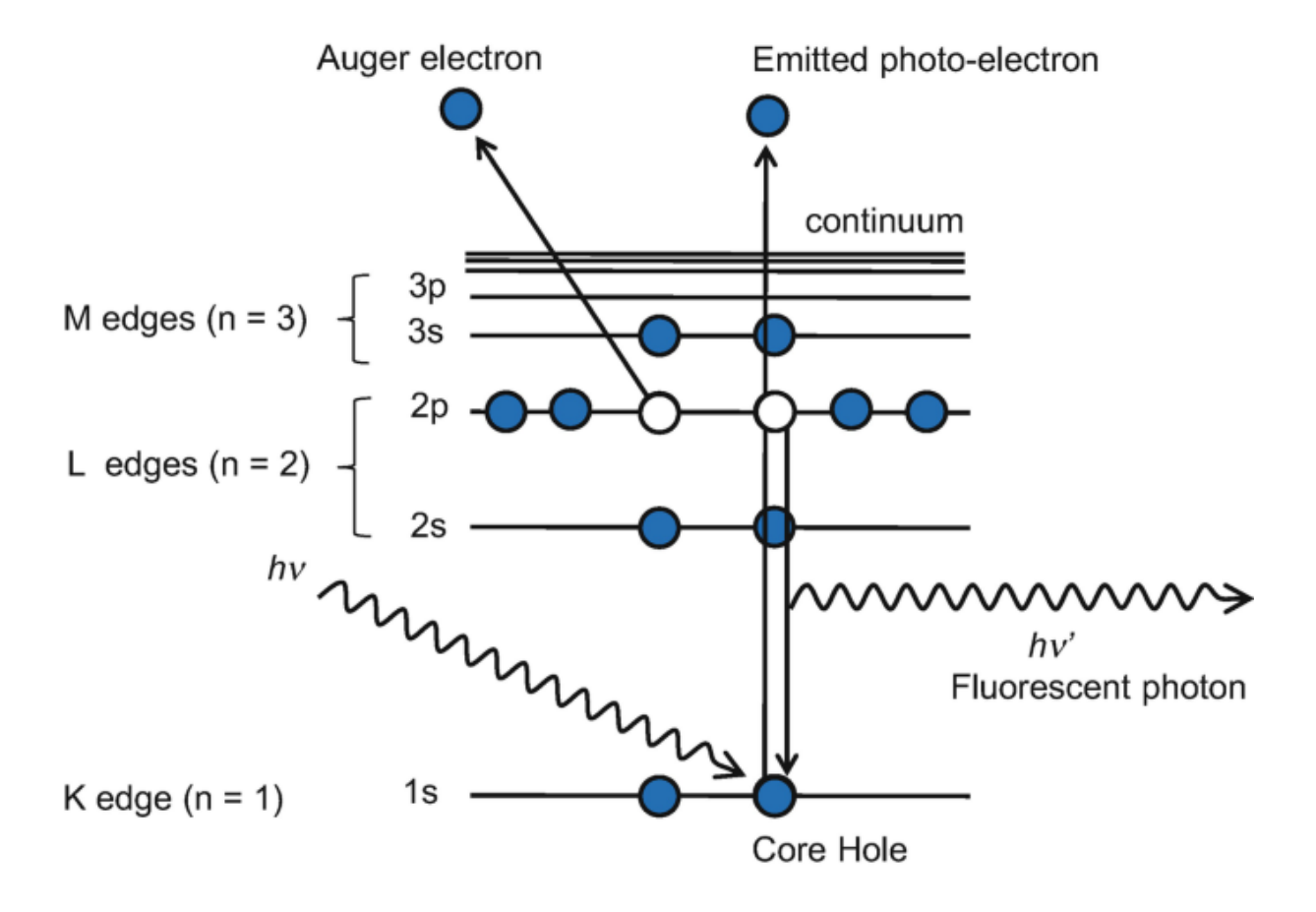


Figure 3.8: Auger effect when core electron is ejected, creating a hole. An electron from a higher energy shell will fill that hole and an Auger electron will be released to balance the energy difference. Reproduced from [173] with permission from Springer Nature.

Measuring the intensity of the resulting released photon of this process gives the fluorescent yield whereas the counting of the emitted electrons (including Auger electrons) during the process, give the total electron yield.

Probing these states in TM elements might show additional contributions of oxygen (whose states are close to the Fermi level and might get oxidised during deintercalation processes during battery cycling) in the fluorescence yield, thus giving a less accurate picture. These so-called lineshape distortions can be avoided by using other techniques like *resonant inelastic*

X-ray scattering (RIXS) and other integrating methods for the data like *inverse partial* fluorescence yield (IPFY) or studied by comparing soft XAS and RIXS data. [173] [175]

3.10. X-ray Photoelectron Spectroscopy XPS

XPS also uses the photoelectric effect, as explained in Chapter 3.9, to investigate the surface within a few nanometres of the surface of a sample. It quantitatively depicts the chemical composition by displaying peaks corresponding to the binding energies of a species where the intensity of the peaks is a direct measure of the number of electrons with these binding energies. The local bonding environment of a species and its chemical state can be characterised using the shift in elemental binding energies. This can help with surface species building up during the high temperature calcination step of layered oxide materials or at the surface of the cathode during cycling. In this technique as well, soft and hard X-rays can be used to probe the sample. [175] [157]

3.11. Hard X-ray Photoelectron Spectroscopy (HAXPES)

Hard X-ray photoelectron spectroscopy (HAXPES) utilises hard X-rays of a high energy range to probe the extended surface area (several tens of nanometres) of a sample usually at a synchrotron facility. With this technique, the thickness of surface layers, SEIs or CEIs can be investigated as well as their quantitative chemical composition. Oxygen redox can be also identified by quantifying the bulk oxidised oxygen states at high voltages in battery cathode materials. [175] [157] [176]

3.12. Magnetometry SQUID

To examine the magnetic properties of a material, a *superconducting quantum interference* device SQUID magnetometer is used. Like regular magnetometers, it measures the magnetic susceptibility χ ("chi") induced by the ordering of unpaired electrons within atoms in the material while an external magnetic field and temperature are applied. The SQUID is very sensitive to weak magnetic changes in a material and can help quantify the Ni²⁺ disorder in non-stoichiometric layered oxides.

$$\chi = \frac{C}{T - \theta_{CW}} \tag{3.13}$$

Using the Curie-Weiss law in Equation 3.13, important magnetic parameters like the Curie Constant C, a measure of unpaired electrons in the compound and the Weiss constant/Curie-Weiss temperature θ_{CW} , indicating ferromagnetic or antiferromagnetic interactions, can be derived. Additionally, the paramagnetic behaviour of a material at high temperatures can be captured if the plotted data shows linear behaviour.

$$\mu_{eff} = \sqrt{8C} * \mu_B \tag{3.14}$$

The effective magnetic moment per ion μ_{eff} can be calculated according to Equation 3.14, using the Curie Constant C derived from the magnetic measurements. The derived magnetic moment is compared to a calculated value for the ion in question using its g-tensor g_J and its angular momentum J:

$$\mu_{calc} = g_J \sqrt{J(J+1)} * \mu_B \tag{3.15}$$

In the case of 3d TM, the spin-orbit coupling can be ignored due to enhanced coulombic interactions between the 3d orbitals of the transition metal and their ligands orbitals. This simplifies the equation to:

$$\mu_{calc} = g\sqrt{S(S+1)} * \mu_B \tag{3.16}$$

For Ni $^{3+}$ with a spin of ½, the calculated magnetic moment is $1.732\,\mu_B.$ [177]

We examined the lithiated precursor samples synthesised with different Ni:NH₄OH ratios using a Quantum Design SQUID MPM3 magnetometer under *zero-field cooled* (ZFC) and *field cooled* (FC) conditions between 0 and 350 K under a magnetic field of 1000 Oe.

3.13. Muon-Spin Relaxation Spectroscopy µSR

Muon spin relaxation spectroscopy (µSR) is used to detect and track the Li movements in a battery cathode material, determine material properties like the diffusion coefficient, the activation energy for ionic movement as well as the local magnetic fields around the muon. The

advantage of muons is, that their energy can be tuned and so the implantation depth within the sample controlled to be able to study defined regions in the bulk [178].

Spin polarised (initial spin direction is antiparallel to its momentum), positively charged muons are implanted into the bulk of the material and initial thermalisation happens. This energy loss is due to various processes like atom ionisation and inelastic scattering with electrons as well as several electron-capture and -loss reactions where the muon captures an electron, transforms into a muonium (μ^+e^-) and is stripped of its electron again. During the latter phenomenon, the muonium collides with atoms in the structure, leading to final thermalisation until the muons stop close to the oxygen site in the structure, a site of high electron density, forming a stable $\mu^{\!\scriptscriptstyle +} - O^{2 {\scriptscriptstyle -}}$ bond. Its spin direction is influenced by the local field distribution Δ from the static nuclear environments around it and the fluctuation rate v from the dynamic nuclear environments of Li⁺ passing by. When an ion with a nuclear magnetic moment (such as Li⁺) moves past the muon, its spin flips. As the muon decays after an average lifetime of 2.2 µs into a positron and two neutrinos, the positron moves preferentially in the same direction as the muon spin. This time evolution of the positron asymmetry is measured and can be treated as equivalent to the time dependence of the muon ensemble's spin relaxation, which is related to the hopping rate of Li⁺ ions and can be used to calculate the diffusion rate coefficient (Equation (3.15)). Positron direction can be measured by forward and backward facing detector banks mounted around the sample and the positrons asymmetry determined. As the muon's gyromagnetic ratio is smaller than an electron's but larger than a nucleus' ratio, it is very sensitive to small magnetic fields inside a material, even if it is paramagnetic. The asymmetry signal depends on the size of the nuclear magnetic field distribution, the paramagnetic spin dynamics (accounted for by an exponential relaxation exp(-λt)) and how often an ion passed the muon [179] [180] [181] [182] [183]. The diffusion coefficient may be given by:

$$D_{Li} = \sum_{i=1}^{n} \frac{1}{N_i} Z_{\nu,i} s_i^2 \nu_{Li}$$
 (3.15)

Where N_i is the number of Li sites in the *i*th path, $Z_{v,i}$ is the vacancy fraction and s_i is the hopping distance for Li⁺ ions. The muons' spin for a single muon stopping site in a polycrystalline material revolves as:

$$P(t) = \frac{1}{3} + \frac{2}{3}(1 - \Delta^2 t^2) exp\left(\frac{-\Delta^2 t^2}{2}\right)$$
 (3.16)

With P(t) is the polarisation of the muons' spin over time and Δ the static width of the local field distribution. 1/3 accounts for the non-relaxing baseline signal and 2/3 for the signal of randomly oriented grains, whose angles differ due to the polycrystalline nature between the internal field and the muon's spin polarisation [182]. The experimental asymmetry to gain information about the muon's spin polarisation is obtained from this function:

$$A_0 P(t) = A_{bg} + A_{KT} G_{KT}(\Delta, \nu, t, H_{LF}) e^{-\lambda t}$$
(3.17)

Where A_0 is the initial asymmetry, A_{bg} and A_{KT} are the respective amplitudes of background and the *Kubo-Toyabe* (KT) function and G_{KT} is the dynamic form of the KT function, sensitive to the static field distribution width at the muon stopping site Δ and the field fluctuation rate ν with time t and the applied longitudinal field H_{LF} . [182]

Muon spin relaxation spectroscopy on powder samples as well as operando Li/LiNiO₂ half cells, will help understand the influence of structural deviations in the material, like cation mixing, on the Li diffusion. Measurements on the powder sample were taken under zero field (ZF) and *longitudinal fields* (LF) of 5 and 10 Gauss every 20 K between 100 and 400 K on the EMU beamline at ISIS, Didcot, UK.

3.14. X-Ray Diffraction Computed Tomography

X-ray diffraction computed tomography is an experimental technique that combines X-ray diffraction of a powder sample with the imaging technique *computed tomography* (CT). In this technique, the recorded X-ray diffraction patterns are reconstructed to slices of cross-sectional XRD-CT images in which every voxel equates to a local diffraction pattern (Figure 3.9). By stacking the slices and rendering them, a 3D volumetric image of powders or cathodes can be produced, and their crystallographic and structural properties can be obtained. Those images give insight into the relationship between structure and function of the material, as spatially resolved chemical information is gained. In the case of a cathode material cycled to different cut-off voltages, the chemical information and crystallographic orientations of the primary particles within the secondary particle assemblies of the active material can be spatially resolved using this technique and the variation in peak intensity and peak location used to determine the orientation of the primary particles on a voxel to voxel basis. [184]

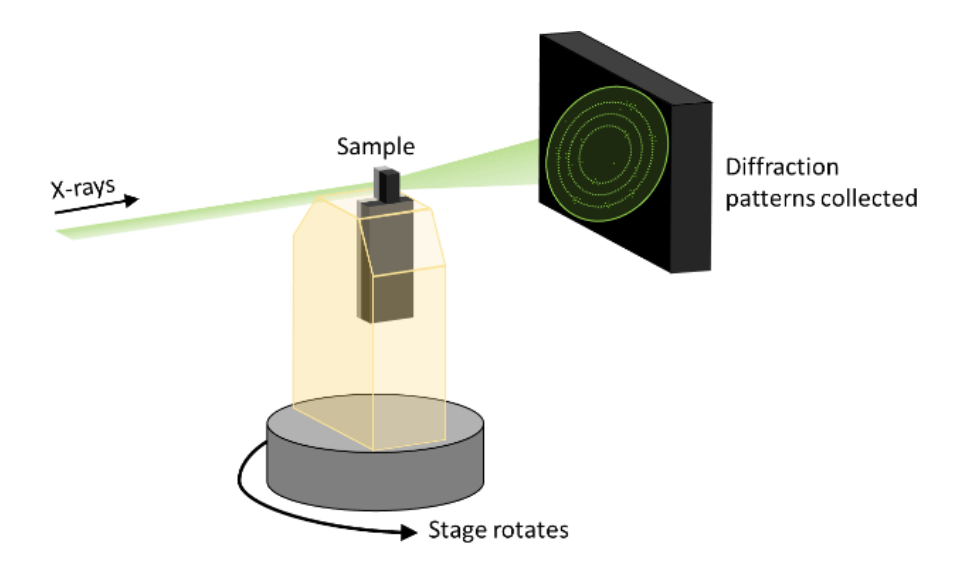


Figure 3.9: Schematic set-up of experiments on ID11 beamline at ESRF, France. Graph by Finden Ltd.

This technique is non-destructive and enables spatially resolves studies in a very short time. The obtained information includes the chemical species, even of low density or low absorption cross-section as well as their physical characteristics like unit cell parameters, crystal size and orientation in a full chemical map. The obtained data will be analysed and reconstructed to full 3D CT images.

The measurements of the optimised LiNiO₂ material produced here and cycled to different SOCs are examined on a micro-focused in-situ XRD-CT beamline at DESY in Hamburg, Germany as well as nano-imaging XRD-CT at the ID11 beamline at ESRF in Grenoble, France in collaboration with Finden Ltd in Didcot, UK, who analysed the data.

4. Optimisation of the Annealing Process for the Layered Oxide Cathode Material LiNiO₂ for Li-Ion Battery Application

4.1. Introduction

The advantages of LiNiO₂ as a cathode material for Li ion batteries due to its very high specific capacity of 274 mAh/g are based on its periodic, ordered layered structure. Yet, during the solid-state synthesis of a Ni source with a Li source at high temperatures, various difficulties arise. Those complications include a loss of Li content during the calcination due to the high vapour pressure of the Li source [50], the movement of Ni²⁺ into the Li layer due to its similar size (Ni²⁺ (0.69 Å); Li⁺ (0.76 Å) [17]) as well as the buildup of Li rich side phase on the surface of the particles. Unfortunately, these issues are all intertwined with each other and depend on each other. Therefore, the solid-state synthesis procedure is a crucial element to be optimised for the cathode material to enable access to the theoretical capacity and to realise the full capability of this promising material. The goal of this chapter is to minimize the appearance of side phases and cation mixing within the sample by adjusting the pre-calcination and annealing step regarding temperature and time. Avoiding high calcination temperatures of 750°C, as often used in literature for layered oxide synthesis, decomposition of LNO is prevented and the formation of Li containing side phases inhibited. This will promote less Li vacancies and less Ni³⁺ \rightarrow Ni²⁺ reduction and thus form more stoichiometric samples.

4.2. Experimental Synthesis Optimisation

The Ni(OH)₂ precursor obtained from synthesis in a stirred tank reactor (this is further detailed in Chapter 5) was used as a Ni source (SEM images of Ni(OH)₂ sample in Figure 4.1) and thoroughly mixed with LiOH•H₂O in a 1:1.03 ratio by hand with a mortar and pestle. A 3% excess of the Li source was used to account for the Li loss during high temperature synthesis. Both compounds were ground together for 20 min before transferring the mixture in an alumina crucible into a tube furnace.

The synthesis was conducted under an oxygen atmosphere which facilitates the necessary oxidation of Ni²⁺ in Ni(OH)₂ to Ni³⁺ in LiNiO₂. The starting parameters for this calcination study was based on prior work on a calcination procedure for NMC materials in the Cussen

research group, where the mixture was pre-calcined at 500°C for 12 h, followed by regrinding and a calcination at 750°C for 15 h. The sample was removed from the furnace at 200°C to mitigate side reactions with air or moisture and quickly transferred into an Ar filled glovebox to further protect it from moisture and air.

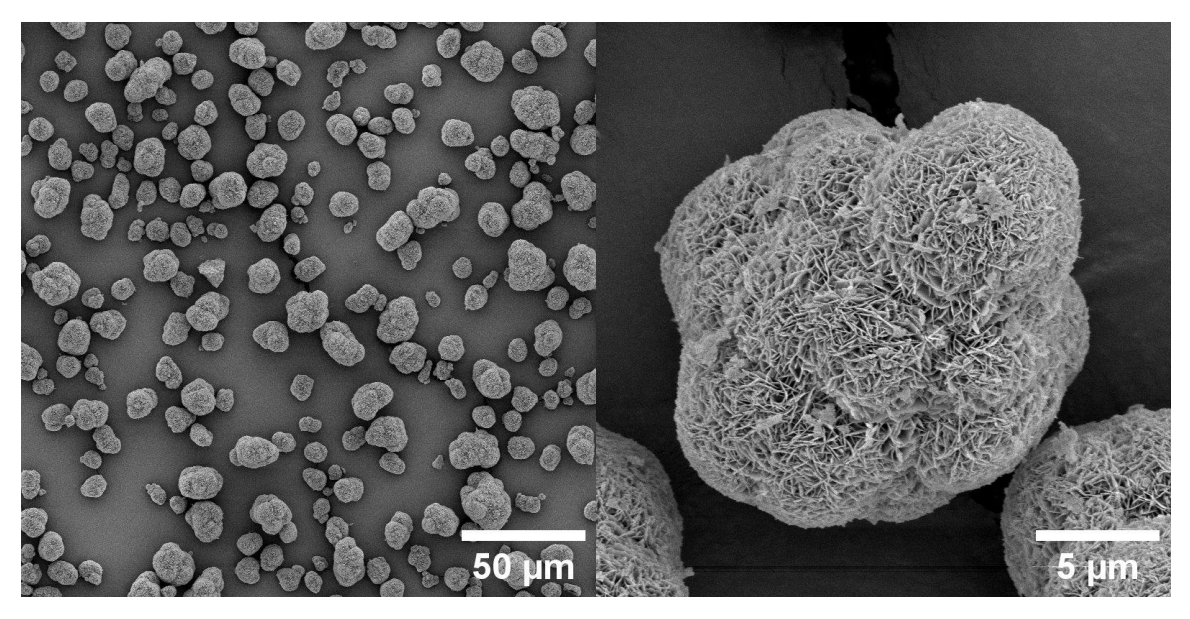


Figure 4.1: SEM images of the Ni(OH)₂ sample precipitated in a stirred tank reactor (Chapter 5) and used for further investigations in this chapter.

To investigate the as-prepared samples, XRD measurements and Rietveld refinements of that data, SEM and electrochemical cycling were conducted and analysed to find a synthesis route optimised regarding the cation mixing in the layered structure and exceptional cycling behaviour. The powders were ground and processed for XRD and SEM measurements within the glovebox and slurries for coin half-cell testing prepared as described in Chapter 3.8.

4.2.1. Intermediate Grinding Evaluation

The necessity of the intermediate grinding step between pre-calcination and calcination of the Ni and Li precursors is not properly validated. On the one hand, pre-annealing the mixture to 500°C leads to dehydration of the precursors, a densified and homogenised mixture at temperatures exceeding the melting temperature of LiOH (462°C). Thus, grinding this mixture helps to break up and homogenise the particles [42], affording enhanced solid-state diffusion during the calcination stage. On the other hand, removing the sample from the furnace to grind, exposes it to air and moisture, increasing the risk of side phases forming on the surface with Li, leading to Li deficiency and introducing more cation mixing.

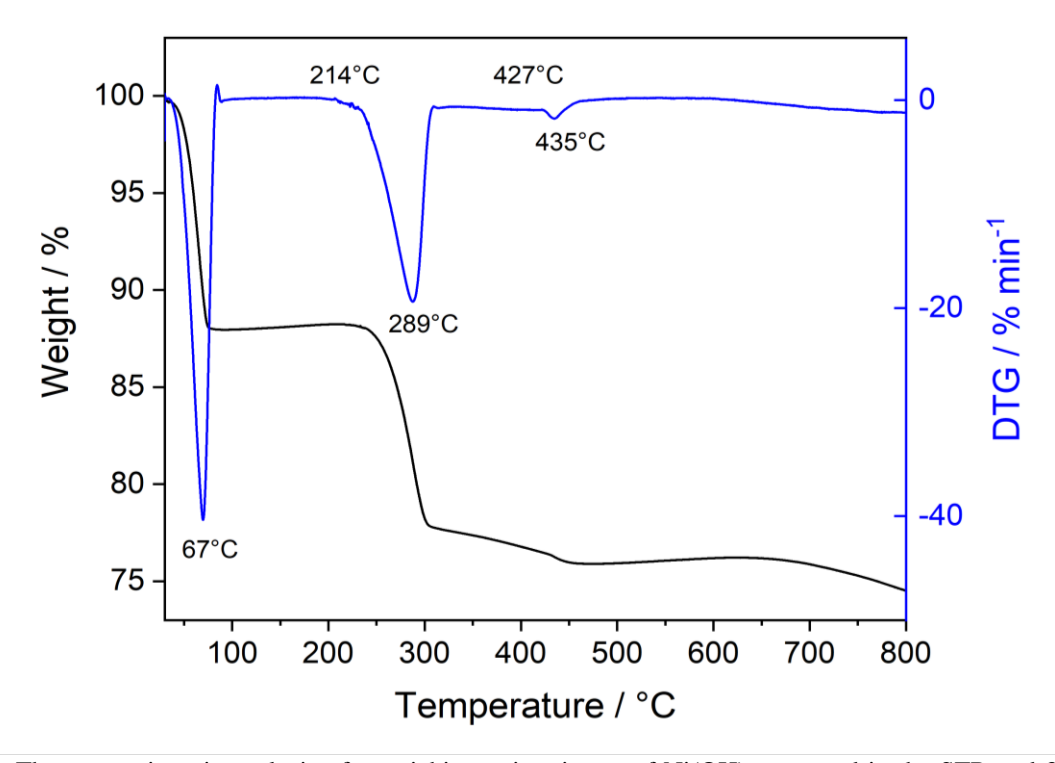


Figure 4.2: Thermogravimetric analysis of a stoichiometric mixture of Ni(OH)₂ prepared in the STR and 3% excess of LiOH•H₂O heated up to 800°C under oxygen flow. TG curve in black and its derivative DTG curve in blue.

To investigate the processes that take place during the pre-calcination in the furnace in depth, a TGA measurement (Figure 4.2) and a HT *operando* XRD (Figure 4.3) was utilised, mimicking the actual reaction. The TGA measurement was done in an oxygen atmosphere between 25 and 800°C with a heating rate of 5 K/min. HT-XRD could only be performed in air as the device was not able to facilitate an oxygen atmosphere. The formation of a Li containing side phase in the XRD pattern is due to this missing oxygen atmosphere.

The DTG curve (blue), which is the derivative of the TGA curve, shows the rate of change of mass with respect to time or temperature. Several downward facing peaks at 67, 289 and 435°C can be seen. These determine the temperature of occurring thermal events like decomposition during the reaction. The TG curve (black) shows steps at these temperatures, which correspond to the actual mass losses which help identifying the process behind. The first step with a mass loss of 13%, complies with the dehydration of the LiOH•H₂O precursor material as shown in Equation 4.1. The second step is accompanied by another mass loss of 13%, assigned to the dehydration of the Ni(OH)₂ precursor and the formation of NiO (Equation 4.2).

$$Ni(OH)_2 + LiOH \cdot H_2O \rightarrow Ni(OH)_2 + LiOH + H_2O \uparrow$$
 (4.1)

$$Ni(OH)_2 + LiOH \rightarrow NiO + LiOH + H_2O\uparrow$$
 (4.2)

The latter mass loss at 435°C might be associated with the melting of LiOH, but further investigations are needed to confirm this observation, as according to safety data sheets of suppliers, the melting point of LiOH•H₂O is 462°C. In total, a mass loss of around 30% can be detected. These results are in accordance with literature reports, where a more detailed TG analysis shows not only the mixture of Ni(OH)₂ and LiOH•H₂O, but also the reactants on their own. This analysis clarifies that the transition at 435°C can be assigned to an early melting of LiOH. The theoretical mass loss of a water molecule from Ni(OH)₂ and LiOH•H₂O equals 13.4%. [42]

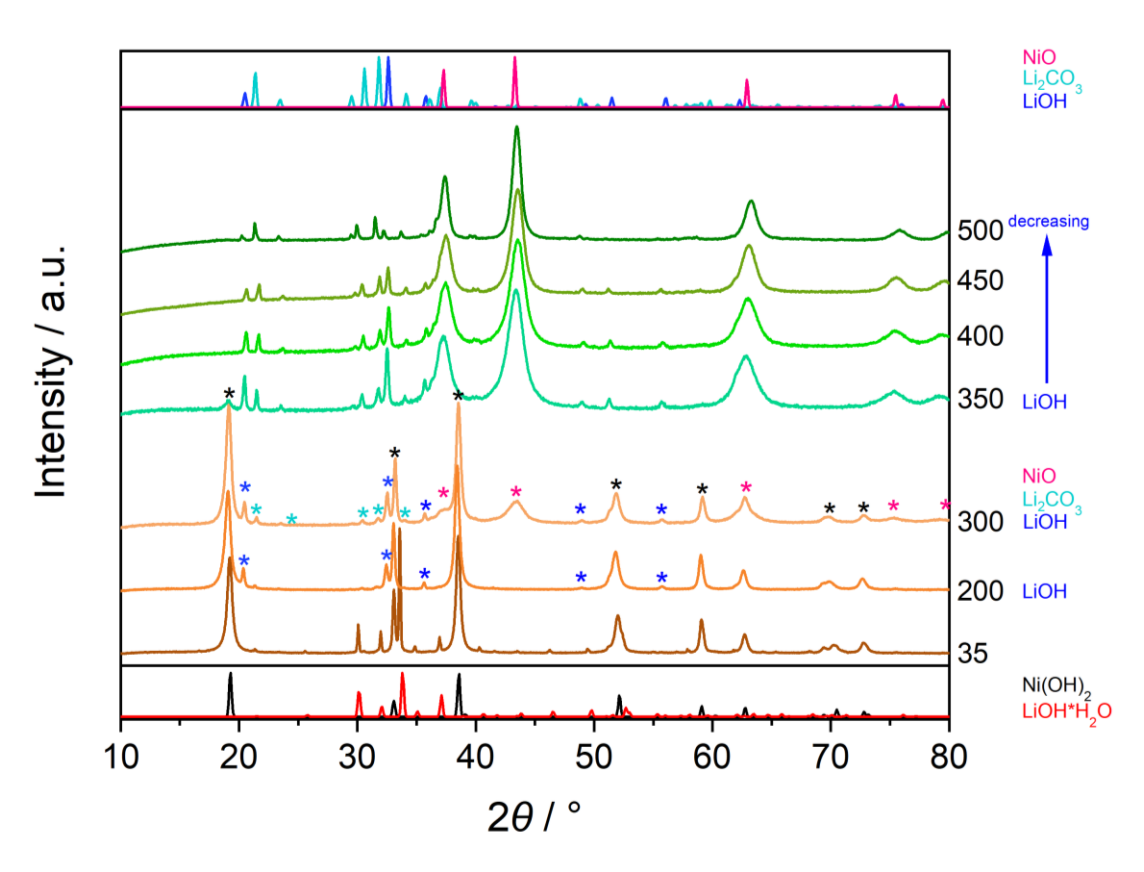


Figure 4.3: High temperature operando X-ray diffraction patterns of a mixture of $Ni(OH)_2$ and $LiOH \cdot H_2O$ in air between 35 and $500^{\circ}C$. Calculated patterns of $LiOH \cdot H_2O$ (red, collection code 9138 [183]) and $Ni(OH)_2$ (black, collection code 169978 [36]) at the bottom, calculated patterns from the ICSD of NiO (pink, collection code 9866 [186]), Li_2CO_3 (turquoise, collection code 100324 [185]) and LiOH (blue, collection code 27543 [184]) at the top. Measured patterns between 35 and 300°C in orange and between 350 and 500°C in green.

Further insights into the synthesis can be discovered from HT XRD (Figure 4.3). In between the calculated patterns of Ni(OH)₂ (ICSD collection code 169978 [36]) in black and LiOH•H₂O (ICSD collection code 9138 [185]) in red at the bottom and the calculated patterns of LiOH (ICSD collection code 27543 [186]) in blue, Li₂CO₃ (ICSD collection code 100324 [187]) in

cyan and NiO (ICSD collection code 9866 [188]) in pink at the top, derived from the ICSD, the collected pattern of the as-prepared mixture is shown. A clear threshold can be found when fundamental changes occur during the reaction. Below 350°C, the loss of H₂O from both precursors can be seen while forming NiO and LiOH. Li₂CO₃ is formed as a side phase due to the missing oxygen atmosphere, as Li is able to react, in this experiment, with O₂ or CO₂ from the air during the calcination. Above 350°C, the unit cell of NiO changes drastically, when Li⁺ is being incorporated into its structure to form Li₂Ni₁₋₂O₂. This corresponds well with the TGA results as any surplus of H₂O was released and the host structure of NiO was formed below 300°C. During a typical synthesis, the cubic lithiated NiO structure then transforms into a rhombohedral unit cell with Li layers alternating Ni layers connected via oxygen atoms due to steric effects between Li⁺ and Ni³⁺ during the occurring Ni oxidation Ni²⁺ to Ni³⁺. This last step of unit cell change cannot be detected here yet, as the highest possible temperature in this experiment is only 500°C and the further absence of a pure oxygen environment will impede the oxidation of Ni²⁺.

These results show clearly that a pre-calcination temperature of 350°C is sufficient to remove all the moisture and thus transform the precursors Ni(OH)₂ and LiOH•H₂O into LiOH and NiO. As the reaction stayed below the melting point of LiOH•H₂O for this transformation, no melting together of the reaction mixture and its separated secondary particles is happening and the intermediate grinding step is not necessary for a successful homogeneous formation of the LiNiO₂ particles.

4.2.2. Characterisation of LiNiO₂

After the initial trial during which the intermediate grinding step was omitted, and the analysis of HT XRD measurements of the pre-calcination processes, an experimental design for the optimisation of the calcination procedure was developed and its parameters can be seen in Table 4.1. For the pre-calcination, either no pre-heating step at all or heating to 350°C or 500°C for 5h were selected. As a continuous process, the calcination temperature was then increased to either 670, 710 or 750°C and maintained for 15 h. The heating and cooling rates were both set to 5 K/min and the reactions were performed under pure oxygen flow (Table 4.1). Particle morphology and size were determined via SEM. The phase purity was determined using X-ray diffraction, the ratios of the Bragg peaks (003)/(104) and (006/102)/(101) were analysed from the as obtained XRD patterns and lattice parameters and Ni²⁺ occupancies in the lattice confirmed via refinements of these patterns.

Pre	-calcination	Calcination		
Time	Temperature	Time	Temperature	
[h]	[°C]	[h]	[°C]	
-	-	5	670	
5	350	10	710	
5	500	15	750	

Finally, cathode slurries were prepared and tested in coin half-cells vs. Li/Li⁺ between 3 – 4.3 V for 100 cycles at a constant current corresponding to a rate of C/20 for the first two cycles followed by C/2 and the electrochemical behaviour examined. In the end, correlations between lattice parameters, Ni²⁺ occupancies and the electrochemical behaviour were examined to find the most suitable annealing process with a high initial capacity, a good capacity retention over 100 cycles and a low cation mixing.

4.2.2.1. Structural Characterisation

The measured XRD patterns of selected as-prepared samples according to the experimental design can be seen in Figure 4.4. All samples shown here are pre-calcined for 5 h at 500°C and calcined for 15 h at 670°C (purple), 710°C (green) and 750°C (blue). A calculated powder

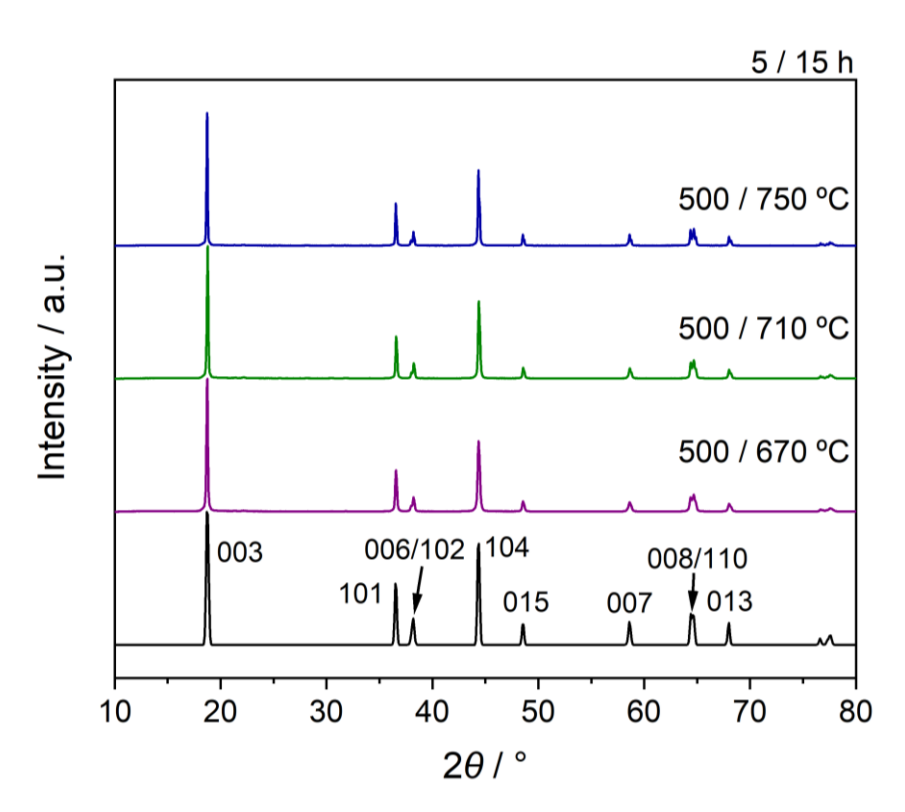


Figure 4.4: Powder X-ray diffraction patterns of selected as prepared LiNiO₂ samples. These samples are all pre-calcined for 5 h at 500°C and calcined for 15 h at 670°C (purple), 710°C (green) and 750°C (blue). Calculated LiNiO₂ pattern from ICSD (black, collection code 78687 [187]) as comparison including Bragg peak labels. Remaining XRD patterns can be found in the supplementary information.

pattern of LiNiO₂ (ICSD collection code 78687 [189]) from the ICSD is depicted at the bottom for comparison of peak positions and intensities. The main peaks of the desired product LiNiO₂ are clearly obtained compared with the ICSD pattern. All three patterns show the essential Bragg peaks of LiNiO₂, and no obvious side phase is detected here. The Bragg peak ratio of the (003) and (104) peaks and the ratio of the split (006/102) peaks and the (101) peak were determined from these patterns using the programme Origin and calculating the areas under these peaks (the integrated intensity). XRD patterns of the remaining samples can be found in the appendix in Figure 10.1 to Figure 10.8.

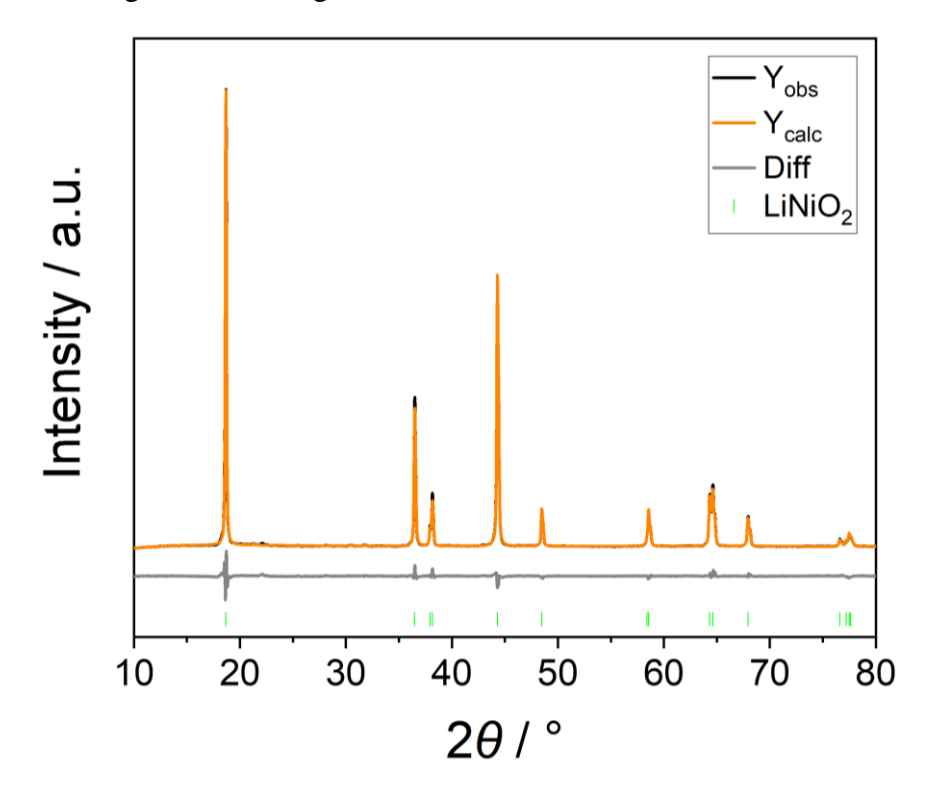


Figure 4.5: Refinement of measured Cu source XRD pattern of $LiNiO_2$ pre-calcined for 5 h at $500^{\circ}C$ and calcined for 5 h at $710^{\circ}C$. Measured pattern (black), calculated pattern of $LiNiO_2$ (orange, collection code 78687 [187]) and the difference between observed and calculated patterns (grey). Peak positions of $LiNiO_2$ in green.

All the powder patterns were refined taking into account a mixed occupancy in the Li layer, due to the potential formation of Li vacancies and the subsequent filling of those vacancies with Ni²⁺ from the Ni layer. Figure 4.5 shows the measured pattern in black, the calculated pattern from the refinement in orange and the difference between both in grey. Additionally, the peak positions of LiNiO₂ (green, ICSD collection code 78687 [189]) are depicted as markers in green at the bottom of the graph. The calculated pattern matches the observed pattern very well, with a *weighted R-factor* wR value below 3 % and a *goodness of fit* GOF value below 5. These values are a measure of the refinement quality. The refined values including their standard deviation

can be found in Table 4.2. Refinement plots of the other samples investigated in this chapter, can be seen in the appendix in Figure 10.9 to Figure 10.21.

Table 4.2: Lattice parameters, unit cell volumes and Ni^{2+} occupancies derived from Rietveld refinements for asprepared LiNiO₂ samples. Standard deviations in brackets. Green shading depicts down selection of samples for further examination in the next chapters.

Precal- cination	Cal- cination	c	a	Volume	Ni ²⁺	wR	GOF
t [h] /	T [°C]	[Å]	[Å]	$[\mathring{A}^3]$	[%]	[%]	
-	15/670	14.196(2)	2.8797(3)	101.964(3)	2.7(1)	2.33	2.79
-	15/710	14.199(1)	2.8806(3)	102.037(2)	3.6(1)	2.41	2.86
-	15/750	14.194(1)	2.8799(3)	101.958(2)	3.6(1)	2.49	2.98
5/350	15/670	14.197(2)	2.8795(3)	101.944(3)	3.0(1)	2.02	2.40
5/350	15/710	14.192(2)	2.8779(3)	101.801(3)	1.6(1)	2.92	3.50
5/350	15/750	14.193(3)	2.8790(6)	101.904(4)	2.5(1)	2.59	3.11
5/500	15/670	14.195(2)	2.8787(4)	101.878(3)	1.9(1)	2.21	2.66
5/500	15/710	14.197(2)	2.8797(3)	101.963(3)	3.1(1)	2.43	2.92
5/500	15/750	14.193(1)	2.8783(3)	101.832(2)	1.8(1)	2.61	3.13
-	10/670	14.204(2)	2.8824(4)	102.203(3)	5.8(1)	1.82	2.13
_	10/710	14.198(2)	2.8804(3)	102.019(3)	3.3(1)	2.36	2.79
-	10/750	14.193(2)	2.8787(4)	101.866(3)	2.1(1)	2.86	3.29
5/350	10/670	14.194(2)	2.8788(4)	101.881(3)	2.3(1)	2.30	2.75
5/350	10/710	14.196(2)	2.8800(3)	101.982(3)	2.8(1)	2.35	2.79
5/350	10/750	14.195(2)	2.8794(4)	101.931(3)	2.8(1)	3.01	3.54
5/500	10/670	14.194(2)	2.8789(4)	101.893(3)	2.4(1)	2.27	2.72
5/500	10/710	14.194(1)	2.8790(3)	101.897(2)	2.7(1)	2.98	3.38
5/500	10/750	14.195(2)	2.8786(3)	101.874(3)	2.3(1)	2.39	2.72
-	5/670	14.205(3)	2.8851(5)	102.412(4)	11.0(1)	1.70	1.98
-	5/710	14.201(2)	2.8815(4)	102.127(3)	4.9(1)	2.17	2.60
-	5/750	14.193(4)	2.8796(8)	101.930(5)	5.4(1)	4.74	5.74
5/350	5/670	14.198(3)	2.8807(4)	102.041(4)	4.1(1)	1.96	2.29
5/350	5/710	14.200(2)	2.8806(3)	102.053(3)	3.1(1)	2.24	2.62
5/350	5/750	14.195(1)	2.8795(3)	101.941(2)	2.8(1)	2.47	2.82
5/500	5/670	14.194(3)	2.8800(5)	101.961(4)	4.9(1)	1.88	2.24
5/500	5/710	14.196(2)	2.8798(3)	101.964(3)	3.1(1)	2.44	2.88
5/500	5/750	14.200(2)	2.8823(3)	102.175(3)	5.8(1)	2.74	3.28

According to various research groups [47] [49] [51] [92], the integrated intensity ratio of (003)/(104) peaks indicate the degree of cation mixing and according to Dahn et al. [57], the integrated intensity ratio of (006/102)/(101) reflections can be used to measure the amount of Li present in the Li layer. The larger the (003)/(104) ratio and the smaller the (006/102)/(101) ratio, the more Li is present in the Li layer. These ratios including the c/a ratio of the refined unit cell dimensions can be found in Table 4.3.

The c/a ratio is a measure of the hexagonal distortion of the cubic lattice of NiO where the Li is incorporated to form a layered structure. The c/a ratio for a cubic lattice is 4.90 and it increases to 4.93 due to the layering. According to Rougier et al., an increasing amount of Ni²⁺

in the Li layer leads to an increase in cell parameters a and c, which can be confirmed during this current study. This leads to a decreased c/a ratio for an increased amount of cation mixing in the structure. The ratio shows values above 4.93 if the amount of Ni²⁺ in the Li layer is below 2.5%. With an increased calcination time of 15h, the cation mixing in the structure seems to be stable below 4% no matter the temperatures or pre-calcination procedures applied. Samples calcined for 5h only, show increased cation mixing at lower calcination temperatures of 670°C. Increased cation mixing for the 5h samples can also be detected for high calcination temperatures of 750°C in combination with high pre-calcination temperature of 500°C. Both cases lead to the suggestion that the calcination time is insufficient in combination with a very low calcination temperature, suggesting an incomplete calcination as well as in combination with an increased calcination temperature above the decomposition temperature for LiNiO₂.

Table 4.3: Ratio of lattice parameter and Bragg peak ratios from X-ray diffraction patterns of as-prepared samples of LiNiO₂. Standard deviations in brackets. Green shading depicts down selection of samples for further examination in the next chapters.

Precal- cination	Cal- cination	Ni ²⁺	c/a ratio	(003)/(104) ratio	(006/102)/(101) ratio
t [h] /	t [h] / T [°C]				
-	15/670	2.7(1)	4.930	1.280	0.458
-	15/710	3.6(1)	4.929	1.231	0.497
	15/750	3.6(1)	4.929	1.219	0.491
5/350	15/670	3.0(1)	4.930	1.231	0.479
5/350	15/710	1.6(1)	4.931	1.316	0.443
5/350	15/750	2.5(1)	4.930	1.282	0.454
5/500	15/670	1.9(1)	4.931	1.302	0.460
5/500	15/710	3.1(1)	4.930	1.248	0.488
5/500	15/750	1.8(1)	4.931	1.299	0.449
-	10/670	5.8(1)	4.928	1.160	0.594
-	10/710	3.3(1)	4.929	1.248	0.490
-	10/750	2.7(1)	4.930	1.302	0.480
5/350	10/670	2.3(1)	4.931	1.272	0.484
5/350	10/710	2.8(1)	4.929	1.259	0.503
5/350	10/750	2.8(1)	4.930	1.278	0.485
5/500	10/670	2.4(1)	4.931	1.302	0.479
5/500	10/710	2.7(1)	4.930	1.272	0.457
5/500	10/750	2.3(1)	4.931	1.289	0.466
-	5/670	11.0(1)	4.924	0.975	0.678
-	5/710	4.9(1)	4.929	1.188	0.543
-	5/750	5.4(1)	4.929	1.214	0.459
5/350	5/670	4.1(1)	4.929	1.213	0.507
5/350	5/710	3.1(1)	4.930	1.287	0.479
5/350	5/750	2.8(1)	4.930	1.268	0.468
5/500	5/670	4.9(1)	4.929	1.224	0.509
5/500	5/710	3.1(1)	4.930	1.247	0.491
5/500	5/750	5.8(1)	4.927	1.215	0.578

A larger (003)/(104) ratio indicating lower cation mixing in the structure holds true for values of cation mixing above a certain threshold. The same is true for the (006/102)/(101) ratio but inverse. The cation mixing is more dependent on the reaction temperatures with shorter calcination time. As conventional XRD cannot detect lighter elements like Li, it would be advantageous to employ neutron diffraction for refinements and peak ratio analysis. Neutron diffraction opposed to X-ray diffraction, is able to detect Li. Utilising measured diffraction data for Li during refinements, will give a more accurate and reliable values for site occupancy and more reliable statements regarding the cation mixing and its influence on the structural and electrochemical behaviour of the synthesised LiNiO₂.

As there are 27 samples in total, a pre-selection based on the lattice parameters and Bragg peak ratios, was made. The pre-selection was made based on the Ni²⁺ content in the structure as well as peak splitting in the XRD patterns, indicating a layered structure and the Bragg peak ratios, a measure for cation mixing and electrochemical reactivity. Low values for Ni²⁺ content and the (006/102)/(101) ratio and high values for the (003)/(104) ratio were the selection criteria, leaving 9 remaining samples, one out of each section of the table, to investigate further. These samples are highlighted in Table 4.2 and Table 4.3. SEM images for morphological investigations as well as coin cells were assembled with cathodes of these selected samples, for electrochemical evaluation and the results shown in the following chapters.

4.2.2.2. Morphological Characterisation

SEM images were taken for the pre-selected samples by carefully grinding the powder to break apart agglomerated secondary particles without crushing them. The powders, added onto a SEM stub, were gold coated to prevent charging during the measurement. SEM images for samples calcined for 15, 10 and 5 h can be seen in Figure 4.6, Figure 4.7 and Figure 4.8, respectively.

On the left-hand side lower magnification images show the secondary particle assemblies. They exhibit very similar secondary particle size and particle size distributions for all the samples. Several secondary particles are still agglomerated and quite a few residues of not fully formed particles can be detected. The secondary particle size, shape and size distribution was preserved during the high temperature solid-state reaction (compare to Figure 4.1), whereas the primary particle shape changed and thus the density of the secondary particles. The right-hand side images show one secondary particle each at a higher magnification where more details and differences across the primary particles can be seen. In Figure 4.6 a) to c), samples 15/670, 5/350-15/710 and 5/500-15/750 are depicted, respectively and the primary particles size and packing density increases with increasing calcination temperatures, which is expected.

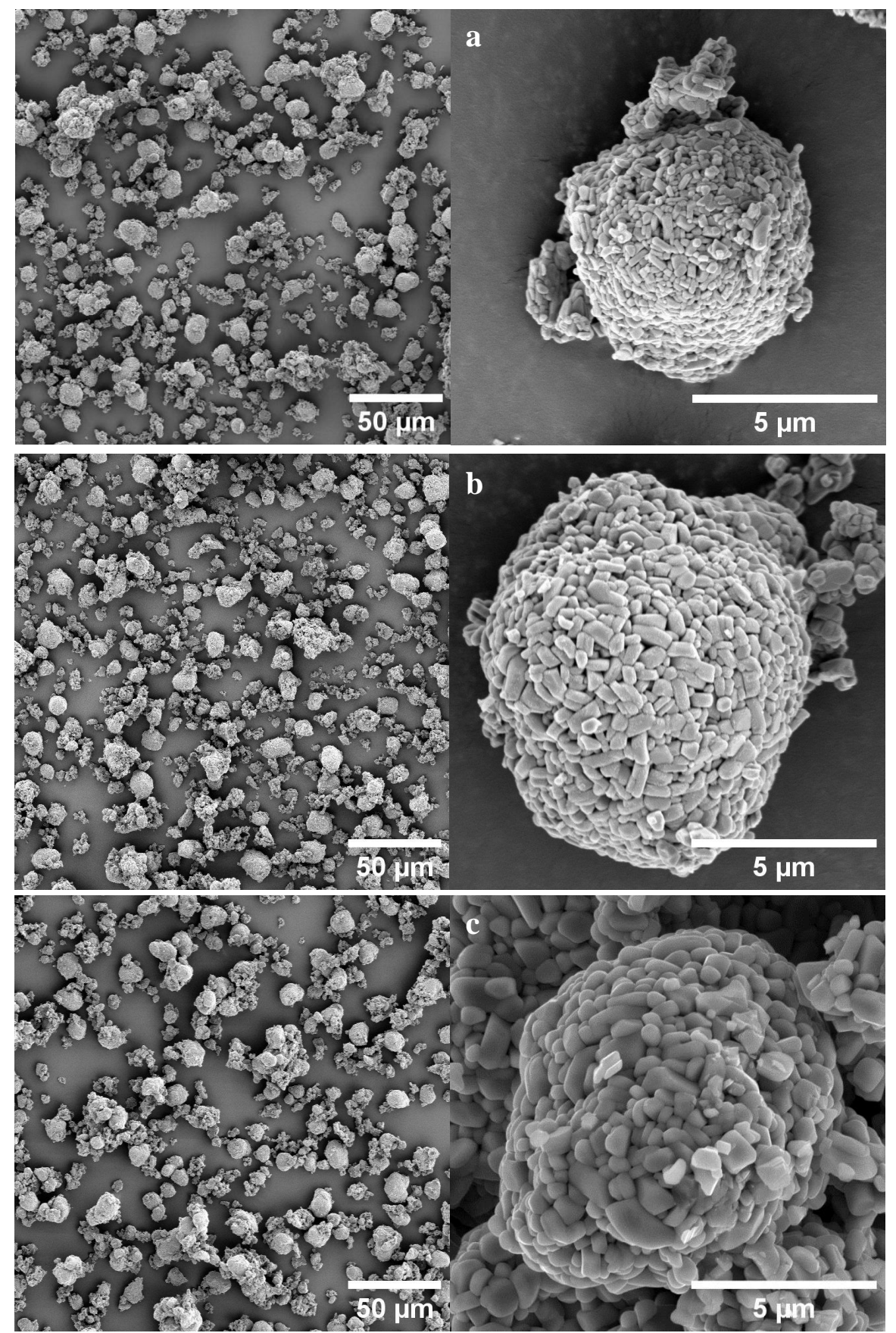


Figure 4.6: SEM images of LiNiO₂ samples calcined for 15 h. a) sample 15/670, b) sample 5/350-15/710, c) sample 5/500-15/750. Lower magnification images (left) and higher magnification (right).

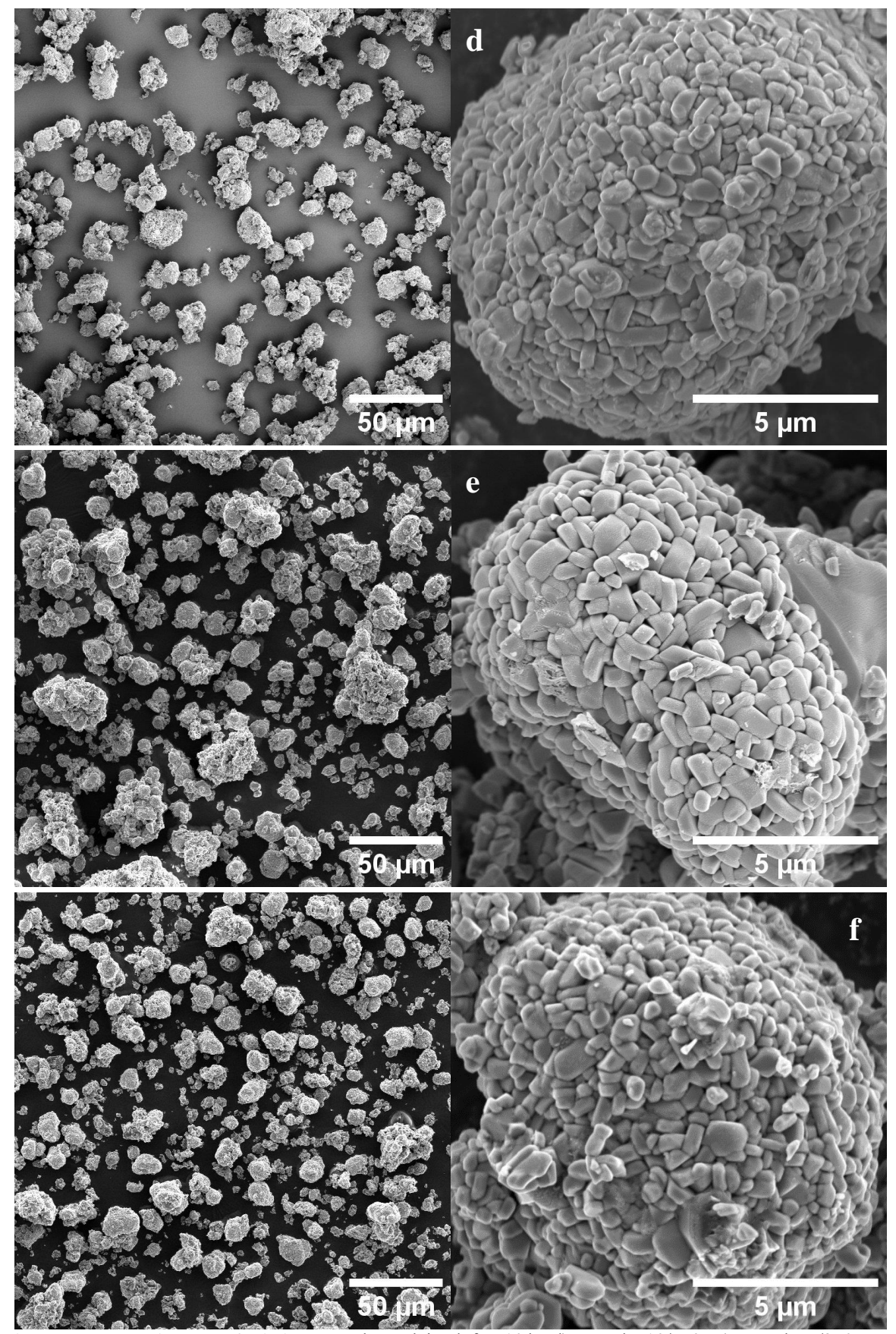


Figure 4.7: SEM images of LiNiO₂ samples calcined for 10 h. d) sample 10/750, e) sample 5/350-10/750, f) sample 5/500-10/710. Lower magnification images (left) and higher magnification (right).

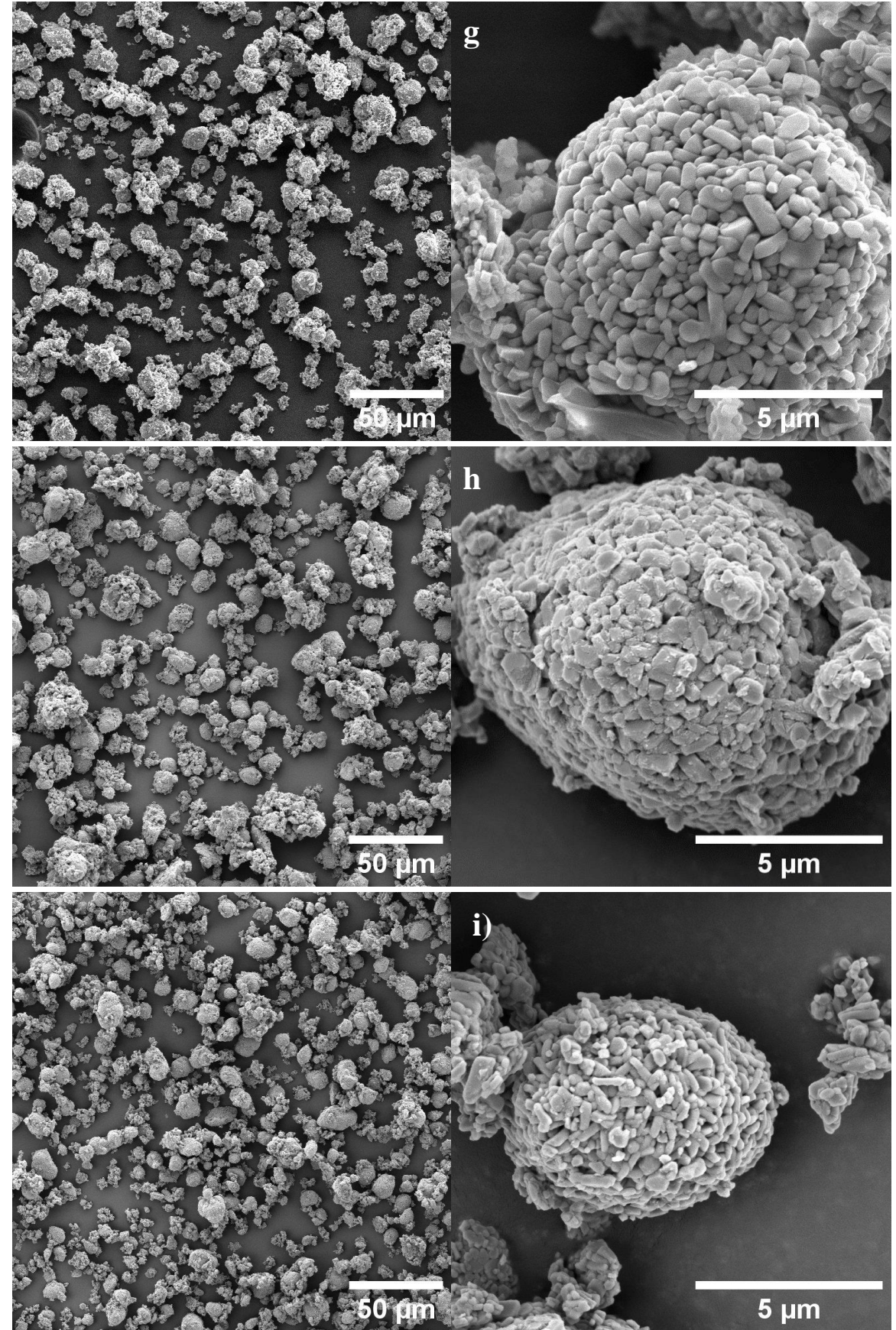


Figure 4.8: SEM images of LiNiO₂ samples calcined for 5 h. g) sample 5/750, h) sample 5/350-5/750, i) sample 5/500-5/710. Lower magnification images (left) and higher magnification (right).

A variety of primary particle sizes and shapes can be found in all of them. The samples calcined for 10h in Figure 4.7, show quite large ($> 1 \,\mu m$) primary particles within the secondary assembly compared to other calcination times in this study. Sample 5/350-10/750 in Figure 4.7 e), seems more densely packed than the other two 10h samples. Its primary particles are more even and uniform within the secondary particle assembly regarding their size and shape whereas in the other 10h samples, a larger distribution of size and shape can be found.

Figure 4.8 depicts the samples calcined for 5 h only. Figure 4.8 g) shows the sample 5/750 and reveals more elongated primary particles and a fairly dense structure than the other two 5 h samples. The sample 5/350-5/750 in Figure 4.8 h) has more uniform primary particles of bigger size ($\sim 1 \, \mu m$) and a layer of very small particles stuck to the surface can be detected, but doesn't appear as dense as the sample 5/350-10/750 in Figure 4.7 e). Figure 4.8 i) shows sample 5/500-5/710 and its secondary particle assembly as well as its primary particles are smaller than the other samples in this study . They also seem more elongated compared to the other samples and look less dense. Both, longer reaction times and higher reaction temperatures facilitate the primary particle growth and thus also the secondary particle growth, which can be validated with the current samples and their SEM images.

4.2.2.3. Electrochemical cycling

The electrochemical performance of the as-synthesised materials was investigated in coin half-cells vs. Li/Li⁺. The cells were cycled in environmental chambers at a controlled temperature of 25°C for 100 cycles in the voltage range of 3 to 4.3 V. After a resting period of 2 h, a constant current corresponding to a rate of C/20 for the first two cycles and at C/2 for the remaining 98 cycles was applied, where 1 C = 220 mAh/g. Three cells were prepared and cycled for each sample. Results are combined in plots for each calcination time (15, 10 and 5 h) for easier comparison in Figure 4.9 to Figure 4.11 for samples calcined for 15 h, in Figure 4.12 to Figure 4.14 for samples calcined for 10 h and in Figure 4.15 to Figure 4.17 for samples calcined for 5 h. Measured charge and discharge capacities for the first three cycles, the 1st cycle capacity loss and the coulombic efficiencies as well as the capacity retention after 100 cycles, can be seen in Table 4.4 for the cycled cells.

The capacity plot for the samples 15/670, 5/350-15/710 and 5/500-15/750, all calcined for 15 h, are shown in Figure 4.9. It depicts the charge and discharge capacities of the first three cycles, the first cycle capacity loss and the drop in capacity when moving to a faster current of C/2. Initial charge capacities of 257, 262 and 256 mAh/g and corresponding discharge capacities of 222, 222 and 216 mAh/g were achieved during the first cycle with a 1st cycle capacity loss of

35, 40 and 40 mAh/g, respectively. Li diffusion happens along the Li layers, with the repulsion between NiO₆ layers increasing the Li slab height, making it easier for the Li to move along. In case of parasitic Ni²⁺ in the Li layer, the Ni²⁺ weakens that repulsion between the NiO₆ layers, but also disrupts the Li pathways [190] [191]. Furthermore, Ni²⁺ will oxidise to Ni³⁺ during cycling and due to the decrease in ionic radii $(r(Ni^{2+}) > r(Ni^{3+}))$ further decrease the Li slab height and add to the irreversible capacity loss between first cycle charge and discharge as less Li is able to reintercalate [61]. An additional but expected decrease of capacity for all three samples can be seen from 1st to 3rd cycle. This capacity loss is due to the kinetic changes, when the applied current changes from C/20 to a faster rate of C/2.

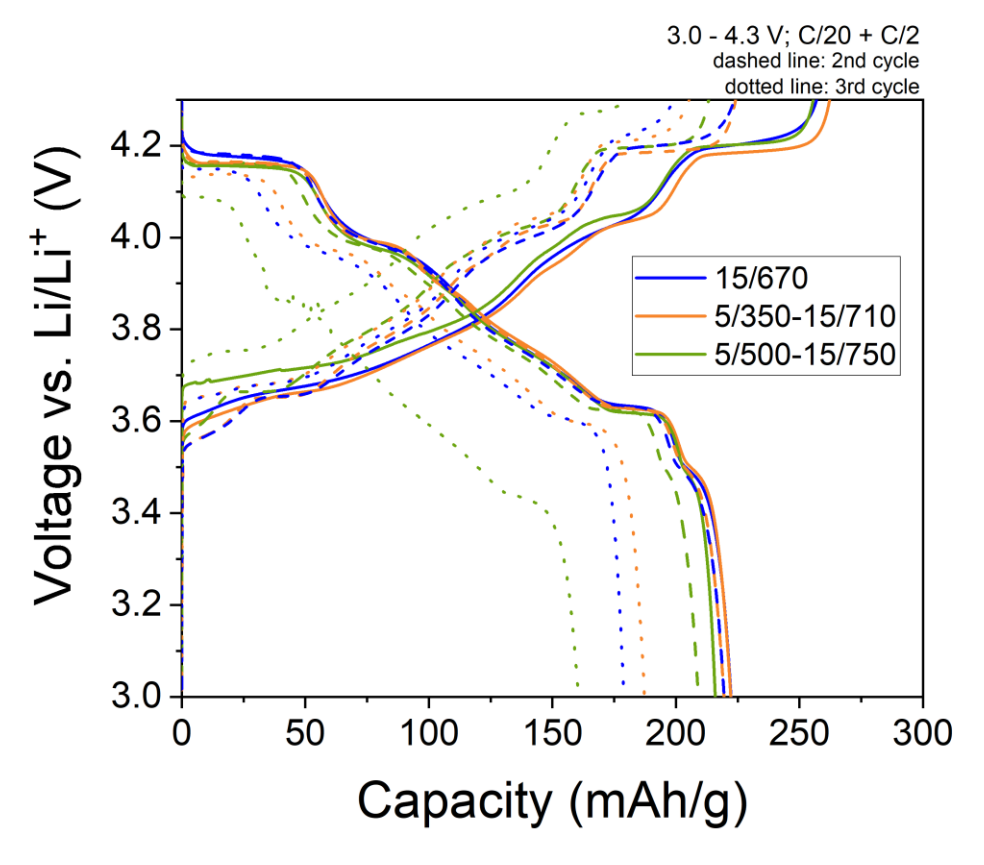


Figure 4.9: Charge/discharge plot for LiNiO₂ synthesised via a solid-state route, sample 15/670 (blue), sample 5/350-15/710 (orange) and sample 5/500-15/750 (green). Cycled between $3-4.3\,\mathrm{V}$ vs. Li/Li⁺ at a rate of C/20 for two cycles and C/2 for the third cycle. Solid line shows 1^{st} cycle, dashed line depicts 2^{nd} cycle and dotted line represents the 3^{rd} cycle.

The discharge capacity retention plot in Figure 4.10 shows a similar decrease in discharge capacity over 100 cycles for the examined samples 5/350-15/710 and 5/500-15/750, with 68.1 and 67.9%, respectively. These two samples also exhibit the lowest cation mixing in this series and it has been reported, that Ni²⁺ in the Li layer can act as a pillar, preventing the structure from collapsing. Having less cation disorder in the structure, leads then to more structural

degradation during cycling and a worse capacity retention over 100 cycles. Sample 15/670 displays improved capacity retention of 81.5% over 100 cycles. The coulombic efficiencies during cycle one are 86.5, 84.7 and 84.5%, respectively, but it increases close to 100% after the first initial formation cycles for samples 15/670 and 5/350-15/710. Lower efficiencies are expected for the first cycle due to possible Li deficiency in the electrode after manufacturing. During cycling, Li is being reintercalated in the LNO cathode structure from the pure Li anode. The efficiency will be expected to be 100% due to the indefinite amount of Li in the Li anode. Sample 5/500-15/750 has larger deviations of the coulombic efficiency during the 100 cycles and seems less stable This might be due to temperature fluctuations during the cycling.

The differential capacity plot (dQ/dV) of these three samples in Figure 4.11 translates the steps seen in the capacity plot into more obvious phase transitions depending on the voltage. Oxidation as well as reduction peaks seen in these plots show two-phase regions, where phase transitions happen, whereas plateaus depict regions where only one phase is present. The second cycle for the samples 15/670, 5/350-15/710 and 5/500-15/750 in Figure 4.11 a), b) and c), respectively, are compared to each other, to review any changes correlated to the cation mixing. The first cycle is not taken into account regarding phase transition examination as the cell is

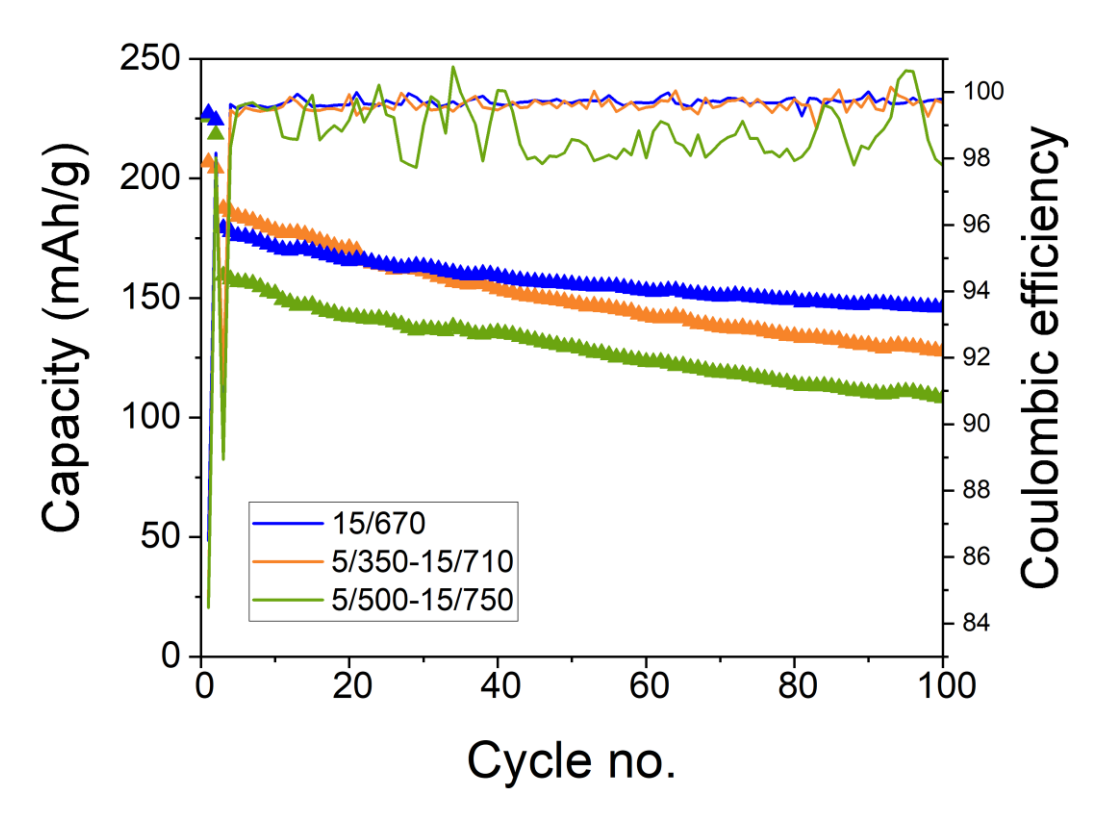


Figure 4.10: Discharge capacity retention plot including coulombic efficiencies over 100 cycles for LiNiO₂ synthesised via a solid-state route, sample 15/670 (blue), sample 5/350-15/710 (orange) and sample 5/500-15/750 (green). Cycled between 3-4.3 V vs. Li/Li⁺ at a rate of C/20 for two cycles and C/2 for the third cycle.

undergoing conditioning and might not give a real picture of what happens. Additionally, cycle three and 100 are compared to evaluate changes during long-term cycling. Comparisons between cycle two and three are not plausible due to the change in C-rate. Peaks and transitions will shift towards higher voltages for oxidation and lower voltages for reduction due to the faster charging.

During charge, the hexagonal pristine phase H1 transitions into the monoclinic distorted phase at around 3.65 V, this also denotes the redox processes of Ni in the structure. The broad plateau of the monoclinic phase is followed by a transition into another hexagonal phase H2 at around 4V and finally into the hexagonal H3 phase at 4.2 V. All the peaks, signifying two-phase regions, are shifted towards lower voltages during discharge. This shift between oxidation and reduction features is due to a decrease in polarisation, indicating enhanced electrode

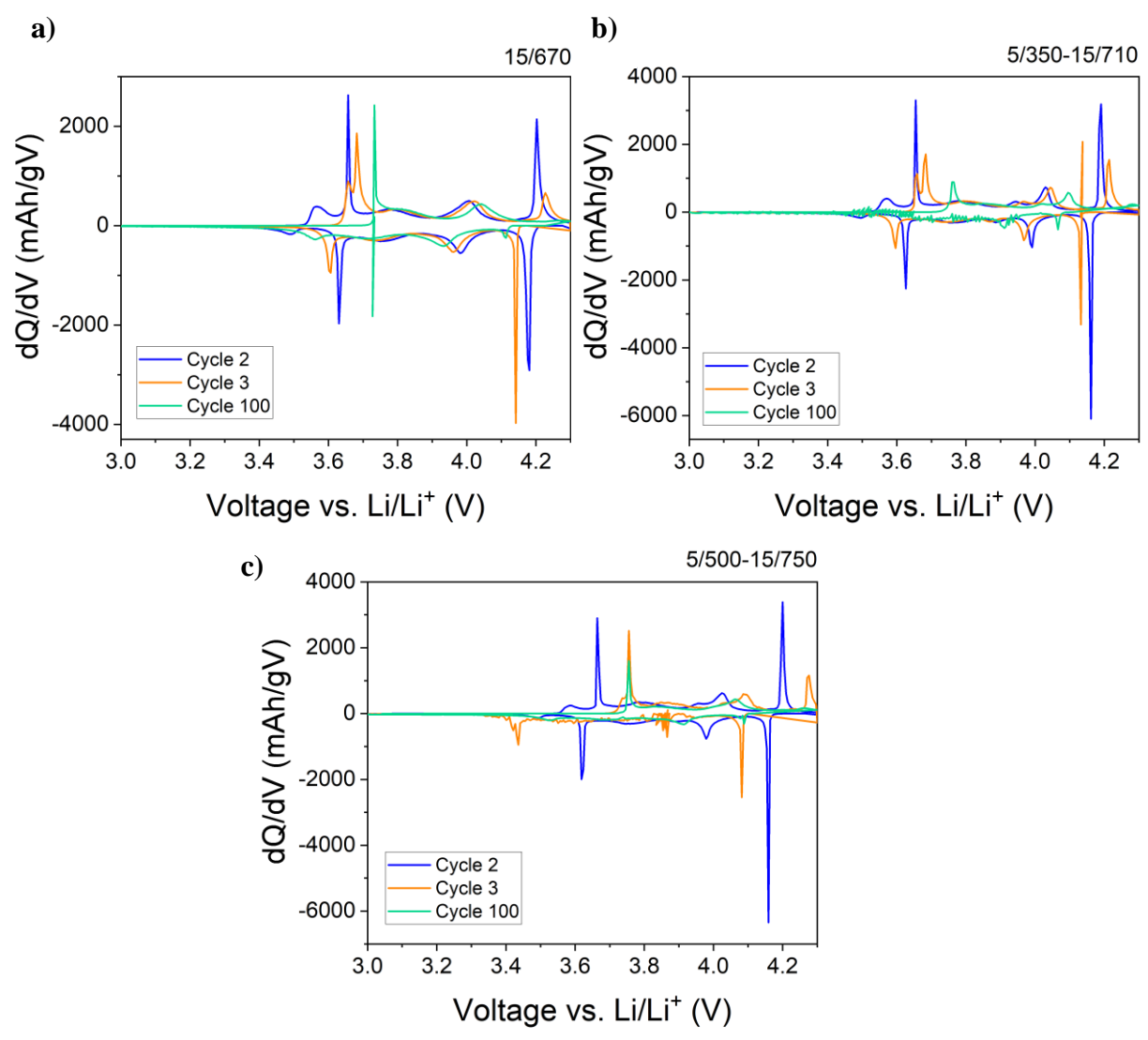


Figure 4.11: Differential Capacity plots obtained for LiNiO₂ synthesised via a solid-state route, a) sample 15/670, b) sample 5/350-15/710 and c) 5/500-15/750. Coin half cells cycled between 3 – 4.3 V vs. Li/Li⁺ at a rate of C/20 for two cycles and C/2 for the third cycle. 2nd cycle depicted in blue, 3rd cycle in orange and 100th cycle in green.

reversibility. All three samples exhibit these transitions as expected whereas samples 5/350-15/710 and 5/500-15/750 shows a difference for the M/H2 transition, as they reveal an additional small peak. This feature is due to the low cation mixing in these samples. Another feature seen in the second cycle is the peak at around 3.55 V for charge and 3.5 V for discharge. According to literature, this is an electrochemical reaction happening only at slow charge rates like C/20 and the corresponding peaks are not present beyond cycles three due to the faster C-rate. This additional reaction results in an increase in polarisation and thus higher charge and discharge capacities for cycles one and two and explains the capacity drop in cycle three. It is also responsible for an increase in coulombic efficiencies during the slower charged cycles. [45] [192] [84] [72]

During cycling at lower C-rates, from cycle three onwards, all peaks shift to higher voltages, as mentioned before and intensities are in general decreased due to kinetic reasons. The additional peak seen in cycle two can still be seen in cycle three during charge but already disappeared during discharge due to the faster charge rate. In cycle 100, the phase transitions move to even higher voltages during charge, the H2/H3 transition is not accessed at all as it moves beyond the upper cut-off voltage of 4.3 V. The shift to higher voltages is caused by an overpotential, which can be assigned to surface reactions at the cathode-electrolyte interface, the loss of active material due to the formation of parasitic passivating surface layers. Less and less Li is incorporated after each cycle, leading to a loss in capacity and structural changes due to phase transitions, especially the H2/H3 transition has a huge influence and leads to constant volume changes within the structure and the formation of microcracks. Whereas the shift of the peaks is only minor for the samples 15/670 and 5/350-15/710, sample 5/500-15/750 in Figure 4.11 c) exhibits a larger shift towards higher voltages during charge for all the transitions at cycle three.

All samples calcined for 15 h, exhibit very similar initial capacities, 1st cycle capacity losses as well as 1st cycle coulombic efficiencies. Samples 5/350-15/710 and 5/500-15/750 show increased structural ordering, reflected in the Li/Ni disorder gained from Rietveld refinements below 2%. The differential capacity graphs look very similar, exhibiting the second peak of the M/H2 transition, but also showing the worst capacity retention over 100 cycles of below 70%. Comparing charge and discharge capacities of the 3rd cycle for all three samples, sample 5/500-15/750 develops the biggest decrease in capacity and also shows the biggest overpotential in the dQ/dV plot. Sample 15/670 on the other hand, displays the lowest first cycle capacity loss of all tested samples in this chapter.

The electrochemical data for the samples calcined for 10 h, samples 10/750, 5/350-10/750 and 5/500-10/710 is shown in Figure 4.12. Initial charge and discharge capacities derived from coin half cells vs. Li/Li⁺ are 281, 266 and 263 mAh/g as well as 241, 213 and 225 mAh/g, respectively. The charge capacity of sample 10/750 of 281 mAh/g is above the theoretical capacity for LiNiO2, which might be due to some Li-containing side phases at the surface of the particles that contribute to the capacity or additional Li is intercalated into the Ni layer due to a Ni deficiency during the solid-state synthesis. Corresponding 1st cycle capacity loss is found to be 40, 53 and 38 mAh/g, respectively. Figure 4.13 shows the discharge capacity retention over 100 cycles as well as the coulombic efficiency. Samples 10/750, 5/350-10/750 and 5/500-10/710 exhibit discharge capacity retention of 72.9, 72.7 and 79 % over 100 cycles and coulombic efficiencies of the 1st cycle of 85.9, 84.8 and 85.3, respectively. Again, the coulombic efficiency increases after the 1st cycle close to 100 %.

The dQ/dV plot in Figure 4.14 shows a very similar electrochemical behaviour for all three samples calcined for 10 h. The transitions and phases H1/M \rightarrow M/H2 \rightarrow H2/H3 are all located at the expected voltages with slight deviations for samples 10/750 and 5/350-10/750.

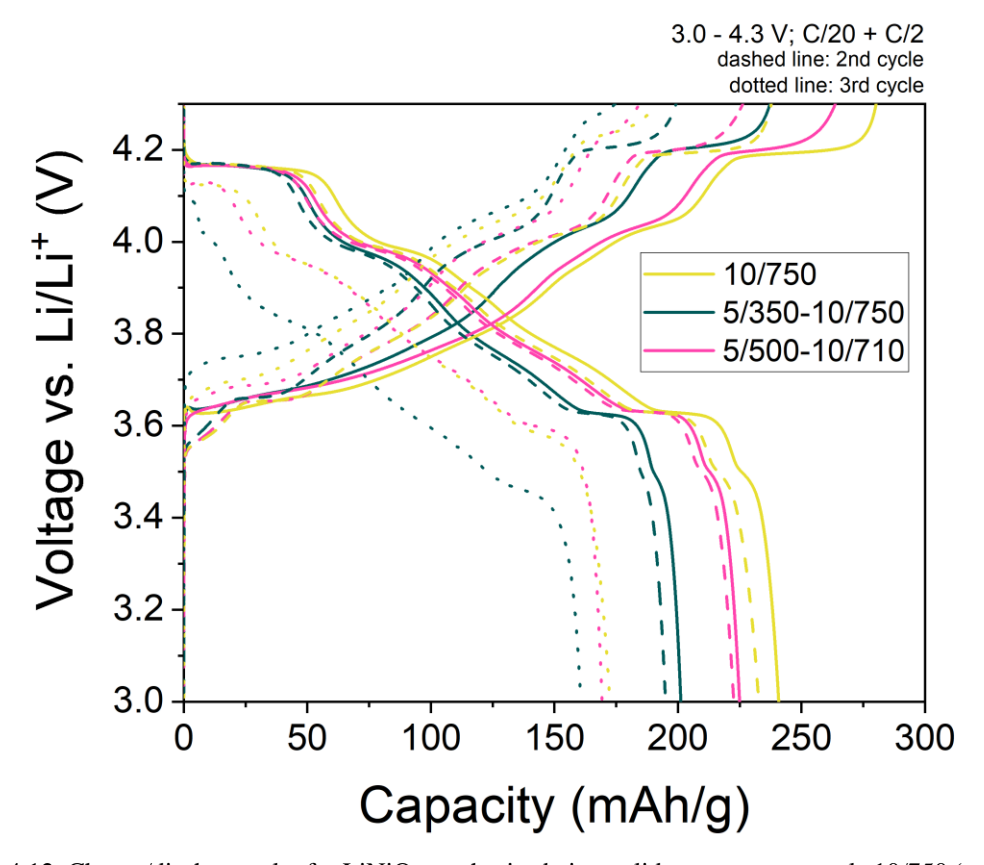


Figure 4.12: Charge/discharge plot for LiNiO₂ synthesised via a solid-state route, sample 10/750 (yellow), sample 5/350-10/750 (turquoise) and sample 5/500-10/710 (pink). Cycled between 3-4.3 V vs. Li/Li⁺ at a rate of C/20 for two cycles and C/2 for the third cycle. Solid line shows 1^{st} cycle, dashed line depicts 2^{nd} cycle and dotted line represents the 3^{rd} cycle.

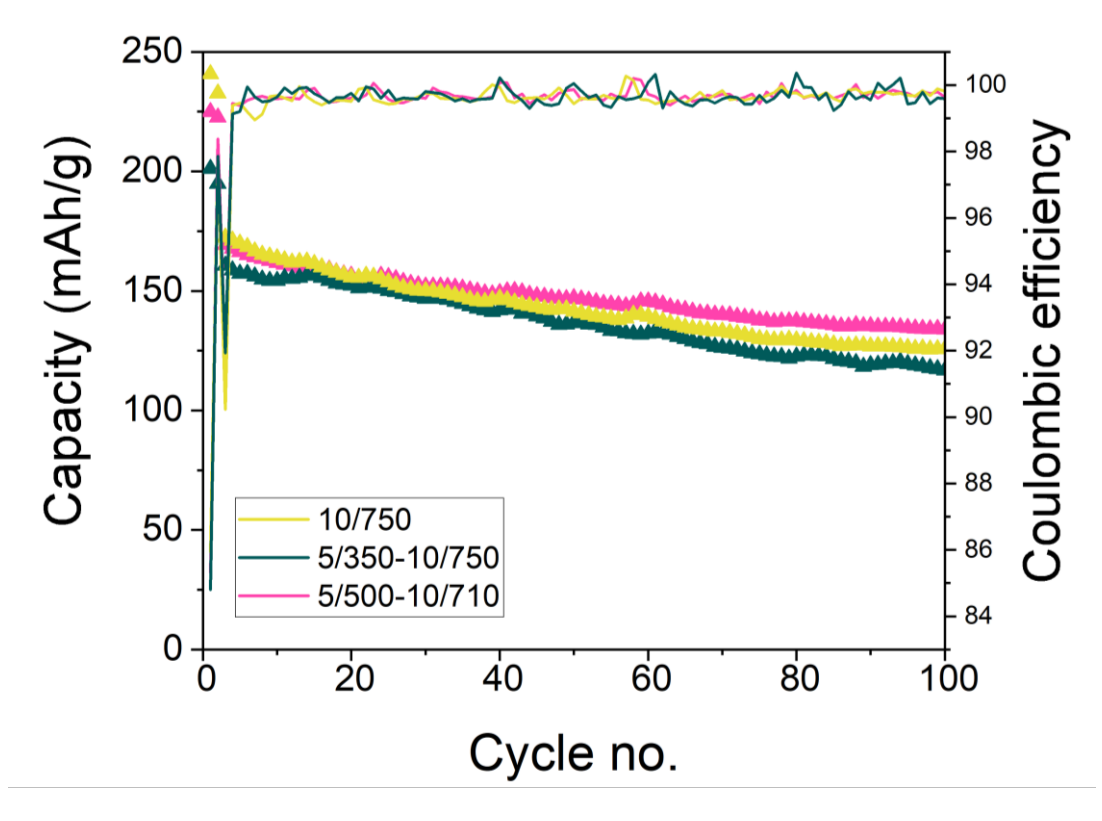


Figure 4.13: Discharge capacity retention plot including coulombic efficiencies over 100 cycles for LiNiO $_2$ synthesised via a solid-state route, sample 10/750 (yellow), sample 5/350-10/750 (turquoise) and sample 5/500-15/710 (pink). Cycled between 3 – 4.3 V vs. Li/Li $^+$ at a rate of C/20 for two cycles and C/2 for the third cycle.

Sample 10/750 shows higher intensities for the H1/M and H2/H3 transition during charge, whereas sample 5/350-10/750, develops higher intensities of said transitions during the discharge. All samples also exhibit the additional 3.5 V electrochemical reaction in the second cycle at a slower charge rate. The transitions shift to higher voltages during charge and to lower voltages during discharge for cycles 3 to 100, as described before. Intensities decrease whereas peaks get broader and the H2/H3 transition disappears beyond 4.3 V in the third cycle for samples 5/350-10/750 and 5/350-10/710. There are additional smaller peaks visible in the third cycle at 3.9 V and 4.09 V during charge and discharge, for sample 5/350-10/750 and the data is noisy overall. As the choice of calcination procedure is not only dependent on the first cycle capacity, but also on the capacity retention over 100 cycles as well as the Ni/Li cation mixing, all results need to be considered and drawbacks considered. From these results, it is clear that it is not possible, to have the highest first cycle capacity, the best capacity retention and the lowest cation disorder in one sample. Here, all three samples developed a very similar amount of cation mixing, namely 2.7 or 2.8 %. Their dQ/dV plots, discharge capacity retention as well as coulombic efficiencies are very similar, yet sample 10/750 shows exceptional first cycle

charge and discharge capacities of 281 and 241 mAh/g. Sample 5/350-10/750 exhibits the biggest 1st cycle capacity loss yet the smallest capacity loss between 1st and 3rd cycle.

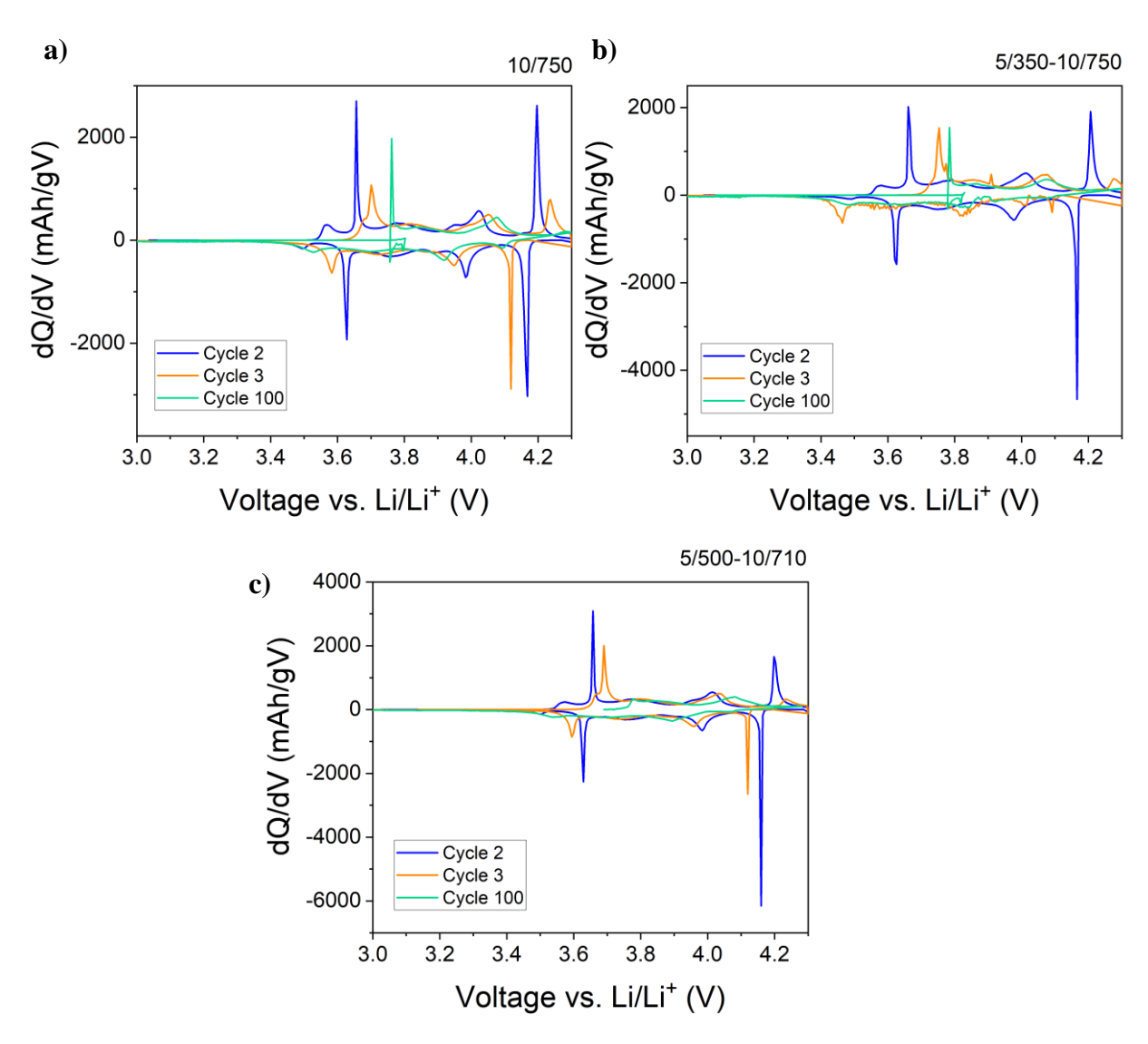


Figure 4.14: Differential Capacity plots obtained for LiNiO₂ synthesised via a solid-state route, a) sample 10/750, b) sample 5/350-10/750 and c) 5/500-10/710. Coin half cells cycled between 3-4.3 V vs. Li/Li⁺ at a rate of C/20 for two cycles and C/2 for the third cycle. 2^{nd} cycle depicted in blue, 3^{rd} cycle in orange and 100^{th} cycle in green.

The last three samples in this trial are depicted in Figure 4.15, these are samples 5/750, 5/350-5/750 and 5/500-5/710. The capacity plot reveals initial charge and discharge capacities of 246, 271 and 287 mAh/g and 206, 232 and 240 mAh/g and a corresponding 1st cycle capacity loss of 40, 39 and 47 mAh/g, respectively. Sample 5/500-5/710, shows the highest charge capacity amongst all the samples investigated here, but also the largest difference in capacity between the 1st and the 3rd cycle. As its charge capacity is above the theoretical value, side phases or additional Li in the structure are suspected. The features during the first charging

cycle for samples 5/750 and 5/500-5/710, are artefacts from cycling, when the cycling was paused for external reasons. The other cycled cells of these samples also exhibit these features.

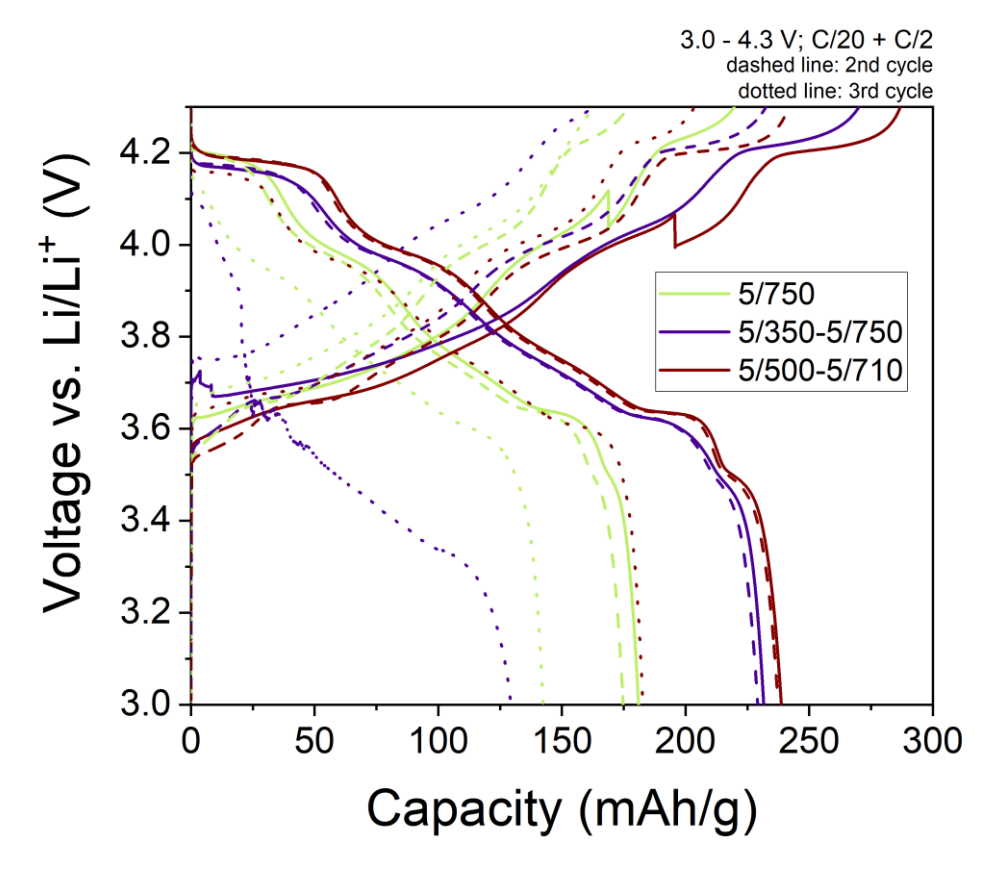


Figure 4.15: Charge/discharge plot for LiNiO₂ synthesised via a solid-state route, sample 5/750 (green), sample 5/350-5/750 (purple) and sample 5/500-5/710 (red). Cycled between 3-4.3 V vs. Li/Li⁺ at a rate of C/20 for two cycles and C/2 for the third cycle. Solid line shows 1^{st} cycle, dashed line depicts 2^{nd} cycle and dotted line represents the 3^{rd} cycle.

Figure 4.16 shows both, capacity retention and coulombic efficiencies over 100 cycles. Whereas the coulombic efficiencies of all three samples reaches almost 100% after the formation cycles, with initial efficiencies of 82.3, 85.7 and 83.5%, respectively, the discharge capacity retention shows more deviation between the samples with 87.9, 96.2 and 82.9% observed.

Sample 5/350-5/750 shows deviations from the other samples in discharge capacity, capacity retention as well as coulombic efficiency. The fluctuations of coulombic efficiencies are quite unusual, as they reach above 100% and the capacity decreases notably during the first 10 cycles but increases again after 20 cycles. The fluctuations in coulombic efficiency can be explained by temperature fluctuations, but when taking a closer look, the capacity plot for this sample some abnormalities can be observed, including at the beginning of the charge.

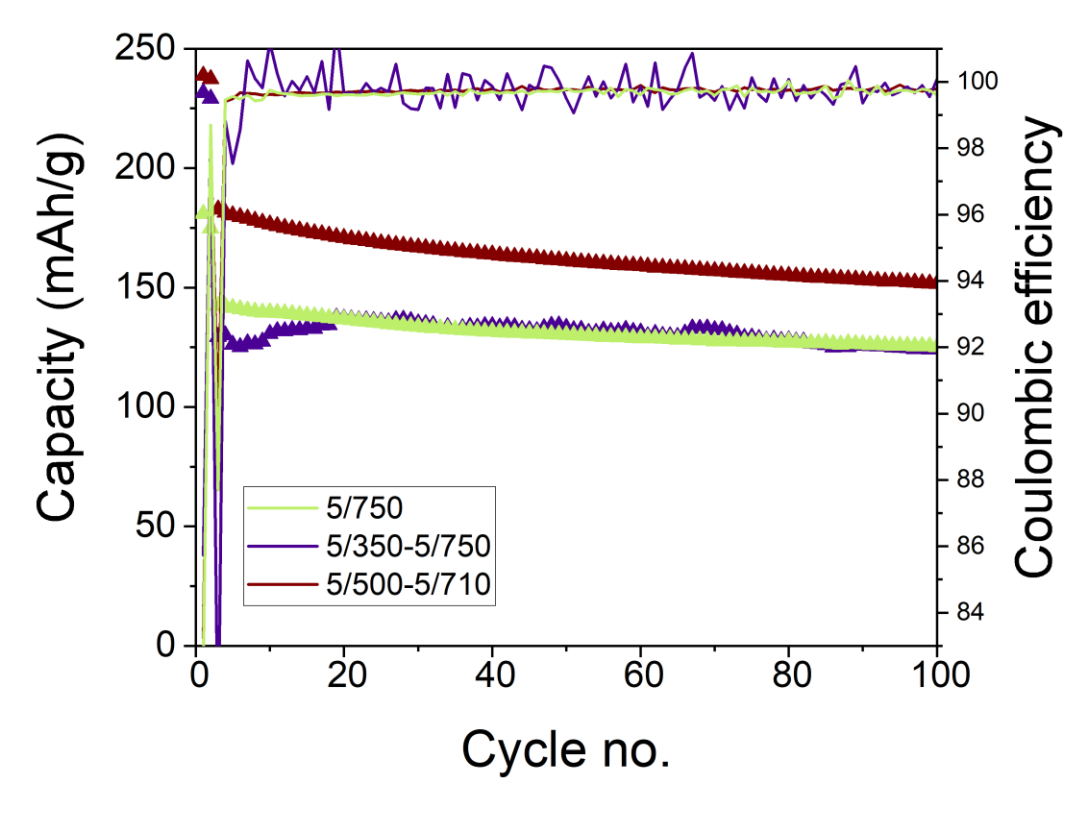


Figure 4.16: Discharge capacity retention plot including coulombic efficiencies over 100 cycles for LiNiO $_2$ synthesised via a solid-state route, sample 5/750 (green), sample 5/350-5/750 (purple) and sample 5/500-5/710 (red). Cycled between 3 – 4.3 V vs. Li/Li $^+$ at a rate of C/20 for two cycles and C/2 for the third cycle.

The 3rd cycle discharge capacity loss is the highest for these samples. Yet, according to the discharge capacity retention plot, the capacity is recovered after about 20 cycles. Examining the SEM images of this sample, a surface layer of very tiny particles of unknown composition can be seen on the secondary particles and might influence the cycling behaviour of that sample. Taking all these details into account, the outstanding discharge capacity retention over 100 cycles for this sample, should be interpreted carefully. All other cells prepared with the cathodes from this material failed within the first cycle, so no other data is available to backup or further investigate this behaviour. Figure 4.17 depicts the differential capacity plot and the phase transitions during charge and discharge of the coin half-cell. All three samples show similar electrochemical behaviour during the 2nd cycle at a C-rate of C/20 with just slight changes in intensity of the transition peaks. The M/H2 transition is depicted only with one peak which is in accordance with the Li/Ni mixing in these samples. All three exhibit the highest cation disorder amongst these experiments, with sample 5/750 standing out with 5.4%, showing the lowest intensities and broadest transitions. Important to mention for this samples as well, is the low intensity of the distinct H2/H3 transition above 4.2 V during the 2nd cycle already. As with

the other samples already described above, the samples here also access the additional electrochemical reaction at 3.55 V during charge and at 3.5 V during discharge when cycled at a lower rate.

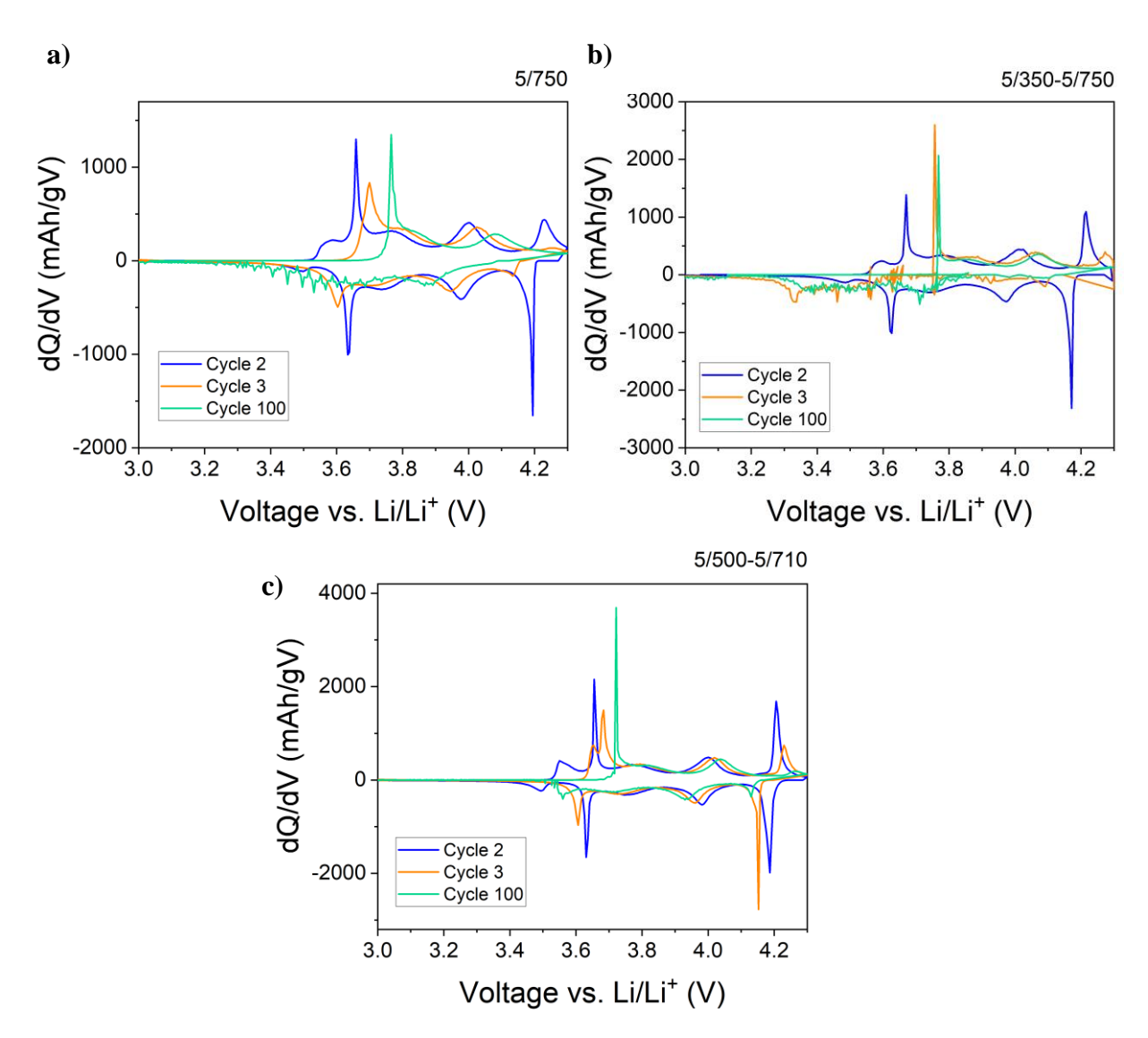


Figure 4.17: Differential Capacity plots obtained for LiNiO₂ synthesised via a solid-state route, a) sample 5/750, b) sample 5/350-5/750 and c) 5/500-5/710. Coin half cells cycled between $3 - 4.3 \,\mathrm{V}$ vs. Li/Li⁺ at a rate of C/20 for two cycles and C/2 for the third cycle. 2^{nd} cycle depicted in blue, 3^{rd} cycle in orange and 100^{th} cycle in green.

Whereas all the transitions shift equally to higher voltages during charge and lower voltages during discharge in the third cycle, the 100th cycle is hard to interpret because of the noise for samples 5/750 and 5/350-5/750. For sample 5/750, the H2/H3 transition almost disappears in cycle 3 already and shifts for all other samples outside of the measured potential window by cycle 100.

Although the samples calcined only for 5 h, seem to exhibit the most impressive electrochemical behaviour regarding initial charge capacity or capacity retention, compared to all the other sample, these samples also show the highest amount of cation mixing as well as unusual behaviour during the cycling.

Table 4.4: Electrochemical values derived from the cycling data of the nine selected samples of as-prepared LiNiO₂ and Ni occupancy in Li layer derived from Rietveld refinements.

Precal- cination	Cal- cination	Ni ²⁺	Discharge Capacity	Charge Capacity	Capacity loss	Coulombic efficiency	Discharge Capacity Retention
t [h] /	T [°C]	[%]	(1st cycle) [mAh/g]	(1st cycle) [mAh/g]	(1st cycle) [mAh/g]	(1 st cycle) [%]	(100 cycles) [%]
	15/670	2.7	222	257	35	86.5	81.5
5/350	15/710	1.6	222	262	40	84.7	68.1
5/500	15/750	1.8	216	256	40	84.5	67.9
	10/750	2.7	241	281	40	85.9	72.9
5/350	10/750	2.8	213	266	53	84.8	72.7
5/500	10/710	2.7	225	263	38	85.3	79
	5/750	5.4	206	246	40	82.3	87.9
5/350	5/750	2.8	232	271	39	85.7	96.2
5/500	5/710	3.1	240	287	47	83.2	82.9

For easier comparison, initial capacities and discharge capacity retention of all nine here further examined samples are depicted in Figure 4.18. Satisfying initial discharge capacities of 241 and 240 mAh/g are reached by sample 10/750 and sample 5/500-5/710, respectively. Capacity retention over 100 cycles clearly shows good performance for the sample 5/500-5/710 as well, closely followed by sample 15/670.

Taking into account the Ni²⁺ amount in the Li layer, derived via refinements of the measured XRD patterns and the peak ratios in Table 4.2 and Table 4.3, sample 5/500-5/710 shows the highest values of cation mixing, which will affect structural stability, side reactions with the electrolyte and overall stability and lifetime of the cell. Further examination of the nature of the very tiny particles on the secondary particle surface and how these may influence the electrochemical behaviour for this sample and its unusual electrochemical behaviour, is still to be investigated.

Finding a compromise amongst all these important values like initial capacity, capacity retention and cation mixing, the calcination procedure of sample 5/350-15/710 was used for further investigations during this thesis. This sample showed a high initial charge and discharge

capacity of 262 and 222 mAh/g, a good capacity retention of almost 70% over 100 cycles, the lowest value of cation mixing (1.6%) in the sample and the lowest/highest value of the Bragg peak ratios (003)/(104) and (006/102)/(101), respectively. Välikangas et al., Bianchini et al. and Kurzhals et al, did similar studies on the calcination of LiNiO2, yet there are quite big differences in precursor synthesis, sample preparation and cycling conditions. Välikangas et al., achieved an initial discharge capacity of 231.7 mAh/g, a first cycle efficiency of 91.3% and a cation mixing of 1.1%. The precursor was prepared via precipitation reaction at 40°C and annealed for 5 h at 670°C. They cycled between 2.6 – 4.3 V at 0.1 C and the lower cut-off voltage resulted in better capacity retention compared to samples annealed at 650 and 700°C within their study. [92] The corresponding sample in this study is sample 5/750. With a higher annealing temperature, higher cation mixing is introduced, and the initial discharge capacity is lower with 206 mA/g. As the precursor was precipitated with different conditions as well as the prepared cathode cycled with a different cycling profile, those samples cannot really be compared. Nevertheless, samples in this study excel the here reported good initial discharge

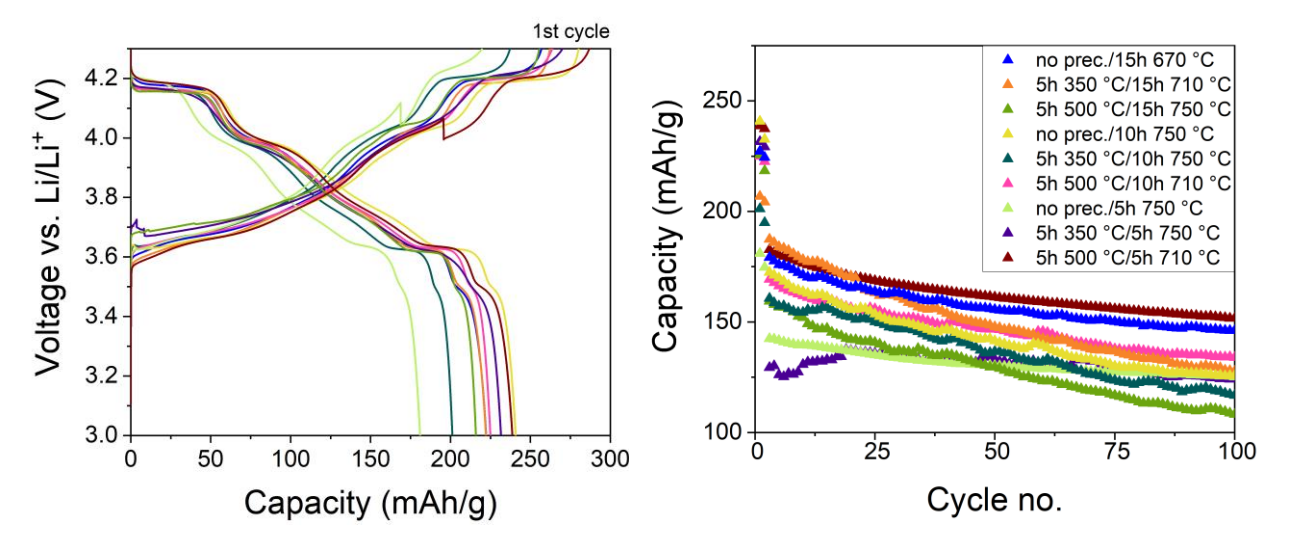


Figure 4.18: Overview and comparison of 1^{st} cycle capacity plot (left) and discharge capacity retention plot (right) of the pre-selected nine samples of LiNiO₂, calcined under different conditions.

capacity while getting close to 1% of cation mixing.

Bianchini et al., show the importance of a pre-annealing step and an annealing temperature below 700°C to mitigate decomposition using extensive examination of the structural evolution, the lattice parameters and cation mixing of the solid-state synthesis of LiNiO₂. They did not perform any electrochemical cycling on their prepared materials. [42] The best samples in this study show that a pre-calcination step in not necessary to achieve great cycling behaviour, yet staying close to the decomposition temperature is beneficial.

As shown here in this chapter, Kurzhals et al., confirm the finding that for small values of Ni²⁺ in the Li layer, the correlation between the 1st cycle capacity loss and the cation mixing is not valid. In accordance with this study, the particle morphology, the packing density of primary particles within the secondary particle assemblies, the surface area of the primary particles and the particle size distribution of secondary particles play a crucial role for the electrochemical behaviour of the high-nickel cathode active layered material. [193] [194]

4.3. Conclusion

The combined results of the study reported in this chapter indicate an optimum pre-calcination temperature of 350°C, to remain below the melting temperature of LiOH and to avoid aggregation of the particles and thus an intermediate grinding step. Combined TGA and HT-XRD studies have shown that an intermediate grinding step is unnecessary when using reaction temperatures below the melting temperature of LiOH. As shown in the HT-XRD analysis, the starting materials Ni(OH)₂ and LiOH•H₂O dehydrate to form the intermediate reactants NiO and LiOH already below 350°C. From here, NiO is acting as a host structure, where Li is incorporated in between the Ni, leading to a layering effect due to steric and energetic constraints when reaching a quantity of 30 % Li in the structure. This shows that it is unnecessary if not disadvantageous, to hold the pre-calcination step at an even higher temperature, as this will lead to a melting of LiOH and thus an aggregation of the particles.

Spherical secondary particle assemblies made out of apparently densely packed primary particles with a narrow particle size distribution will improve the electrochemical behaviour of battery cells. Densely packed particles ensure a maximum amount of Li in the structure and thus a higher packing density of active material in the cathode film. This benefits accessing the theoretical possible capacity of the material. From a solely visual inspection, samples 5/350-15/710, 5/350-10/750 and 5/750, show a seemingly dense structure of primary particles within the secondary particle assembly.

Since the cation mixing in the LiNiO₂ structure plays a crucial role in the overall Li content and thus the maximum capacity, and the additional Ni²⁺ in the Li layer and thus the capacity retention, further analysis of the delicate solid-state synthesis and its consequent electrochemical behaviour is unfolded in this chapter. XRD patterns show a single phase of LiNiO₂, whereas refinements of those patterns suggest a small amount of Li₂CO₃ side phase. Due to this side phase, a compositional analysis as it is common amongst battery researchers to

investigate the actual composition of the solid solution Li_{1-x}Ni_{1+x}O₂, will not result in correct values. Both phases contain Li and using *induced coupled plasma analysis* ICP will not be able to help distinguish how much Li is contained in the main phase and how much in the side phase. As the XRD patterns are gathered from a benchtop XRD with rather low resolution, a determination of the amount of side phase of only a few percent is not regarded as reliable. Thus, in this chapter it was refrained from reporting it. Nevertheless, for the future chapter, when synthesising LiNiO₂ from an optimised precursor material, neutron diffraction studies are aimed for, and the refinement of this data will give a trustworthy statement regarding possible side phases as well as the Ni/Li occupancy in the Li layer.

A Bragg peak analysis of the current XRD data was undertaken as well as refinements of the data. The ratio of the (003)/(104) and (006/102)/(101) peaks as well as the c/a ratio of the refined cell constants were compared to the refined Ni²⁺ amount in the Li layer. As these ratios are a measure for the cation mixing in the structure and the x in the chemical composition and a measure of the hexagonal distortion of a cubic lattice, respectively, conclusions can be drawn from these results. For very low values of cation mixing in the structure, either the statements are incorrect, or the resolution of the data is too low, but for values of above 3 %, the findings from other research groups can be confirmed during this study.

The most important part is to correlate the cation mixing and the optimal particle morphology to the electrochemical data. Coin half cells, cycled between 3.8 and 4.3 V at C/20 for two formation cycles and C/2 for the remaining 98 cycles were considered and analysed. Divided into categories of calcination time for easier comparison of the nine pre-selected samples, the most outstanding samples are summarised here. Taking into account the peak analysis and refined Ni²⁺ content as well as particle morphology, sample 5/350-15/710, exhibits a first cycle discharge capacity of 222 mAh/g, seemingly dense and an evenly distribution of particles in the SEM images as well as the lowest amount of Ni²⁺ in the structure in this study.

Although the sample 5/500-5/710 shows exceptional first cycle charge and discharge capacity of 287 and 240 mAh/g, respectively and the best capacity retention over 100 cycles of 87%, this sample also shows the biggest 1st cycle loss. The first cycle capacity loss is due to the fact that during the first delithiation, Ni²⁺ will oxidise to Ni³⁺ and thus decrease in size. As these Ni³⁺ ions are located in the Li layer, this layer will decrease in size, making it harder for the Li to deintercalate and leave the structure Li depleted. This sample shows a high amount of Ni²⁺ (3.1%) in the Li layer. Sample 5/350-5/750 also stands out with its remarkable capacity retention over 100 cycles of 96.2%, an initial discharge capacity of 232 mAh/g and a very low

amount of Ni²⁺ in the structure. On the other hand, the decrease in capacity between the two formation cycles (C/20) and the remaining ones (C/2), is the largest in all the samples. The SEM images of that sample, reveal a lot of small particles covering the secondary particle surface. The capacity retention plots as well as the coulombic efficiencies over 100 cycles, reveal noisy data and a drop in capacity during the first 10 cycles, which then increases again to its initial state.

Overall, one of the most promising samples in this trial is sample 10/750. This sample shows a very dense structure of primary particles within the secondary particle assembly, a very low amount of Ni²⁺ (2.7%) in the structure and an exceptional first cycle charge capacity of 281 mAh/g and a first cycle discharge capacity of 241 mAh/g. It shows a 1st cycle capacity loss of 40 mAh/g and a capacity retention over 100 cycles of 72.9%. Secondly, sample 15/670 shows excellent capacity retention over 100 cycles (81.5%) and a low 1st cycle capacity loss of 35 mAh/g. Its first cycle charge and discharge capacity of 257 and 222 mAh/g, respectively are superior and the amount of Ni²⁺ in the Li layer is low with 2.7%. Both samples show similar size distributions in their SEM images with cuboid shaped primary particles and quasispherical secondary particle assemblies.

These promising results lead to the assumption, that no pre-calcination step is needed necessarily during the high temperature solid-state synthesis of LiNiO₂. Optimised performance regarding cation mixing as well as initial capacity and capacity retention over 100 cycles can be reached using either a lower calcination temperature for a longer time or by decreasing the calcination time and simultaneously increasing the calcination temperature.

Further investigations on this side will be beneficial to confirm results and find the underlying cause of why certain reaction parameter combinations work better than others regarding their electrochemical performance, like BET and porosity measurements. Tap density and laser diffraction to confirm packing density, particle size and distribution, as most of the assumptions in this chapter are based on a visual examination.

5. Morphology Control of the Ni(OH)₂ Precursor Particles for the Layered Oxide Cathode Material LiNiO₂.

5.1. Introduction

Primary and secondary particle size and morphology have tremendous effects on the physical, chemical, and thermal properties of a material. Increasing the electrode density is key to accessing the full potential of a cathode active material. Smaller secondary particles will lead to more densely packed electrodes and to a higher accessible Li content and higher volumetric energy density. The higher surface area of these electrodes will give rise to an increased reactivity with air or moisture during storage, leading to Li residual compounds at the particle surfaces which can later during cycling lead to increased oxygen evolution. The increased availability of reactive sites on higher surface area particles during cycling on the other hand, will lead to increased interaction with the electrolyte, forming unwanted CEI layers and thus hindering Li diffusion. Additionally, secondary particles of seemingly dense packing of small elongated primary particles are more likely to break when the electrode is calendered for increased packing density. Microcracking during calendaring as well as during electrochemical cycling will lead to an increased surface area and more possible side reactions with the electrolyte, leading to further degradation. Yet utilising larger secondary particles, will give an aggravated volumetric energy density and cracking is more likely when pressure is applied [75] [195] [196]. Thus, the optimum secondary particle size needs to be distinguished and a reliable synthesis protocol developed to achieve the desired size and morphology.

The primary particles within these secondary particle assemblies are elongated and densely packed in either a randomly or radially aligned configurations. Radially aligned primary particles establish easier and faster Li diffusion pathways towards the particle surface and thus influence the rate capability. Adjustments of primary particle size and alignment will influence grain boundaries and void formation and strengthen the structural stability by decreasing strain inside the secondary particle, increasing its mechanical strength and delaying potential particle cracking during cycling [75] [195]. It is vital to alter and optimise the particle size and morphology to access the possible theoretical capacity of a cathode-active battery material and stabilise the particles structurally, chemically, and thermally during cycling.

To control, tailor and investigate particle size, particle size distribution and the morphology of secondary particle assemblies and primary particles of the precursor material Ni(OH)₂, a precipitation synthesis in a batch stirred tank reactor with highly controlled synthesis conditions was utilised. X-ray diffraction peak analysis, *scanning electron microscopy* (SEM) images, laser diffraction, tap density, density measurements, surface area analysis via *Brunauer-Emmett-Teller* (BET) theory and cross-section SEM imaging were applied to characterise the material. The influence of particle size and morphology on the annealing step as well as on the electrochemical behaviour was further investigated by the same methods mentioned before as well as refinements of the XRD patterns. Furthermore, more advanced techniques like *X-ray absorption near-edge structure spectroscopy* (XANES), *soft X-ray absorption spectroscopy* (sXAS), *extended X-ray absorption fine structure spectroscopy* (EXAFS), *hard X-ray photoelectron spectroscopy* (HAXPES), *resonant inelastic X-ray scattering* (RIXS) as well as in situ *X-ray diffraction computer tomography* (XRD-CT) and in situ muon measurements using synchrotron sources were consulted to complete the picture of structure-property relationship in the high nickel layered oxide material.

5.2. Experimental Precursor Synthesis Optimisation

The baseline for this reaction was taken from literature [94] and reaction optimisation for Ni_{0.8}Mn_{0.01}Co_{0.01}(OH)₂ already conducted in the Cussen group. Both sources use a reaction time of 40 h. Over 20 h the transition metal solution, ammonia and sodium hydroxide solutions were fed into the reactor (Figure 5.1) to form the precipitate which was then left in the supernatant for another 20 h, to allow ripening and particle growing. To initially make this reaction more sustainable and less time consuming, the reaction time was optimised. Moreover, the reaction temperature, the TM:NH₄OH molar ratio and the pH were parameters to be modified and their influence on particle size, the particle size distribution and the morphology of the precipitate to be investigated. In the first set of optimisation experiments, a reaction temperature range between 40 and 60°C was used while the other parameters were kept constant. In a second set of experiments, the TM:NH₄OH ratio was altered between 1:1.2 to 1:5 while the other parameters were kept constant. Lastly, the pH was increased above 11 as with a higher Ni content, a higher pH is needed to homogeneously precipitate Ni(OH)₂. The exact used volumes and concentrations for each reaction can be seen in Table 5.1. For all reactions, 356 mL of a 2 M NaOH solution is used.



Figure 5.1: STR set-up containing a precursor solution of nickel sulphate, ammonia and sodium hydroxide.

Table 5.1: Reaction conditions for the optimisation of synthesis of Ni(OH)₂

Re	actor Condition	S	NH	4OH solutio	on 1	NiSO ₄ solution		NH ₄ OH solution 2			
Temp.	TM:NH ₄ O	рН	V_1	V_1 (H ₂ O)	Conc.	m_{TM}	$\begin{array}{c} V_{TM} \\ (H_2O) \end{array}$	Conc.	V_2	V_2 (H ₂ O)	Conc.
[°C]	H ratio	r	[mL]	[mL]	[M]	[g]	[mL]	[M]	[mL]	[mL]	[M]
60	1:1.2	11	15.2	598	0.4	85.06	162	2	10	93	1.5
50	1:1.2	11	15.2	598	0.4	85.06	162	2	10	93	1.5
40	1:1.2	11	15.2	598	0.4	85.06	162	2	10	93	1.5
60	1:1.2	11	14.1	599	0.4	85.06	162	2	9	94	1.5
60	1:2.5	11	29.4	577	0.8	85.06	162	2	19.6	85	3.1
60	1:3.75	11	44	563	1.2	85.06	162	2	29.4	74	4.7
60	1:5	11	59	548	1.6	85.06	162	2	39	64	6.3
60	1:5	11.6	59	548	1.6	85.06	162	2	39	64	6.3
60	1:1.2	11	14.1	599	0.4	85.06	162	2	9	94	1.5
60	1:1.2	10.6	14.1	599	0.4	85.06	162	2	9	94	1.5

The 1 L BioFlo 320 bioprocess control system from Eppendorf, Germany is used with a bottom steel dish to facilitate the necessary temperatures during the reaction, four separate pumps to feed the solutions into the reactor, a marine blade impeller to ensure homogeneous distribution of the added solutions, a nitrogen gas sparger at the bottom of the vessel to create an oxygen free environment within the reactor. Furthermore, a pH sensor is connected and immersed in the reactant solution to control a NaOH feed pump to keep the pH constant to a set value during the complex reaction. A schematic of the reactor is shown in Figure 5.2.

The volume and concentration of the used solutions are dependent on the desired final amount of the precipitate. In this study, the goal is to investigate the influence of different precipitation conditions on the particle size and morphology of the precipitate, thus, a smaller amount of 30 g is prepared in each reaction. The minimum starting volume for the reactor is 600 mL. The entire amount of NH₄OH used for this synthesis is based on the chosen TM:NH₄OH ratio. 60% of the NH₄OH amount is added to the reaction vessel as a starting solution, whereas the remaining 40% is added during the precipitation reaction, to keep the NH₄OH concentration in the vessel constant.

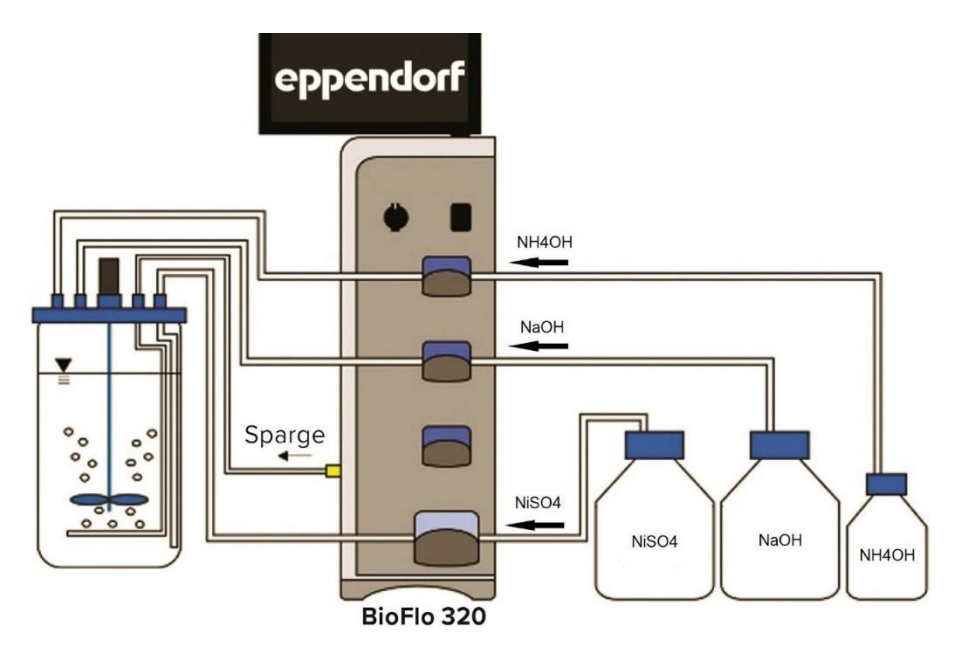


Figure 5.2: Schematic of stirred tank reactor. [212]

The pumps are calibrated to the density of each solution for highest accuracy and the pH sensor is calibrated at the reaction temperature to minimize temperature dependent deviations of the measured pH. The base solution is heated up to the reaction temperature and stirred at $1000 \, \text{rpm}$ to guarantee a homogeneous mixture of all added components during the reaction. N_2 is introduced into the solution from the bottom using a sparger. The pH sensor is inserted into the

vessel and as soon as the base solution settled at the reaction temperature, the pH is set to the desired value, which initiates the corresponding pump to add a 2 M NaOH solution (TM:NaOH ratio of 2.0) dropwise to increase the pH to the desired value. As the pH sensor constantly feeds back the actual measured pH in the vessel, the pump can adjust its flow rate more sensibly due to the programmed cascade loop to prevent a massive overshooting and decrease the time to settle at the desired value. As soon as the pH value is reached, the addition of the NiSO₄ solution and remaining NH₄OH solution are started simultaneously. After the feeding and the dwelling time, the precipitate is vacuum filtrated, washed thoroughly with deionised water and dried either in an oven at 80°C overnight or on top of a drying oven over the weekend. After the precipitate is dried, the powder is ground for XRD measurements and applied to SEM stubs and gold sputter coated to avoid any charging for SEM imaging. Additionally, the as-prepared powder is used for density measurements as well as BET measurements. For particle size and particle size distribution, the powder is dispersed in water for laser diffraction measurements. Furthermore, the most promising precursor were annealed with LiOH•H₂O to form LiNiO₂ utilising the calcination conditions that have been optimised in Chapter 4.

5.2.1. Reaction Time

To increase productivity and make this reaction more sustainable and less time consuming, three reactions were investigated. The feeding times of 5, 9 and 17 h and dwelling times of 14, 10 and 21 h, respectively, are achieved by adjusting the feeding rates of the pumps. The reactions were conducted according to the reaction plan in Table 5.1. The resulting dried precipitates were examined regarding phase purity, particle size and morphology via X-ray diffraction, laser diffraction and scanning electron microscope imaging and the resulting data is shown in Figure 5.3 to Figure 5.5 and Table 5.2.

The obtained XRD patterns in Figure 5.3 show phase pure samples compared to a calculated pattern of β -Ni(OH)₂ (ICSD collection code 169978 [36]) from the ICSD. The peak intensities and broadening of the Bragg peaks in the XRD patterns change with longer precipitation time, suggesting changes in chemistry and less crystallinity. Broadening of the peak corresponding to the c-axis suggesting an increase in interslab space between the NiO₆ layers and thus intercalation of water or anions.

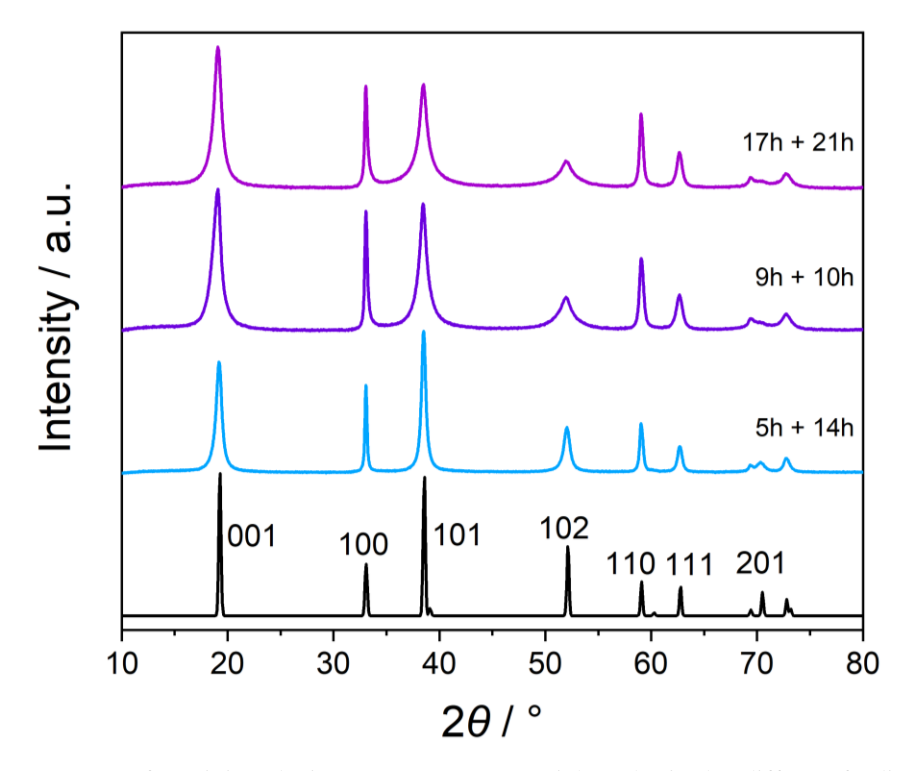


Figure 5.3: XRD patterns of precipitated Ni(OH)₂ precursor material synthesised at different feeding and dwelling times (blue: feeding time of 5h and dwelling time of 14h; purple: feeding time of 9h and dwelling time of 10h; pink: feeding time of 17h and dwelling time of 20h). Calculated Ni(OH)₂ pattern from ICSD (black, collection code 169978 [36]) as comparison including Bragg peak labels.

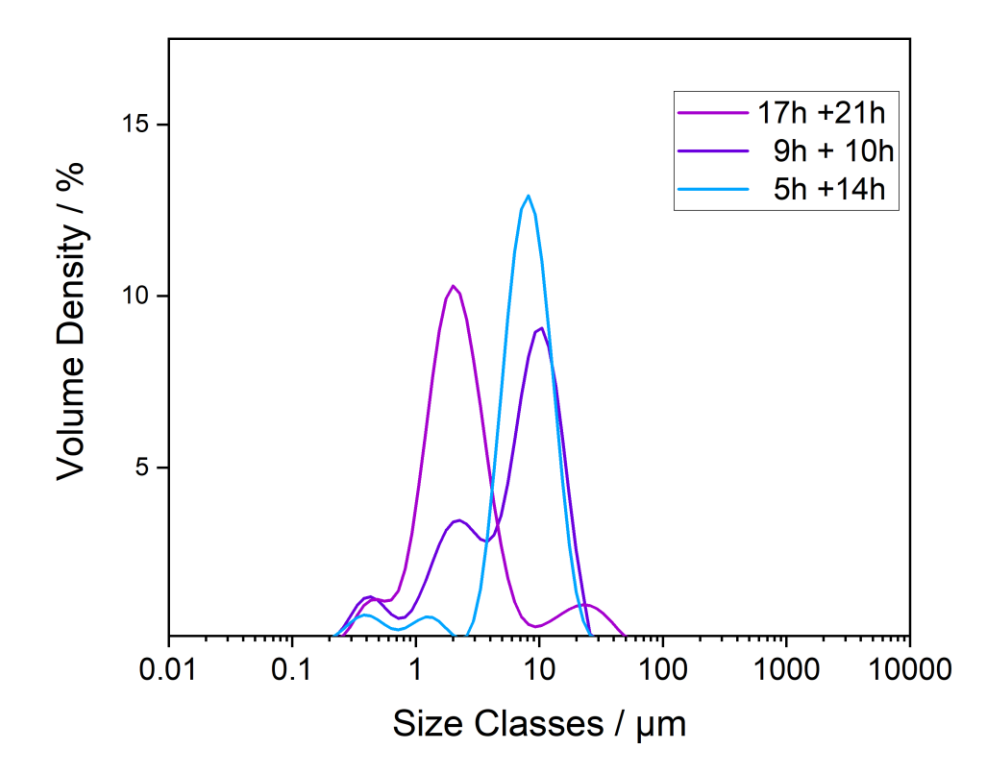


Figure 5.4: Particle size distribution derived from laser diffraction of precipitated Ni(OH)₂ precursor material synthesised at different feeding and dwelling times (blue: feeding time of 5 h and dwelling time of 14 h; purple: feeding time of 9 h and dwelling time of 10 h; pink: feeding time of 17 h and dwelling time of 20 h).

Table 3.2. Falticle Size of Diecibitated MiCOTD at different feaction till	Table 5.2: Particle size of precipitated Ni(OH) ₂ a	it different reaction time
--	--	----------------------------

Reaction Time	Dx (10)	Particle Size Dx (50)	Dx (90)
Time		[µm]	
5 h + 14 h	3.86	7.76	13.7
9h + 10h	2.21	5.30	11.4
17 h + 21 h	0.946	2.12	5.60

Particle size analysis via laser diffraction is depicted in Figure 5.4 and corresponding values listed in Table 5.2. They show similar distributions and sizes for the two shorter feeding times of 5 and 9 h, with an average particle size of 7.76 and $5.30\,\mu m$, respectively. The precipitate harvested from the reaction with the longest feeding time, reveals a particle size distribution with smaller particle sizes with an average size of $2.12\,\mu m$.

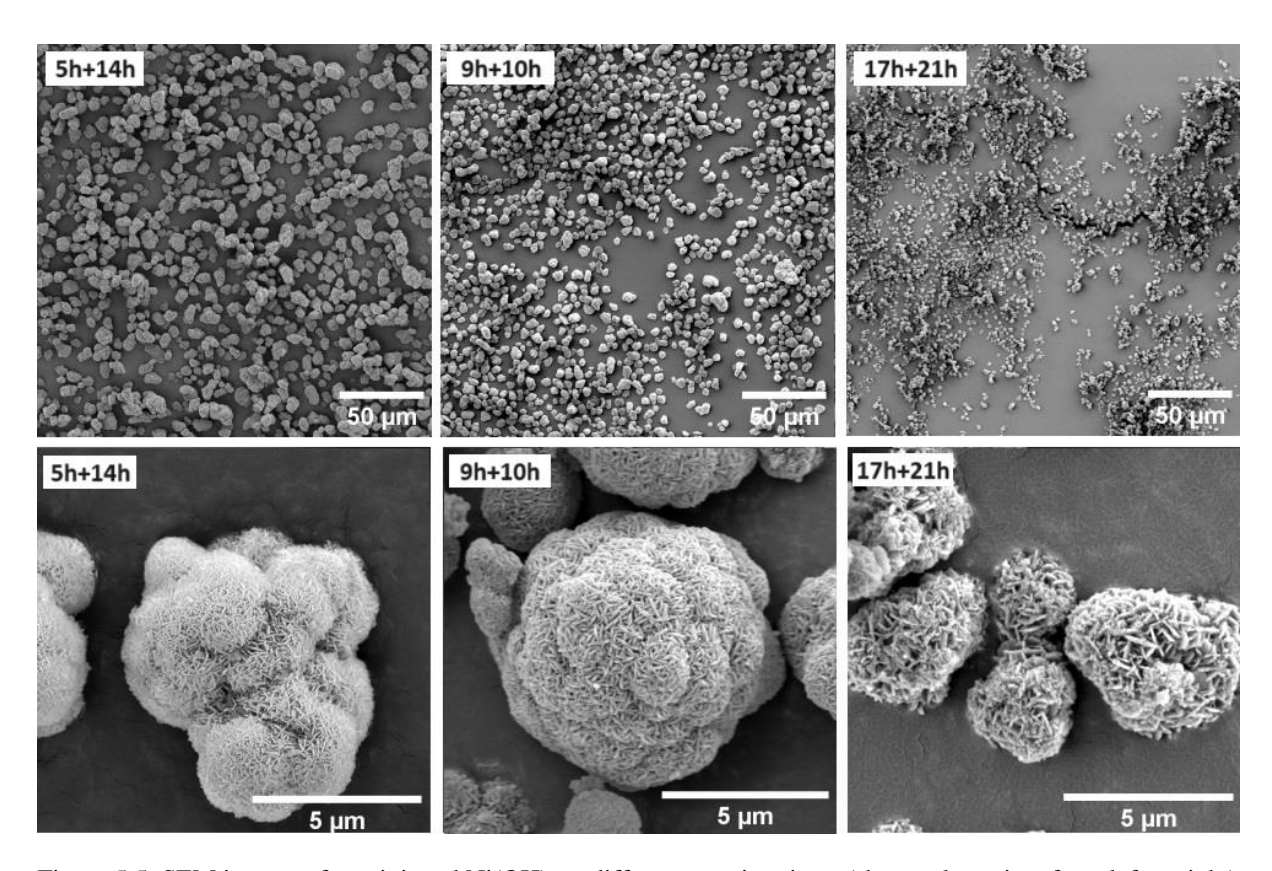


Figure 5.5: SEM images of precipitated Ni(OH)₂ at different reaction times (short to long time from left to right).

Taking the SEM images (Figure 5.5) into account, it can be seen that the secondary particles get smaller with longer feeding time (top row) while at the same time, the primary particles become larger and appear to lose their dense packing at 20 h (bottom row of SEM images) with gaps between the primary particles more evident for the sample. The sample with feeding time

of 9h shows spherical structures of secondary particles agglomerated into a meatball-like structure. A feeding time of 9h appears to deliver particles of a more uniform quasispherical nature compared with 5h and 17h. A major goal of this work is to provide a reliable, reproducible process for the synthesis of the Ni(OH)₂ precursor. As the 9h dwelling time gave the most consistent particle size, shape and packing, this was selected as a route for the remainder of the thesis.

5.2.2. Reaction Temperature

The reaction temperature influences the secondary particle size and the packing density of primary particles within the secondary assembly as shown by several research groups [51] [91] [92]. Thus, it is crucial to optimise the reaction temperature for a higher nickel content, as the nickel content itself influences the precipitation reaction. A higher nickel content increases the supersaturation of Ni²⁺ in the solution and thus influences the balance between particle nucleation and particle growth during precipitation. This determines the population densities of particles and the kinetics of primary particles growth. The secondary particle size, morphology and packing density of primary particles within the assembly, will influence the volumetric energy density of the final cathode material and thus its electrochemical behaviour.

Reactions employing temperatures of 40, 50 and 60°C were executed and the dried precipitate examined using X-ray diffraction which confirmed phase purity (Figure 5.6). Peak broadening can be determined for all samples, suggesting a deviation from pure β -Ni(OH)₂ as is widely observed for transition metal hydroxides synthesised through precipitation routes [39] [40], or a change in crystallite size. The broadening increases with increasing reaction temperature. The collected samples were further investigated regarding their particle size using laser diffraction. The results are shown in Figure 5.7 and Table 5.3. The particle size distributions show similar results for the lower reaction temperatures of 40 and 50°C, with average particle sizes of 9.19 and 10.2 μ m, respectively. The reaction temperature of 60°C, reveals the largest particles of 11.4 μ m with an average particle size of 5.3 μ m. SEM images were taken to show the particle morphology (Figure 5.8). With increasing reaction temperature, the secondary particle size decreases, showing a poly-disperse particle size distribution between 0.2 and 26 μ m. The agglomeration of secondary particles into meatball-like shaped structures becomes increasingly spherical with increasing temperature. The primary particles visually increase in size with increasing reaction temperature and appear denser within the secondary assemblies.

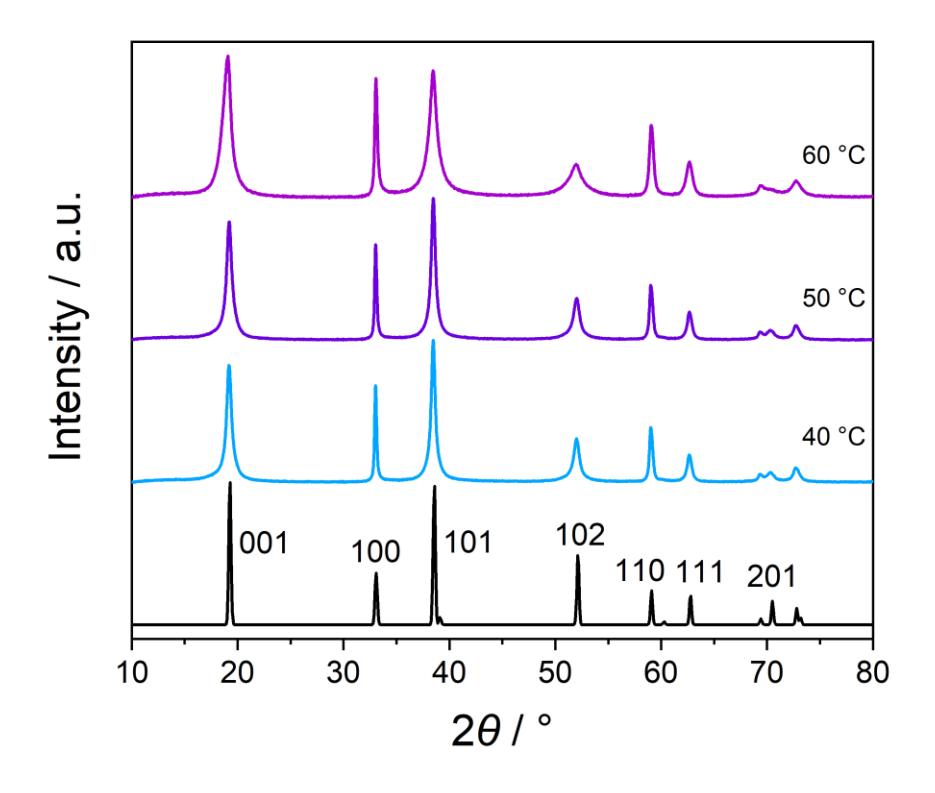


Figure 5.6: XRD patterns of precipitated $Ni(OH)_2$ precursor material synthesised at different reaction temperatures (blue: $40^{\circ}C$; purple: $50^{\circ}C$; pink: $60^{\circ}C$). Calculated $Ni(OH)_2$ pattern from ICSD (black, collection code 169978 [36]) as comparison including Bragg peak labels.

Table 5.3: Particle size of precipitated Ni(OH)₂ at different reaction temperatures

Reaction		Particle Size	
Temp.	Dx (10)	Dx (50)	Dx (90)
[°C]		[µm]	
40	5.39	9.19	25
50	5.65	10.2	41.9
60	2.21	5.30	11.4

With decreasing reaction temperature, the diffraction peaks become narrower, suggesting higher crystallinity and also the particle size distribution is narrower for the lower temperature reactions in comparison to the reaction temperature of 60°C. Yet, the most crucial criteria for choosing the reaction temperature, is the particle morphology and density of primary particles to achieve an optimised energy density. This can be seen in the SEM images of the particles precipitated at 60°C, which shows more spherical and apparently more densely packed secondary particles.

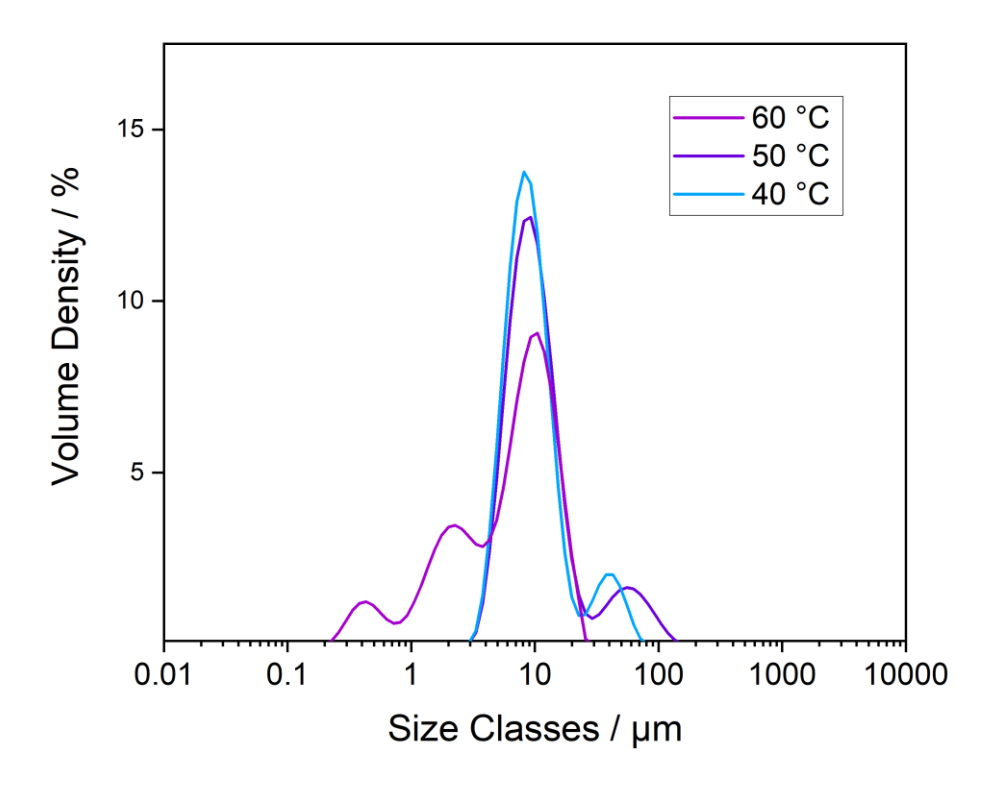


Figure 5.7: Particle size distribution derived from laser diffraction of precipitated $Ni(OH)_2$ precursor material synthesised at different reaction temperatures (blue: $40^{\circ}C$; purple: $50^{\circ}C$; pink: $60^{\circ}C$).

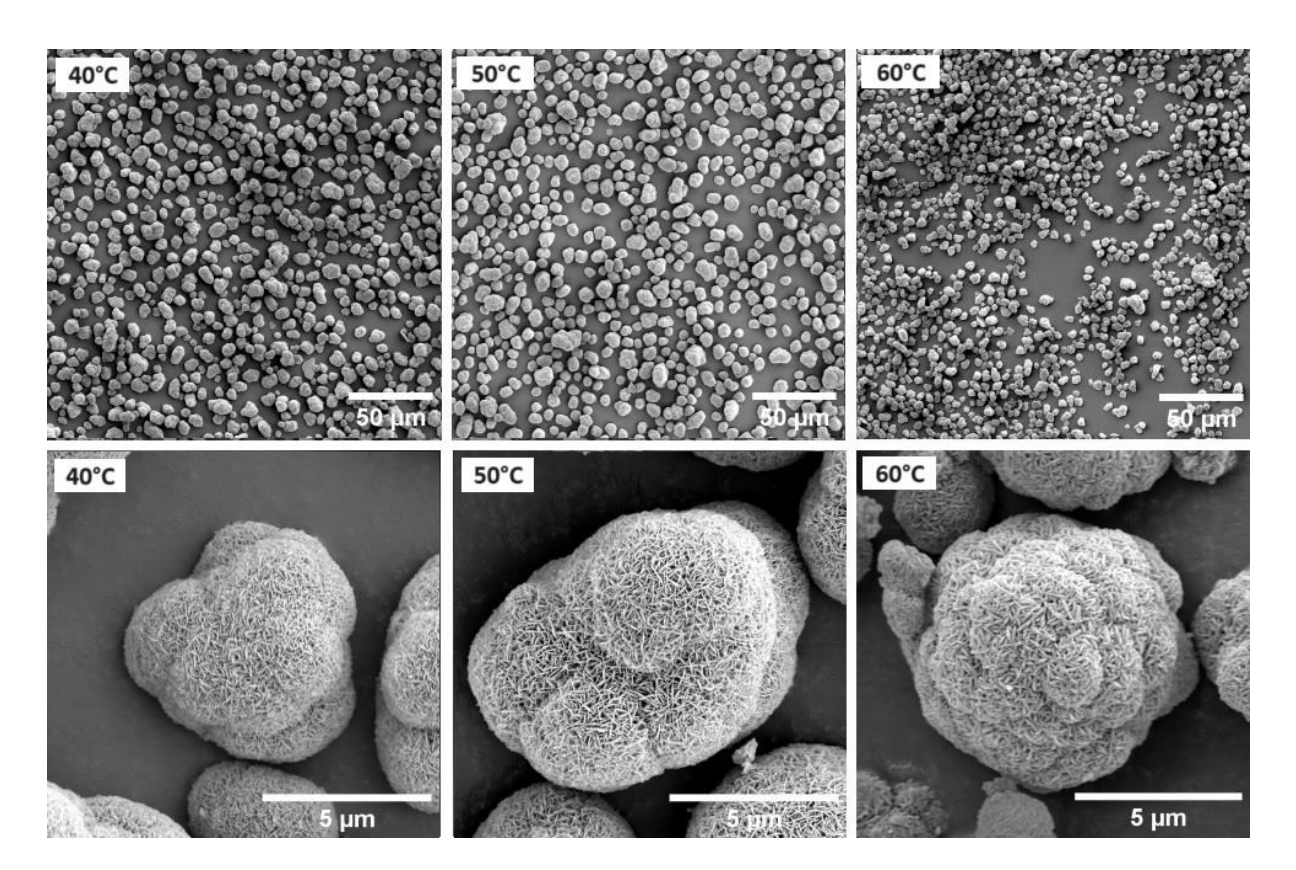


Figure 5.8: SEM images of precipitated $Ni(OH)_2$ at different reaction temperatures (low to high temperature from left to right).

5.2.3. Ni:NH4OH Ratio

The ammonia solution used in the precipitation reaction acts as a chelating agent. The nickel aqua complex in the initial nickel sulphate solution will substitute the H₂O ligand for NH₃. This mechanism decreases the degree of Ni²⁺ supersaturation in the solution and slows down further nucleation. The nickel ammonia complex changes ligands again as NaOH is added, to convert to the lower free energy stable phase Ni(OH)₂. The following dissolution and slow reprecipitation, promotes uniform crystal growth of the particles. In this set of experiments, the nickel ammonia ratio of 1:1.2, commonly used in literature, was used as a starting point and stepwise increased to 1:2.5, 1:3.75 and finally to 1:5.

The as-prepared Ni(OH)₂ precursors were examined for phase purity using X-ray diffraction. The patterns can be seen in Figure 5.9 and as can be seen in comparison with a calculated pattern (ICSD collection code 169978 [36]) from the ICSD database, no additional Bragg peaks of any side phases can be seen in any of the patterns. Peak broadening increases with decreasing Ni:NH₄OH ratio, suggesting a higher crystallinity in the sample using a Ni:NH₄OH ratio of 1:5. Possible stacking faults may be integrated within the crystal structure during the reaction as the peak broadening only occurs for the Bragg peaks corresponding to the c-axis of the lattice, suggesting the intercalation of impurities or rotation or translation of NiO₆ layers. [39] [40]

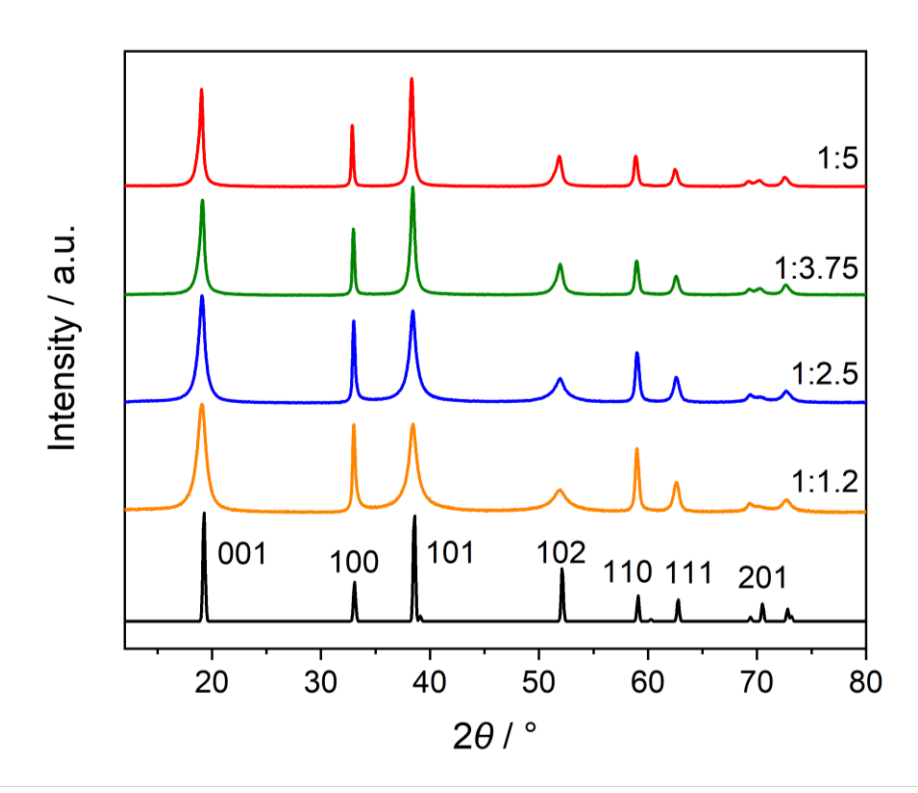


Figure 5.9: XRD patterns of precipitated Ni(OH)₂ precursor material synthesised at different Ni:NH₄OH ratios (orange: ratio 1:1.2; blue: ratio 1:2.5; green: ratio 1:3.75; red: ratio 1:5). Calculated Ni(OH)₂ pattern from ICSD (black, collection code 169978 [36]) as comparison including Bragg peak labels.

Table 5.4: Particle size_and tap density of precipitated Ni(OH) ₂ at different Ni:NH ₄ OH ratios					
NE.NII OH	Particle Size	Top Dongity			

Ni:NH₄OH ratio	Dx (10)	Particle Size Dx (50) [μm]	Dx (90)	Tap Density [g/mL]
1:1.2	0.516	3.37	7.13	1.488
1:2.5	4.5	7.19	11.9	1.835
1:3.75	5.03	7.98	12.7	1.845
1:5	6.93	10.4	17.8	1.938

Results of laser diffraction investigations of as-prepared samples can be seen in Figure 5.10 and Table 5.4. The average particle size increases with increasing Ni:NH₄OH ratio from 3.37 μm at a ratio of 1.2 to 10.4 μm at a ratio of 1:5. The particle size distributions observed indicate polydisperse size distributions for samples 1:1.2 and 1:3.75, whereas the two remaining samples 1:2.5 and 1:5 exhibit monodisperse particle size distribution. Tap densities for as-prepared samples can be seen in Table 5.4 and these are found to increase with increasing Ni:NH₄OH ratio. Particle size and tap density values for the ratios of 1:2.5 and 1:375 are very similar whereas a ratio of 1:1.2 shows a lower tap density of 1.488 g/mL which is expected when considering the distribution of secondary particles between 0.515 and 7.13 μm.

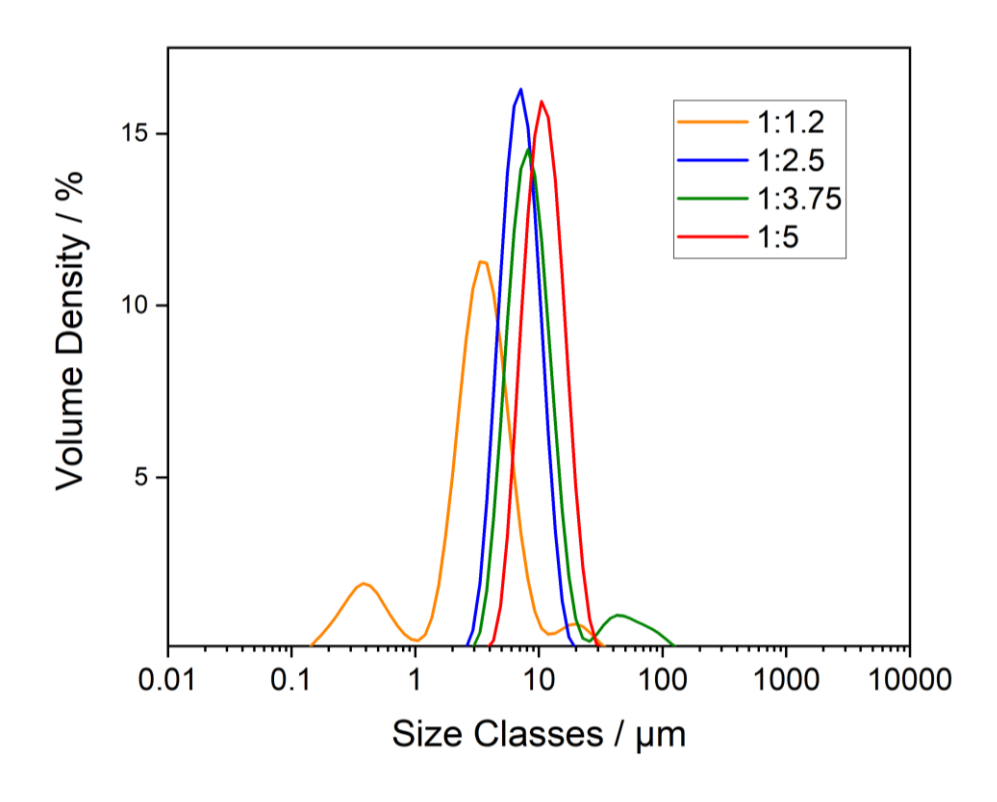


Figure 5.10: Particle size distribution derived from laser diffraction of precipitated Ni(OH)₂ precursor material synthesised at different Ni:NH₄OH ratios; (orange: ratio 1:1.2; blue: ratio 1:2.5; green: ratio 1:3.75; red: ratio 1:5)).

These observations are in accordance with the SEM images that are depicted in Figure 5.11, regarding particle size and size distribution. The images show the secondary particle assemblies containing small plate like primary particles. The secondary assemblies grow with higher Ni:NH₄OH ratio as can be seen in the top row. The bottom row depicts a higher magnification to show a single secondary particle, its size and morphology and also helps to investigate the primary particles. The secondary particles at a low Ni:NH₄OH ratio are below 5 µm and of various shapes, as secondary particles agglomerate together.

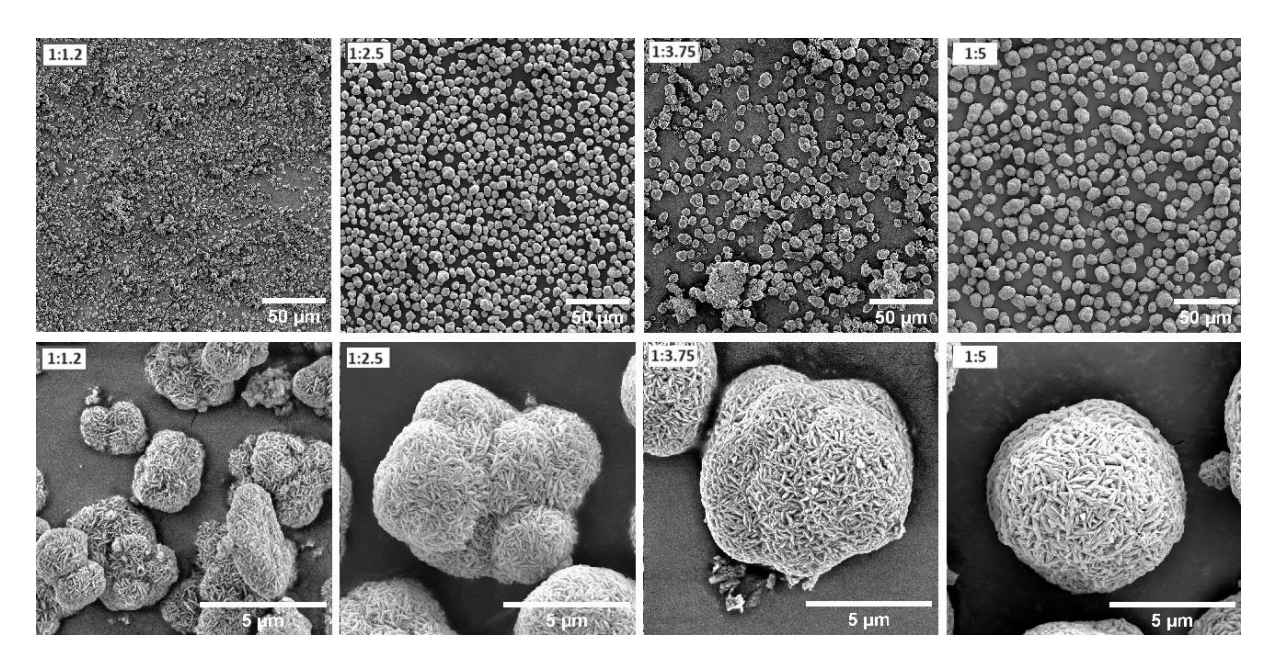


Figure 5.11: SEM images of the precursor material Ni(OH)₂ using different Ni:NH₄OH ratios (low to high ratio from left to right).

These agglomerated structures tend to become more spherical the higher the Ni:NH₄OH ratio, appearing quasispherical in shape up to a size of 10 µm with more densely packed primary particles. For all the different reaction conditions, the primary particles show elongated plate-like morphology. They also increase in size with higher Ni:NH₄OH ratio.

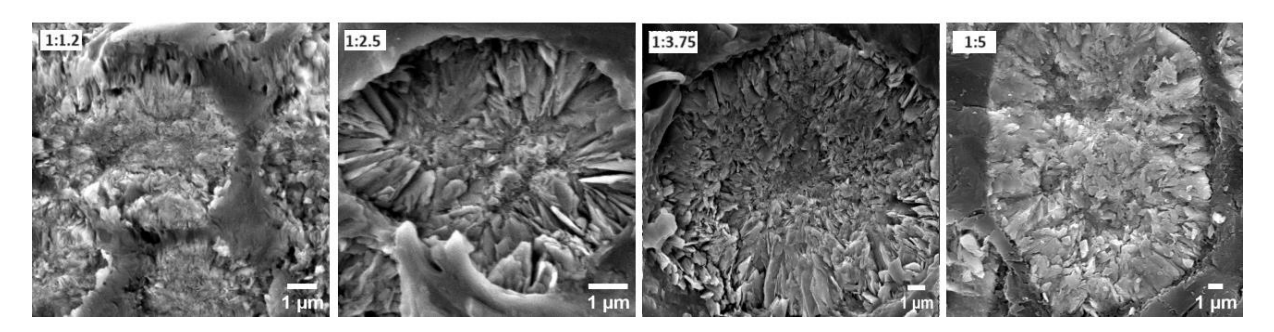


Figure 5.12: SEM images of cross-sections of as-prepared precursor material Ni(OH)₂ using different Ni:NH₄OH ratios (low to high ratio from left to right).

To examine the primary particle growth inside the secondary particles and further investigate the potential effect this may have on the resulting energy density, the particles are embedded in a resin and a cross-section is prepared and studied using a scanning electron microscope (Figure 5.12). From these images, one can invoke a growth mechanism of the Ni(OH)₂ particles during precipitation reaction in the STR. In the core of the secondary particle assemblies, the primary particles are randomly aligned. From there, the primary particles appear to grow in a radially aligned manner towards the particle surface as elongated platelets. It seems like the layer of radially aligned primary particles are similar in width for the samples synthesised at Ni:NH₄OH ratios of 1:2.5 and 1:5. They exhibit a smaller core of randomly aligned primary particles compared to the other samples. These observations will lay the foundation when investigating the morphology and internal structure of the lithiated secondary particles as these primary particle orientations work as pathways for the Li diffusion during cycling. Taking advantage of this knowledge and implementing it towards tailoring desired particle morphologies of cathode active materials could change the electrochemical behaviour for this material and its commercial applicability.

5.2.4. pH

Another important synthesis parameter to be investigated in this study is the pH value. As the Ni content in the hydroxide precursor increases, an increased pH is required to form uniform spherical particles and gather greater control over the reaction process. [94] [100] [197] Reactions were carried out utilising a pH of 10.6, 11 and 11.4, following the reaction procedure described earlier at a temperature of 60°C, a Ni:NH4OH ratio of 1:1.2 and an overall reaction time of 19 h. The resulting precipitate investigated via XRD, laser diffraction and SEM imaging.

The XRD patterns shown in Figure 5.13 for the as-prepared, dried precipitate is not showing any additional peaks of potential side phases. Regarding possible stacking faults within the crystal structure of the obtained Ni(OH)₂ samples, all three samples show peak broadening of Bragg peaks assigned to the *c*-axis The most prominent difference is seen for the highest pH, which was hard to maintain with the used equipment. After several attempts of adding triple the amount of NaOH to reach and maintain this pH throughout the whole reaction time, the SEM images as can be seen in Figure 5.15 as well as the laser diffraction in Figure 5.14 show non uniform particles with a broad particle size distribution. Particle sizes and their distributions can be seen in Table 5.5. No laser diffraction data is available for the sample synthesised with a pH of 10.6.

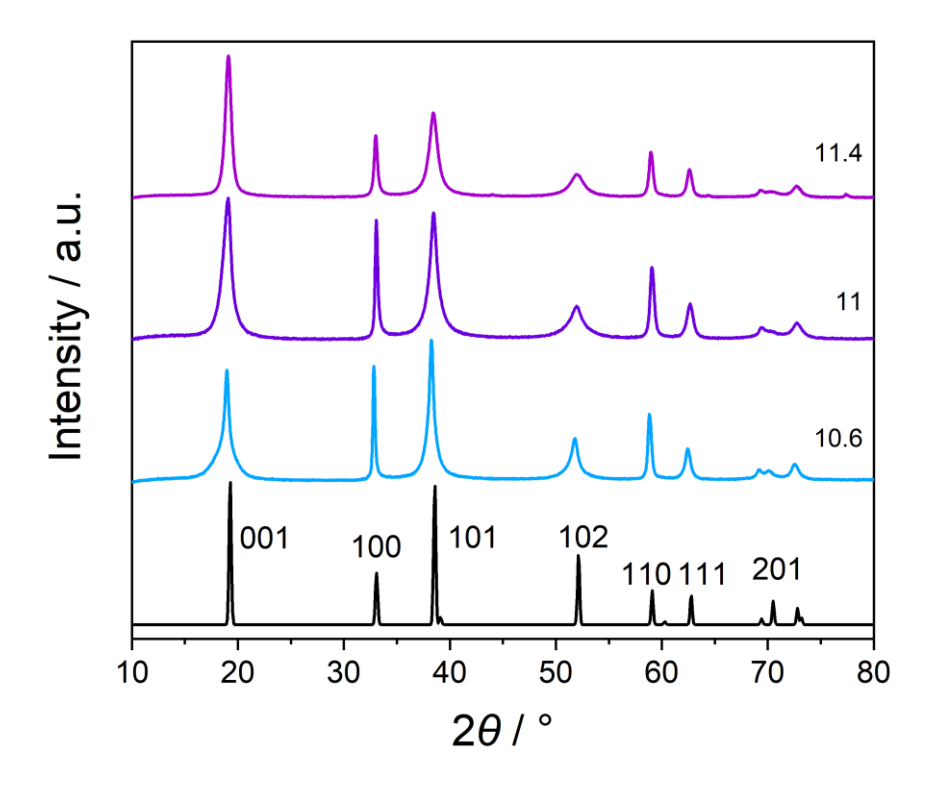


Figure 5.13: XRD patterns of precipitated β -Ni(OH)₂ precursor material synthesised at different pH (blue: 10.6; purple: 11; pink: 11.4). Calculated Ni(OH)₂ pattern from ICSD (black, collection code 169978 [36]) as comparison including Bragg peak labels.

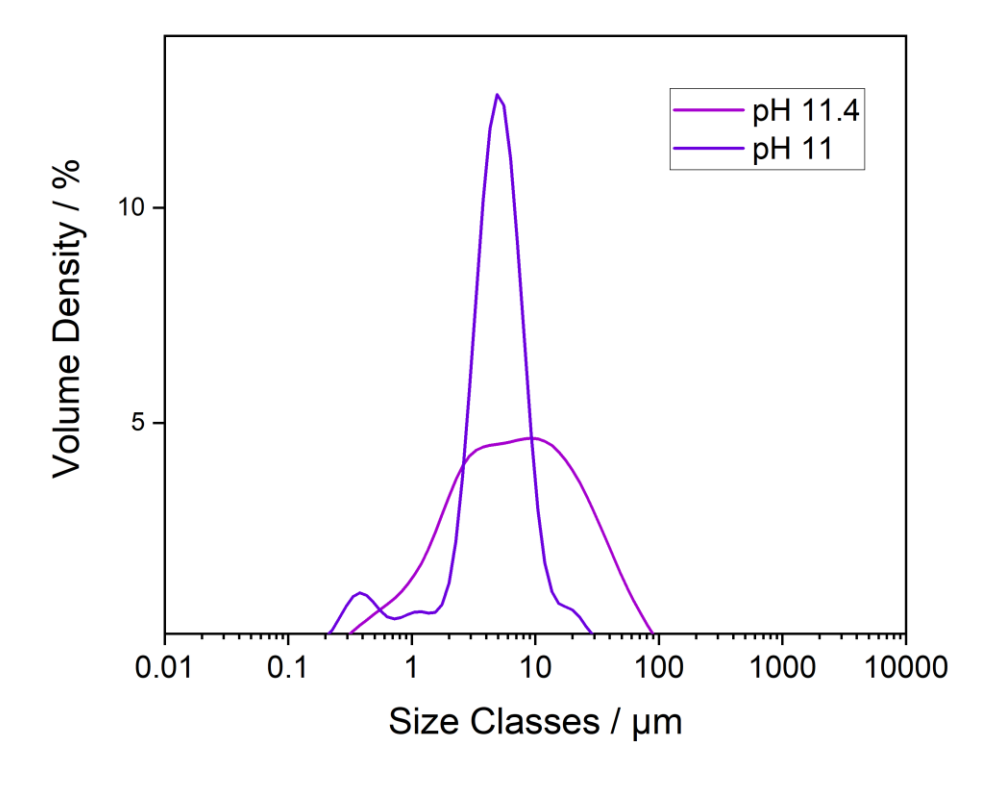


Figure 5.14: Particle size distribution derived from laser diffraction of precipitated Ni(OH)₂ precursor material synthesised at different pH (purple: pH 11; pink: pH 11.4).

The laser diffraction graph in Figure 5.14 reveals different particle size distributions for the samples synthesised at pH 11 and 11.4. Whereas the sample precipitated at pH of 11 shows a distinct maximum at 5.30 µm, the sample precipitated at a pH of 11.4 shows one very broad peak ranging from 0.3 to 90.7 µm with an average particle size D(50) of 6.89 µm. Taking the SEM images in Figure 5.15 into account, this broad particle size distribution in these samples can be understood. The particles are randomly sized and distributed. The particles obtained from the synthesis with a pH of 10.6 show a broad particle size distribution considering the SEM image at lower magnification. A lot of very small particles are seen within the secondary particle distribution. When looking at the higher magnification, the primary particles are very distinct, yet their distribution is less dense compared to the other samples.

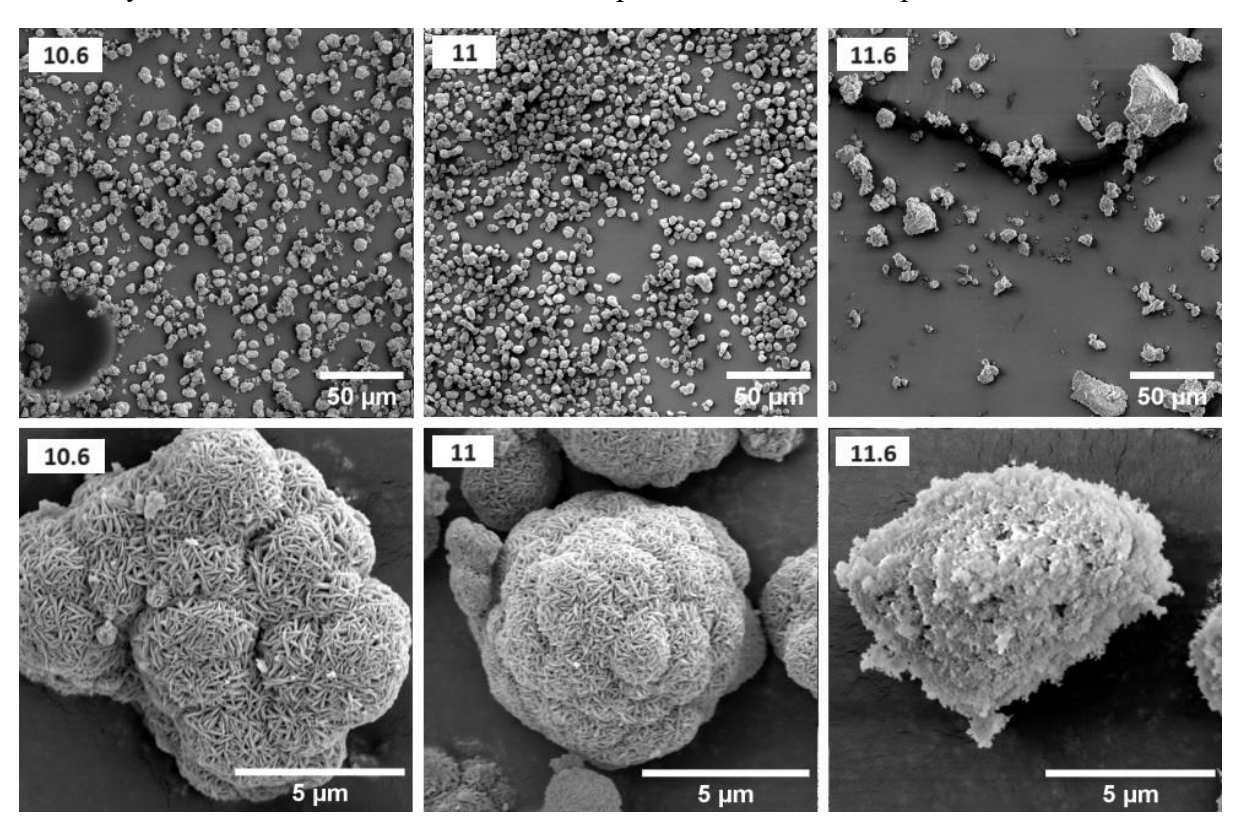


Figure 5.15: SEM images of precipitated Ni(OH)₂ at different pHs (low to high pH from left to right).

Table 5.5: Particle size of precipitated Ni(OH)₂ at different pHs

		Particle Size	
pН	Dx (10)	Dx (50)	Dx (90)
		[µm]	
10.6	-	-	-
11	2.21	5.30	11.4
11.4	1.5	6.89	29.5

Additionally, small particle fragments can be located on the surface of the secondary particle assemblies, making the surface rougher and the secondary particle less uniform in shape. Although the particles precipitated at a pH of 10.6 show a promising morphology and size distribution, a pH of 11 gives a seemingly denser, more spherical agglomeration of secondary particles.

These initial results of as-prepared Ni(OH)₂ precursor samples under varying precipitation reaction conditions, have been investigated and examined with regards to phase purity, particle size, morphology, and density of the precipitate. The most spherical secondary particles with seemingly dense packing of primary particles, a narrow particle size distribution is produced using a reaction time of 10h, a dwelling time of 9h, a temperature of 60°C, a pH of 11 and a TM:NH₄OH ratio of 1:5. As the aim is to investigate battery materials, the next logical step is to lithiate a set of samples and further examine their electrochemical behaviour, investigate the difficulty of synthesising a stoichiometric layered oxide material and study in detail the Ni/Li disorder, the Ni oxidation states in pristine cathode material as well as different states of charge and further, the Li diffusion properties in these materials. The most distinct influence of reaction conditions on the particle size, morphology and density can be seen for the different Ni:NH₄OH ratios as this parameter heavily affects the balance between particle nucleation and growth during the reaction. For the ongoing research of LiNiO₂ as a cathode active material for Li-ion batteries, these four samples will be further study in their lithiated structure.

5.3. Characterisation and Electrochemical Cycling of LiNiO₂ using different Ni:NH₄OH ratios in Precursor Synthesis

The set of samples acquired from the precipitation synthesis with varying Ni:NH₄OH ratios were chosen to be investigated further by annealing the precursor with a Li source to examine the electrochemical behaviour in a half coin cell. The precursors were thoroughly mixed for 10 min in a mortar and pestle with a 3% molar excess of pre-ground LiOH•H₂O. The added excess accounts for the possible evaporation of Li during the high temperature annealing step. The mixture is calcined in an oxygen atmosphere at 350°C for 5 h and for another 15 h at 710°C. The mixture is taken out of the furnace at 200°C to avoid any contamination or reactions with air or moisture and stored in an argon-filled glovebox. Samples for XRD measurements and laser diffraction were taken out of the glovebox to be examined and results shown in Figure 5.16 and Figure 5.17. SEM samples were prepared inside the glovebox before taken out to instantly coat them with a gold film to protect them from air and moisture exposure but also to prevent the sample from charging during the SEM investigations (Figure 5.18).

The XRD patterns (Figure 5.16) exhibit phase pure samples. Bragg peaks at 38° 2θ and 64.5° 2θ are split for all the samples, as can be seen in the magnified sections on the right of Figure 5.16, which indicates a highly layered and ordered structure. Ratios of the peaks (003)/(104) and (006/102)/(101), reflecting the degree of ordering and the cation mixing within the layered structure, are shown in Table 5.6. Sample 1:3.75 shows the highest value of 1.385 for the (003)/(104) ratio, followed by sample 1:1.2, whereas the lowest value of the (006/102)/(101) ratio is found for sample 1:2.5, very closely followed by sample 1:3.75. Rietveld refinements will give more precise values for the Ni²⁺ occupancy in the Li layer and the correlation between the Li/Ni mixing and the peak ratio analysis. These results will be discussed later in this chapter.

Table 5.6: Peak analysis of XRD patterns (Cu source, higher resolution) of annealed as-prepared precursor Ni(OH)₂ at different Ni:NH₄OH ratios

Ni:NH4OH ratio	(003)/(104) ratio	(006/102)/(101) ratio
1:1.2	1.334	0.464
1:2.5	1.237	0.449
1:3.75	1.385	0.457
1:5	1.270	0.498

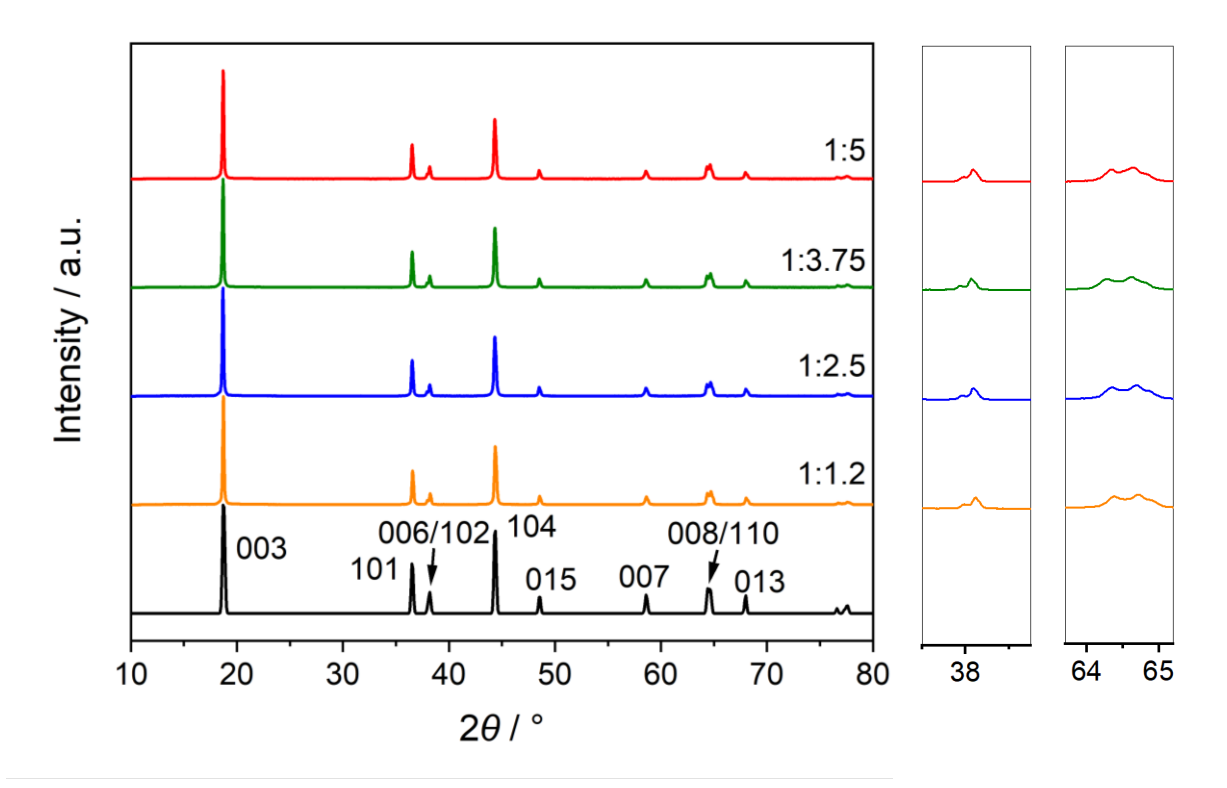


Figure 5.16: XRD patterns of LiNiO₂ material synthesised using different Ni:NH₄OH ratios during precursor synthesis (orange: ratio 1:1.2; blue: ratio 1:2.5; green: ratio 1:3.75; red: ratio 1:5). Calculated LiNiO₂ pattern from ICSD (black, collection code 78687 [187]) as comparison including Bragg peak labels. Zoomed-in sections of split Bragg peaks 006/102 at $38^{\circ}2\theta$ and 008/110 at $64.5^{\circ}2\theta$ on the right.

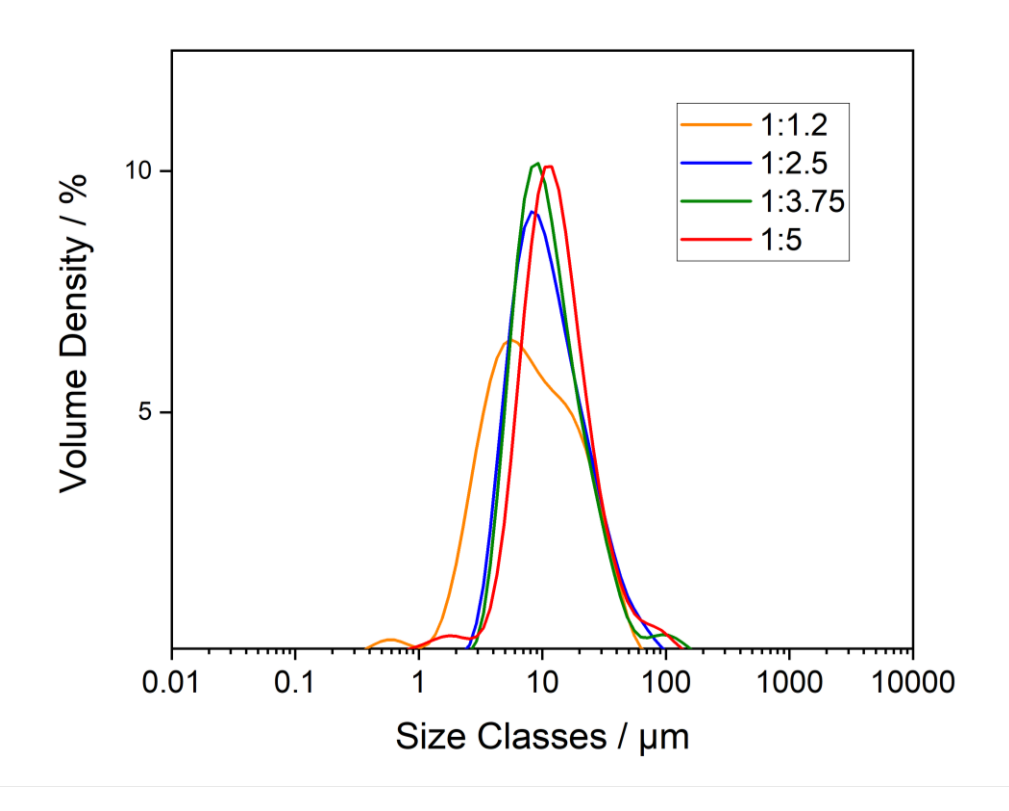


Figure 5.17: Particle size distribution derived from laser diffraction of LiNiO₂ material synthesised using different Ni:NH₄OH ratios during precursor synthesis (orange: ratio 1:1.2; blue: ratio 1:2.5; green: ratio 1:3.75; red: ratio 1:5).

The particle size distribution, tap density as well as BET surface analysis of the as prepared samples, are listed in Table 5.7 and Table 5.8. Size classes of the particle size distribution can be seen in Figure 5.17. The particle size analysis shows that the particles grew more during the synthesis with higher Ni:NH4OH ratios resulting in larger particles. Samples 1:2.5 and 1:3.75 exhibit a very similar average particle size of 10.8 and 10.9 µm. Sample 1:1.2 has an average particle size of 8.05 µm and sample 1:5 of 12.3 µm. Compared to the particle sizes of the precursors used, the secondary particles increase in size following the trend of the precursors. Here as well, samples 1:2.5 and 1:3.75 are similar in particle size with 7.19 and 7.98 µm. The corresponding tap densities are very similar for the samples with lower Ni:NH4OH ratio, namely samples 1:1.2 and 2:5, with 1.267 and 1.3 g/mL, respectively. The tap density does not increase with increasing Ni:NH4OH ratio though. Sample 1:3.75 exhibits the highest tap density with 1.743 g/mL. This trend is different from the precursor material, where the tapped density increases with increasing Ni:NH4OH ratio.

Table 5.7: Particle size and tap density of annealed as-prepared precursor Ni(OH)2 at different Ni:NH4OH ratios

Ni:NH4OH ratio	Dx (10)	Particle Size Dx (50)	Dx (90)	Tap Density
		[µm]		[g/mL]
1:1.2	2.76	8.05	26.3	1.267
1:2.5	5.05	10.8	27.9	1.300
1:3.75	5.44	10.9	27.3	1.743
1:5	5.86	12.3	27.3	1.561

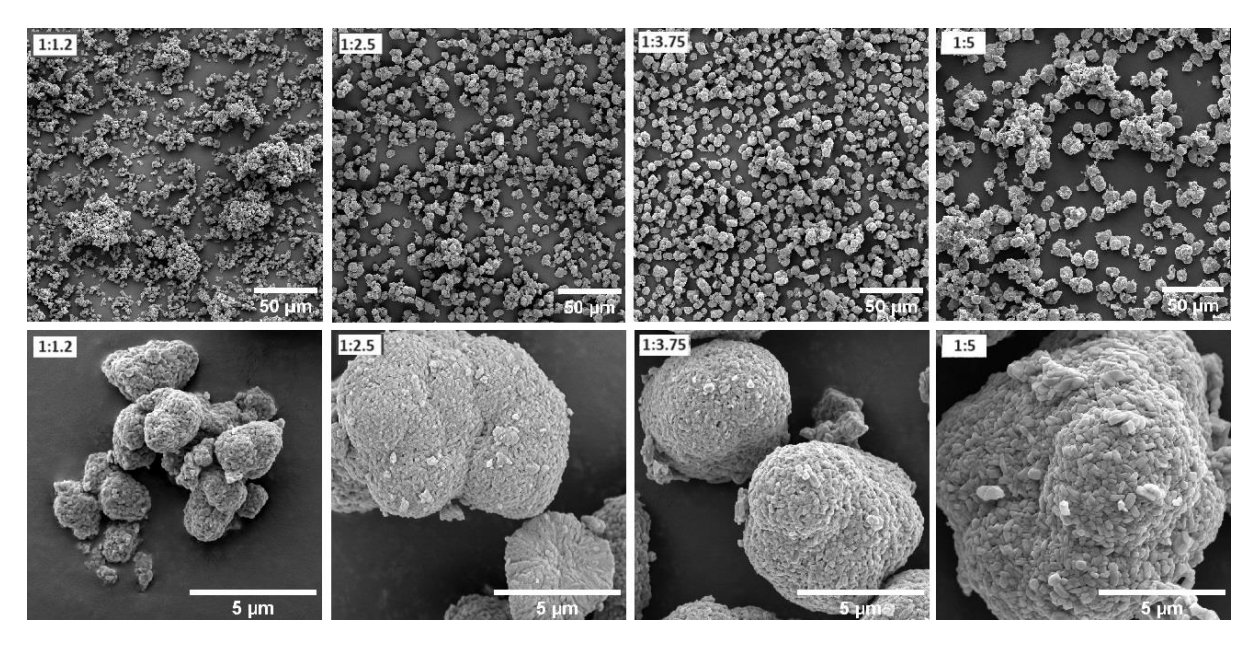


Figure 5.18: SEM images of annealed as-prepared precursor Ni(OH)₂ using different Ni:NH₄OH ratios (low to high ratio from left to right).

SEM images in Figure 5.18 of as-prepared LiNiO₂ particles depict the secondary particle assemblies and also give more details about the primary particles. The secondary particles increase in size with increasing Ni:NH₄OH ratio. They are mostly spherical and appear densely packed with primary particles. Their shape appears to change from an elongated arrangement in the precursor to a more three-dimensional cuboid shape after annealing. For more detailed insights into the core, cross-sections of the secondary particles were prepared and investigated using SEM and can be seen in Figure 5.19. The top row shows the cross-sections of the precursor secondary particles and the bottom row the cross-sections of the lithiated secondary particles. The core of randomly aligned particles as well as the shell of radially aligned particles was preserved even though the primary particles changed from elongated to cuboid shape. This packing and density of the secondary particle assemblies was further investigated using a multipoint BET surface analysis. The results of the BET analysis are summarised in Table 5.8. Figure 5.20 shows the linear fit of the BET analysis results of the samples, validating the reliability of the results. Three samples of each of the as-prepared materials were assessed and the average values taken to obtain viable surface areas for the LiNiO₂ powders.

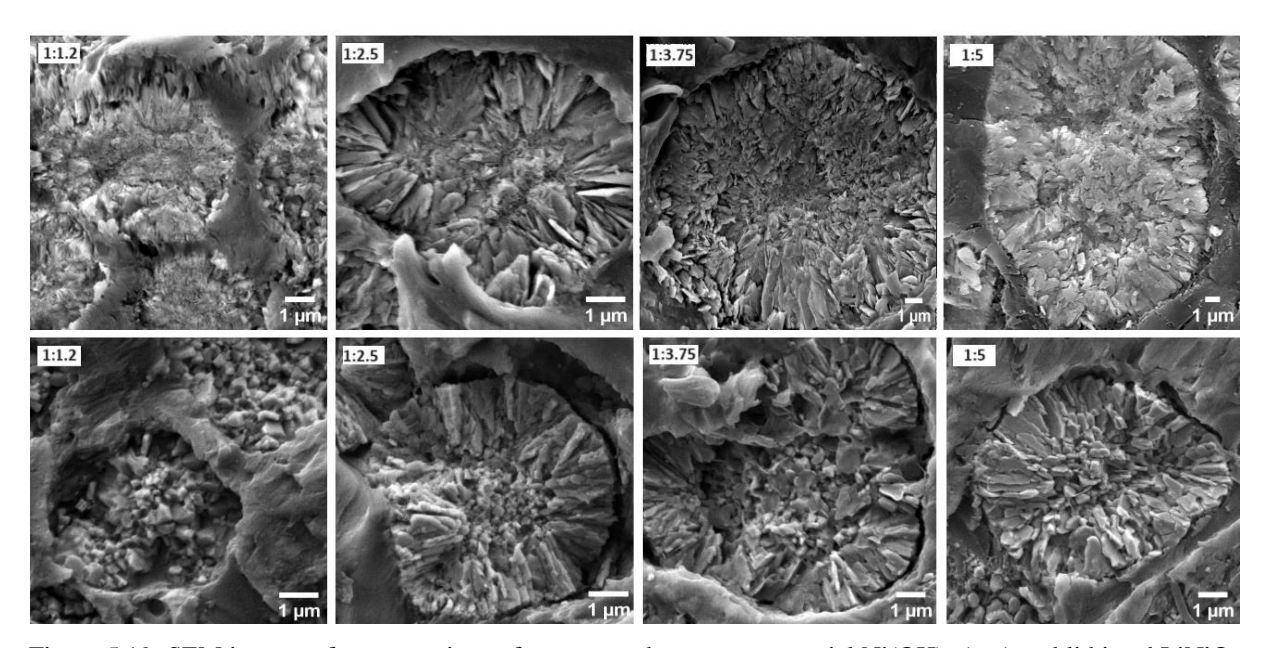


Figure 5.19: SEM images of cross-sections of as-prepared precursor material $Ni(OH)_2$ (top) and lithiated $LiNiO_2$ (bottom) using different $Ni:NH_4OH$ ratios (low to high ratio from left to right).

The BET surface analysis of the investigated samples synthesised with different Ni:NH₄OH ratios show a decreasing surface area with increasing particle size, which is expected. Sample 1:3.75 with a measured surface area of 0.3768 m²/g does not follow this trend. Additionally, a very low C constant was detected for this sample. The C constant of the BET analysis is a

measure of the enthalpy of adsorption of the adsorbate gas on the sample surface which is the relative strength of interaction between surface layer and the first layer of adsorbed gas molecules. A large value of C suggests that the monolayer formation is completed already at lower pressures, whereas a sample with a lower C value needs higher relative pressure to form a complete layer. To obtain more reliable BET surface area values, the C constant needs to be positive during fitting which can be achieved by adjusting the pressure range of the fitting. A higher surface area of the battery active material gives more opportunities for sites participating in redox reactions and for the Li to de-/intercalate during charge and discharge but also to more side reactions with the electrolyte during operation. Nevertheless, another reason for an increased surface area would be an increased porosity of the particles.

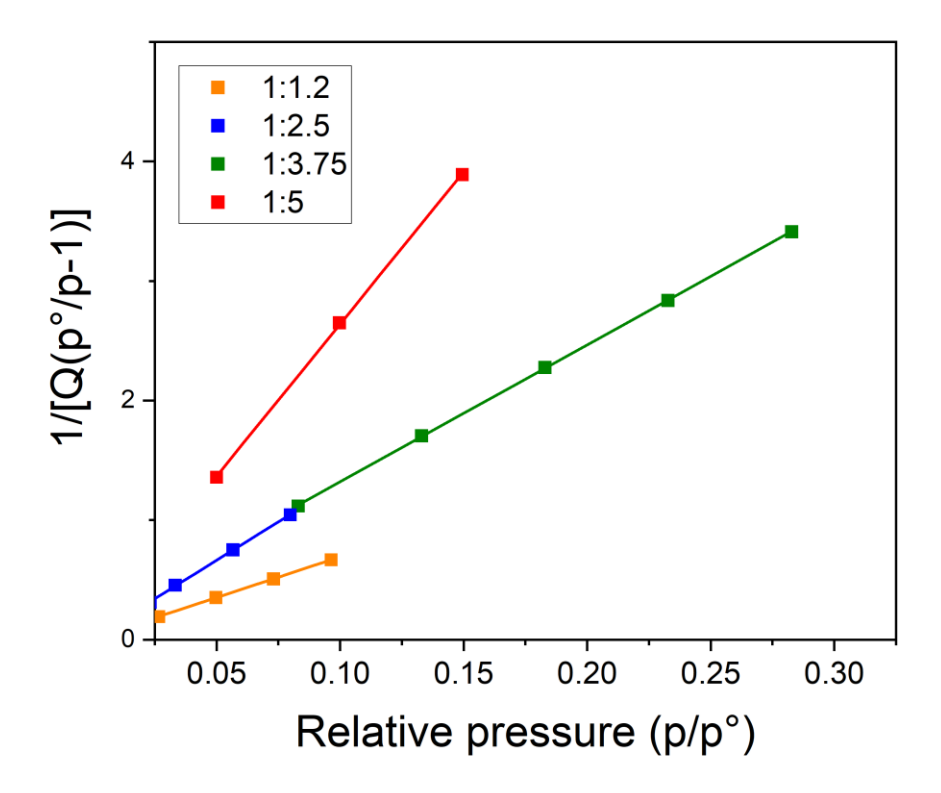


Figure 5.20: Multi point BET surface analysis and linear fits of annealed as-prepared precursor Ni(OH)₂ at different Ni:NH₄OH ratios (orange: ratio 1:1.2; blue: ratio 1:2.5; green: ratio 1:3.75; red: ratio 1:5)).

Table 5.8: Multi point BET surface analysis data of annealed as-prepared precursor $Ni(OH)_2$ at different $Ni:NH_4OH$ ratios

Ni:NH4OH ratio	BET surface area [m²/g]	Standard deviation [m ² /g]	C constant
1:1.2	0.6466	0.0031	547
1:2.5	0.3194	0.0013	628
1:3.75	0.3768	0.0023	65
1:5	0.1750	0.0053	269

To gain further insights in the structural changes during the lithiation step, the change from a cubic to a rhombohedral layered structure and to determine to what extend a cation mixing is present in the samples, refinements of the XRD patterns were undertaken. XRD measurements were carried out using a Mo source transmission powder diffractometer and shown in Figure 5.21 and Table 5.9. The XRD patterns exhibit all Bragg peak associated with the simulated pattern of LiNiO₂ derived from the ICSD. No additional peaks from side phases can be detected. Refinements of these XRD patterns give more accurate and precise Ni²⁺ occupancies in the Li layer as the Mo source provides a higher resolution. In the near future additional diffraction data will be executed at a neutron synchrotron source. As conventional X-ray diffraction is not suitable to detect light elements like Li, the refinements done here, are solely based on the Ni diffraction in the sample while neutron diffraction will give reliable values for the Li site occupations in the structure as well.

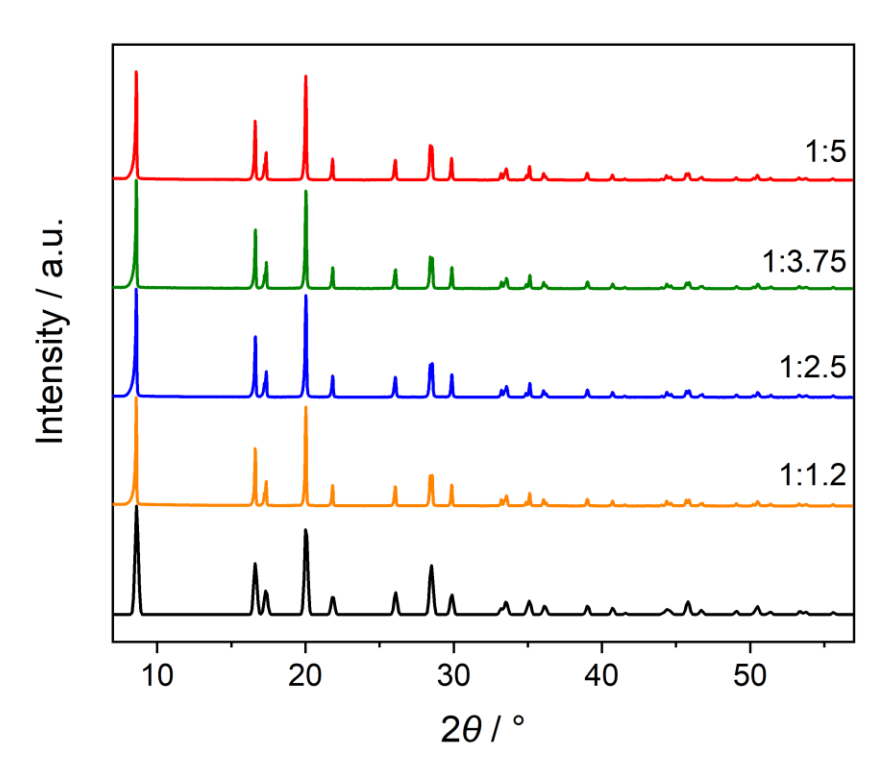


Figure 5.21: Mo source XRD patterns of LiNiO₂ material synthesised using different Ni:NH₄OH ratios during precursor synthesis (orange: ratio 1:1.2; blue: ratio 1:2.5; green: ratio 1:3.75; red: ratio 1:5). Calculated LiNiO₂ pattern from ICSD (black, collection code 78687 [187]) as comparison. [187]

The refinement of the Mo source XRD powder patterns of LiNiO₂ synthesised via precipitation using different Ni:NH₄OH ratios and its Rietveld refinements, can be seen in Figure 5.21 and Figure 5.22, respectively. The remaining refinement graphs can be found in Figure 10.22 – Figure 10.25 in the appendix and the unit cell values and Ni²⁺ occupancies in Table 5.9 derived from these refinements. The measured patterns do not show any additional peaks,

leading to the assumption that the samples are phase pure. Refined unit cell parameters are close to the ideal values of $c = 14.18 \,\text{Å}$ and $a = 2.88 \,\text{Å}$ for a α -NaFeO₂ lattice with a $R\overline{3}m$ unit cell and do not show huge differences between the analysed samples. The c/a ratios are all showing the transition to a hexagonal distorted lattice from 4.90 to 4.93. Ni²⁺ occupancies on 3a Wyckoff sites in the lattice vary between 1.4 and 1.9%, which is quite low. The quality of the refinements is validated by the standard deviations stated for each unit cell parameter and the low wR and GOF values.

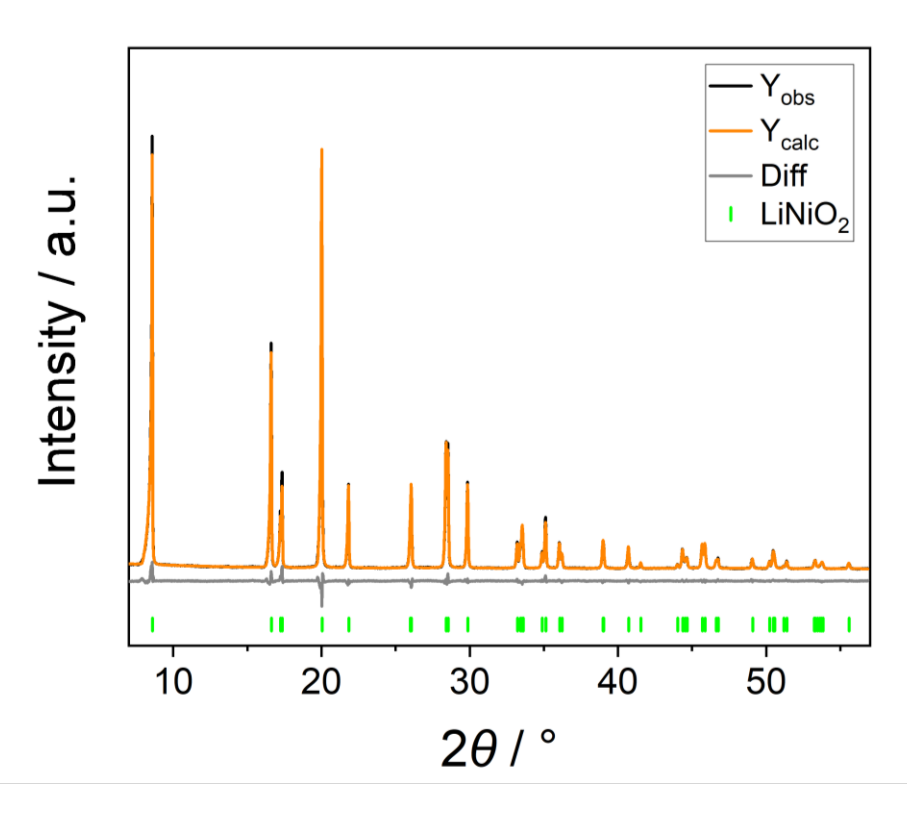


Figure 5.22: Refinement of measured Mo source XRD pattern of LiNiO₂ pre-calcined for 5 h at 350°C and calcined for 15 h at 710°C. Measured pattern (black), calculated pattern of LiNiO₂ (orange, collection code 78687 [187]) and the difference between observed and calculated patterns (grey). Peak positions of LiNiO₂ in green.

Table 5.9: Lattice parameters and Ni occupancy in Li layer (higher resolution Mo source) of annealed as-prepared precursor Ni(OH)₂ at different Ni:NH₄OH ratios. Standard deviation in brackets.

Ni:NH4OH ratio	С	a	<i>c∕a</i> ratio	V	Ni^{2+} on $3a$ site	wR	GOF
	[Å]	[Å]		$[\mathring{\mathbf{A}}^3]$	[%]		
1:1.2	14.1895(1)	2.87523(4)	4.935	101.589(3)	1.7(1)	5.15	3.30
1:2.5	14.1882(2)	2.87581(5)	4.934	101.620(3)	1.9(1)	5.21	1.03
1:3.75	14.1876(2)	2.87526(6)	4.934	101.577(4)	1.8(1)	5.43	1.04
1:5	14.1904(1)	2.87578(4)	4.934	101.635(3)	1.4(1)	5.30	1.17

The as-prepared LiNiO₂ samples were processed further in the glovebox to manufacture electrodes for coin half cells vs. Li metal for electrochemical cycling. Three cells per sample were cycled after a resting period of 2h in a temperature-controlled chamber at 25°C between 3–4.3 V at C/20 for the first two cycles and at C/2 for another 98 cycles. The cycling data was analysed and correlated with the structural and morphological changes of the samples. Further cells were prepared and cycled to specific cut-off voltages, decrimped and the most promising sample examined via more advanced methods like XANES, EXAFS, HAXPES, RIXS and XRD-CT and can be found in Chapter 5.4.

Capacity and capacity retention plots are depicted in Figure 5.23 and Figure 5.24, respectively and dQ/dV plots of all samples in Figure 5.25. The most important cycling values are given in Table 5.10 and the depicted data in the graphs are averaged over the three cycled cells.

Table 5.10: Electrochemical values derived from the cycling data of the as-prepared $LiNiO_2$ using $Ni(OH)_2$ precursor synthesised with different $Ni:NH_4OH$ ratios.

Ni:NH4O H	Discharge Capacity [mAh/g]		Charge Capacity [mAh/g]		Capacity loss	Coulombic efficiency	Discharge Capacity retention		
ratio	1^{st}	2^{nd}	3^{rd}	1^{st}	2^{nd}	3^{rd}	(1st cycle)	(1st cycle)	(100 cycles)
	cycle	cycle	cycle	cycle	cycle	cycle	[mAh/g]	[%]	[%]
1:1.2	247	244	173	252	256	199	5	109	82.2
1:2.5	254	257	168	282	259	204	28	111	85.2
1:3.75	214	216	190	245	218	214	31	115	79.1
1:5	220	218	179	267	223	202	47	82	81.8

The capacity vs. voltage plot in Figure 5.23 shows the first three cycles of the as-prepared samples using precursor materials synthesised at different Ni:NH₄OH ratios of 1:1.2 (orange), 1:2.5 (blue), 1:3.75 (green) and 1:5 (red). Initial charge capacities are 252, 282, 245 and 267 mAh/g and first cycle discharge capacities are 247, 254, 214 and 220 mAh/g with a first cycle capacity loss between charge and discharge of 5, 28, 31 and 47 mAh/g, respectively. Charge capacities exceeding the theoretical capacity of 274 mAh/g for LiNiO₂, like sample 1:2.5, might be due to an increased amount of Li content in the structure or side reactions involving Li-containing surface species like Li₂CO₃. The first cycle capacity loss is, as described earlier, due to the cation disorder in the structure. As Ni²⁺ gets oxidised to Ni³⁺ during cycling, the Li slabs shrink, making it harder for Li to reintercalate back into the host structure.

The capacity loss between first and third cycle is due to kinetic issues, when changing the C-rate from C/20 to C/2. The biggest change between 1st and 3rd cycle can be seen for sample 1:2.5 followed by sample 1:1.2, both samples with the highest initial capacities. Coulombic efficiencies and capacity retention over 100 cycles can be seen in Figure 5.24. First cycle coulombic efficiencies for samples 1:1.2, 1:2.5 and 1:3.75 reveal efficiencies above 100%, which is associated with the additional peaks before the H1/M transition during oxidation and after the H1/M transition during reduction, during the cycles with a slower C-rate. Capacity retention after 100 cycles is 82.2, 85.2, 79.1 and 81.1%, respectively. As the cation disorder in these samples ranges between 0.7 and 2%, no big differences are expected.

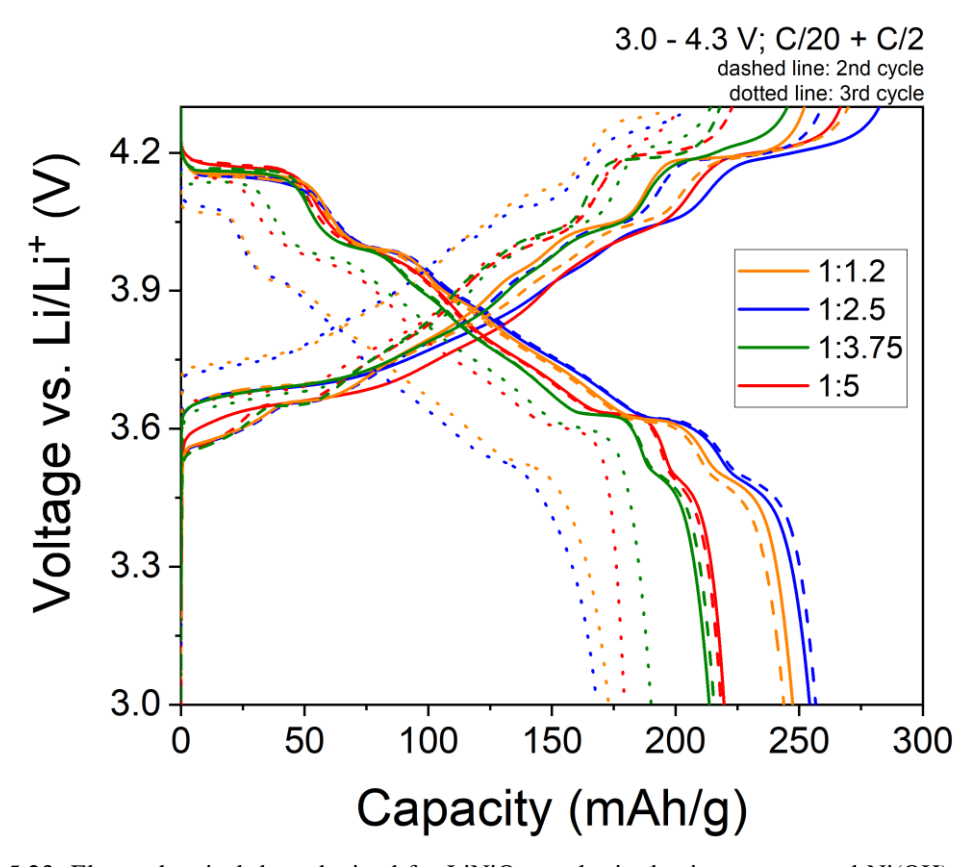


Figure 5.23: Electrochemical data obtained for LiNiO₂ synthesised using as-prepared Ni(OH)₂ precursor with different Ni:NH₄OH ratios. Precursors pre-calcined for 5h at 350° C and calcined for 10h at 710° C. Charge/discharge plot between 3-4.3 V vs. Li/Li⁺ at a rate of C/20 for two cycles and C/2 for the third cycle. Solid line shows 1st cycle, dashed line depicts 2nd cycle and dotted line represents the 3rd cycle. Ni:NH₄OH ratio of 1:1.2 (orange), 1:2.5 (blue), 1:3.75 (green) and 1:5 (red).

The differential capacity plot in Figure 5.25, depicts cycles 2, 3 and 100 for the here investigated samples. All four samples show very similar two-phase transition peaks at similar voltages as well as single phase plateaus in cycle two. The Ni redox processes lead to a phase change from hexagonal to monoclinic H1/M which is seen at around 3.7 V. The M/H2 transition takes place just above 4 V and the H2/H3 transition at 4.2 V. The reduction peaks are all shifted to lower

voltages. The additional peaks before the H1/M transition during oxidation at 3.6 V and after the H1/M transition during reduction at around 3.5 V, are kinetic features and are lost at higher SOC. These features also contribute to the capacity and the increased coulombic efficiency during the first cycles. [45] [192] [84] [72]

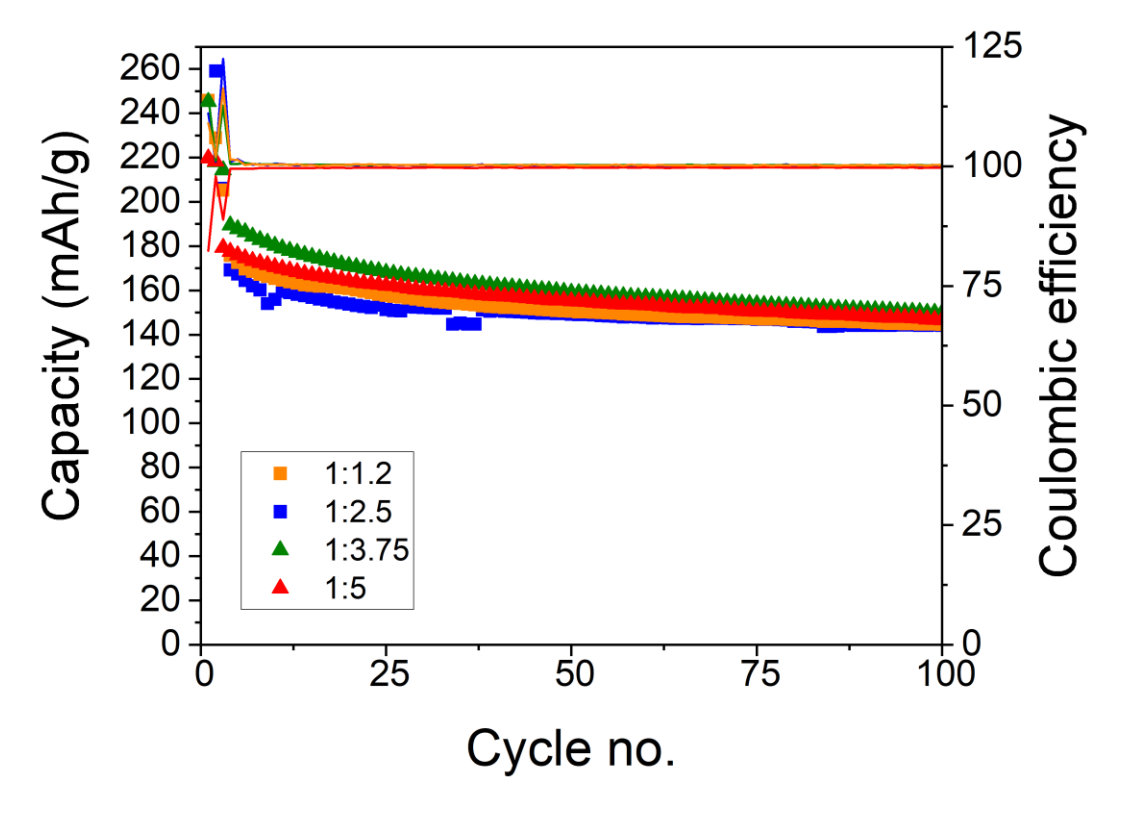


Figure 5.24: Discharge capacity retention and coulombic efficiencies obtained for LiNiO₂ synthesised using as-prepared Ni(OH)₂ precursor with different Ni:NH₄OH ratios. Precursors pre-calcined for 5 h at 350°C and calcined for 10 h at 710°C. Solid line shows 1st cycle, dashed line depicts 2nd cycle and dotted line represents the 3rd cycle. Ni:NH₄OH ratio of 1:1.2 (orange), 1:2.5 (blue), 1:3.75 (green) and 1:5 (red).

During cycling at C/2, the transition peaks shift to higher voltages for oxidation and to even lower voltages during reduction. The H2/H3 transition is outside the potential operating window for both, oxidation and reduction processes at cycle 100. Furthermore, transition peaks become more narrow and less intense during cycling as less Li is reintercalated and capacity is lost. As the samples show very similar morphological and structural features, the dQ/dV plots look very similar. Sample 1:5 (red) stands out, as the M/H2 transition only shows one distinct peak instead of the two peaks identified for the other samples.

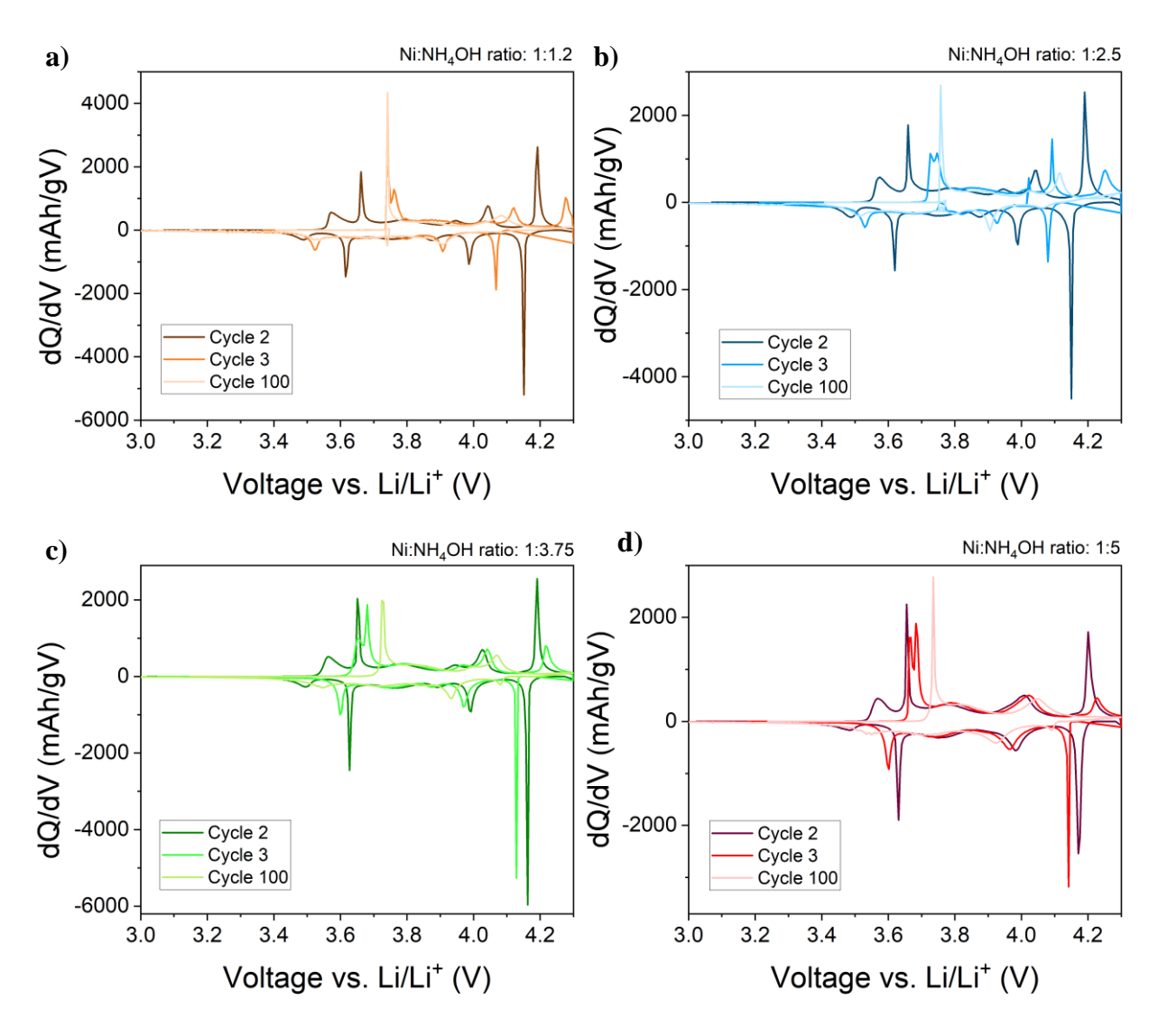


Figure 5.25: Differential capacity plots obtained for LiNiO₂ synthesised using as-prepared Ni(OH)₂ precursor with a Ni:NH₄OH ratio of a) 1:1.2 (orange), b) 1:2.5 (blue), c) 1:3.75 (green) and d) 1:5(red). Precursors were pre-calcined for 5 h at 350°C and calcined for 10 h at 710°C. Potential window between 3 - 4.3 V vs. Li/Li⁺ at a rate of C/20. Comparison between second cycle (after conditioning), third cycle and 100^{th} cycle.

Comparing the as prepared and characterised samples, sample 1:2.5 exhibits the highest initial capacities as well as the best capacity retention over 100 cycles. Yet this sample also has the largest decrease in capacity when charging at a faster rate. This sample is similar to sample 1:3.75 regarding particle size and distribution, BET surface area as well as cation disorder in the structure. Both samples have similar 1st cycle capacity losses. From a visual perspective of the SEM images at lower magnitude, sample 1:3.75 seems more porous and the higher surface area in the BET measurements although having a very similar size to sample 1:2.5 leads to the assumption, that the sample is less dense and thus exhibits the lowest capacity retention over 100 cycles. Taking the cross-section SEM images of the secondary particles into account, this sample shows a larger core of randomly aligned primary particles in comparison to the radially

aligned primary particles facilitating easier and faster Li diffusion, than sample 1:2.5, which supports the assumption of less dense secondary particles in sample 1:3.75. Sample 1:1.2 shows similar good initial capacities as sample 1:2.5 with a comparable tap density. Yet it stands out with the lowest first cycle capacity loss and the lowest cation disorder. Its capacity retention as well as capacity loss due to a faster C-rate are average among these sample. It exhibits the smallest secondary particles, but the highest BET surface area and looking at the cross-section image, mostly randomly aligned primary particles are noticed. Sample 1:5 shows very good cycling behaviour which can be assigned to very dense looking secondary particles, a low BET surface area as well as a small core of randomly aligned primary particles in comparison to the larger area of radially aligned primary particles, and a low amount of cation mixing of 1.4%. These properties improve the Li diffusion pathways for Li from the core and lead to advanced electrochemical behaviour.

To gain more insights in the structure-property relationship of these samples, more advanced techniques are used in the next chapter that might help distinguish the best synthesis method for the optimum morphology of the particles in comparison with its electrochemical properties.

For further investigations and doping of LNO, the Ni(OH)₂ precursor utilising a Ni:NH₄OH ratio of 1:5 is used. At a temperature of 60°C, a pH of 11 and an overall reaction time of 19 h, the precursor is precipitated. This Ni(OH)₂ is then used to form the optimised LNO by calcining it with LiOH H₂O under oxygen for 5 h at 350°C and 12 h for 710°C.

5.4. Advanced Methods of Characterisation of LiNiO₂

5.4.1. Hard XAS

With higher energy X-rays, the Ni K-edge of the bulk of a material can be probed, by exciting the 1s electron and tracking the energy of the released photon during the process. The obtained Ni K-edge spectrum is split into two regions, the near edge XANES and the extended region EXAFS, and gives electronic as well as structural information like the coordination number, the bond length and angles between Ni and neighbouring atoms, respectively. XANES and EXAFS measurements were undertaken by Muhammad Ans, for as-prepared polycrystalline LNO cathodes synthesised with a Ni:NH4OH ratio of 1:5 during precipitation of the precursor, cycled in half-cells to different SOCs like *open-circuit voltage* (OCV), 3.8 V, 4.2 V, 4.5 V, 4.7 V as well as charged to 4.2 V and discharged to 3 V and corresponding graphs can be examined in Figure 5.26 – Figure 5.28.

Figure 5.26 shows the XANES spectra of all examined samples, depicting the pre-edge feature around 8335 eV, the actual edge, and the onset of the extended regions. An additional inlet in the graph magnifies the region at half height of the normalised spectra, which is used to

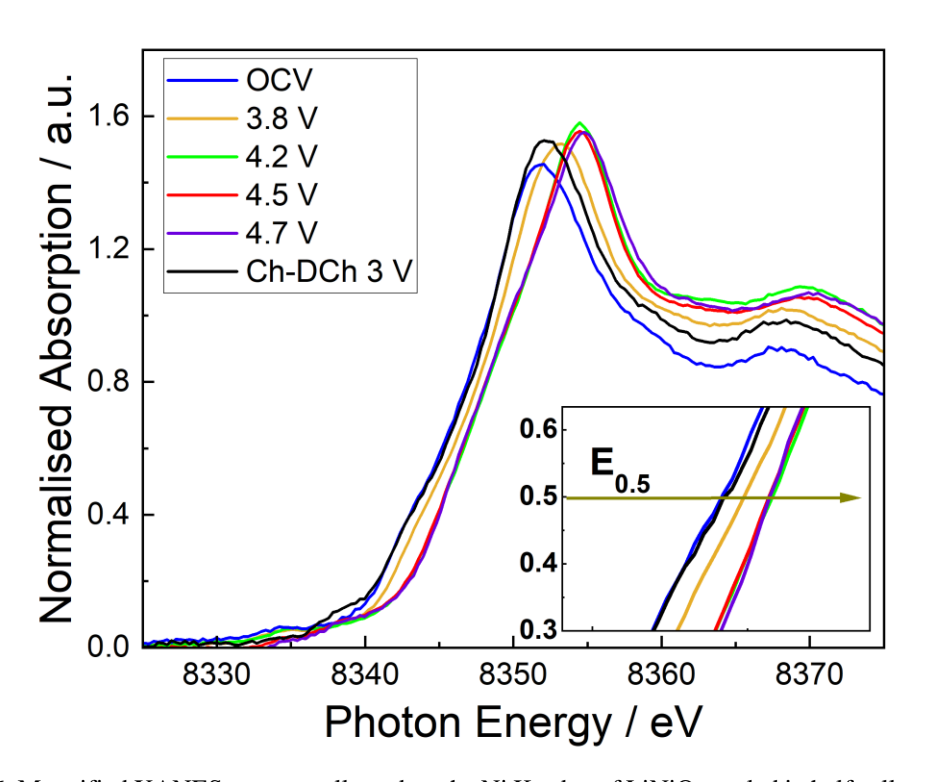


Figure 5.26: Magnified XANES spectra collected on the Ni K-edge of LiNiO₂ cycled in half cells to different states of charge. OCV (blue), $3.8\,V$ (yellow), $4.2\,V$ (green), $4.5\,V$ (red), $4.7\,V$ (purple) and charged to $4.3\,V$ and discharged to $3\,V$ (black). Inset shows a magnified view of the absorption edge at half height (E_{0.5}) of the normalised spectra.

determine the oxidation state in comparison to known samples of pure Ni²⁺ and Ni⁴⁺ oxidation. As there is no known material with only Ni³⁺ oxidation state, the analysis can only be done qualitatively, not quantitatively. For a better overview, these reference samples are not depicted in this graph.

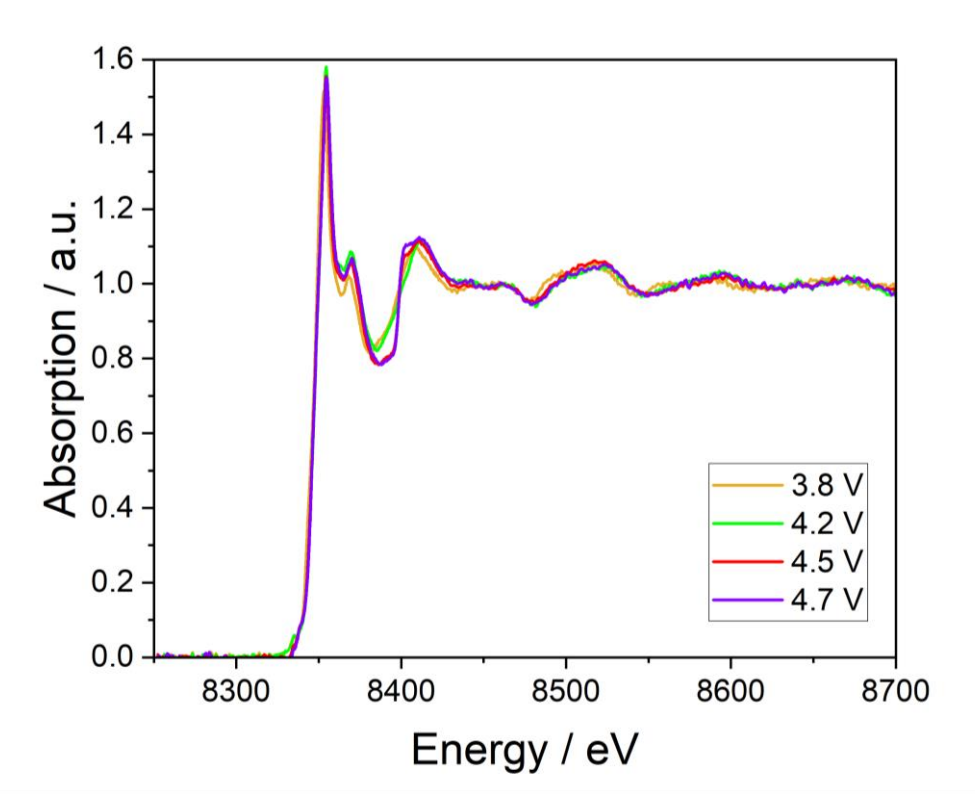


Figure 5.27: Full range of hard XAS spectra collected on the Ni K-edge of LiNiO₂ cycled in half cells to 3.8 V (yellow), 4.2 V (green), 4.5 V (red) and 4.7 V (purple).

The inset clearly shows the starting point of the Ni oxidation state in the OCV cell, which is a mixture of Ni²⁺ and Ni³⁺. Ni then gets oxidised from Ni^{2+/3+} to Ni⁴⁺ with increasing state of charge. The sample charged to 4.3 V and discharged to 3 V, reaches a state close to the OCV sample, indicating that the cathode electronic structure is almost restored to its initial condition. The Li reintercalation is not fully reversible, as expected due to capacity loss during high-voltage cycling. No notable differences can be seen above 4.2 V regarding a change Ni oxidation state, indicating an oxygen participation. Figure 5.27 depicts the full range of the XAS measurements on the Ni K-edge of optimised LiNiO₂ at SOCs of 3.8 V, 4.2 V, 4.5 V and 4.7 V, while Figure 5.28 magnifies the Fourier transformed EXAFS region between 8370 – 8700 eV to access Ni-O and Ni-Ni bond lengths.

The Ni-O bond length decreases with increasing voltages due to the phase transitions taking place. As Ni³⁺ is oxidised to Ni⁴⁺, its ionic radius gets smaller, increasing the covalency between the Ni and the O. Due to a negative charge transfer and the p-d hybridisation during the H2/H3 transition at above 4.1 V between the oxygen 2p and the nickel 3d state, the Ni-O bond length increases slightly when charged up to 4.2 V. The Ni-Ni bond length shows reversed behaviour, it decreases up to 4.5 V as the Li is removed between the Ni layers. With increasing charge, the oxidation state of Ni increases and its ionic size decreases, decreasing the distance between neighbouring Ni sites.

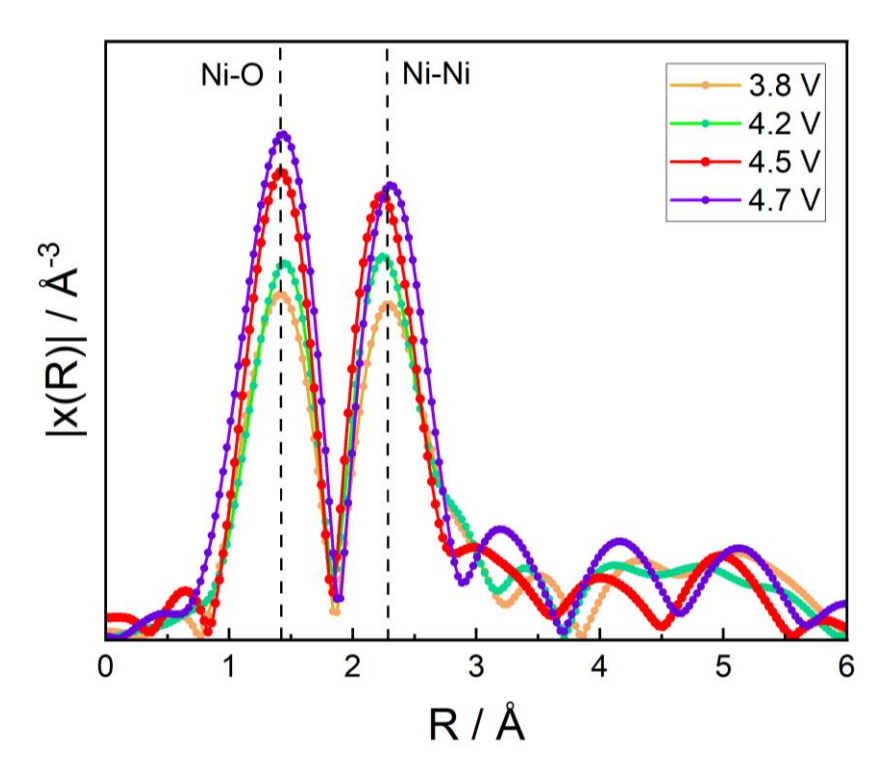


Figure 5.28: Magnified Fourier transformed EXAFS spectra collected on the Ni K-edge of LiNiO $_2$ cycled in half cells to 3.8 V (yellow), 4.2 V (green), 4.5 V (red) and 4.7 V (purple). Dashed lines highlight the Ni-O and Ni-Ni distances.

5.4.2. Soft XAS

Soft XAS is measured using lower energy X-rays to excite electrons of the 2p orbital in the Ni L-edge and the 1s orbital in the oxygen K-edge, to study occupied or unoccupied states close to the Fermi level in a cathode-active material. The oxygen occupied states may be very close to the Fermi level and thus get oxidised unintentionally during deintercalation processes and thus cause safety problems during battery operation. TEY is the surface-sensitive electron yield up to 10 nm depth and can give information about the surface structures present in the material.

The data is normalised using the incident flux of a gold target, calculated from the gold absorption and the measured current of the gold target.

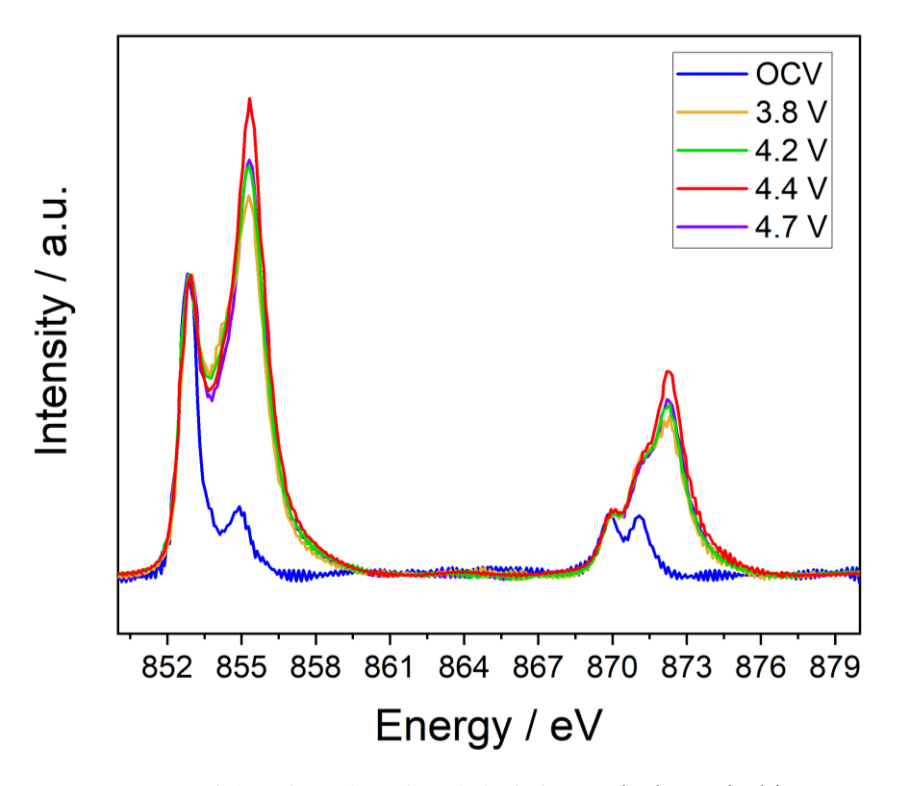


Figure 5.29: sXAS spectra of the Ni L-edge of cycled LiNiO₂ cathodes probed in TEY mode at OCV (blue), 3.8 V (yellow), 4.2 V (green), 4.4 V (red) and 4.7 V (purple). Optimised LNO was used made with a precursor synthesised at a Ni:NH₄OH ratio of 1:5. The cathode contains 90% of LNO, 5% of carbon black and 5% of PVDF.

Half-cells were cycled to certain cut-off voltages of 3.8 V, 4.2 V, 4.4 V and 4.7 V as well as OCV, decrimped and the cathodes used for sXAS measurements at the I09 beamline at Diamond, UK by Muhammad Ans. The corresponding electrochemical data of these cells is shown in Figure 10.26 in the appendix. TEY mode was used to probe the Ni L-edge and O K-edge and the resulting data is shown in Figure 5.29 and Figure 5.30. During electrochemical cycling of a battery, SEI layers are formed at the surface of the cathode-active material as the electrolyte reacts with the cathode surface. These SEI layers can be examined using sXAS TEY measurements. The Ni L₃-edge consists of 3 different electronic contributions of the Ni in different oxidation states, with Ni²⁺ peaks at around 852.5 and 854 eV, Ni³⁺ peaks between 853 – 855 eV and Ni⁴⁺ exhibits its most pronounced peak at 855 eV. The L₂-edge on the other hand, shows two Ni²⁺ peaks at around 869 eV, a pronounced Ni³⁺ peak at 870 eV and a Ni⁴⁺ peak at 871 eV, derived from calculated spectra measured in a octahedral crystal field. [198] Figure 5.29 depicts the Ni L-edge at different SOCs with peaks at 853 eV and 854.9 eV for OCV and 855.3 eV for the charged samples as well as 870 and 871 eV for the OCV sample

and 871 and 872.3 eV for the charged materials. The 853 eV peak corresponds to Ni²⁺ in the system and stays constant during charging for all the samples. This suggests that the Ni²⁺ which is located in the Li layer, does not oxidise. Ni³⁺ is represented in peaks between 853 and 855 eV but also Ni⁴⁺ presents its most pronounced peak at 855 eV. This peak increases in intensity with SOC up to 4.4 V and decreases again above. Similar behaviour is seen for the higher energy region of the L₂-edge. The small peak at 869.5 eV corresponds to Ni²⁺ again and does not change much during cycling for any of the samples. For the OCV sample, another peak at 871 eV is visible, showing Ni³⁺ in the system. This peak merges with the peak at 872 eV for cycled samples, as the amount of Ni⁴⁺ increases during charging. Again, the intensity increases up to a SOC of 4.4 V and then decreases again above this voltage suggesting oxygen loss at those high voltages.

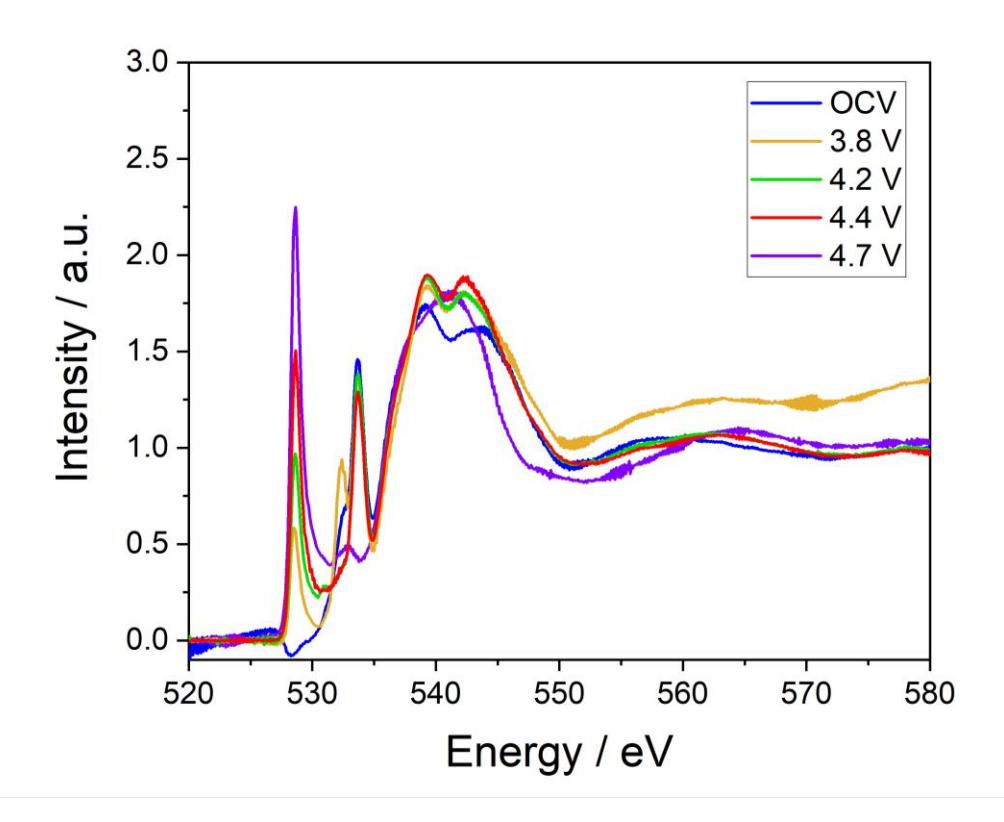


Figure 5.30: sXAS spectra of the O K-edge of cycled $LiNiO_2$ cathodes probed in TEY mode at OCV (blue), 3.8 V (yellow), 4.2 V (green), 4.4 V (red) and 4.7 V (purple). Optimised LNO was used made with a precursor synthesised at a Ni:NH₄OH ratio of 1:5. The cathode contains 90% of LNO, 5% of carbon black and 5% of PVDF

Additionally, the O K-edge is examined, showing a pre-edge feature between $528 - 534 \,\text{eV}$, originating due to the hybridisation states of localized TM - 3d and O - 2p bands and its intensity is correlated to the oxidation state of the transition metal. [199] A peak at $531 \,\text{eV}$ is found to be due to the formation of NiO and the peak at $534 \,\text{eV}$ due to oxygen species like Li_2O_2 or O_2 , but for layered oxide materials, the pre-peak feature overlaps with the oxygen redox feature and the

exact oxygen species and its contribution to the peaks cannot be determined with certainty only using sXAS measurements. The broad peak region after 534 eV depicts the TM - 4s,p and O 2p hybridisation. [200] Figure 5.30 depicts the O K-edge of the samples at OCV and in charged states. All charged samples show a peak at 528 eV, which is associated with the TM 3d – O 2p hybridisation and increases with increased charge. The pre-peak at 533.7 eV depicts the Li₂CO₃ phase at the surface and decreases with increasing charge. The broad peak feature exhibits peaks at 539 and 542 eV for all samples except the purple sample. This sample, charged up to 4.7 V, depicts only one broad peak at 540.8 eV. The lineshape changes with higher charge, is more likely to be due to the TM oxidation state than due to oxygen redox happening. Pre-peak and broad-peak features increase in intensity with increased state of charge up until 4.4 V and decreases again above.

The cycled LNO samples show a mixture of Ni²⁺ and Ni³⁺ in the pristine state, with Ni²⁺ located in the Li layer, as the corresponding peak does not change in intensity during charging to high voltages suggesting no contribution in the redox behaviour. Ni³⁺ although is oxidised to Ni⁴⁺ as expected. The amount of Ni⁴⁺ in the cycled samples reaches its maximum at 4.4 V. Taking both, the Ni and O edge into account, the amount of O species and Ni⁴⁺ decreases above 4.4 V, suggesting the transition of the surface layers into a rock salt structure. A decrease in intensity of the pre-peak region, associated with the 3d-states, in relation to the broad peak region, associated with the 4s,p-band, is seen as a decrease in unoccupied 3d-states of the TM available to mix with the O 2p states. [200] In our case, the pre-peak region increases in intensity with higher charge up until 4.4 V and then decreases when charged to 4.7 V. This suggests oxygen loss above 4.4 V and reduced Ni participation. The corresponding increase in the O K-edge pre-peak shows increased Ni-O rehybridisation which is also in accordance with the bond lengths changes derived from EXAFS measurements.

5.4.3. HAXPES

Using hard X-ray Photoelectron Spectroscopy, the chemical composition of the surface of a material can be determined. Especially for battery cathode material, the formation of a surface layer during cycling due to reactions between the electrolyte and the cathode active material can be examined and determined as well as any possible oxygen redox happening. Figure 5.31 and Figure 5.32 depict the carbon, oxygen and nickel 1s and 3p electronic state, respectively, at different states of charge.

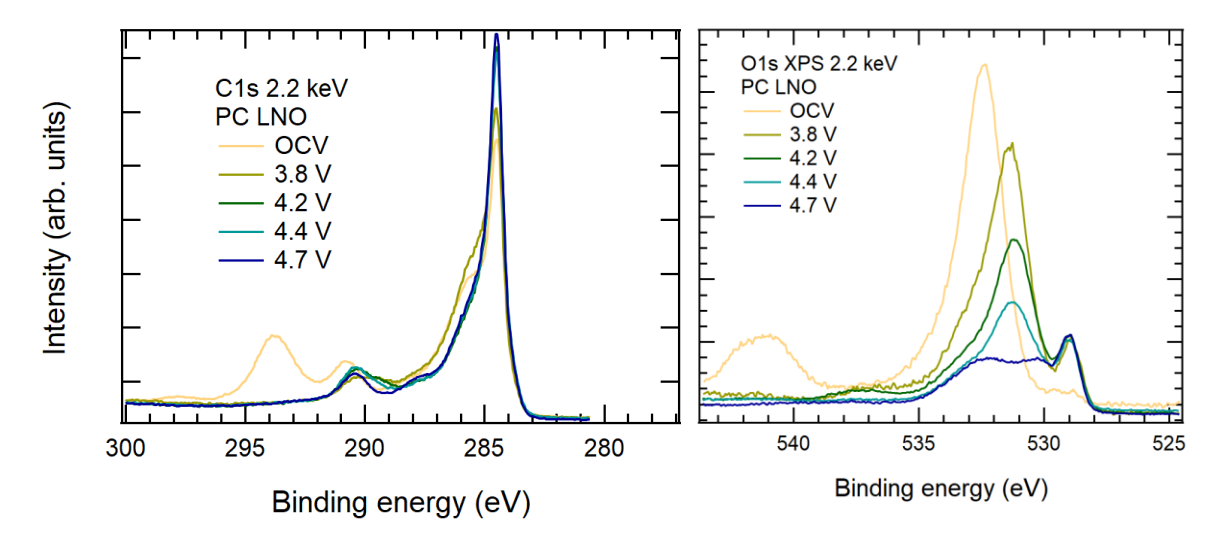


Figure 5.31: HAXPES data from the C 1s (left) and O 1s (right) regions of cycled LNO electrodes using an incident X-ray energy of 2.2 keV. OCV data is shown in yellow, 3.8 V in light green, 4.2 V in dark green, 4.4 V in light blue and 4.7 V in dark blue.

These in-situ measurements of decrimped, cycled, optimised LNO cathodes at OCV, 3.8 V, 4.2 V, 4.4 V and 4.7 V were collected at the I09 beamline at Diamond by Ashok Menon and the graphs prepared by WMG. The corresponding electrochemical data of these cells is shown in

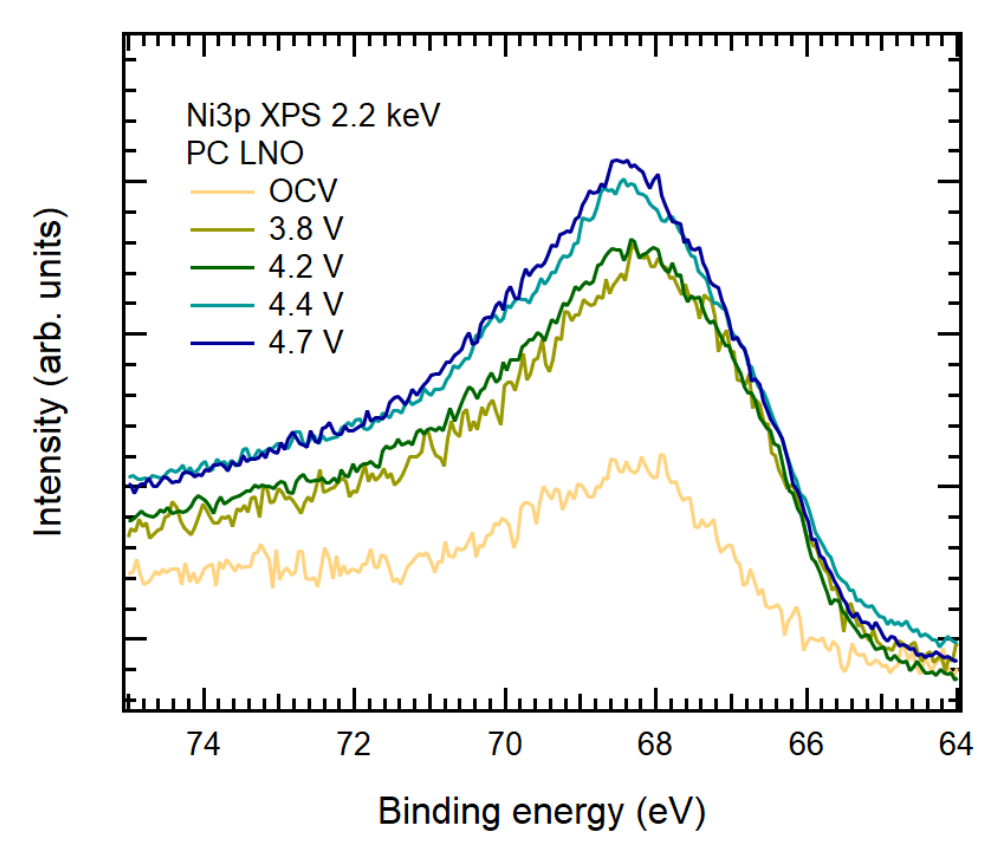


Figure 5.32: HAXPES data from the Ni 3p region of cycled LNO electrodes using an incident X-ray energy of 2.2 keV. OCV data is shown in yellow, 3.8 V in light green, 4.2 V in dark green, 4.4 V in light blue and 4.7 V in dark blue.

Figure 10.27 in the appendix. The determined spectra of carbon and oxygen show an additional peak at lower binding energy at 293 and 541 eV for OCV in Figure 5.31, respectively. These peaks disappear when the cells are charged, like the oxygen K-edge in the sXAS measurements, where the amount of side phase decreases with increasing charge.

An intensity comparison for peaks at higher binding energies with the peak at 529 eV for oxygen, shows a high intensity for superficial species on the surface. With a thicker CEI, the Ni oxidation shown in Figure 5.32 exhibits a lower intensity, yet the oxidation during charging can clearly be distinguished and is in accordance with soft and hard XAS measurements.

5.4.4. Magnetometry

The magnetic properties of LiNiO₂ are dependent on its stoichiometry and ordering, so Ni²⁺ in the Li layer plays a crucial role. In an ideal stoichiometrically ordered crystal lattice of LiNiO₂, the magnetic Ni layers, containing Ni³⁺ ions in a low spin trivalent state $t_{2g}^{6}e_{g}^{1}$ with spin = 1/2, are separated by 3 non-magnetic layers (O-Li-O) with a Ni-Ni distance of 4.37 Å. This leads only to 2D in-plane interactions between Ni (Ni-Ni distance 2.88 Å). With an increasing amount of Ni²⁺ in the Li layer in non-stoichiometric samples, the NiO₂ slabs are strongly coupled. The additional Ni²⁺ in the interslabs interacts with the Ni³⁺ in the slabs, introducing local ferromagnetic interactions as the Curie-Weiss linearity gets lost. The Weiss constant is the temperature onset where the molecular field in the material aligns with the external field, which causes ferromagnetic intraplane interactions between neighbouring Ni layers and can be used as a measure of the cation disorder in the LNO system [70] [201] [202] [177].

Measured magnetic susceptibility curves were used to derive the magnetic moments μ_{eff} and the Curie-Weiss temperature θ_{CW} for all lithiated samples using Ni(OH)₂ precursor produced with different Ni:NH₄OH ratios in the STR. A Curie-Weiss fit could be applied to the data between 100 and 300 K as can be seen in Figure 5.33. The graph is showing linear behaviour for all samples, which is indicative for paramagnetism, the alignment of the internal magnetic fields with the external applied magnetic field. Additionally, a positive Weiss constant can be obtained from these fits, suggesting net ferromagnetic interactions in the materials.

Figure 5.34 depicts the ZFC and FC magnetic susceptibility curves for all four examined samples and reveals several phase transitions. Below 100 K, a ferromagnetic ordering is detected in the material, as the NiO₂ slabs couple ferromagnetically via bridging Ni²⁺ ions present in the Li layers, resulting in an increase in susceptibility. This can be seen for all the

samples with similar slopes for samples 1:1.2, 1:2.5 and 1:3.75. Sample 1:5 shows an increased slope and the susceptibility curves exhibits a cusp in the ZFC data at low temperatures, which is referred to as antiferromagnetic / ferrimagnetic ordering onset [70] [202] [203] [204].

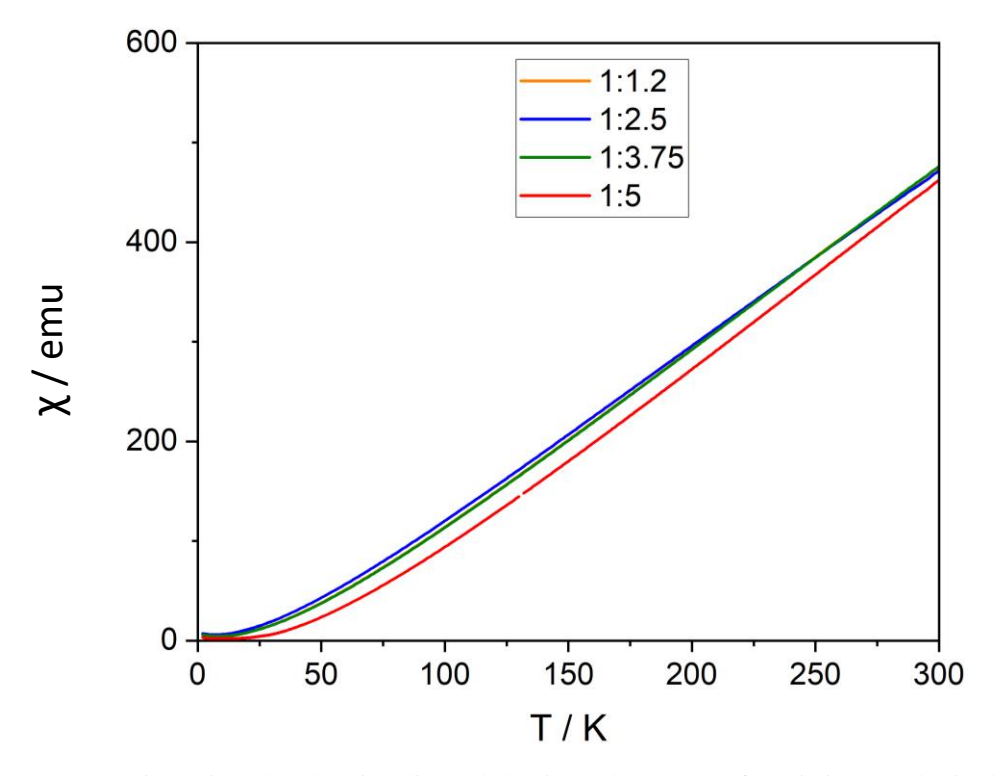


Figure 5.33: Curie-Weiss plot showing linear behaviour above $50\,\mathrm{K}$ for LiNiO₂ synthesised with different Ni:NH₄OH ratios during the precursor synthesis.

The temperature of this magnetic transition in the ZFC measurements is also used as a measure of cation disorder, the amount of Ni^{2+} in the structure. The more Ni^{2+} in the Li layers, the higher the transition temperature T_N between antiferromagnetic / ferrimagnetic and ferromagnetic ordering [45] [202] [177]. Additionally, with increasing Ni^{2+} in the Li layers, the local magnetic coupling increases between the layers, disabling long range antiferromagnetic ordering [177] [205]. The peak maximum for this transition is shifted to higher temperatures in accordance with a higher cation mixing for the investigated samples.

 Ni^{3+} is mostly present in trigonal distorted octahedral surroundings in this structure. Due to the $t_{2g}{}^6e_g{}^1$ configuration, a local Jahn-Teller distortion is induced. Parasitic Ni^{2+} in the Li layers with a spin S=1 ($t_{2g}{}^6e_g{}^2$) prevents a long-range JT distortion. Competitive interactions between the ferromagnetic coupling of Ni^{3+} - Li^+ - Ni^{3+} and antiferromagnetic/ferrimagnetic coupling of Ni^{3+} - Ni^{2+} - Ni^{3+} prevent long range magnetic ordering [202] [204] [206]. Thus, the magnetic moment μ_{eff} is expected to increase with an increasing amount of Ni^{3+} or a decreasing amount of Ni^{2+} in the compound.

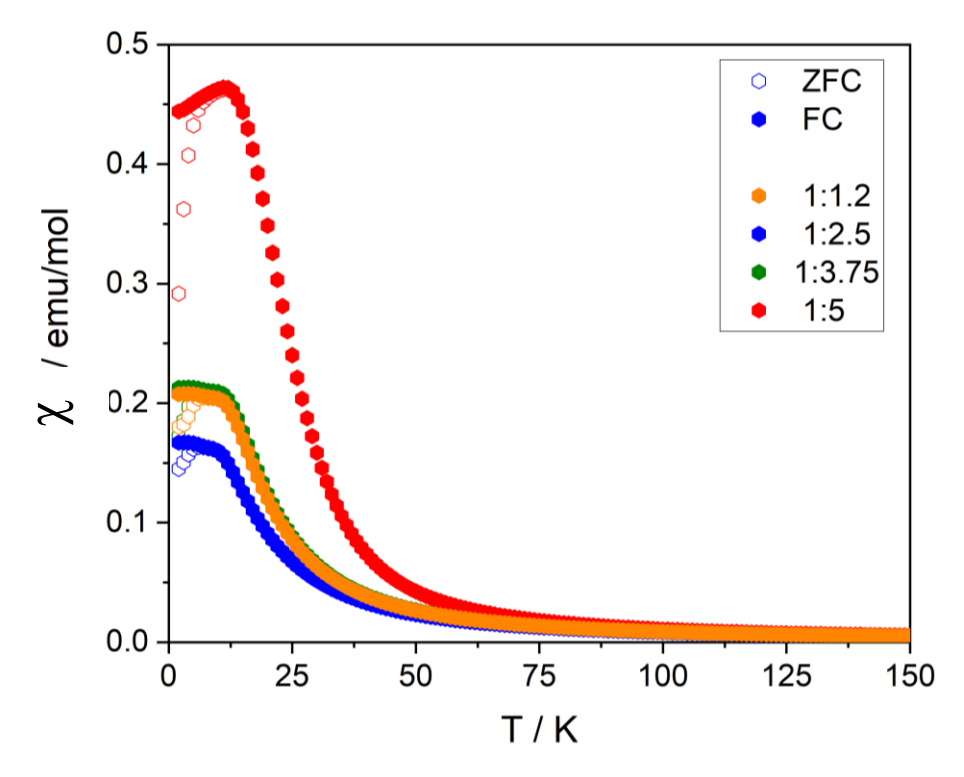


Figure 5.34: Susceptibility curve for LiNiO₂ synthesised with different Ni:NH₄OH ratios during the precursor synthesis.

Table 5.11: Magnetic moments and constants obtained from SQUID measurements of LiNiO₂ synthesised with different Ni:NH₄OH ratios during the precursor synthesis. Ni²⁺ occupancy in Li layer from Rietveld refinements of Mo XRD patterns included.

Ni:NH4O H ratio	Ni^{2+} on $3a$ site	Weiss constant	Curie constant	T_{N}	$\mu_{ ext{eff}}$
	[%]	[A]		[K]	
1:1.2	1.7(1)	40.2	0.55	7	10.41
1:2.5	1.9(1)	32.69	0.57	6	7.06
1:3.75	1.8(1)	41.19	0.54	7	8.86
1:5	1.4(1)	55.50	0.53	11	8.79

The magnetic moments μ_{eff} , the Weiss constants θ_{CW} and Curie constants C derived from both graphs, are given in Table 5.11 for the examined samples and compared to the Ni²⁺ occupancies derived from refinements of Mo source X-ray diffraction.

The Weiss constant θ_{CW} is overall increasing with increasing amount of cation disorder in the system. The higher θ_{CW} , the higher the magnetic moments μ_{eff} [201] [206], which both are measures for the ferromagnetic local coupling that is supposed to interfere with the low temperature antiferromagnetic interlayer coupling and the paramagnetic behaviour at higher temperatures. The Curie Constant C is used to calculate the magnetic moment per ion as it is related directly to the number of unpaired electrons.

For a very low Ni^{2+} occupancy in the Li layer, these values differ a bit and are not following the expected trend. In the sample utilising a Ni:NH₄OH ratio of 1:2.5, the cation mixing is equal to the sample with a Ni:NH₄OH ratio of 1:3.75 but its Weiss constant, Curie Constant, T_N and μ_{eff} are slightly off the trend. Whereas the samples using a Ni:NH₄OH ratio of 1:1.2 and 1:3.75 have very similar magnetic values, although the Ni²⁺ occupancy is increased by 0.1% in the first sample compared to the later one.

Ni³⁺ with a spin of ½ obtains a calculated magnetic moment of $1.732\,\mu_B$ according to Equation 3.16. In these experiments, the obtained magnetism values are higher than the calculated magnetic moment for Ni³⁺. They are decreasing with increasing amount of Ni²⁺ in the Li layer, which is counterintuitive. So far, this can be only assigned to either the very low amount of Ni²⁺ in the Li layer or additional cation mixing in the layers with Li in the Ni layers or additional Ni²⁺ in the Ni layers. This can be further evaluated using neutron diffraction data from a synchrotron source, where the Li in the structure can be evaluated and added into refinements.

5.4.5. Muon Spin Relaxation Spectroscopy

A powder sample of the as-prepared optimised LNO as well as *operando* half cells composed of a Li anode and a LiNiO₂ cathode were examined using muon spin relaxation spectroscopy at the EMU beamline at ISIS, Didcot, UK. The cells were prepared using a thick electrode with a 90% mass loading to improve the number of muons implanted in the active material during operando measurements.

Figure 5.35 shows the raw data of the powder sample at 300 K. To isolate the contributions of the Li⁺ movement, the 3 datasets measured at ZF, LF of 5 and 10 Gauss were fitted simultaneously using a dynamic Gaussian Kubo-Toyabe function (Equation 3.16). The fits are shown as solid lines in the graph. The muon spins are depolarised rapidly by internal fields of electronic and nuclear origin as well as fluctuating fields of any paramagnetic ions present, following a Kubo-Toyabe type relaxation. The relaxation is decreasing with increasing applied field as the muon spins are gradually decoupling from the influence of the static nuclei. With increasing field strength of the longitudinal field (parallel to the initial muon spin direction), the nuclear field distribution is quenched by the field, leading to a decoupling of the electronic from the nuclear contribution.

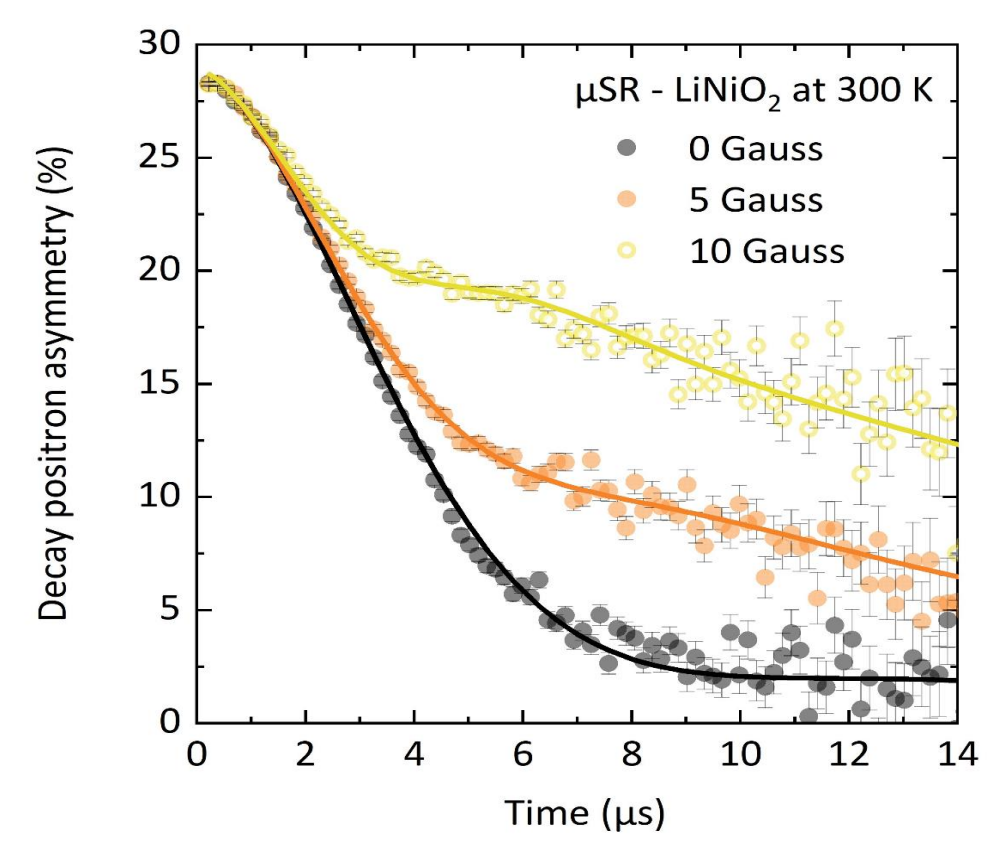


Figure 5.35: Decay positron asymmetry obtained from μ SR measurements at 300 K for a powder sample of LiNiO₂ synthesised using a precursor with a Ni:NH₄OH rate of 1:5. Data from zero field (black), applied longitudinal fields at 5 Gauss (orange) and 10 Gauss (yellow) and corresponding fits using a dynamic Kubo-Toyabe function. Plot by Innes McClelland.

The fitting of the measurements taken every $20\,\mathrm{K}$ between $100-400\,\mathrm{K}$, was done according to (Equation 3.17), with a fixed averaged background (accounts for the muon fraction stopping in the titanium sample holder) and relaxation asymmetry and a fixed relaxation rate λ obtained from the $300\,\mathrm{K}$ measurement. The static field distribution Δ and the fluctuation rate ν are plotted against the temperature to gain insights into the temperature dependency of the Li movement and its magnetic contributions (Figure 5.36). The temperature dependency of the static field distributions at the muon stopping site Δ in blue gradually decreases as expected. This is attributed to a motional narrowing effect (similarly observed in NMR measurements) as a result of more rapid lithium diffusion as the temperature increases. This reduces the local nuclear field experienced by the muon at its stopping site. The temperature dependency of the fluctuation rate ν although shows initially a flat region as the ionic motion is too slow to observe. As the temperature increases, the fluctuation rate increases as well, as the thermally activated Li^+ diffusion processes overcome the energetic barriers and are set in motion. The origin of the peak at around $200\,\mathrm{K}$ is unknown and subject to further investigations in this material as well as doped LNO and similar layered oxide materials.

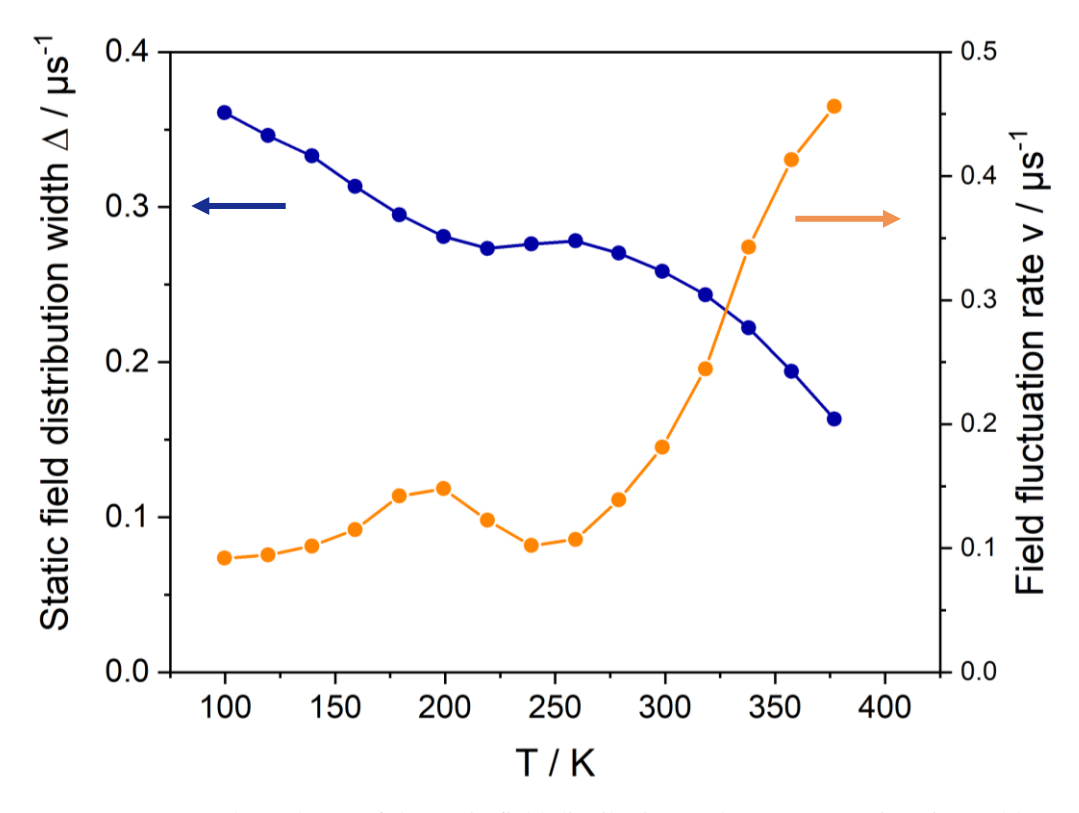


Figure 5.36: Temperature dependency of the static field distribution at the muon stopping site Δ (blue) and the fluctuation rate ν (orange) for μSR data collected for a powder sample of LiNiO₂ synthesised using a precursor with a Ni:NH₄OH rate of 1:5.

The electrochemical cycling behaviour of the 1^{st} cycle charge and discharge, the zero field data of muon relaxation as well as the static field distribution and the field fluctuation rate during the 1^{st} cycle of the operando cell is shown in Figure 5.38 – Figure 5.39. The cell was cycled between $2.5-4.4\,\mathrm{V}$ and shows the expected electrochemical behaviour in the charge/discharge curves with an initial discharge capacity of $208\,\mathrm{mAh/g}$ as well as the dQ/dV plot including the known phase transitions taking place in the active cathode material LiNiO₂ in Figure 5.38.

The zero field raw data of the cycled operando cell in Figure 5.37 depicts the decay positron asymmetry as a function of time and de-/relithiation of the active cathode material during $1^{\rm st}$ cycle charge and discharge, respectively. The largest change in relaxation rate can be seen between $20-40\,\%$ state of charge. The obtained raw data from the operando cell was fitted with a flat background and a dynamic Kubo-Toyabe function to gain insights into the nuclear field experienced by the muon as well as the Li hopping rate during $1^{\rm st}$ cycle charge and discharge and is depicted in Figure 5.38 – Figure 5.39. There is a clear correlation between the μ SR data and the electrochemistry of the cell. The static field distribution Δ curve in Figure 5.38 correlates strongly with the phase transitions appearing during delithiation of the material.

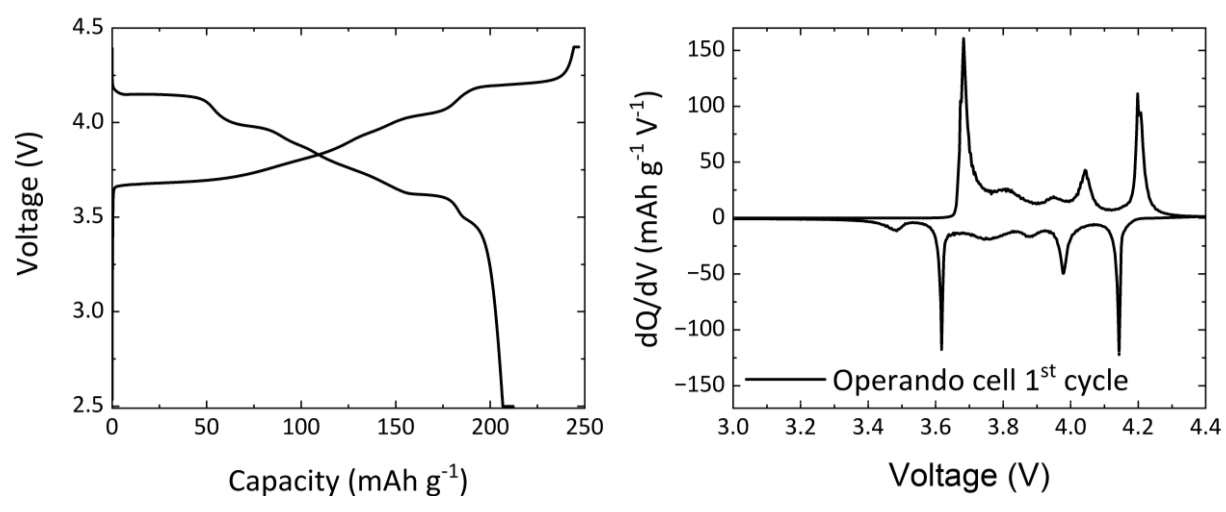


Figure 5.38: 1st cycle charge/discharge curve (left) and dQ/dV plot (right) of muon operando cell with Li anode and LiNiO₂ cathode. Plot by Innes McClelland.

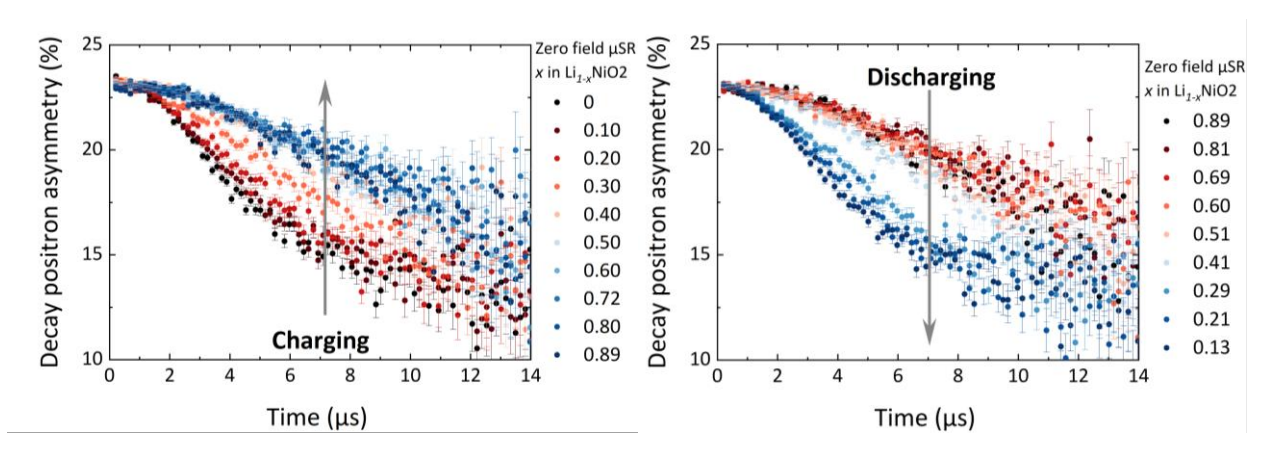


Figure 5.37: Muon relaxation rates during operando μSR measurements of LiNiO₂ cell during 1st cycle charge (left) and discharge (right). Plot by Innes McClelland.

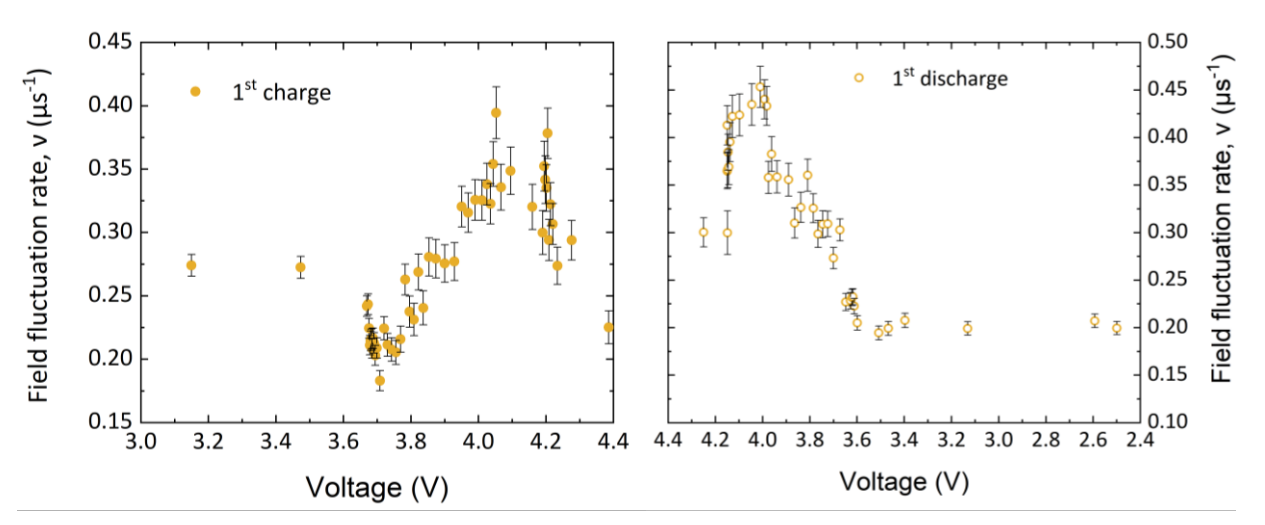


Figure 5.39: Field fluctuation rate ν of 1st cycle charge (left) and discharge (right) during operando μSR measurements of LiNiO₂ cell. Plot by Innes McClelland.

During charge, Δ drops during the H1/M transition, which is also in accordance with the change in muon relaxation between $20-40\,\%$ state of charge in Figure 5.37. Another peak is seen at around 4.0 V, which can be assigned to the M/H2 transition. During discharge, the behaviour of the data is reversed, as are the phase transitions. The Li hopping, described by the field fluctuation rate nu also evolves according to the phase transitions. Figure 5.39 shows a no change during the transition of H1/M but increases rapidly during the M/H2 transition and decreases again above 4.0 V when the H2/H3 transition takes place accompanied by a significant reduction in lattice parameters. These trends are again reversible during discharge.

5.4.6. in-situ XRD-CT

Coin cells of optimised LiNiO₂ were prepared and cycled to different cut-off voltages of 3.8 V, 4.2 V, 4.4 V and 4.7 V as well as OCV and long-term cycled for 100 cycles between 3 – 4.2 V. The cells were decrimped and the cathodes cut into slices and stacked for XRD-CT imaging at a synchrotron facility. A zigzag scan method was used to scan through the cathode slices and for each scanned row, the beam intensity as well as the zigzag offset corrected. A sinogram was created for each sample and reconstructed into 3D volumetric images using a filtered back projection algorithm.

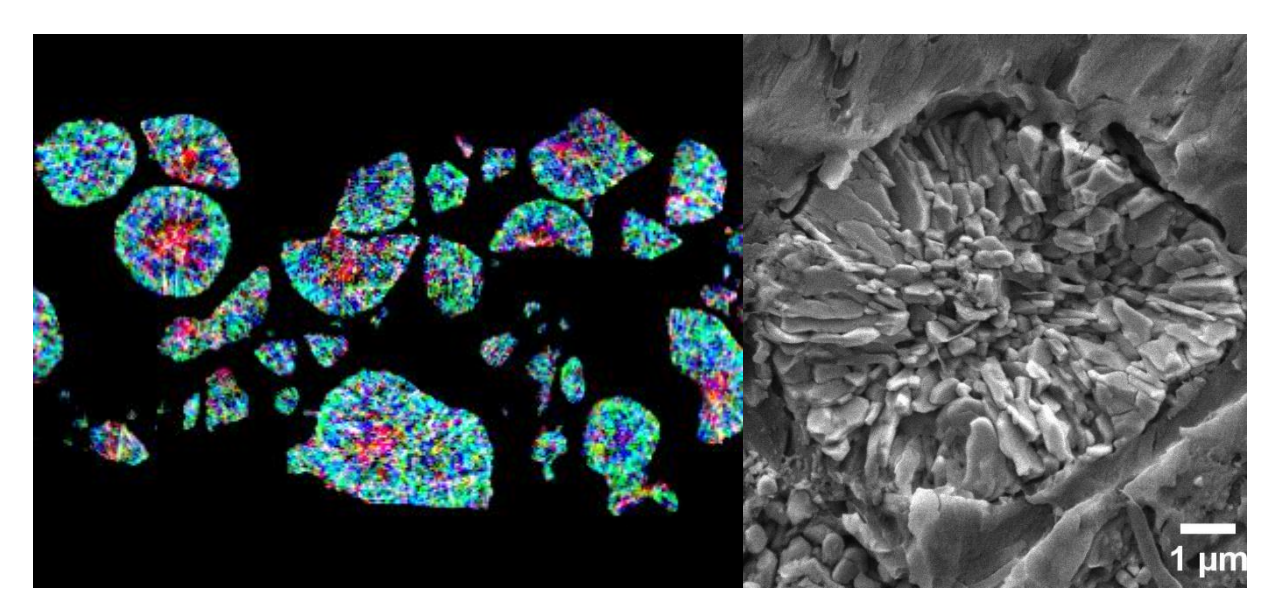


Figure 5.40: Crystallite alignment from XRD-CT corrected and reconstructed 3D volumetric images. Bragg reflections (003) in red, (101) in green and (104) in dark blue. Image by Finden Ltd (left). Secondary pristine $LiNiO_2$ particle cross-section SEM (right).

The 3D images of active cathode particles in the cycled cathode (example in Figure 5.40 left) show how the core behaves differently from the shell in LiNiO₂ particles. The images were

inspected by a voxel-to-voxel basis, revealing large differences in peak intensities associated with LiNiO₂. Whereas in the core, the particles are randomly aligned according to SEM images and the (003) reflection is seen very strongly but the (101) and (104) reflections rather weak, the shell shows radially aligned particles with a lack of (003) reflection but stronger (101) and (104) reflections. The lack of several reflections in the primary particles gives insights in how the crystallites are oriented and thus can shed light on the Li pathways in the structure which is in accordance with SEM cross-sections of the pristine LNO secondary particle (Figure 5.40 right). Here, the core of the secondary particle consists of randomly aligned primary particles and a shell of radially aligned particles. In comparison to regular bulk powder diffraction, the incident X-ray beam size is larger than the crystallite size, so a large number of crystallites randomly aligned are covered by the beam, whereas for nanosized XRD-CT, the beam and the crystallites are of similar size and the orientation of the grains has more influence on the measured local diffraction patterns. Viewed along the c-axis, the (003) reflection is most intense, while in a diffraction pattern recorded along the a- or b-axis, the (003) peak is parallel to the direction of view and thus not visible as can be seen in Figure 5.41.

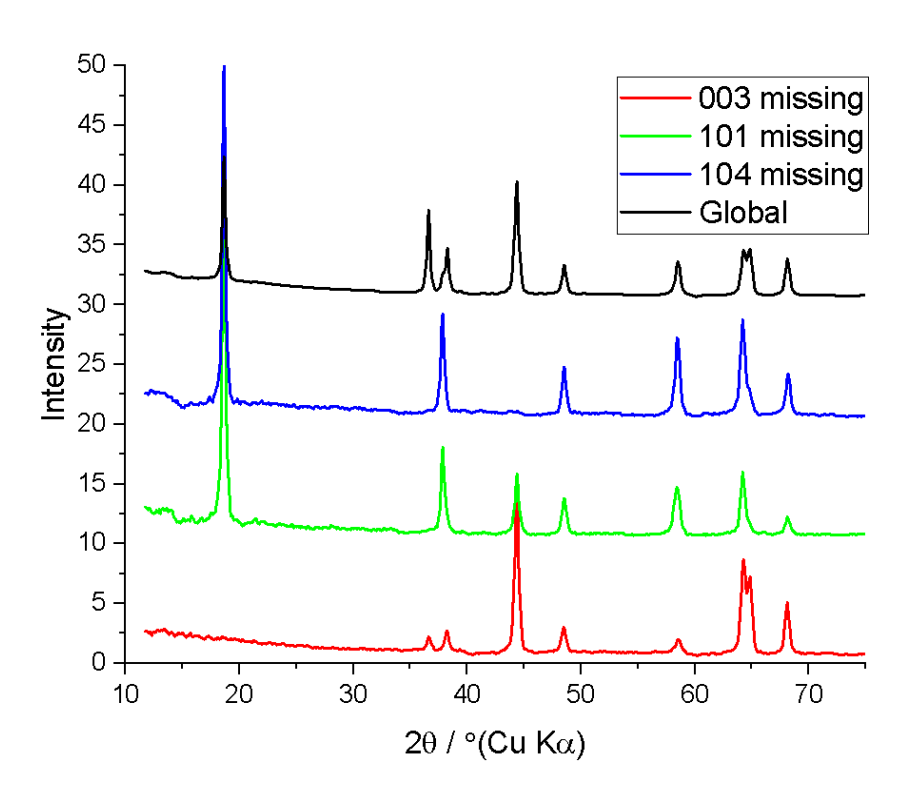


Figure 5.41: Comparison of global XRD patterns of LiNiO2 (black) and local XRD patterns (red, green and dark blue) showing localised differences in peak intensities. Graph by Finden Ltd.

As the Li diffuses along the grains and as the volume changes during cycling, the *c*-axis contraction is happening radially as well, weakening the intergranular contact, and making it easier for fractures to happen between the primary grains. This weakened radial intergrain contact links with (higher) impedance and mechanical testing data (decreased mechanical strength) for NMC811 data and for LNO as well due to their very similar structural properties. Li may diffuse easily along the grain boundaries in the radially aligned primary particle section, but the diffusion speed will be hindered in the core, when randomly aligned primary particles may face the Li pathways perpendicularly. Due to time restrictions, these additional examinations could not be performed in this work.

5.5. Summary and Conclusion

To optimise the precipitation reaction of Ni(OH)₂ for the cathode active material LiNiO₂, the overall reaction time, the reaction temperature, the pH and the TM:NH₄OH ratio was evaluated by visual inspection of SEM images, particle size distribution via laser diffraction, phase purity via XRD and finally for the TM:NH₄OH ratio samples, the evaluation of the electrochemical behaviour via GPLC, as well as some advanced methods like magnetometry.

Altering the reaction time leads to changes in secondary particle size and morphology as it allows more time for particle growth the longer the precipitate dwells in the mother liquid [93], 9 h dwelling time gave the most uniform distribution of quasispherical secondary particles and is industrially feasible. Changes in reaction temperature lead to changes in primary and secondary particle sizes. In accordance with other reports, the secondary particle size decreases with increasing reaction temperature while the primary particle size increased with increasing reaction temperature. [91] [92] The last device-controlled parameter to be investigated, is the pH. It is suggested to increase the pH with increasing Ni content as the particle growth depends on TM as well as pH at the same time. [94] [100] [197] In this study, a pH above 11 was hard to maintain throughout the synthesis and no spherical particle growth took place. A lower pH below 11 produced agglomerations of secondary particles with nicely defined primary particles, yet a pH of 11 yielded more spherical secondary particles with a reasonable particle size of around 5 µm.

The only variable that is not equipment related, is the TM:NH₄OH ratio used for this reaction. This ratio determines the supersaturation of Ni in the solution and determines the particle nucleation, its growth and Ostwald ripening. With higher TM:NH₄OH ratio, the particle size

and sphericity of the secondary particles of the Ni(OH)₂ precursor increases as well as the tap density. The core of the secondary particles shows randomly aligned primary particles and radially growths from there towards to outside. These samples are annealed using the optimised conditions from Chapter 4 and further investigated regarding their structural, physical, and electrochemical properties.

The annealed samples show the same trend for particle size as the precursors. The particles grow with increased Ni:NH4OH ratio. The cross-section SEMs keep the morphology of randomly aligned primary particles in the core and towards the surface radially aligned primary particles, although the primary particles change from needle-like in the precursor, to a cuboid shape in the annealed material. The trend for tapped density cannot be confirmed, sample 1:375 has an increased tap density. Yet this sample also has an increased surface area according to BET analysis whereas the other samples' surface area decreases with increasing particle size and thus Ni:NH₄OH ratio. According to the cross-section SEMs, the morphology of randomly aligned primary particles in the core and radially aligned primary particles towards the surface is maintained, although the primary particles change from needle-like in the precursor to a cuboid shape in the annealed material. The electrochemical cycling of 3 cells per synthesised material, reveals the highest first cycle charge and discharge capacity for sample 1:2.5 with 254 and 282 mAh/g, which is higher than theoretically possible. Due to side phases contributing to the overall capacity. This sample also exhibits the highest cation mixing in this experimental set-up of 1.9%. The most reliable results are observed for sample 1:5 with a first charge and discharge capacity of 267 and 220 mAh/g, a capacity retention of 81.8% over 100 cycles and a very low cation mixing of 1.4%. This sample is further investigated with more advanced methods.

XANES and EXAFS examinations of the sample 1:5 after cycling to different SOCs, reveals an increase in Ni oxidation state when increasing the state of charge. This is in accordance with what is expected. At 4.2 V already, all Ni is oxidised to Ni⁴⁺ as the curves for higher SOC overlap with the one at 4.2 V. When charged up to 4.3 V and discharged again to 3 V, the Ni K-edge overlaps nearly identically with the Ni K-edge of the OCV curve in this study, meaning almost all Ni is reversed again to its initial state. EXAFS calculations of the Ni-O and Ni-Ni bond show a decrease for Ni-O and increase for Ni-Ni distance with increasing charge. As Ni gets oxidised, its radius decreases, leading to a shorter distance between neighbouring Ni in the structure.

Looking at XAS and XPS measurements, it seems that additional Li₂CO₃ side phases present at the surface, evidenced by the C 1s and O 1s peaks at OCV in the HAXPES data as well as the pre-peaks (531 and 534 eV) of the O K-edge in the sXAS data, dissolve during charging. They form NiO at the surface due to oxygen loss or transition into other phases forming CEI layers on the cathode surface while reacting with the electrolyte. More investigations looking at post-cycling XRD patterns as well as RIXS data, would give additional compositional information as well as oxygen loss evidence, which might happen during cycling.

The magnetic measurements show a paramagnetic behaviour of LiNiO₂ at higher temperatures. When cooled down, the system gets magnetically ordered in a ferromagnetic structure as Ni²⁺ in the Li layers bridge the interaction between Ni³⁺ in neighbouring NiO slabs. Further cooling leads to an antiferromagnetic/ferromagnetic coupling as the amount of Ni²⁺ in the material increases. Competitive interactions between the ferromagnetic coupling of Ni³⁺ - Li⁺ - Ni³⁺ and antiferromagnetic/ferrimagnetic coupling of Ni³⁺ - Ni²⁺ - Ni³⁺ prevent long range magnetic ordering [202] [204] [206]. Thus, the magnetic moment μ_{eff} is expected to increase with an increasing amount of Ni³⁺ or a decreasing amount of Ni²⁺ in the compound. Essential magnetic values like the Curie and the Weiss-constant, as well as T_N, align with the cation mixing derived from refinements of X-ray diffraction data for these materials. Yet the magnetic moment μ_{eff} is not following the trend.

Muon spin relaxation spectroscopy gives the static field distribution Δ and the fluctuation rate ν , which are plotted against the temperature to gain insights into the temperature dependency of the Li movement and its magnetic contributions (Figure 5.36). The temperature dependency of the static field distributions at the muon stopping site Δ in blue gradually decreases as expected. This is attributed to a motional narrowing effect (similarly observed in NMR measurements) as a result of more rapid lithium diffusion as the temperature increases. This reduces the local nuclear field experienced by the muon at its stopping site. The temperature dependency of the fluctuation rate ν although shows initially a flat region as the ionic motion is too slow to observe. As the temperature increases, the fluctuation rate increases as well, as the thermally activated Li⁺ diffusion processes overcome the energetic barriers and are set in motion. The peak at around 200 K will need to be assigned to maybe some magnetic phenomenon.

There is a clear correlation between the μSR data and the electrochemistry of the cell. The static field distribution Δ curve in Figure 5.36 correlates strongly with the phase transitions appearing during delithiation of the material. During charge, Δ drops during the H1/M transition, which

is also in accordance with the change in muon relaxation between $20-40\,\%$ state of charge in Figure 5.37. Another peak is seen at around 4.0 V, which can be assigned to the M/H2 transition. During discharge, the behaviour of the data is reversed, as are the phase transitions. The Li hopping, described by the field fluctuation rate nu also evolves according to the phase transitions. Figure 5.39 shows a no change during the transition of H1/M but increases rapidly during the M/H2 transition and decreases again above 4.0 V when the H2/H3 transition takes place accompanied by a significant reduction in lattice parameters. These trends are again reversible during discharge.

3D volumetric XRD-CT images of cycled LNO cathodes show the agreement of SEM images of cross-sections of secondary LNO particles synthesised in the STR with optimised synthesis conditions and the lattice parameters from the operando XRD-CT measurements. While in the core of the secondary particle, the primary particles are randomly aligned, showing more pronounced (003) reflections, the shell of the secondary particle contains radially aligned primary particles with improved Li pathways along the grain boundaries and stronger (101) and (104) reflections. XRD-CT is an excellent method to confirm and visualise the orientation of crystallites in a material and help battery active materials to be developed, improved, and tailored to specific needs and applications.

The advanced characterisation of the here-optimised LiNiO₂ shows the examined properties and crystal structure of the material. Ni oxidation states and bond lengths in the structure as well as the magnetic properties of the optimised LiNiO₂ in accordance with literature results and known properties and features of LNO. New data were gained via muon spectroscopy and combined XRD-CT and reveals interesting results that either need further evaluation or can be determined for doped LNO or similar layered oxide materials, to learn more about possible Li diffusion mechanism and how to improve or adjust Li diffusion in layered oxides.

Overall, improving the morphology and size of the precursor material Ni(OH)₂ during the precipitation reaction, leads to improved electrochemical behaviour. Additionally, it is possible to tailor the particle size and morphology to certain needs by adjusting the synthesis conditions. Advanced methods confirmed the suggested mechanisms of structural changes and changes in properties regarding cation mixing within the structure and during cycling. Operando muon spin relaxation spectroscopy and in-situ XRD-CT showed some new insights to deepen the understanding of the structure-property relationships of this promising layered oxide cathode active material. Features in the muon spin relaxation data that cannot be explained completely, might benefit from NMR or neutron diffraction experiments due to the probably magnetic

nature of these features. Further investigations need to be done to uncover the exact correlation of the primary particle size on the electrochemical properties. The exact chemical composition can be determined by using ICP-OES and combining it with a titration method to distinguish between the Li in the LNO structure and the Li from side phases.

6. Doped LiNiO₂

6.1. Introduction

To investigate further possible improvements of the layered oxide LiNiO₂ as an active cathode material for Li-ion batteries, different dopants are implemented into the structure of the precursor material Ni(OH)₂ during the precipitation synthesis in the stirred tank reactor. The aim is, to reach the theoretical capacity of LNO (274 mAh/g) and while maintaining a rate capability above 80% over 100 cycles by optimising the secondary particle morphology. This way, maximum access to theoretical capacity by improved Li diffusion pathways and controlled cation mixing as well as improved chemical, thermal and mechanical stability is expected. By tailoring the particle size and morphology of the secondary particles, increasing the packing and thus energy density by growing secondary particle assemblies with primary particles randomly aligned in the core and radially aligned towards the surface, a new threshold of discharge capacity of > 250 mAh/g could be established with a cation mixing of less than 3 % for the undoped material. The crucial H2/H3 transition happening at the upper voltage limit still remains active although maybe in a less intrusive way. This transition is responsible for structural instabilities due to constant volume changes during cycling and many dopants will attenuate or shift this transition so that all the available Li in the structure can be used and at the same time the structure collapse prevented.

Dopants are expected to substitute for the nickel in the structure and increase the structural stability of the material during cycling or increase the theoretical capacity by contributing to the redox processes. Different dopants like Co, Mn, Cu, Zn, Sn, Zr, Ti and W were used, based on the literature research in Chapter 2.

6.2. Synthesis

The aim of doping the precursor material of the cathode active precursor material Ni(OH)₂ is to control the morphology of the particles at the same time but also to study the influence of different dopants on the synthesis. Often, dopants are introduced to the system during the high temperature lithiation step with several possible sites to intercalate in the structure. The dopant can substitute the nickel as well as the lithium. It could form a surface layer on the secondary particle or migrate into the layered structure and form a layer on the primary particles or on the

grain boundaries. Here, we investigate the integration of various dopants into the $Ni(OH)_2$ precursor structure during the precipitation reaction in a stirred tank reactor. 3 mol % of Ni is replaced by a dopant, mixed into the Ni sulphate solution and fed into the stirred tank reactor during the reaction. The same procedure for the precipitation reaction as described in Chapter 5.2 is applied, while a TM:NH4OH ratio of 1:5, a reaction temperature of 60°C and a pH of 11 is maintained throughout the reaction. The precipitate is treated the same way as the undoped material, it is washed several times with deionised water until a pH of 7 is reached and then dried overnight between 80 - 100°C. The doped precursor material is then lithiated with LiOH (3% excess) in a solid-state reaction, to form the desired doped LNO and characterised regarding its structure, morphology and electrochemical behaviour during cycling.

6.3. Characterisation

To characterise the doped precursor material as well as the final doped LNO, XRD measurements to investigate phase purity, shifts in unit cell size and their refinements, SEM images to visualise the particle morphology of secondary and primary particles as well as EDX investigations of particle cross-sections, to study the dopant distribution, are used. Additionally,

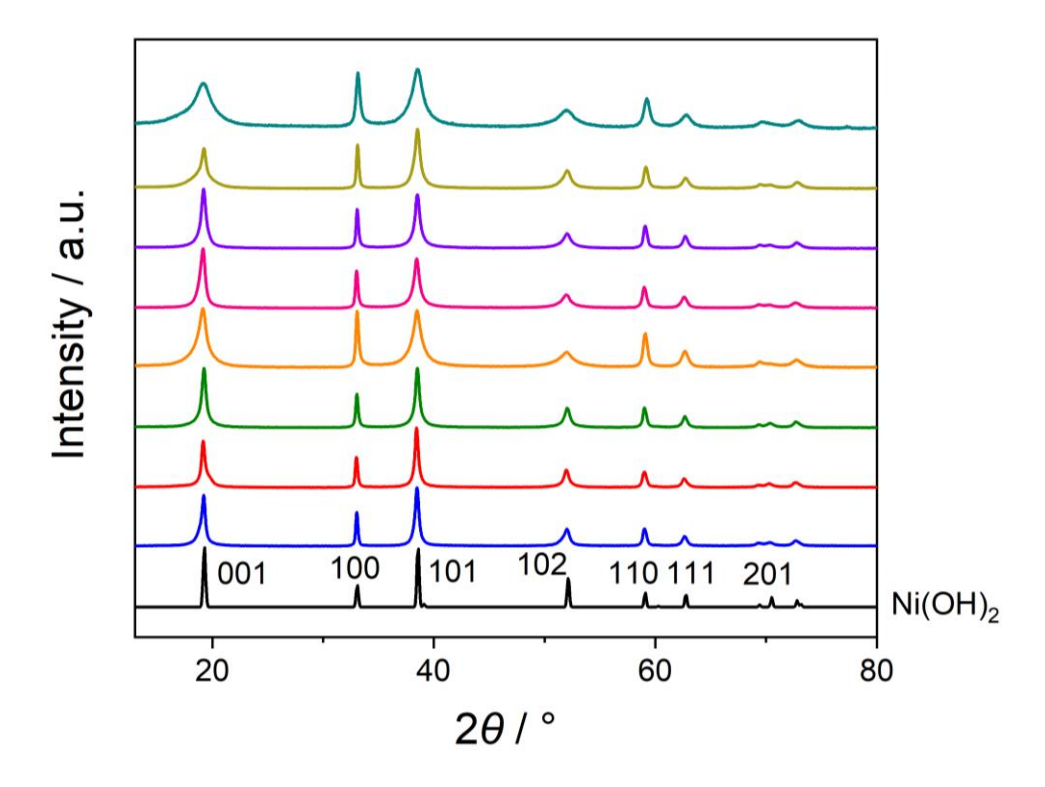


Figure 6.1: XRD patterns of as prepared doped Ni(OH)₂ samples. Co-doped (blue), Mn-doped (red), Cu-doped (green), Zn-doped (orange), Sn-doped (pink), Zr-doped (purple), Ti-doped (yellow) and W-doped (turquoise). Calculated Ni(OH)₂ pattern from ICSD (black) as comparison including Bragg peak labels.

coin half cells are prepared to investigate the influences of the dopants on the electrochemical behaviour of the layered oxide material.

Figure 6.1 shows the XRD patterns of the doped precursor materials including the undoped pattern of Ni(OH)₂ for comparison. All recorded diffraction patterns show the associated Bragg peaks of the $P\overline{3}m$ structure, no obvious additional peaks are detected. A noticeable change in the patterns of the doped samples, is the broadening of the peaks as well as peak intensities compared to the undoped material. The broadening can be assigned to changes in crystallite size, microstrain or stacking faults within the structure. Changes in peak intensities stem from varying scattering powers of different atom types. As we implemented often larger dopants into the structure, peak broadening as well as changes in peak intensities are expected. Some peaks, in the Co-doped, Mn-doped and W-doped Ni(OH)₂ diffraction patterns, show asymmetry in their peak broadening, especially the (001) Bragg peak. This is again attributed to the implementation of different sized dopants into the lattice, leading to contracted or expanded d-spacings, variation within crystallite sizes or stacking faults. The diffraction patterns of the as-prepared doped LiNiO₂ are shown in Figure 6.2. They exhibit sharp diffraction peaks at the associated 2 θ angles of the crystal structure of undoped LNO. The W-doped material shows

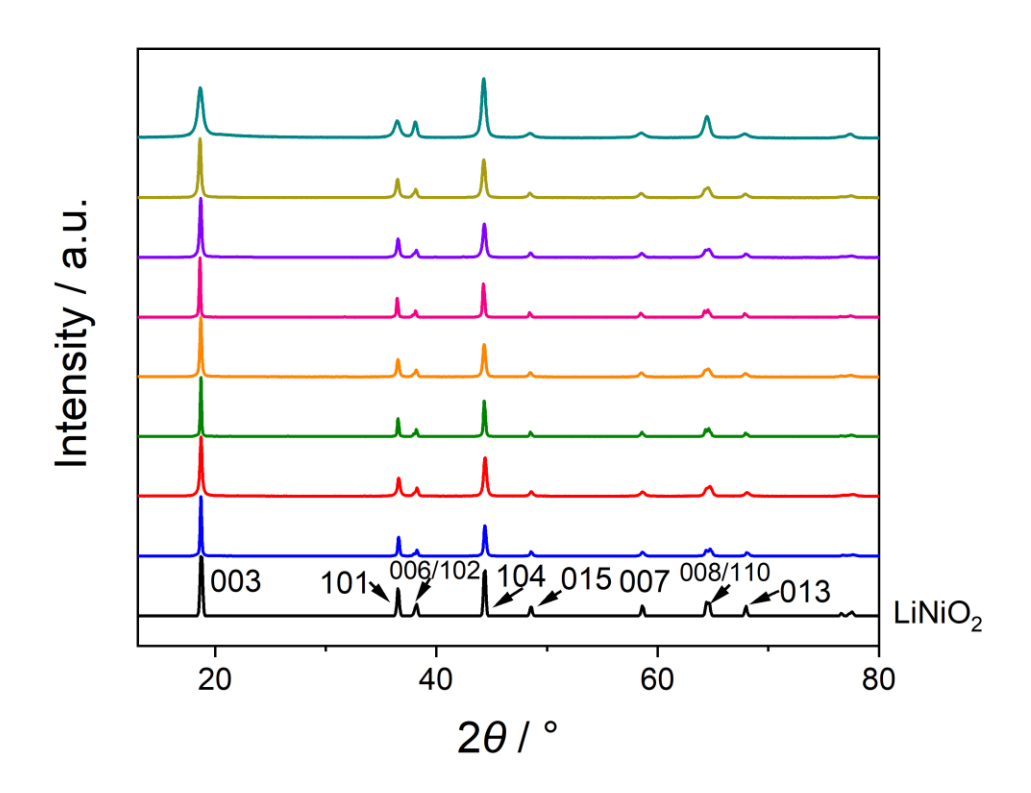


Figure 6.2: XRD patterns of as prepared doped LiNiO₂ samples. These samples are all pre-calcined for 5h at 350°C and calcined for 15h at 710°C. Co-doped (blue), Mn-doped (red), Cu-doped (green), Zn-doped (orange), Sn-doped (pink), Zr-doped (purple), Ti-doped (yellow) and W-doped (turquoise). Calculated LiNiO₂ pattern from ICSD (black) as comparison including Bragg peak labels.

severe peak broadening and changes in peak intensities compared with the other samples. XRD patterns as well as SEM images and electrochemical cycling plots will be discussed in detail for each dopant separately.

Table 6.1: Ratio of lattice parameter and Bragg peak ratios of as-prepared samples of doped LiNiO₂. Standard deviations in brackets.

Dopant	Ni ²⁺ [%]	c/a ratio	(003)/(104) ratio	(006/102)/(101) ratio
Со	1.6(1)	4.936	1.315	0.483
Mn	4.1(1)	4.935	1.300	0.479
Cu	5.0(1)	4.931	1.121	0.555
Zn	3.0(1)	4.934	1.449	0.464
Sn	2.8(1)	4.933	1.227	0.462
Zr	3.3(1)	4.935	1.431	0.463
Ti	2.7(1)	4.935	1.226	0.469
W	12.7(1)	4.923	1.496	0.594
undoped	1.4(1)	4.934	1.270	0.498

Table 6.1 and Table 6.2 show the peak analysis and diffraction pattern refinement values obtained for all the doped LiNiO₂ samples. Refinement plots of the samples can be seen in Figure 10.36 to Figure 10.42 in the appendix. The peak ratios in Table 6.1 are a measure for the Li/Ni mixing in the layered structure and as mentioned in a previous chapter, these values seem to be significant only above a certain amount of Ni²⁺ in the Li layer. Nevertheless, there is no coherent relation between those values in the case of the doped samples, as larger values for the (003)/(104) ratio are expected to show lower Li/Ni mixing in the structure, whereas here, Snand Ti-doped samples show lower cation mixing but also a low Bragg peak ratio. It is possible, that dopants occupy the Li site or that the scattering of the dopants affects the obtained ratios due to the influence of the atoms scattering power on the peak intensities, as mentioned earlier. Same is true for the (006/102)/(101) ratio, where lower values are expected for low Li/Ni mixing but the determined ratios of the Co-doped sample are higher than the ratio of the Mn-doped sample for example, although its cation mixing is lower. There is still the possibility, that the resolution of the measured diffraction patterns is not good enough to give reliable values due to the small number of dopants or Ni²⁺ in the Li layer and that more reliable values could be obtained via an instrument with higher resolution or a neutron source. The c/a ratio seems to be more accurate as the actual refined lattice parameters are used to evaluate the degree of layering in the structure. Higher values are a measure for more uniform layered materials with less stacking faults or cation mixing. Unit cell parameters as well as refined concentrations of Ni²⁺ in the Li layer and the measures of the quality of the fit, wR and GOF are summarised in Table 6.2.

Table 6.2: Lattice parameters, volume and Ni^{2+} and dopant occupancies derived from XRD patterns and its refinements for as-prepared LiNiO₂ samples. Standard deviations in brackets.

Dopant	c [Å]	a [Å]	Volume	Ni ²⁺	Dopant	wR	GOF
Co	14.1982(2)	2.87627(4)	101.725(3)	1.6(1)	3.0	1.91	2.31
Mn	14.1943(4)	2.87636(7)	101.703(6)	4.1(1)	3.0	2.33	2.65
Cu	14.2076(2)	2.88129(4)	102.147(3)	5.0(1)	3.0	2.33	2.71
Zn	14.2133(1)	2.88963(3)	102.142(1)	3.0(1)	3.0	2.84	3.32
Sn	14.2172(3)	2.88211(6)	102.275(5)	2.8(1)	3.0	2.14	2.43
Zr	14.2138(5)	2.88015(8)	102.111(7)	3.3(1)	3.0	2.52	2.95
Ti	14.2066(2)	2.87900(7)	101.978(3)	2.7(1)	3.0	2.69	3.15
W	14.1970(1)	2.88390(2)	102.260(1)	12.7(1)	3.0	5.10	5.78
undoped	14.1904(1)	2.87578(4)	101.635(3)	1.4(1)	-	5.30	1.17

The refinement of the dopant concentration did not give any reliable physical values, as the difference in electron density between dopant and nickel is too small to have an influence on the diffraction patterns. Thus, only irrational arbitrary values were obtained, and the dopant concentration was fixed at 3% for further refinements. In this case, neutron diffraction would be a better way to get meaningful refined values, but these measurements were not conducted during this work. Ni²⁺ occupancies in the Li layer are very low for the Co-doped material (1.6%) as well as for the Sn- and Ti-doped compound (2.8 and 2.7%), whereas the Mn-, Cu-and W-doped materials exhibit the highest amount of Li/Ni mixing of 4.1, 5.0 and 12.7%, respectively.

The lattice parameters a and c as well as the unit cell volume show a dramatic increase in unit cell size for Sn-doped as well as Cu-, Zn-, Zr- and Ti-doped materials. As suggested by various literature reports, Sn, Zr and Ti ions are doped into the structure as tetravalent ions, leading to increased Li-spacing as the electrostatic repulsion between the Ni-layers is increased. The divalent ions Cu and Zn mitigate the Ni³⁺ reduction to maintain the overall charge balance and thus decrease or suppress the Ni migration into the Li layer. [207] [122] [129] [141]

Figure 6.3 and Figure 6.5 show the electrochemical cycling plots of all as-prepared doped samples, which were investigated using coin half-cells vs. Li/Li $^+$. The cells were cycled in environmental chambers at a controlled temperature of 25°C for 100 cycles in the voltage range of 3 – 4.3 V. After a resting period of 2 h, a constant current corresponding to a rate of C/20 for the first two cycles and at C/2 for the remaining 98 cycles was applied, where 1 C = 220 mAh/g.

Three cells were prepared and cycled for each sample. The electrochemical data for each sample is presented separately in the appendix in Figure 10.28 to Figure 10.35. The voltage-capacity plot in Figure 6.3 shows superior and very good discharge capacities for the Sn- (278 mAh/g) and Co-, Mn-, Zr- and Zn-doped (240, 214, 229 and 203 mAh/g) samples, respectively.

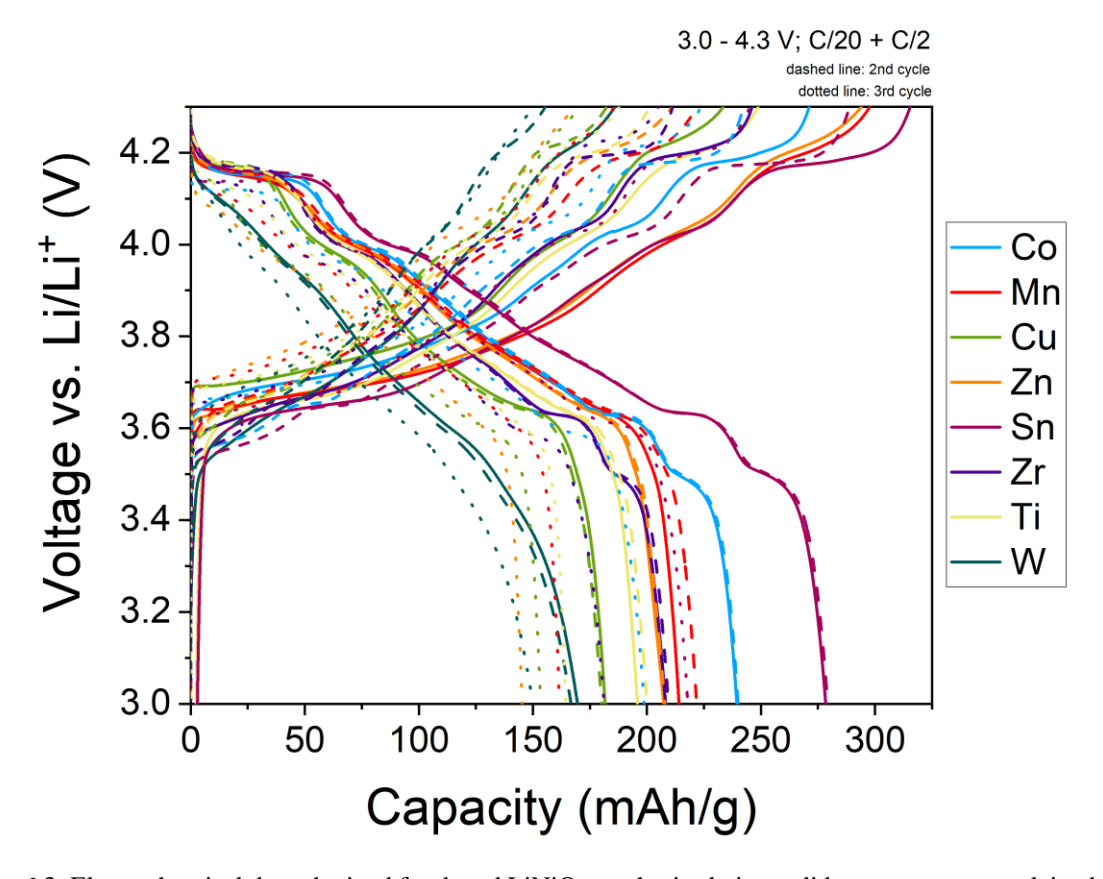


Figure 6.3: Electrochemical data obtained for doped LiNiO $_2$ synthesised via a solid-state route, pre-calcined for 5 h at 350°C and calcined for 15 h at 710°C. Charge/discharge plot between 3 – 4.3 V vs. Li/Li $^+$ at a rate of C/20 for two cycles and C/2 for the third cycle. Solid line shows 1st cycle, dashed line depicts 2nd cycle and dotted line represents the 3rd cycle. Co-doped (blue), Mn-doped (red), Cu-doped (green), Zn-doped (orange), Sn-doped (pink), Zr-doped (purple), Ti-doped (yellow) and W-doped (turquoise).

The W-doped sample exhibits the lowest charge and discharge capacities of 186 and 170 mAh/g, respectively. The first cycle capacity loss, demonstrating the irreversible loss between charge and discharge within one cycle due to decreased Li slab height and parasitic Ni²⁺ in the Li layer and thus disrupted Li pathways. It is lowest for the Zr- and W-doped samples (16 and 17 mAh/g) and highest for the Mn- and Zn-doped samples (84 and 70 mAh/g) in this experimental setting. An expected decrease in capacities between 1st and 3rd cycle due to kinetic changes as a result of the change in C-rate (C/20 to C/2) can be seen for all the samples.

Table 6.3 summarises the charge and discharge capacities of the first three cycles, as well as

Dopant	Discharge Capacity mAh/g			Charge Capacity mAh/g			Capacity loss	Coulombic efficiency	Discharge Capacity retention
	1st cycle	2nd cycle	3rd cycle	1st cycle	2nd cycle	3rd cycle	(1st cycle) [mAh/g]	(1st cycle) [%]	(100 cycles) [%]
Со	240	240	199	271	241	222	31	88	77
Mn	214	222	162	298	222	186	84	72	81
Cu	182	180	153	234	182	169	52	78	81
Zn	203	203	151	273	209	174	70	74	83
Sn	278	279	218	315	287	245	37	88	78
Zr	229	230	181	246	211	202	17	85	74
Ti	195	200	165	249	201	184	54	79	88
W	170	168	150	186	156	150	16	91	69

the first cycle capacity loss and coulombic efficiency and the capacity retention over 100 cycles for the as-prepared doped LiNiO₂ samples. The Coulombic efficiencies for all samples range between 72 - 91% for the first cycle and after the initial formation cycles, settles just below 100% for the subsequent cycles. A lower efficiency is expected in the first cycles due to potential Li-deficiency in the prepared pristine compounds. As the Li anode supplies an indefinite amount of Li, enough Li can reintercalate to increase the coulombic efficiencies of the cells to 100%.

Table 6.3: Electrochemical values derived from the cycling data of the as-prepared $LiNiO_2$ using doped $Ni(OH)_2$ precursor.

Dopant	Discharge Capacity mAh/g			Charge Capacity mAh/g			Capacity loss	Coulombic efficiency	Discharge Capacity retention
	1 st cycle	2 nd cycle	3 rd cycle	1 st cycle	2 nd cycle	3 rd cycle	(1st cycle) [mAh/g]	(1 st cycle) [%]	(100 cycles) [%]
Co	240	240	199	271	241	222	31	88	77
Mn	214	222	162	298	222	186	84	72	81
Cu	182	180	153	234	182	169	52	78	81
Zn	203	203	151	273	209	174	70	74	83
Sn	278	279	218	315	287	245	37	88	78
Zr	229	230	181	246	211	202	17	85	74
Ti	195	200	165	249	201	184	54	79	88
W	170	168	150	186	156	150	16	91	69

The capacity retention after 100 cycles is above 80% for the Mn-, Cu-, Zn- and Ti-doped samples, with the W-doped sample holding the lowest capacity retention of only 69% after 100 cycles. These parameters are also graphically presented in the capacity retention plot in Figure 6.5. The dQ/dV plot in Figure 6.4 reveals the phase transitions during charge and discharge of the second cycle of the as-prepared doped samples. The first cycle is not depicted and used for

evaluation, as cell conditioning is happening, and graphical features are not representative for the real cycling behaviour. Cycle three and 100, cycled at C/2, will be plotted in separate graphs and compared for each dopant separately, later in this chapter. Two-phase regions in the differential capacity plots are represented as peaks, whereas single-phase regions are shown as plateaus. The general order of transition for layered oxide materials is H1/M (3.65 V) – M/H2 (4 V) – H2/H3 (4.2 V) for oxidation and the reverse order for reduction. A shift of transition features towards lower voltages during discharge is due to a decrease in polarisation. An additional peak can be detected just before the H1/M transition, at 3.5 V for slower charged cycles at C/20, which is responsible for higher charge and discharge capacities during the first two cycles compared to faster charging rates of C/2 from cycle three onwards. The reaction happening at this voltage increases the polarisation and leads to an increase in coulombic efficiencies in the first two cycles running at a slower C-rate of C/20.

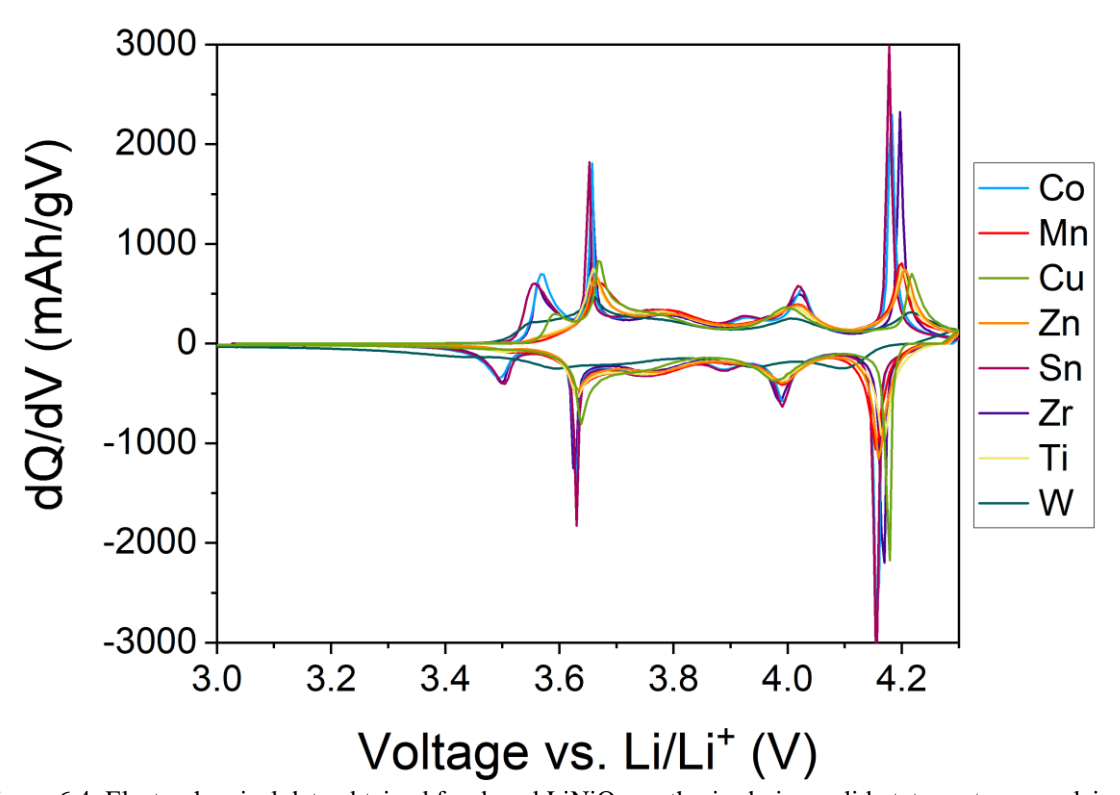


Figure 6.4: Electrochemical data obtained for doped LiNiO $_2$ synthesised via a solid-state route, pre-calcined for 5 h at 350°C and calcined for 15 h at 710°C. Differential capacity plot dQ/dV for the second cycle. Potential window between 3 – 4.3 V vs. Li/Li $^+$ at a rate of C/20. Co-doped (blue), Mn-doped (red), Cu-doped (green), Zn-doped (orange), Sn-doped (pink), Zr-doped (purple), Ti-doped (yellow) and W-doped (turquoise).

Furthermore, some samples show an additional peak immediately before the M/H2 transition at 3.95 V, which is only detectable for samples with a low cation mixing. Another influence on the dQ/dV plot due to the cation mixing, is the peak broadening that is visible when a higher disorder is present in the structure. [45] [192] [84] [72]

Some general observations can be made for the as-prepared doped samples in this study. The Co-, Sn- and Zr-doped samples in blue, wine-red and purple, as well as the Mn-, Zn- and Ti-doped samples in red, orange and yellow, show a very similar behaviour in the differential capacity plots, whereas the Cu-doped sample in green and the W-doped sample in turquoise show a different behaviour from all of them.

The Cu-, Sn- and Zr-doped samples exhibit the highest intensities for the H1/M transition at 3.66 V, including a pre-peak at 3.5/3.6 V as well as the H2/H3 transition at 4.18/4.2 V for the oxidation. The corresponding peaks for the reduction also show the highest intensities for the H3/H2 transitions between 4.15 – 4.17 V and for the M/H1 transitions at 3.63 V with a pre-peak at 3.5 V. These samples also all show an additional pre-peak of the M/H2 transition at 3.93/3.95 V for oxidation and at 3.9 V for reduction. This pre-peak corresponds to the Li/Ni cation mixing in the lattice. It is unclear, if potential dopant substitution on the Ni as well as the Li site, influence that refined value. It was not considered during the refinements, but the Zn-and the Ti-doped samples also show very low values of Li/Ni mixing in the refinements, yet this specific peak does not show in the dQ/dV plot.

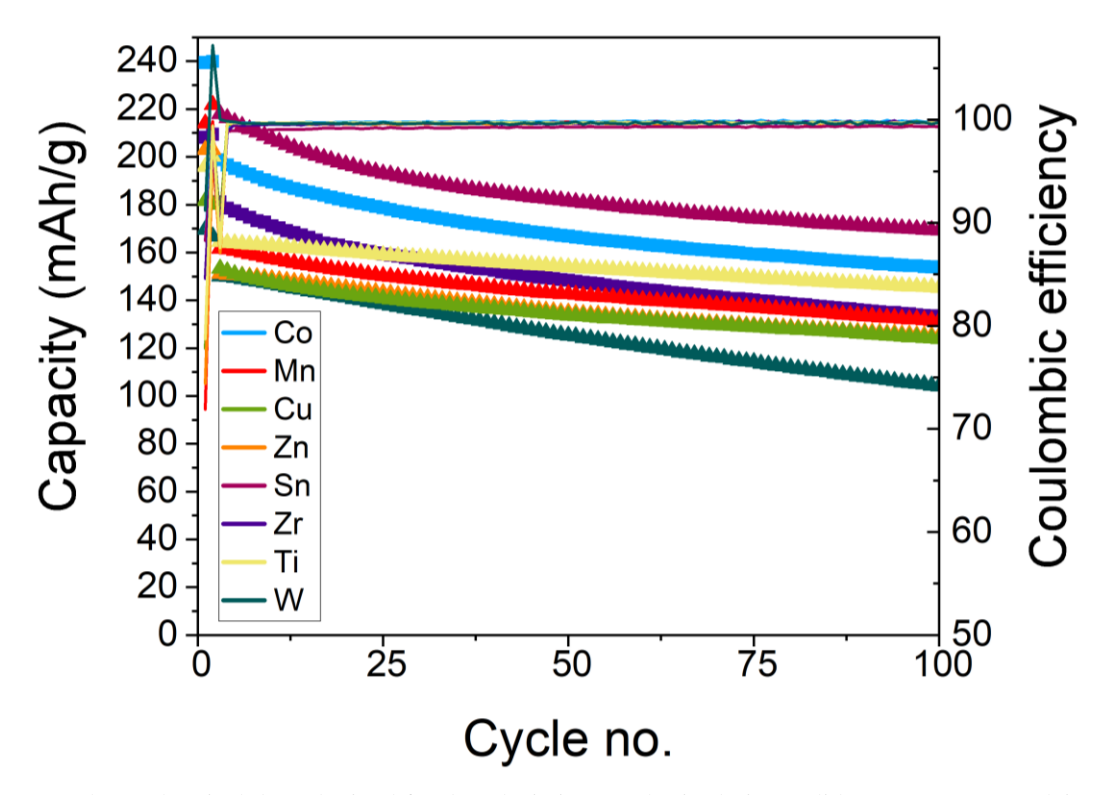


Figure 6.5: Electrochemical data obtained for doped LiNiO₂ synthesised via a solid-state route, pre-calcined for $5\,h$ at $350\,^{\circ}$ C and calcined for $15\,h$ at $710\,^{\circ}$ C. Discharge capacity retention and coulombic efficiencies over 100 cycles. Co-doped (blue), Mn-doped (red), Cu-doped (green), Zn-doped (orange), Sn-doped (pink), Zr-doped (purple), Ti-doped (yellow) and W-doped (turquoise).

The Mn-, Zn- and Ti-doped samples show reduced intensities for all transitions and broader transition peaks, leading to reduced areas of single-phase regions in between the transitions. The reduced intensity for the H2/H3 transition is beneficial, as the detrimental volume changes are not as intense, and the lattice collapse and the corresponding failure mechanisms will be delayed for these cells. The W-doped sample shows even more reduced and broader peaks, both in oxidation and reduction features.

The Cu-doped sample exhibits reduced intensities for all the peaks but also a pre-peak to the H1/M transition at 3.6 V for the oxidation and a delayed H2/H3 peak at 4.22 V during oxidation. During reduction, the H3/H2 transition is more pronounced and there is no pre-peak of the M/H1 transition at all.

6.3.1. Cobalt-doped LNO

3% of cobalt is doped into the layered LiNiO₂ structure as a trivalent ion and substitutes the trivalent Ni located at the 3*b* Wyckoff position. [98] No charge compensation is required, thus, no big changes in the structural and morphological properties are expected. The XRD patterns in Figure 6.6 compare the measured pattern of the as-prepared Co-doped LiNiO₂ with a pristine

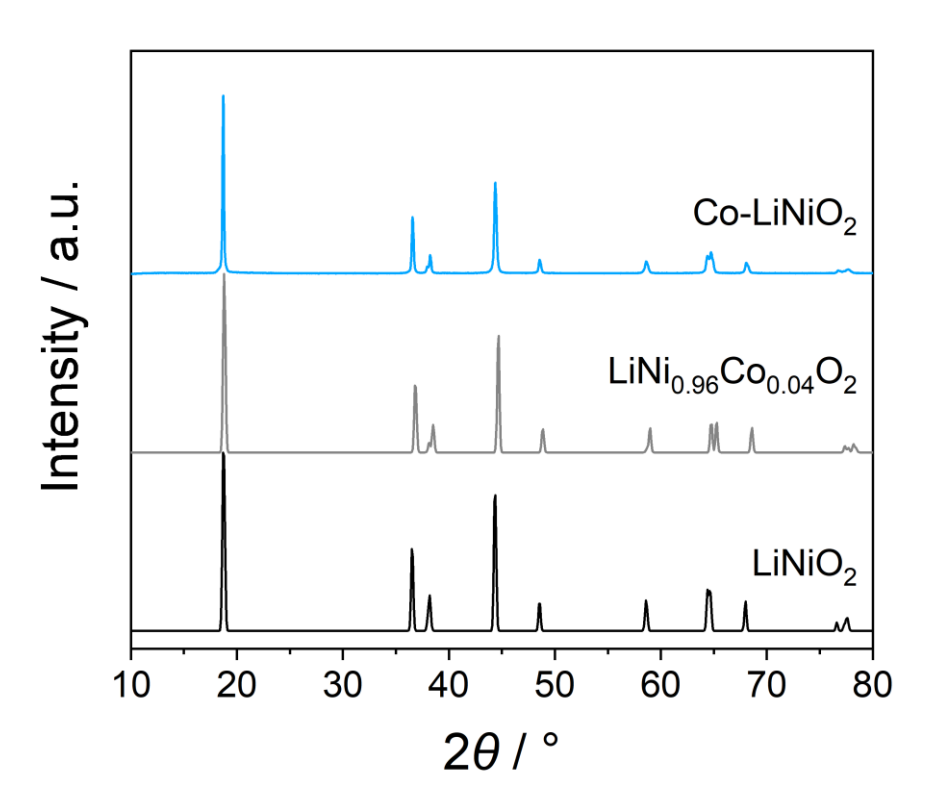


Figure 6.6: XRD pattern of Co-doped LiNiO₂, pre-calcined for 5 h at 350°C and calcined for 15 h at 710°C. Calculated LiNiO₂ (black, collection code 78687 [187])) and LiNi_{0.96}Co_{0.04}O₂ (grey, collection code 83303 [103]) patterns from ICSD for comparison.

LiNiO₂ in black and LiNi_{0.96}Co_{0.04}O₂ in grey. The obtained pattern exhibits all the corresponding narrow Bragg peaks to the pristine LiNiO₂ structure. Small differences can be seen in the splitting of the (006)/(102) peak. The (102) peak is more pronounced than the (006) peak, which is in accordance with the 4% Co-doped LNO from literature. No noticeable side phase can be detected visually and via Rietveld refinements, a Li/Ni mixing of 1.6% is determined as well as a c/a ratio of 4.936. The c/a ratio is a measure of the ordering in the structure and both exceptional values can be assigned to the implementation of Co³⁺ ions into the structure, as confirmed by other reports in literature. [102] [105]

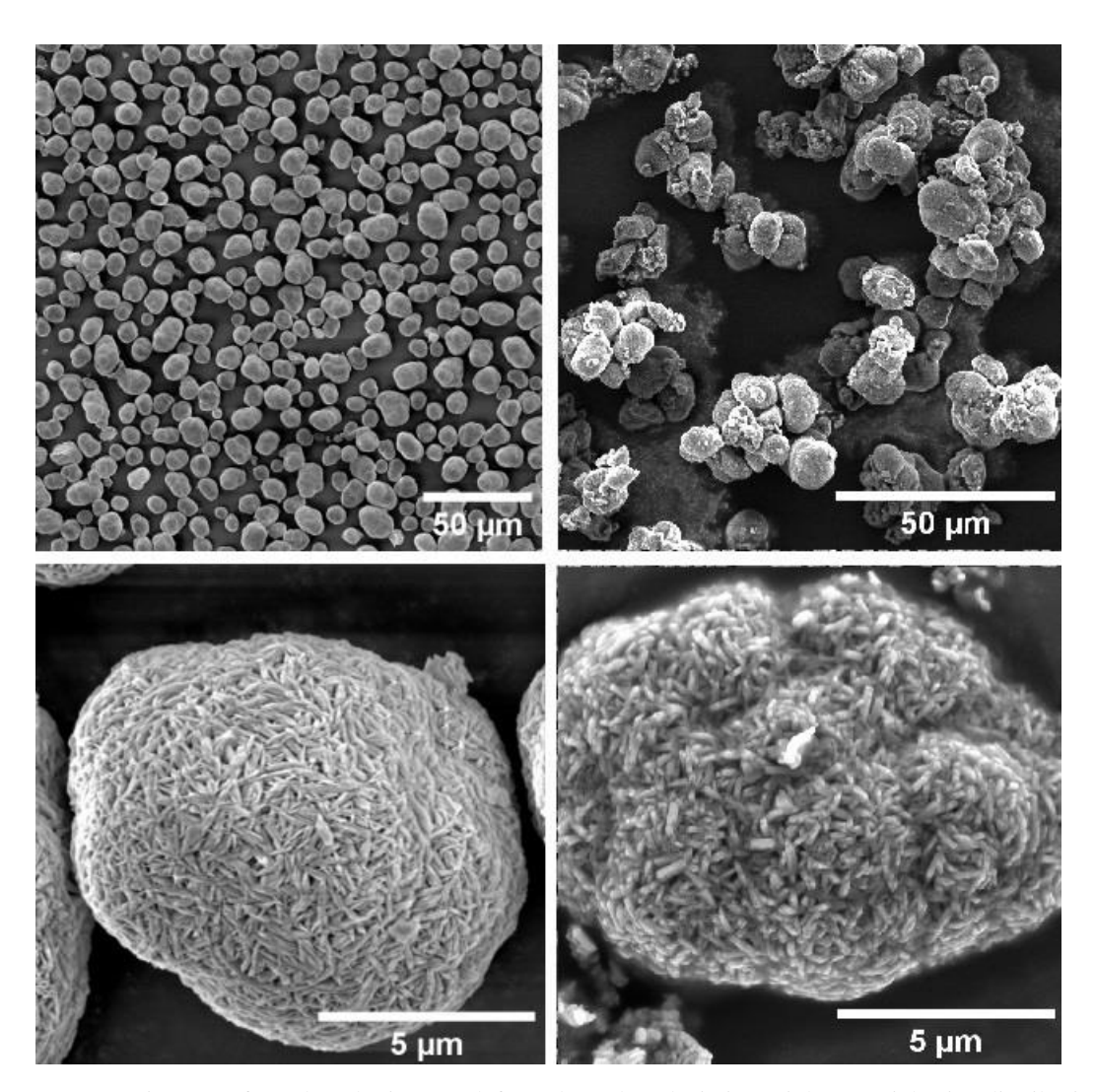


Figure 6.7: SEM images of Co-doped $Ni(OH)_2$ (left) and Co-doped $LiNiO_2$ (right). Particle size distribution of secondary particle assemblies using smaller magnification in the top row and primary particles at higher magnification in the bottom row.

SEM images of the Co-doped precursor Ni(OH)₂ and the lithiated Co-doped LNO in Figure 6.7 left and right, respectively, show fairly spherical secondary particles and a narrow particle size

distribution, in the top row. The primary particles, depicted in the bottom row of the graph, show a densely packed structure with small, elongated particles for the precursor and more cubic primary particles for the lithiated compound. Overall, the secondary as well as primary particles look very similar to the pristine Ni(OH)₂ and LiNiO₂ prepared via co-precipitation under the same conditions. Figure 6.8 shows cross-sections of as-prepared precursor and lithiated particles. These cross-sections were examined additionally via energy-dispersive X-ray analysis EDX, to give an idea about the dopant distribution within the particle. The cross-section itself reveals that inside the secondary particles.

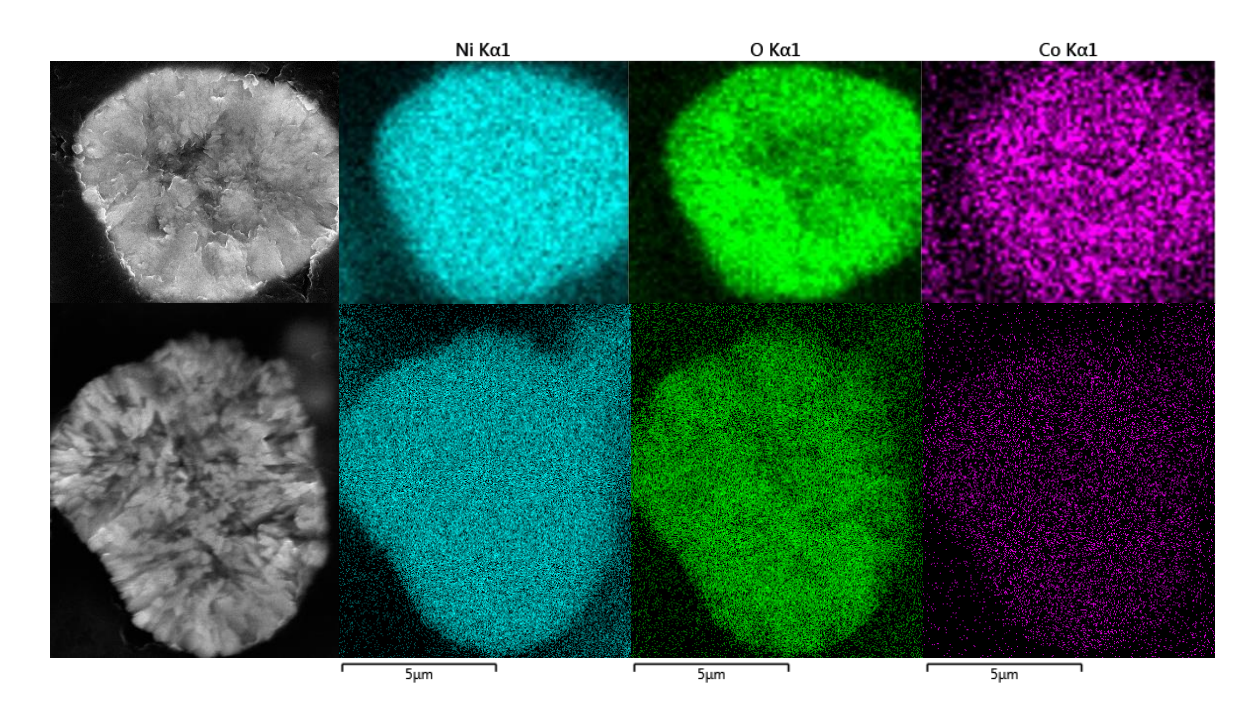


Figure 6.8: SEM image of a particles cross-section (left) and EDX analysis of the cross-section of as-prepared Co-doped Ni(OH)₂ precursor (top row) and Co-doped LiNiO₂ (bottom row). Elemental mapping of nickel (turquoise), oxygen (green) and cobalt (pink).

The primary particles are randomly aligned and then grow radially towards the outside, maintaining very good Li diffusion pathways for electrochemical cycling. The dopant is evenly distributed in the precursor and maintains that distribution during the HT solid-state synthesis to prepare the final cathode material LiNi_{0.97}Co_{0.03}O₂. As Co can contribute with its redox reactions, to the overall potential of an electrochemical cell, an increased capacity is expected. The investigation of the electrochemical behaviour of three cells of Co-doped LiNiO₂ cathode material, reveals initial charge and discharge capacities of 271 and 240 mAh/g with a first cycle capacity loss of 31 mAh/g. After the initial conditioning cycles at C/20, a lower C-rate of C/2 exhibits charge and discharge capacities of 222 and 199 mAh/g. The first cycle coulombic efficiency of 88% is achieved, which increases to 100% after the conditioning cycles. After

100 cycles, 77% of the capacity can be retained, which is below the desired threshold of 80%. Those values do not exceed the determined values of the pristine LiNiO₂ and there does not seem to be a huge contribution of the $Co^{2+/3+}$ redox reaction. As this redox couple is overlapping with the O₂ p-orbital, oxygen release is expected, leading to a decreased lifetime and a lower capacity retention, which can be confirmed when looking at this analysis results.

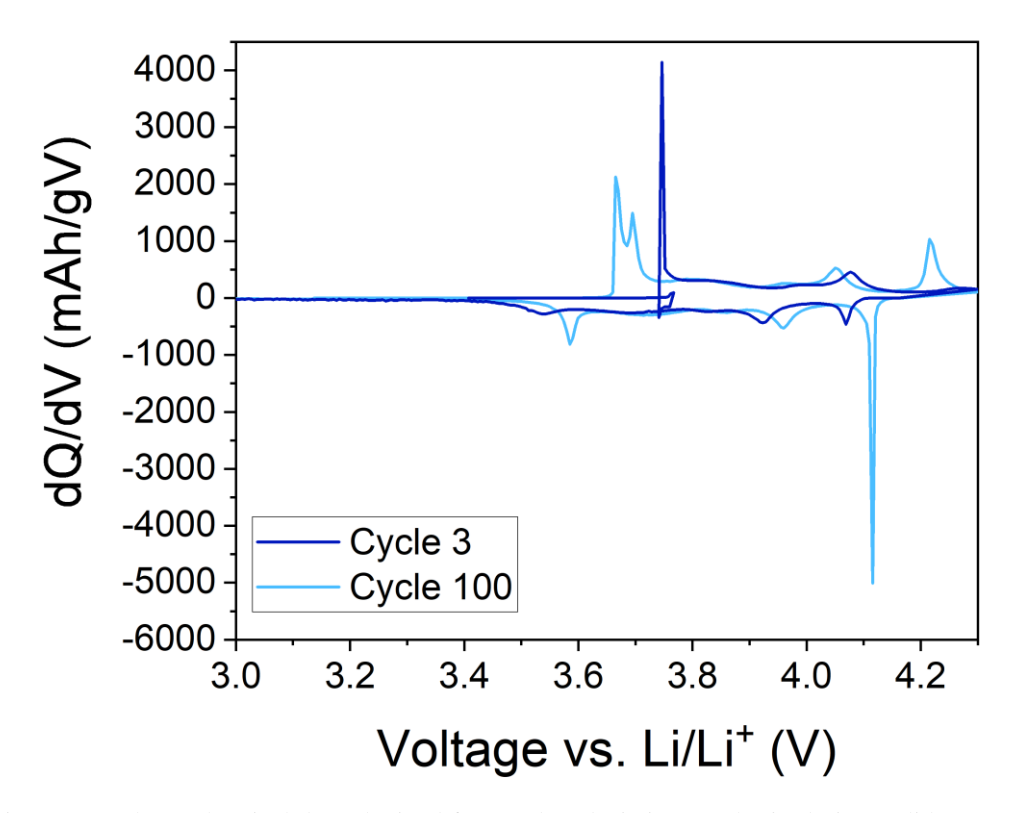


Figure 6.9: Electrochemical data obtained for Co-doped LiNiO₂ synthesised via a solid-state route, pre-calcined for 5 h at 350° C and calcined for 15 h at 710° C. Differential capacity plot dQ/dV comparing cycle 3 and 100. Potential window between 3-4.3 V vs. Li/Li⁺ at a rate of C/20.

A closer look at the differential capacity plot in Figure 6.9, compares the third cycle and the 100^{th} cycle. The graph reveals the additional peak corresponding to the M/H2 transition, assigned to a low cation mixing of only 1.6%, at around 3.9 V. Yet moving from cycle 3 to 100, the transitions are shifted to higher voltages, the intensities are lower and the H2/H3 transition is not in the potential window of this set-up anymore. This shift is caused by parasitic surface reactions that take place during cycling and as oxygen is released and used to form a passivating surface layer on the particles, preventing Li from re-intercalating and causing increasingly more structural damage and shows in a worse capacity retention.

6.3.2. Manganese-doped LNO

Manganese on the other hand is substituted as Mn^{4+} ions, replacing the smaller Ni^{3+} ions. [98] To compensate the charge imbalance, some Ni^{3+} will be reduced to Ni^{2+} , increasing the possibility of Li/Ni cation mixing in the structure. Figure 6.10 shows a comparison between the Mn-doped LNO, a pristine LNO and LiNi_{0.5}Mn_{0.5}O₂. All three compounds exhibit the Bragg peaks associated with space group $R\bar{3}m$ and a layered structure, yet the intensity ratio is different for the (003)/(104) peaks. Whereas a doping level of only 3% still shows a higher intensity for the (003) peak, like the pristine compound, a substitution of 50% reverses the ratio and the (104) is revealing a higher intensity now. The compound seems phase pure by visual inspection and Rietveld refinements does not suggest a side phase. Yet the refinement reveals an increased cation mixing, as expected from literature [111], of 4.1% and following from that, the highest 1st cycle capacity loss of 84 mAh/g of this study, with an initial charge and discharge capacity of 298 and 214 mAh/g, respectively. SEM images of the particles still show very spherical secondary particles, both in the precursor as well as in the lithiated material in Figure 6.11. A closer look at a higher magnification reveals the primary particles, seen in the bottom row, which are elongates needle-like in the precursor secondary particles.

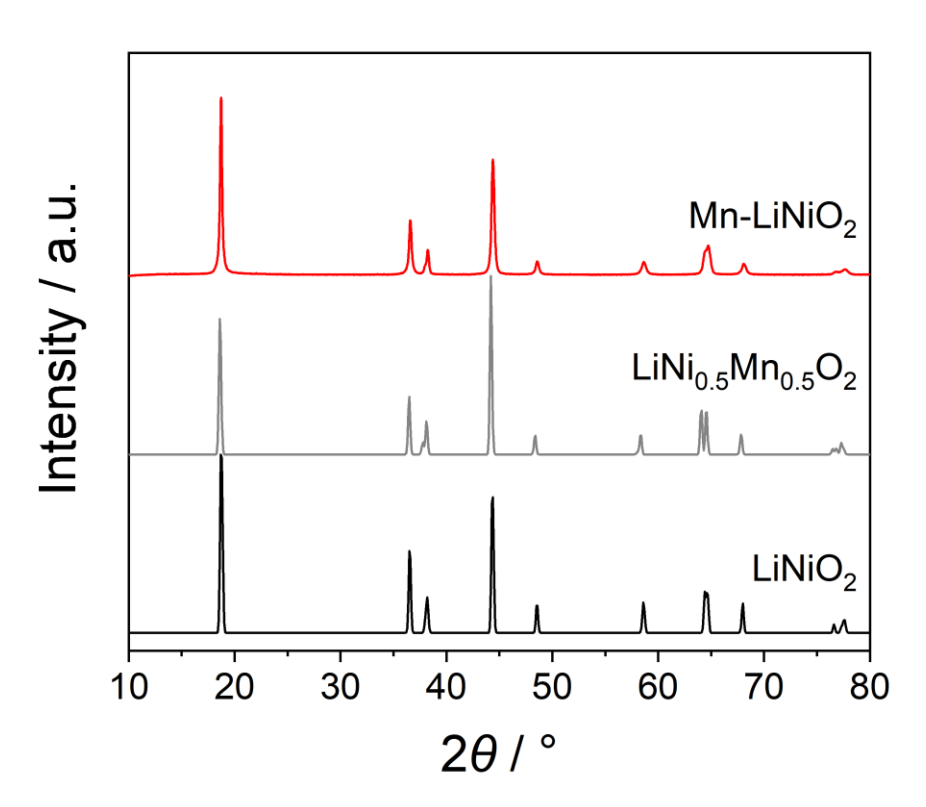


Figure 6.10: XRD pattern of Mn-doped LiNiO₂, pre-calcined for 5h at 350°C and calcined for 15h at 710°C. Calculated LiNiO₂ (black, collection code 78687 [187])) and LiNi_{0.5}Mn_{0.5}O₂ (grey, collection code 152273 [208]) patterns from ICSD for comparison.

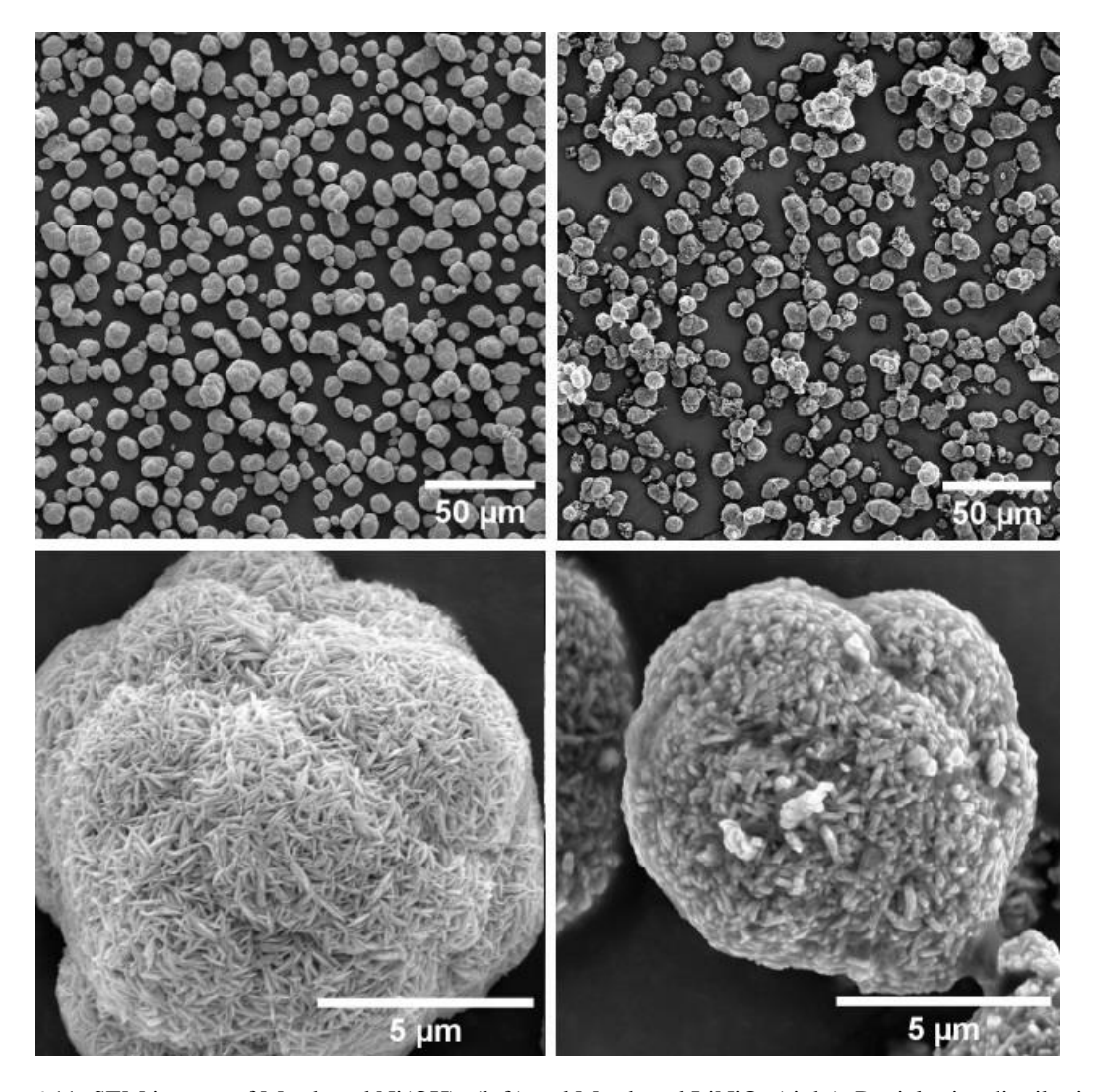


Figure 6.11: SEM images of Mn-doped $Ni(OH)_2$ (left) and Mn-doped $LiNiO_2$ (right). Particle size distribution of secondary particle assemblies using smaller magnification in the top row and primary particles at higher magnification in the bottom row.

The lithiated secondary particles still show more elongated primary particles but they seem to stick together within some kind of matrix. Taking an even closer look at the cross-sections via SEM and EDX in Figure 6.12, the precursor primary particles in the core of the secondary particles are randomly aligned with a large layer of radially aligned primary particles towards the surface. The radially aligned layer is smaller for the lithiated sample in the bottom row of Figure 6.12. The Manganese is evenly distributed within the secondary particles for both the precursor and the lithiated sample. Mn⁴⁺ ions are supposed to stabilise the structure during cycling, and this can be seen in Figure 6.13, the differential capacity plot comparing cycle 3 and cycle 100. The intensity of the phase transitions does not change significantly during the long-term cycling, which is also related to the improved capacity retention. Yet, the expected

shift of all transitions towards higher voltages can still be recognised, as the H2/H3 transition during the oxidation is out of the applied potential window, above 4.3 V.

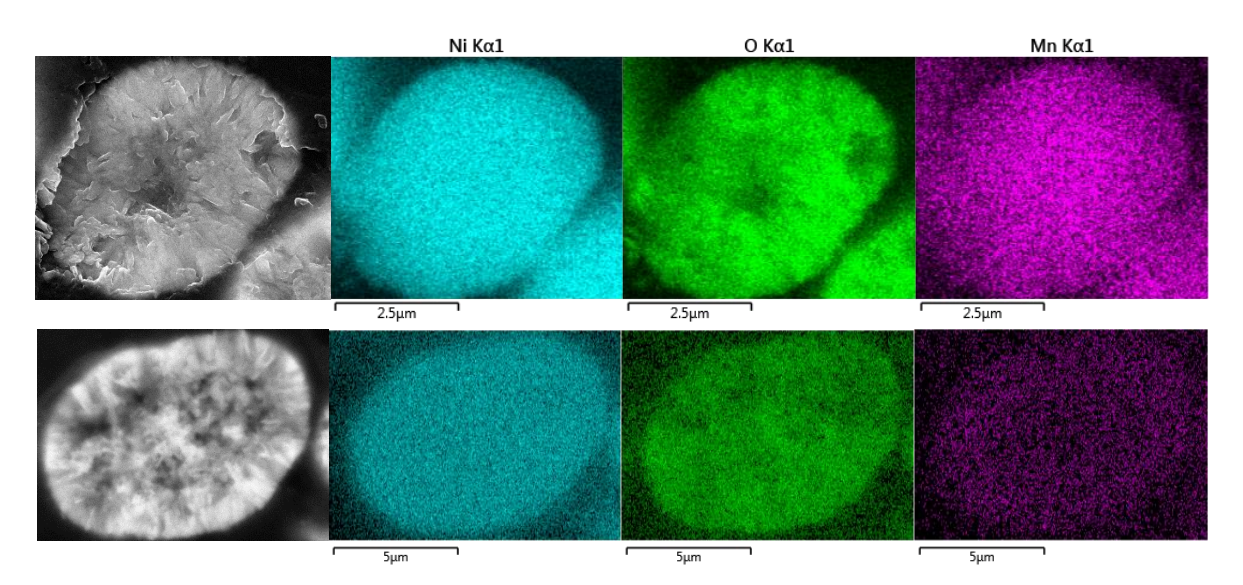


Figure 6.12: SEM image of a particles cross-section (left) and EDX analysis of the cross-section of as-prepared Mn-doped Ni(OH)₂ precursor (top row) and Mn-doped LiNiO₂ (bottom row). Elemental mapping of nickel (turquoise), oxygen (green) and manganese (pink).

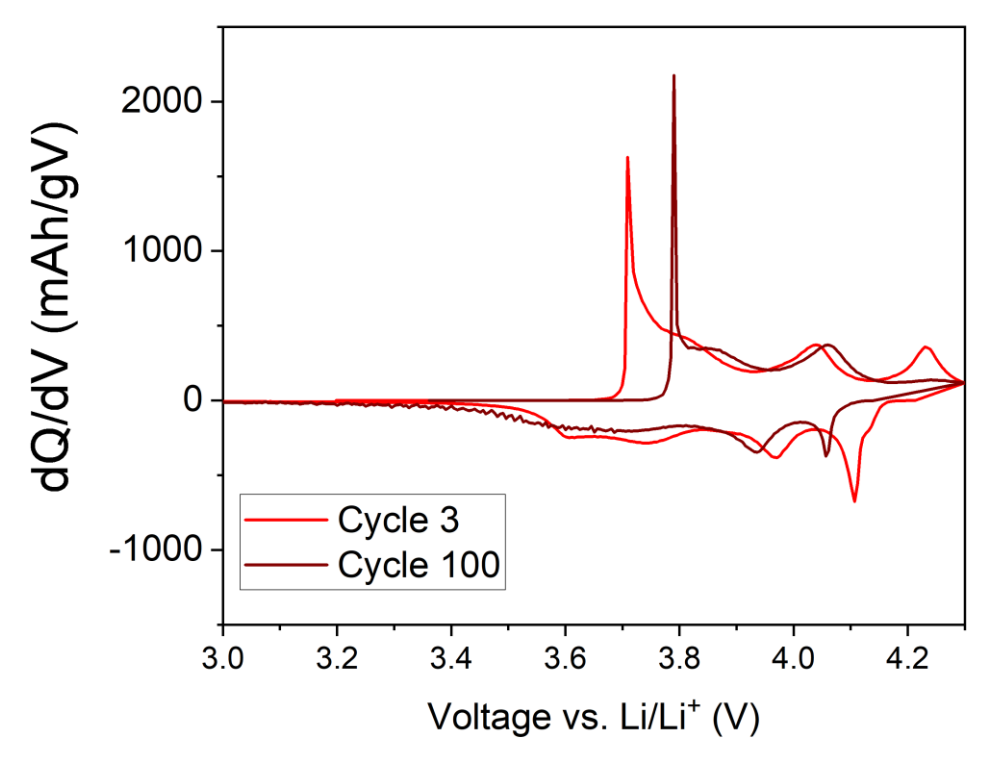


Figure 6.13: Electrochemical data obtained for Mn-doped LiNiO $_2$ synthesised via a solid-state route, pre-calcined for 5 h at 350°C and calcined for 15 h at 710°C. Differential capacity plot dQ/dV comparing cycle 3 and 100. Potential window between 3 – 4.3 V vs. Li/Li $^+$ at a rate of C/20.

6.3.3. Copper-doped LNO

Divalent dopants like Cu²⁺, can reduce the cation mixing as they hinder Ni³⁺ reduction to Ni²⁺ and occupy the sites in the Li layer. Thus, an increased Li spacing, an elongation of the unit cell in the c-axis and consequent better Li diffusion and improved capacity retention is expected. [116] The XRD pattern in Figure 6.14 shows a layered compound that exhibits narrow Bragg peaks at 2θ angles corresponding to the α-NaFeO₂ structure, as well as a Li₂CO₃ side phase. The only visible difference compared to the pattern of the pristine LNO is a decreased intensity of all peaks except (003). Rietveld refinements reveal an increased Li/Ni mixing of 5%, marginally increased unit cell parameters which leads to the lowest c/a ratio in this study, suggesting a less ordered structure. Other studies suggest Cu²⁺ possibly occupying the Li site [117], which could be a reason for a less ordered structure and an increased cation mixing. Correlating these findings to the electrochemical behaviour of the Cu-doped LNO half cells, the initial charge and discharge capacities of 234 and 182 mAh/g, respectively, are on the lower end of this study. A 1st cycle coulombic efficiency of 78% and capacity loss of 54mAh/g complement the mediocre performance. These results coincide with other literature reports, where Cu-doping leads to poor electrochemical behaviour as well as structural instabilities. [119]

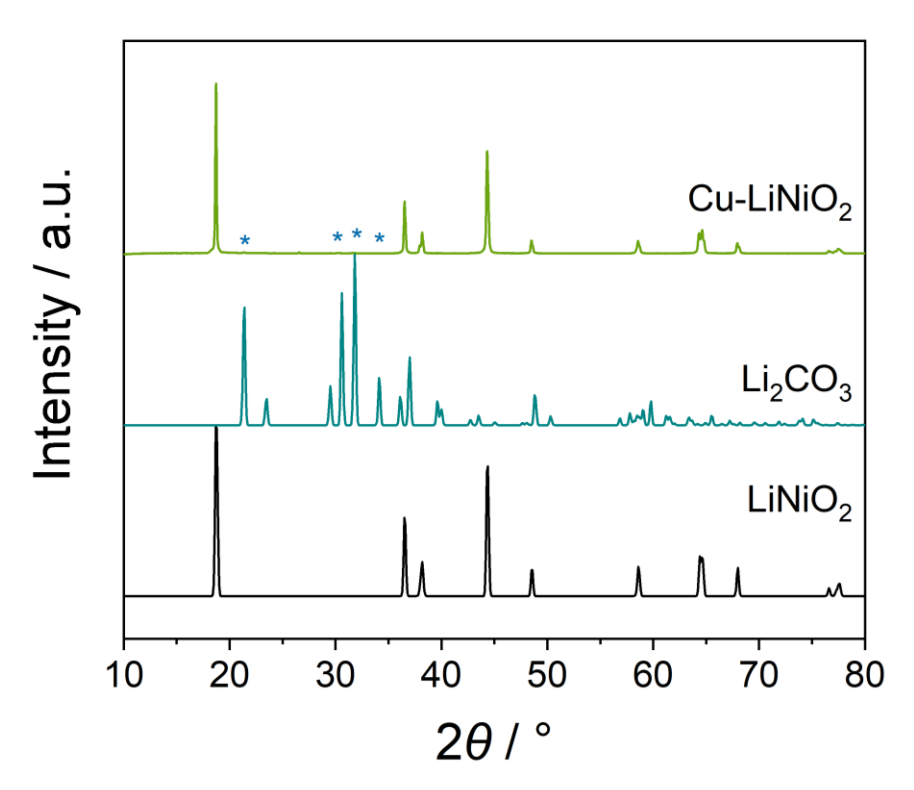


Figure 6.14: XRD pattern of Cu-doped LiNiO₂, pre-calcined for 5 h at 350°C and calcined for 15 h at 710°C. Calculated LiNiO₂ (black, collection code 78687 [187])) and Li₂CO₃ (turquoise, collection code 100324 [185]) patterns from ICSD for comparison. Asterisks mark corresponding Bragg peaks.

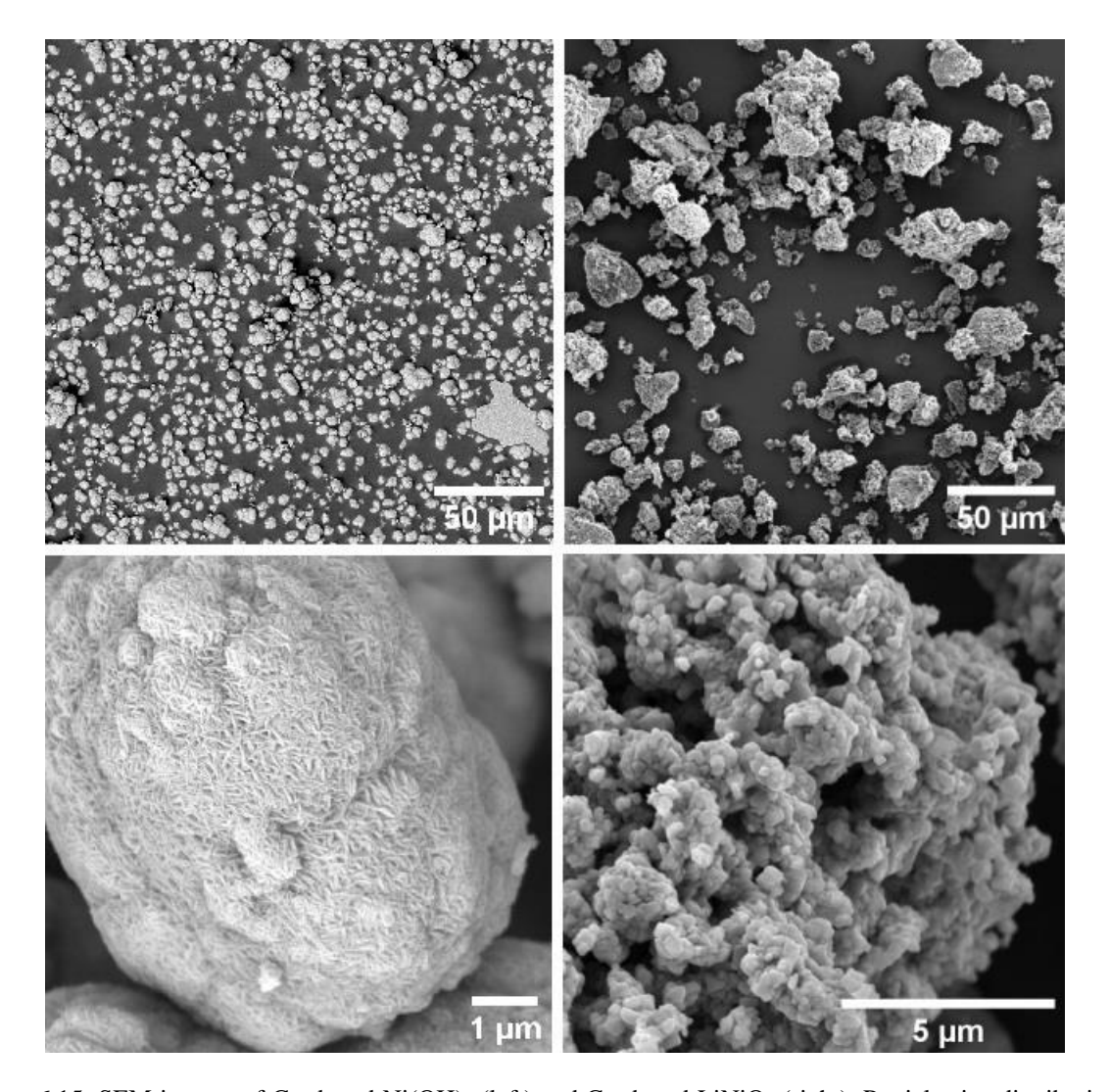


Figure 6.15: SEM images of Cu-doped $Ni(OH)_2$ (left) and Cu-doped $LiNiO_2$ (right). Particle size distribution of secondary particle assemblies using smaller magnification in the top row and primary particles at higher magnification in the bottom row.

The obtained SEM and EDX observations in Figure 6.15 and Figure 6.16 show chunks of particles rather than spherical agglomerations of primary particles for both precursor and lithiated material. It is hard to detect primary particles in the precursor material, yet the lithiated material shows cube-like primary particles apparently densely packed secondary particle assemblies with big voids. EDX analysis suggests an even distribution of Cu.

The electrochemical long-term cycling of the cells using Cu-doped LiNiO₂ cathodes is further shown in the differential capacity plot in Figure 6.17. As expected from the high cation mixing in the structure, the peak usually located at around 3.9 V before the M/H2 transition, is absent. Nevertheless, the Cu-doping seems to supress the H2/H3 transition at 4 V in cycle 3, leading to an increased capacity retention over 100 cycles. Further investigations are needed to evaluate

the location of the Cu ions and find the optimal dopant concentration to improve the cycling performance.

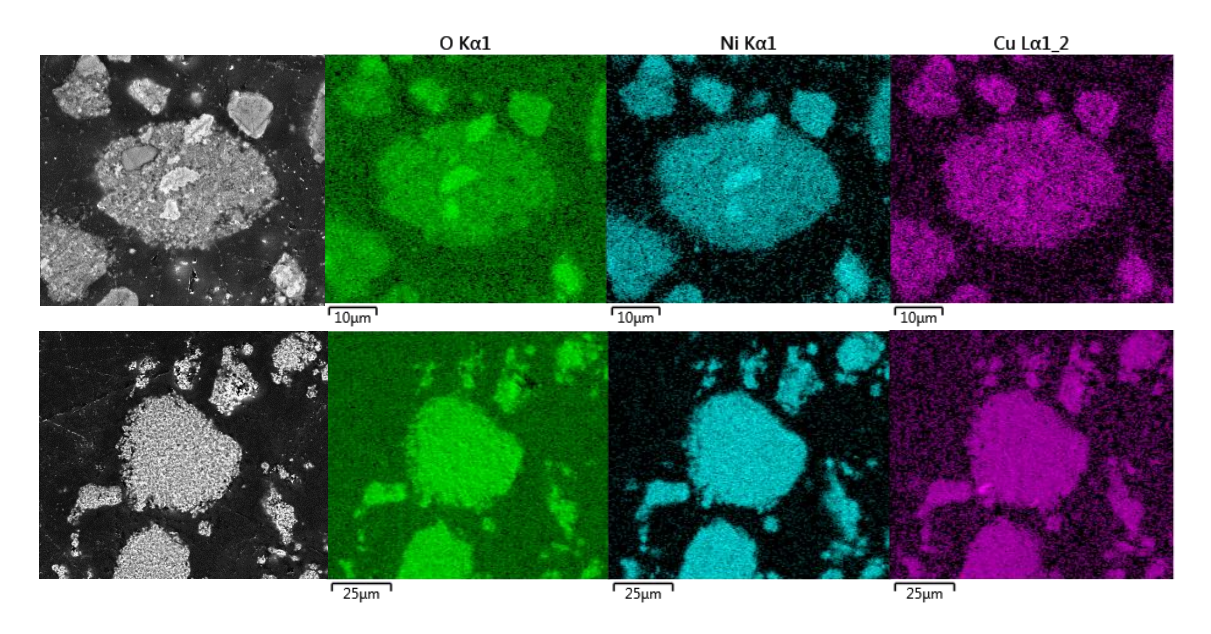


Figure 6.16: SEM image of a particles cross-section (left) and EDX analysis of the cross-section of as-prepared Cu-doped Ni(OH)₂ precursor (top row) and Cu-doped LiNiO₂ (bottom row). Elemental mapping of nickel (turquoise), oxygen (green) and copper (pink).

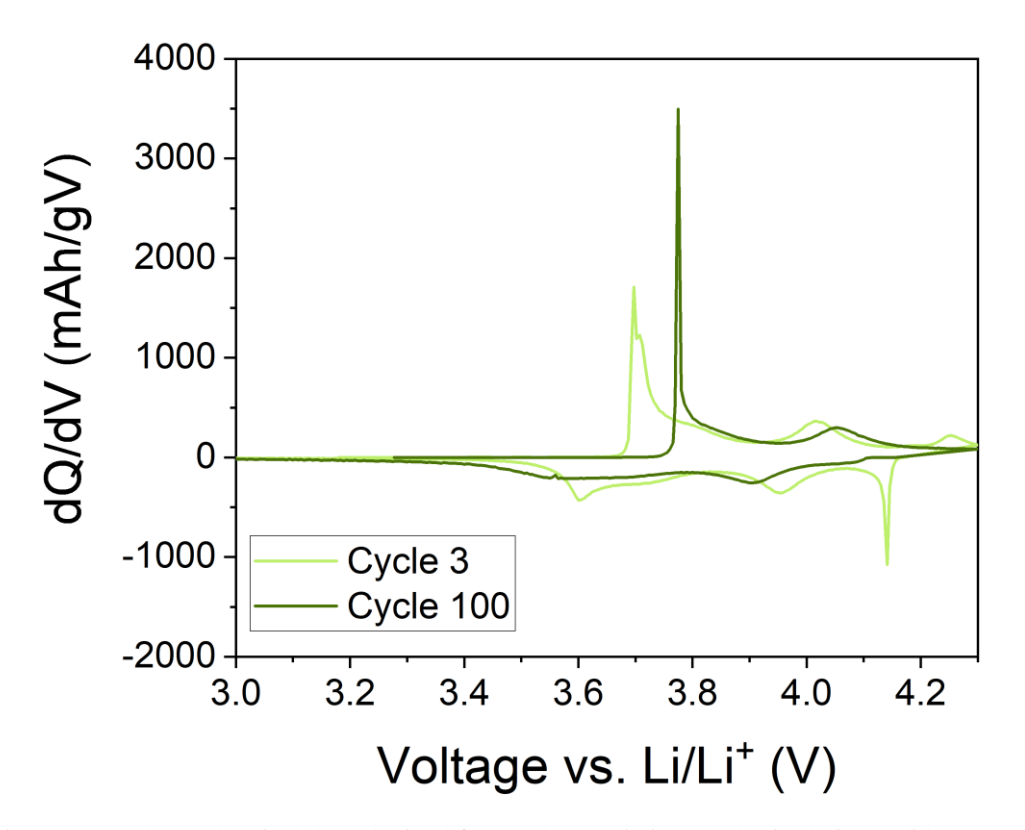


Figure 6.17: Electrochemical data obtained for Cu-doped LiNiO $_2$ synthesised via a solid-state route, pre-calcined for 5h at 350°C and calcined for 15h at 710°C. Differential capacity plot dQ/dV comparing cycle 3 and 100. Potential window between $3-4.3\,V$ vs. Li/Li $^+$ at a rate of C/20.

6.3.4. Zinc-doped LNO

Zn, as well as copper, is integrated into the layered structure as a divalent ion, sitting on the Ni³⁺ sites, preventing the parasitic Ni²⁺ movement into the Li layer and improving Li diffusion by increasing the Li slab spacing. [98] [124] Yet again, Zn²⁺ might also be able to sit on Li sites, which on the one hand can improve the structural stability but also lead to decreased capacities and overall cycling performances. The XRD pattern in Figure 6.18 shows a phase-pure compound. In the Cu-doped material, the unit cell is slightly enlarged suggesting improved Li diffusion as literature reports states. [122] [123] The Li/Ni mixing is low with only 3% and the first cycle charge and discharge capacities are 273 and 203 mAh/g with a first cycle capacity loss of 70 mAh/g and an improved capacity retention of 83%.

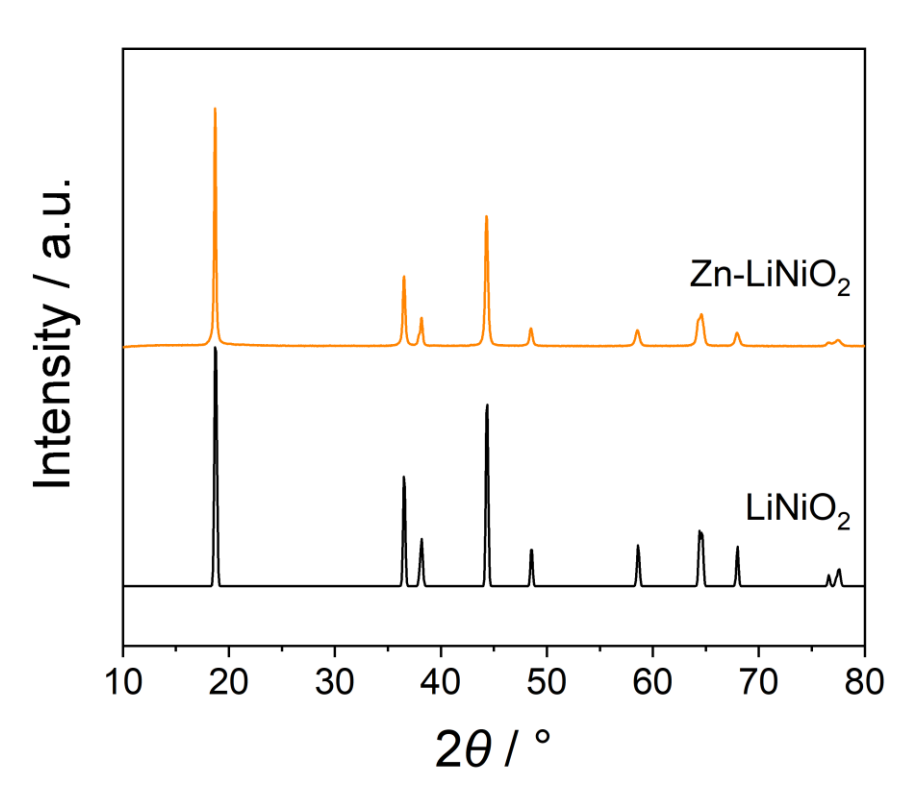


Figure 6.18: XRD pattern of Zn-doped LiNiO₂, pre-calcined for 5 h at 350°C and calcined for 15 h at 710°C. Calculated LiNiO₂ (black, collection code 78687 [187])) pattern from ICSD for comparison.

The particle morphology of the 3 % Zn-doped precursor (Figure 6.19 left) and Zn-LNO (Figure 6.19 right), exhibits small spherical secondary particles with a narrow size distribution. The primary particles are small and seemingly dense packed. The EDX images in Figure 6.20 show an even distribution of the Zn dopant overall and the cross-section images suggest a core of randomly aligned primary particles and a broad layer of radially aligned primary particles, for both, precursor and lithiated material.

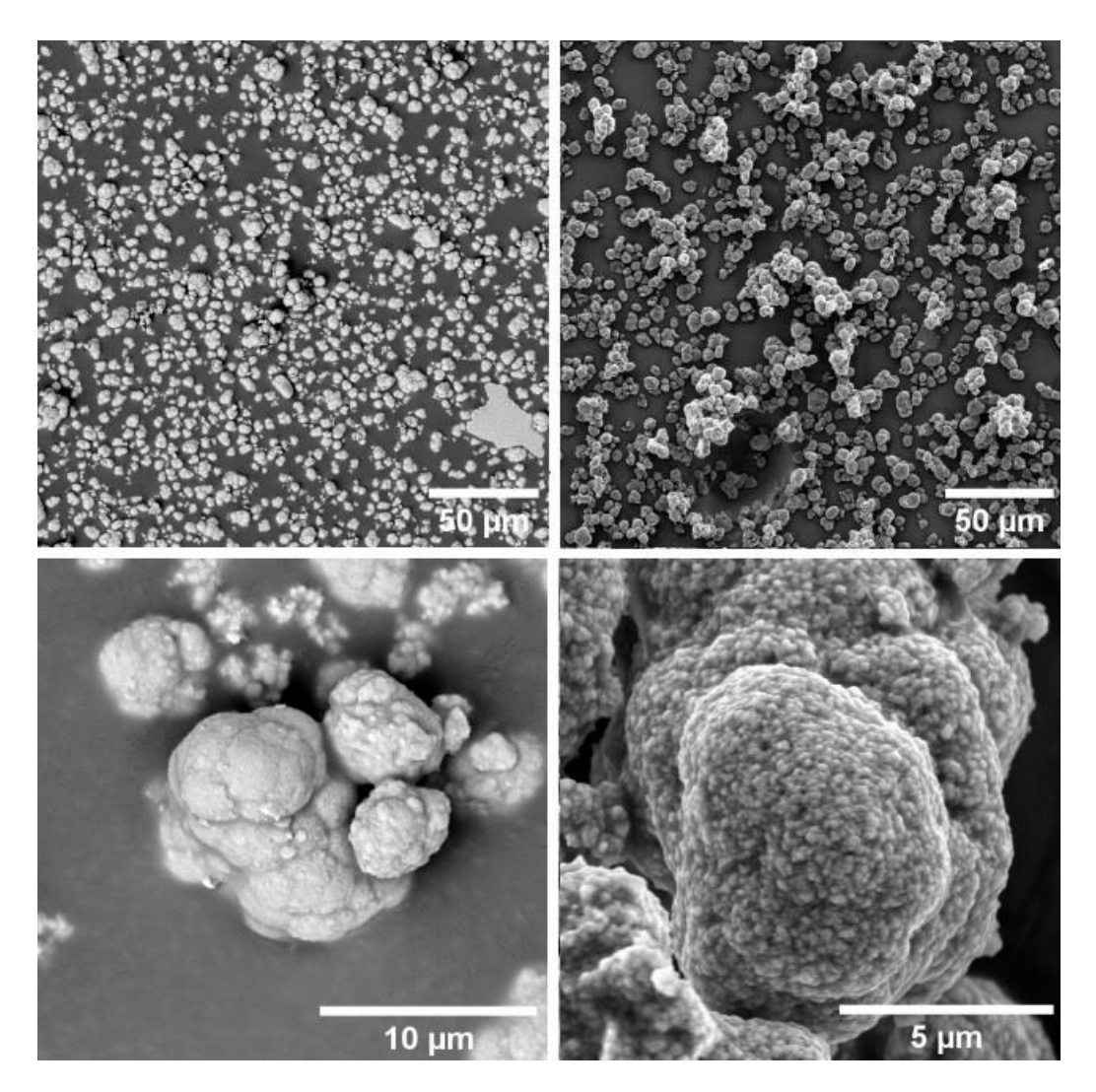


Figure 6.19: SEM images of Zn-doped $Ni(OH)_2$ (left) and Zn-doped $LiNiO_2$ (right). Particle size distribution of secondary particle assemblies using smaller magnification in the top row and primary particles at higher magnification in the bottom row.

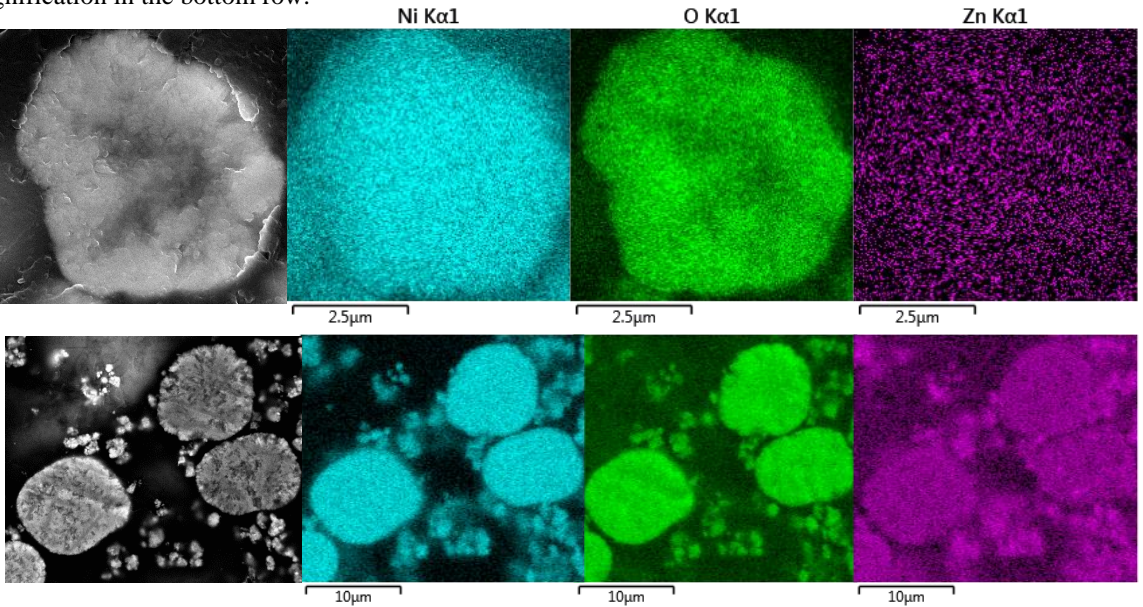


Figure 6.20: SEM image of a particles cross-section (left) and EDX analysis of the cross-section of as-prepared Zn-doped Ni(OH)₂ precursor (top row) and Zn-doped LiNiO₂ (bottom row). Elemental mapping of nickel (turquoise), oxygen (green) and zinc (pink).

The dQ/dV plot of the Zn-doped LiNiO₂ cathodes in Figure 6.21 show very low intensities for the phase transitions and a very narrow monoclinic region. The H2/H3 transition is suppressed already during the 3rd cycle and even more during cycle 100 for both, oxidation and reduction, entailing the improved capacity retention over 100 cycles of 83%.

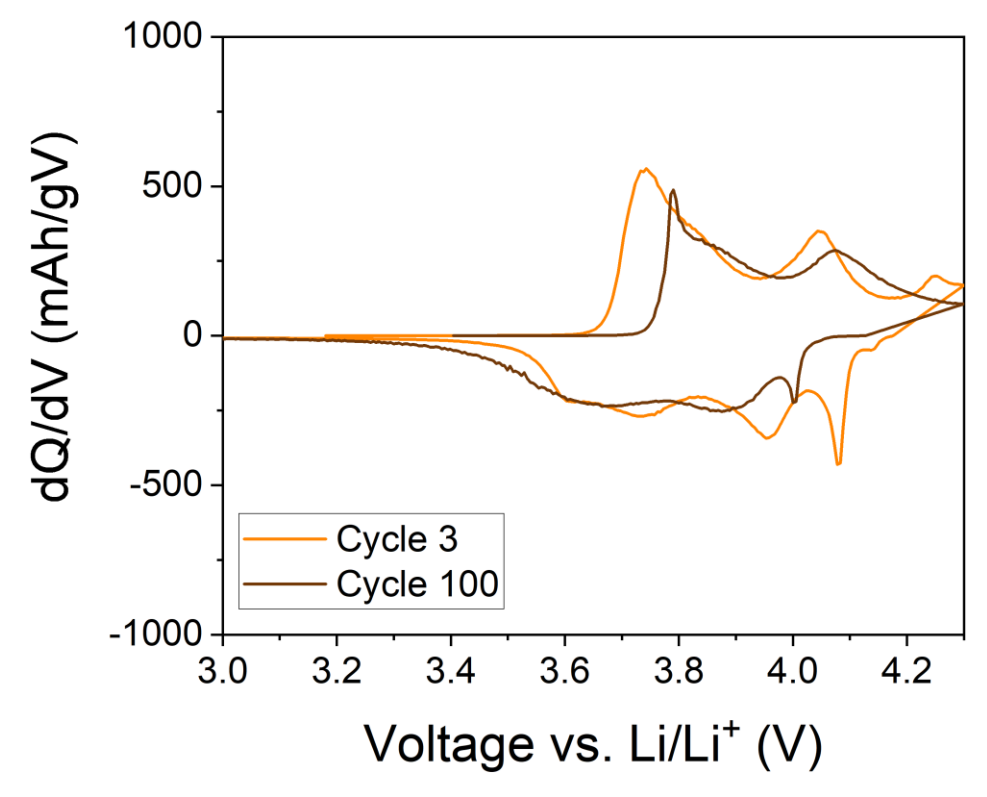


Figure 6.21: Electrochemical data obtained for Zn-doped LiNiO $_2$ synthesised via a solid-state route, pre-calcined for 5h at 350°C and calcined for 15h at 710°C. Differential capacity plot dQ/dV comparing cycle 3 and 100. Potential window between 3 – 4.3 V vs. Li/Li $^+$ at a rate of C/20.

6.3.5. Tin-doped LNO

The following dopants, tin, zirconium and titanium, substitute into the layered oxide lattice as tetravalent ions. Literature suggests a Sn-containing side phase Li₂SnO₃ [129] [130] [133] which cannot be confirmed here (Figure 6.22). The as-prepared Sn-doped LNO does not show any signs of a Sn-containing side phase, yet it does show additional peaks that match with the Bragg peaks of Li₂CO₃. Rietveld refinements detect a cation mixing of 2.8%, which is low in agreement with other literature results [130] [133]. A lattice volume of 102.3 Å³ suggests improved Li diffusion and an increased capacity retention. The initial charge and discharge capacity of 315 and 278 mAh/g, respectively, exceeding the theoretical capacity of LNO, which could be due to additional Li being present from the side phase. A first cycle coulombic efficiency of 88% is one of the highest in this study.

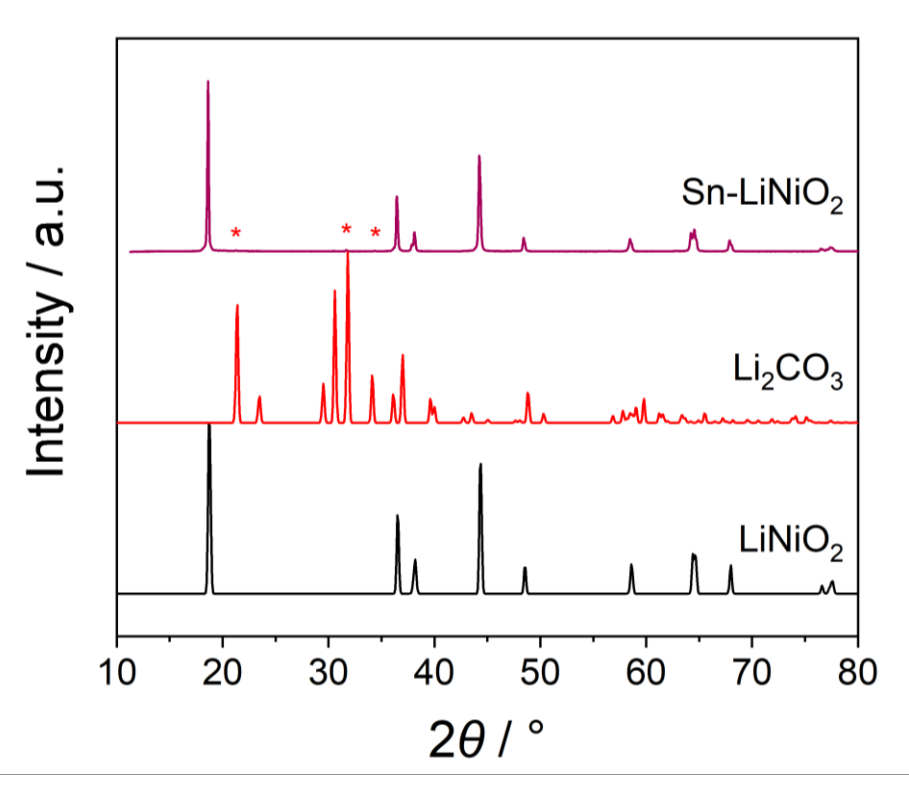


Figure 6.22: XRD pattern of Sn-doped LiNiO₂, pre-calcined for 5h at 350°C and calcined for 15h at 710°C. Calculated LiNiO₂ (black, collection code 78687 [187])) and Li₂CO₃ (red, collection code 100324 [185]) patterns from ICSD for comparison. Asterisks mark corresponding Bragg peaks.

SEM images of the particle morphology in Figure 6.23 show spherical secondary particles for the precursor material (left) as well as the lithiated sample (right). Although the primary particles are hard to distinguish in the precursor, the images on the right appear to be densely packed cubic primary particles in an even size distribution. The similarity to the undoped material is exceptional.

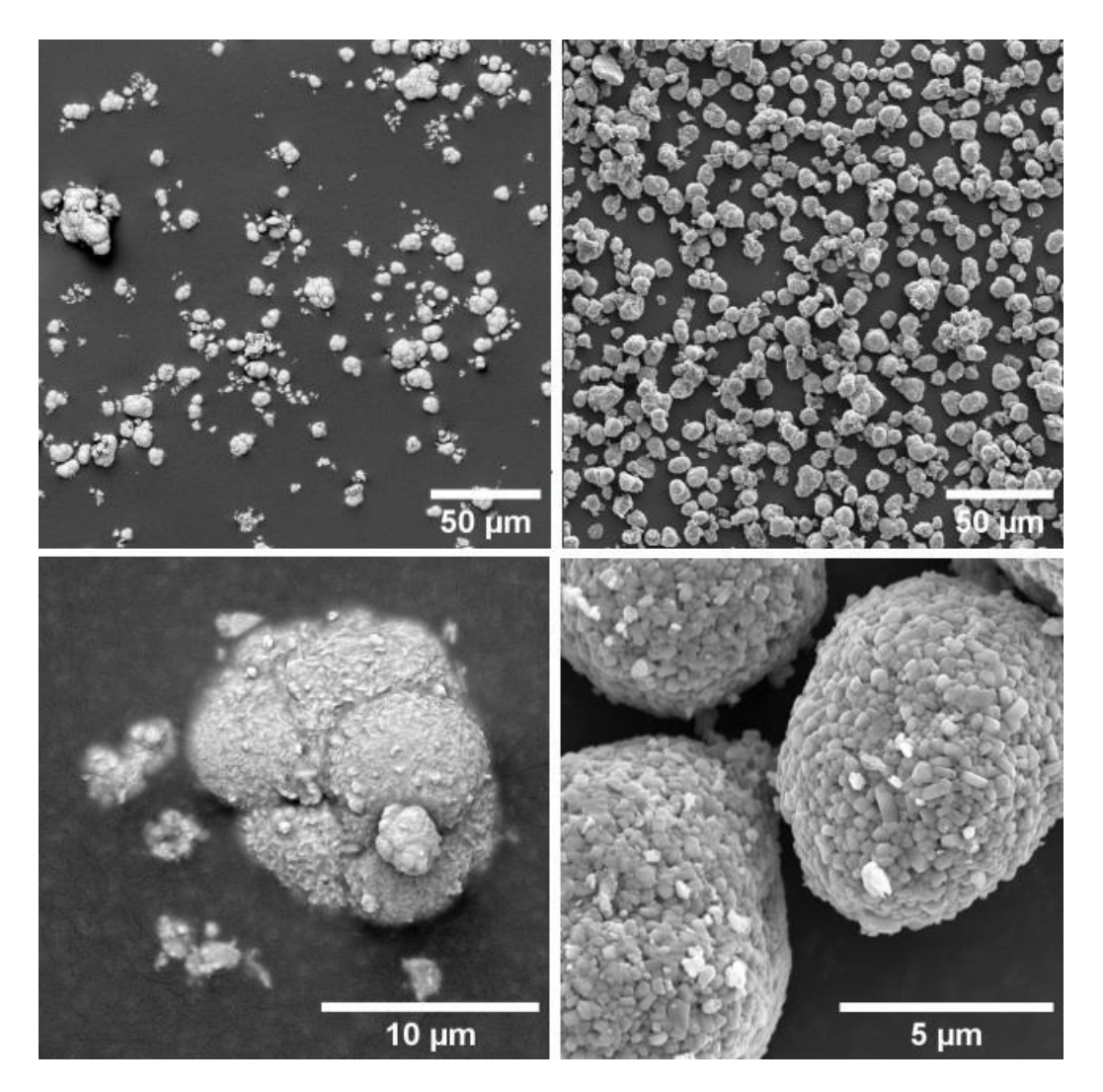


Figure 6.23: SEM images of Sn-doped Ni(OH)₂ (left) and Sn-doped LiNiO₂ (right). Particle size distribution of secondary particle assemblies using smaller magnification in the top row and primary particles at higher magnification in the bottom row.

Additional EDX investigations show an even distribution of the Sn dopant over the particle cross-section in Figure 6.24. These images suggest a small core of randomly aligned particles and radially aligned primary particles towards the surface of the secondary particle, improving Li diffusion. The Sn-O bond dissociation energy is increased compared to the pristine material [129] [132] [133], suggesting suppressed oxygen loss and a stabilised structure for the tetravalent cations mixed into LNO. This can be confirmed, looking at the capacity retention of 78% over 100 cycles. The differential capacity plot in Figure 6.25 of the Sn-doped LiNiO₂, shows the additional peak at 3.93 V that stems from a low cation mixing as well as a slightly suppressed H2/H3 transition at 4.18 V. Moving to the 100th cycle, the H2/H3 transition moved out of the investigated potential window.

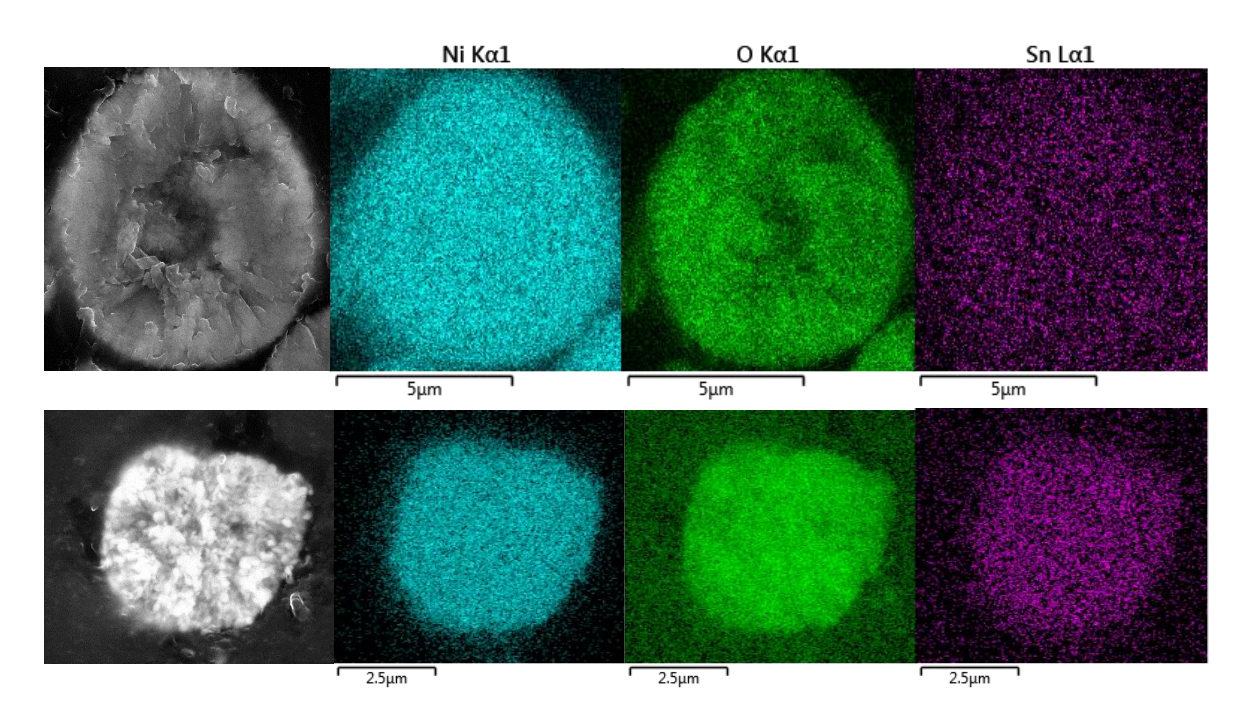


Figure 6.24: SEM image of a particles cross-section (left) and EDX analysis of the cross-section of as-prepared Sn-doped Ni(OH)₂ precursor (top row) and Sn-doped LiNiO₂ (bottom row). Elemental mapping of nickel (turquoise), oxygen (green) and tin (pink).

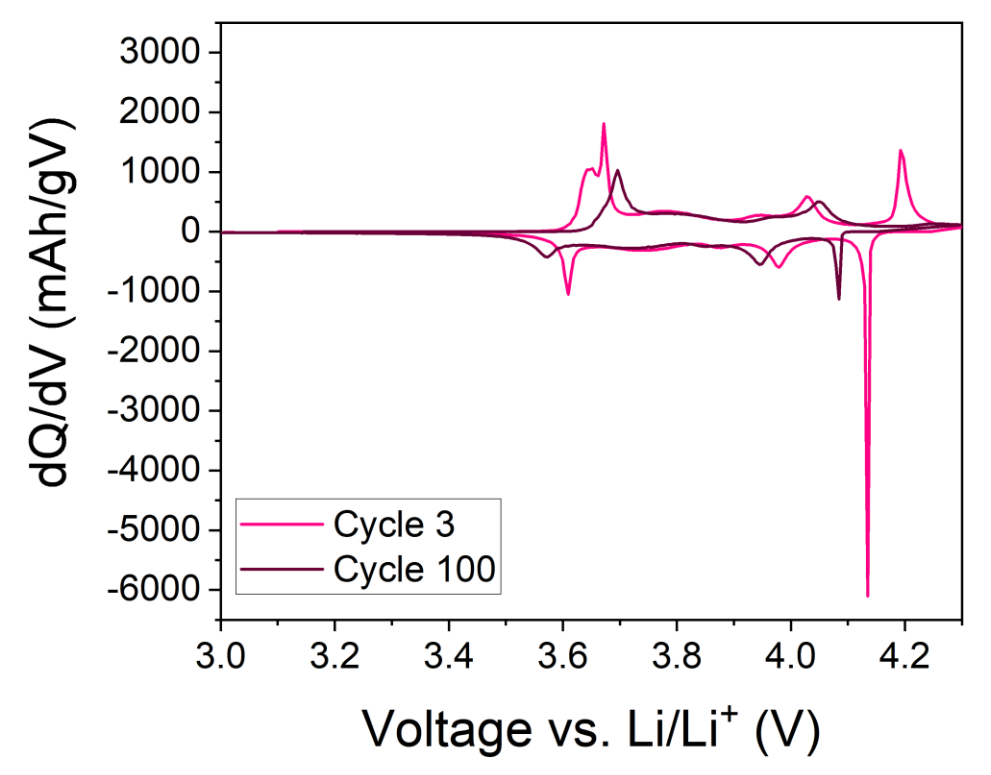


Figure 6.25: Electrochemical data obtained for Sn-doped LiNiO₂ synthesised via a solid-state route, pre-calcined for 5 h at 350°C and calcined for 15 h at 710°C. Differential capacity plot dQ/dV for the first, second and third cycle. Potential window between $3-4.3\,V$ vs. Li/Li⁺ at a rate of C/20.

6.3.6. Zirconium-doped LNO

Another tetravalent ion that is doped into the layered structure of LiNiO₂ via co-precipitation of the precursor Ni(OH)₂, is zirconium. A Li₂ZrO₃ side-phase can be detected in the as-prepared material as can be seen in Figure 6.26. This material is used in literature to coat layered oxides [135] and it is seen to decrease the cation mixing. [138] Rietveld refinements determine a cation mixing of 3.3% and improved Li spacing in the structure due to an elongated unit cell in *c*-direction. The first cycle charge and discharge capacity is 246 and 229 mAh/g, respectively, with an irreversible capacity loss of only 17 mAh/g and a first cycle coulombic efficiency of 85%.

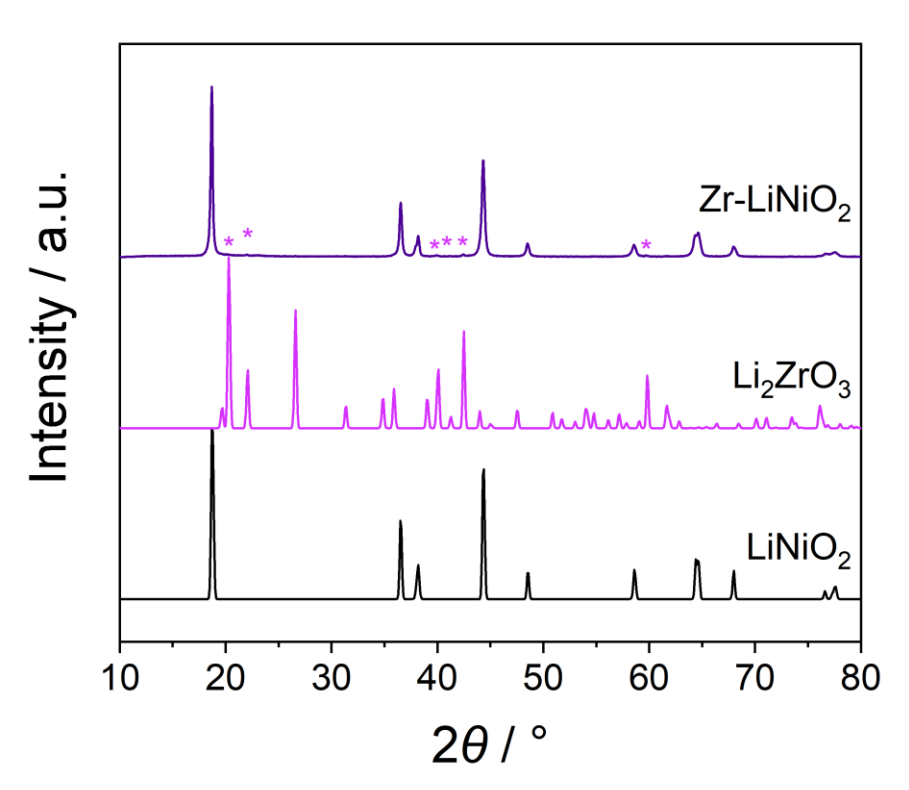


Figure 6.26: XRD pattern of Zr-doped LiNiO₂, pre-calcined for 5 h at 350°C and calcined for 15 h at 710°C. Calculated LiNiO₂ (black, collection code 78687 [187]) and Li₂ZrO₃ (pink, collection code 94893 [209]) patterns from ICSD for comparison. Asterisks mark corresponding Bragg peaks.

The visual inspection of the particle morphology can be seen in Figure 6.27. The secondary particle assemblies are elongated spherical but also large chunks of material without a specific form are present. The surface of the secondary precursor particles seems to be smoothed out, the primary particles are not easy to detect, but they are elongated and needle-like. The EDX analysis in the top row of Figure 6.28 shows an increased amount of Zr at the surface of the secondary precursor particles. The lithiated material still has elongated needle-like primary

particles and EDX images suggest that the Zr formed the side phase Li₂ZrO₃ as concentrated regions or separate small particles on top of the secondary Zr-LNO particles. The cross-section images show a layer of radially aligned primary particles around a small core of randomly aligned particles for the precursor, as well as the lithiated material.

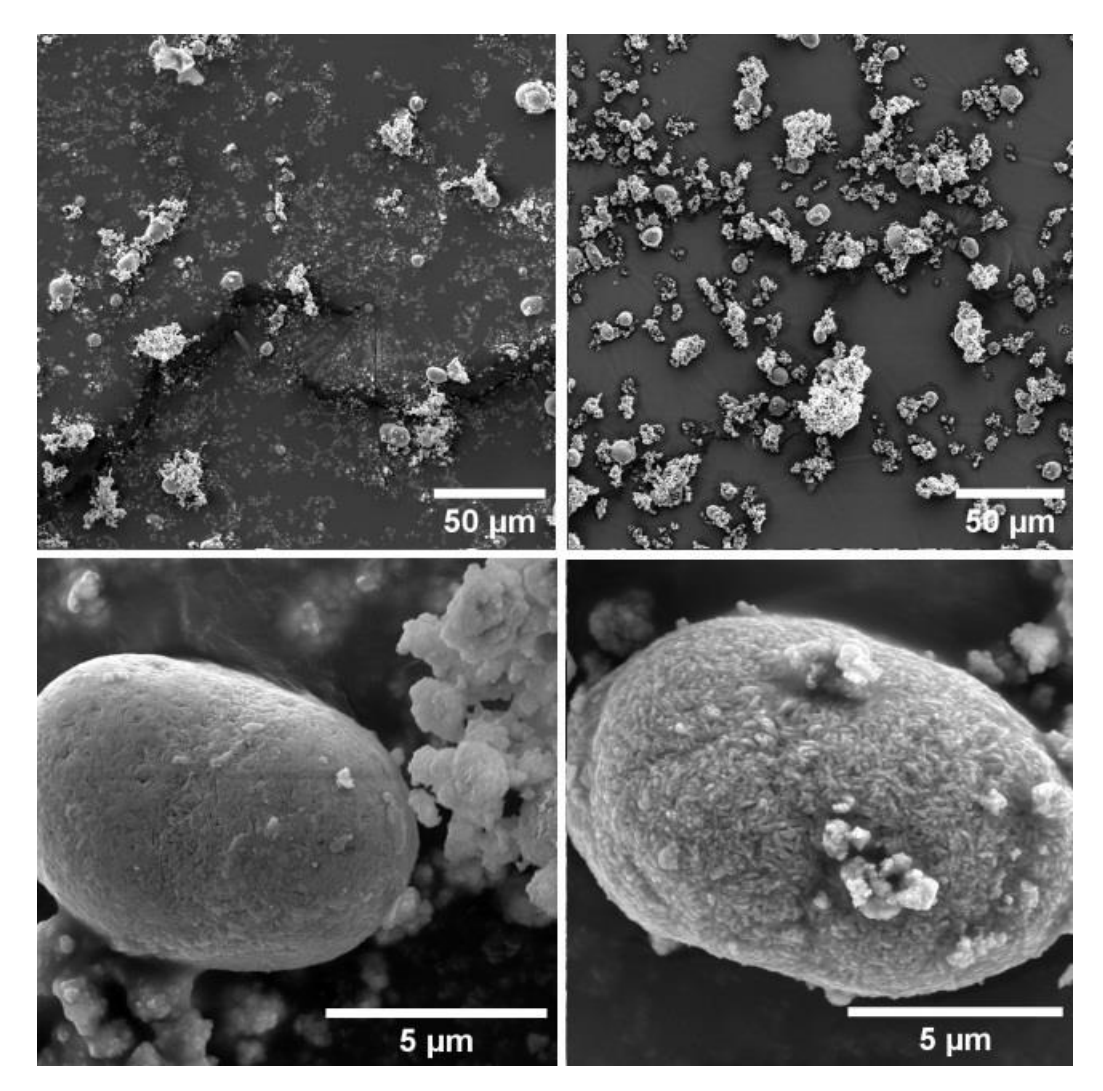


Figure 6.27: SEM images of Zr-doped $Ni(OH)_2$ (left) and Zr-doped $LiNiO_2$ (right). Particle size distribution of secondary particle assemblies using smaller magnification in the top row and primary particles at higher magnification in the bottom row.

Although the cation mixing in this compound is quite low, the peak associated with a lower cation mixing at around 3.9 V, can only be recognised as the shoulder of the M/H2 transition at 4.02 V in the differential capacity plot in Figure 6.29. The peaks, both during oxidation as well as reduction, shift towards higher voltages from cycle 3 to 100, yet the shift is only marginally. The H2/H3 transition is still within the potential window at cycle 100.

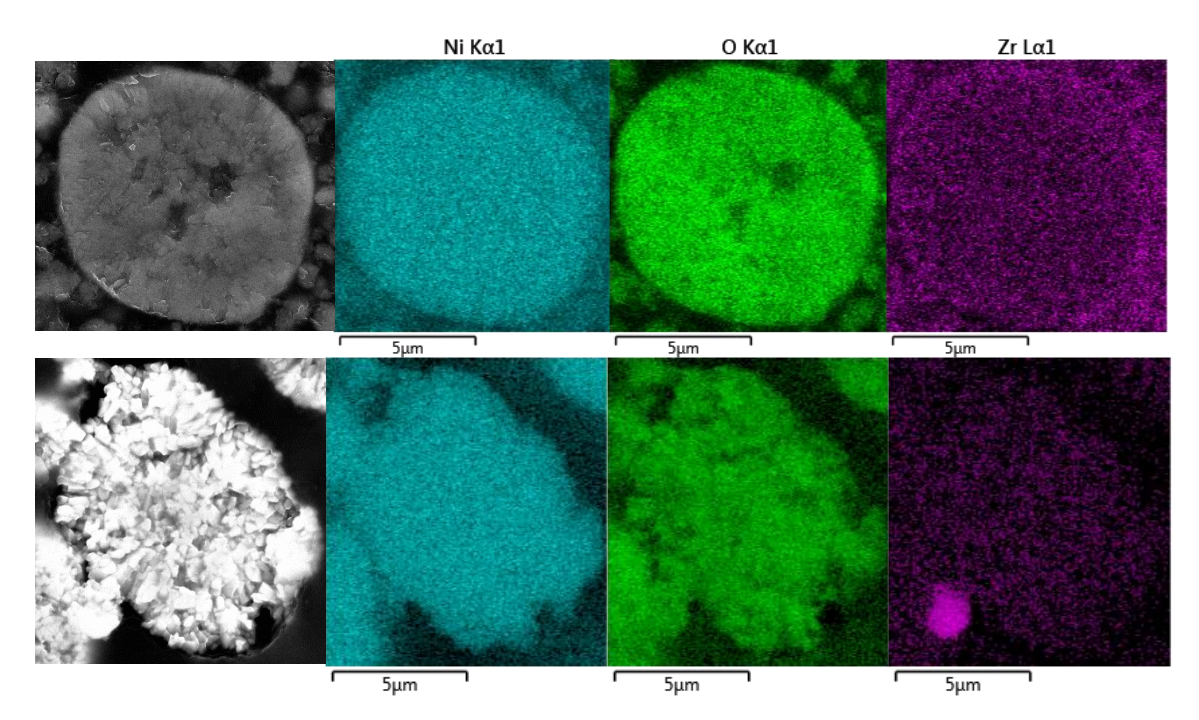


Figure 6.28: SEM image of a particles cross-section (left) and EDX analysis of the cross-section of as-prepared Zr-doped Ni(OH)₂ precursor (top row) and Zr-doped LiNiO₂ (bottom row). Elemental mapping of nickel (turquoise), oxygen (green) and zirconium (pink).

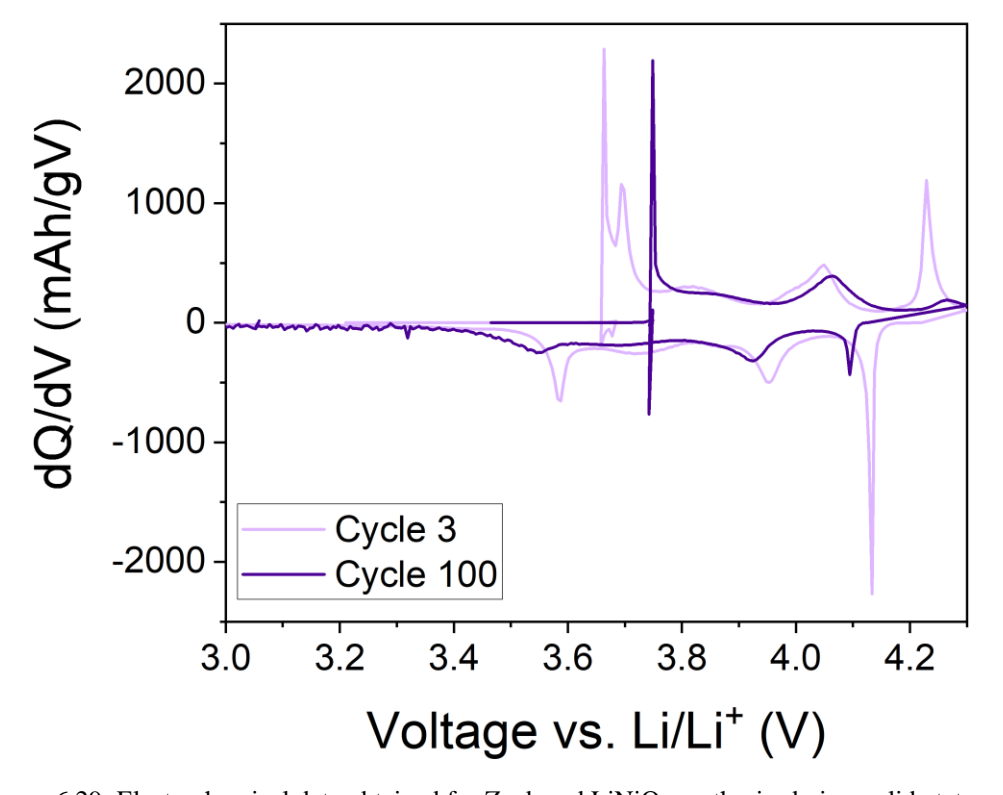


Figure 6.29: Electrochemical data obtained for Zr-doped LiNiO₂ synthesised via a solid-state route, pre-calcined for 5 h at 350°C and calcined for 15 h at 710°C. Differential capacity plot dQ/dV for the first, second and third cycle. Potential window between $3-4.3\,V$ vs. Li/Li⁺ at a rate of C/20.

6.3.7. Titanium-doped LNO

Figure 6.30 compares the as-prepared Ti-doped LiNiO₂ powder XRD pattern with an undoped LiNiO₂ and LiNiO_{1.7}Ti_{0.3}O₂ pattern from the ICS database. In all depicted compounds, the Bragg peaks associated with the layered $R\overline{3}m$ structure are located at the corresponding angles. No side phase can be detected. For a higher Ti doping, the peak intensities of the (003) and (104) peaks change as can be seen in the LiNi_{0.7}Ti_{0.3}O₂ pattern, yet this is not happening for a 3 % doping. Rietveld refinements of this as-measured pattern, determines a Li/Ni mixing of 2.7 % and slightly increased unit cell parameters. These findings are in accordance with literature. [141] [145] The first charge and discharge capacities of 249 and 195 mAh/g, respectively, and the first cycle capacity loss of 54 mAh/g shows good cycling behaviour. A low irreversible capacity loss in the first cycle as suggested by literature [142] could not be confirmed, compared to other samples in this study.

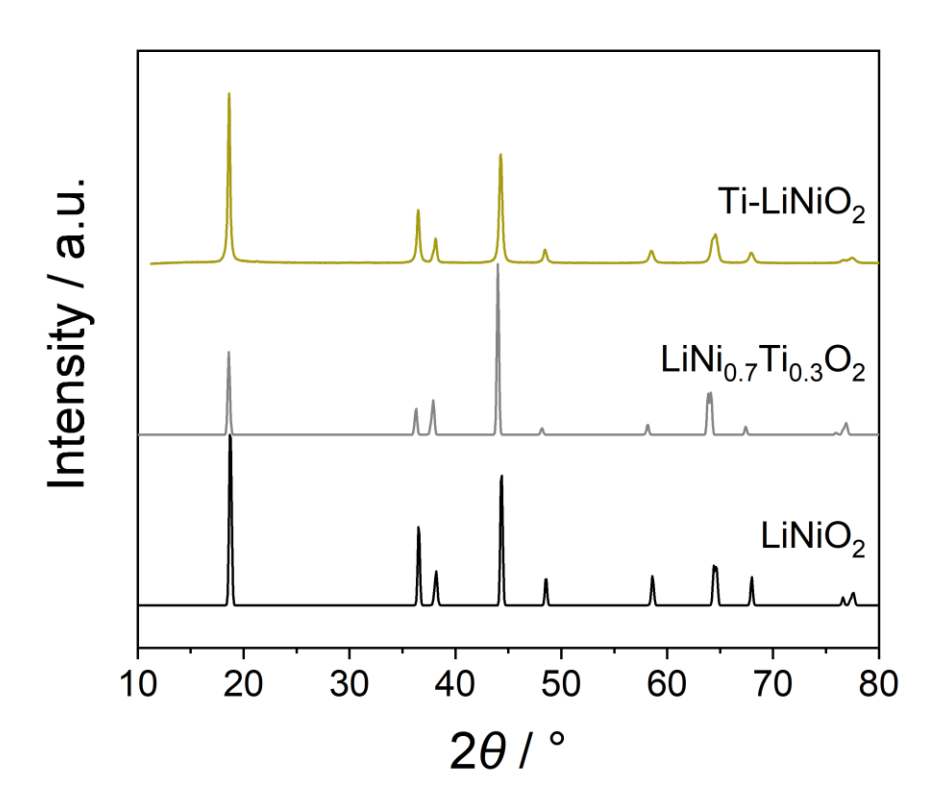


Figure 6.30: XRD pattern of Ti-doped LiNiO₂, pre-calcined for 5 h at 350°C and calcined for 15 h at 710°C. Calculated LiNiO₂ (black, collection code 78687 [187])) and LiNi_{0.7}Ti_{0.3}O₂ (grey, collection code 83283 [210]) patterns from ICSD for comparison.

SEM images in Figure 6.31 depict spherical secondary particles with a narrow particle size distribution for the precursor as well as the lithiated material. The higher magnification of the particles in the bottom row of Figure 6.31, show elongated, needle-like densely packed primary

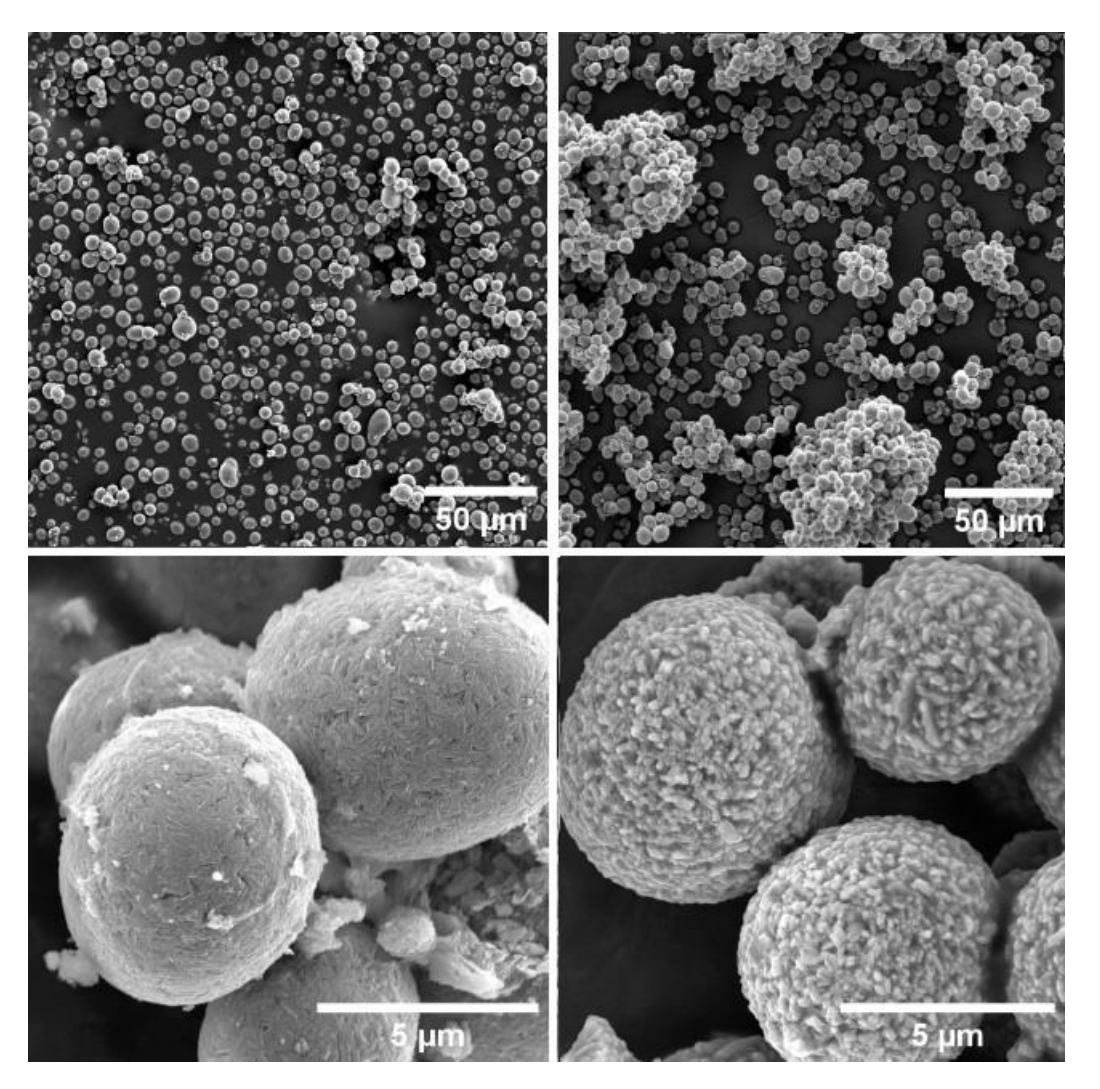


Figure 6.31: SEM images of Ti-doped $Ni(OH)_2$ (left) and Ti-doped $LiNiO_2$ (right). Particle size distribution of secondary particle assemblies using smaller magnification in the top row and primary particles at higher magnification in the bottom row.

particles for the precursor on the left and densely packed, small cubic primary particles within the lithiated sample on the right. The EDX analysis (Figure 6.32) shows an even distribution of Ti throughout the particles and the cross-sections reveal a core of randomly aligned primary particles and radially aligned ones towards the surface, for both, the precursor and the lithiated material. Similar to the Zr doped sample, the dQ/dV plot in Figure 6.33, does not show the peak related to a low cation mixing and the H2/H3 transition is still within the potential window after 100 cycles. Nevertheless, the intensity of the detrimental H2/H3 transition is low from cycle 3 already, increasing the overall structural stability and reflecting in the extraordinary capacity retention of 88% after 100 cycles.

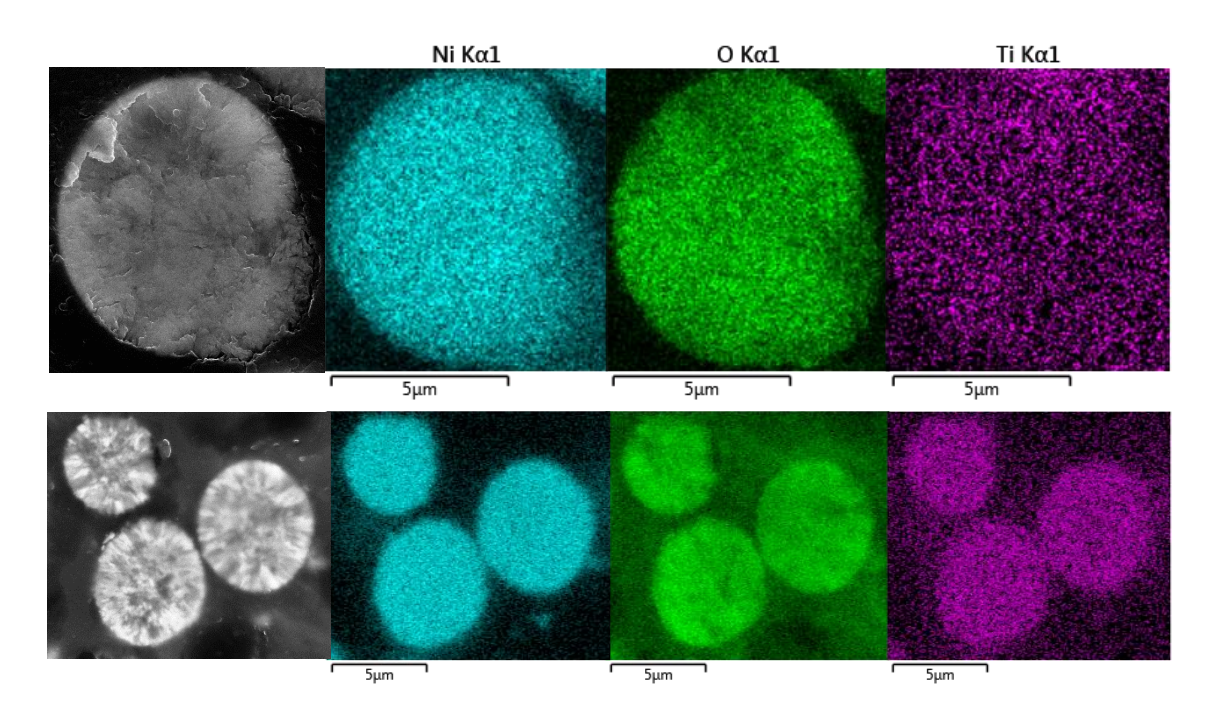


Figure 6.32: SEM image of a particles cross-section (left) and EDX analysis of the cross-section of as-prepared Ti-doped $Ni(OH)_2$ precursor (top row) and Ti-doped $LiNiO_2$ (bottom row). Elemental mapping of nickel (turquoise), oxygen (green) and titanium (pink).

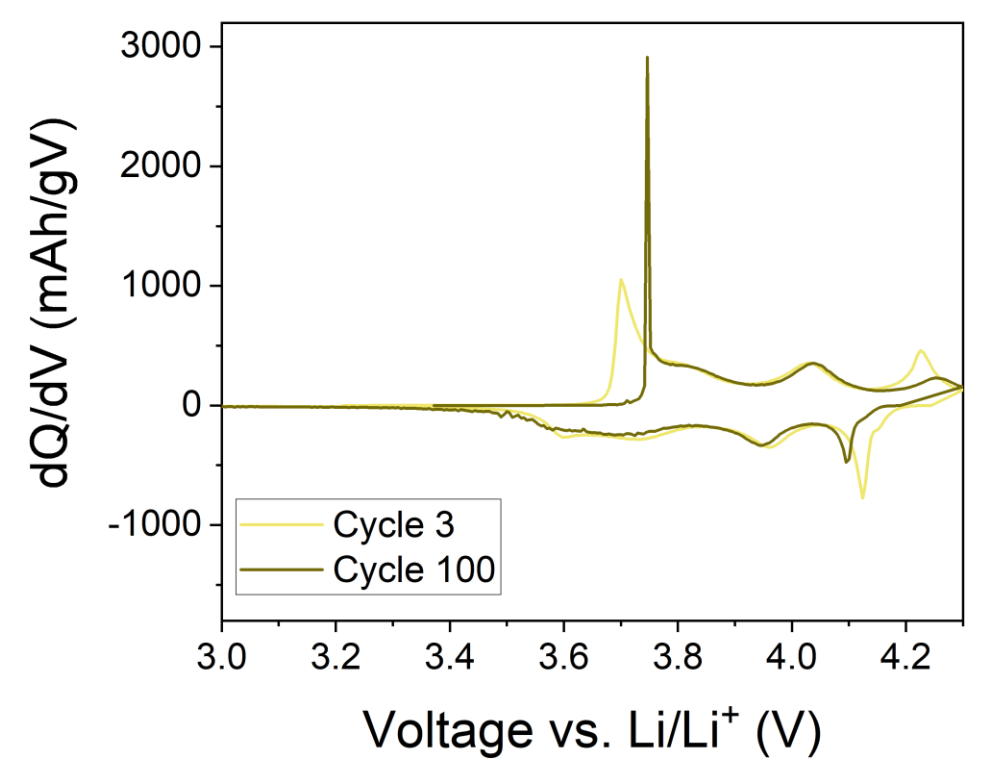


Figure 6.33: Electrochemical data obtained for Ti-doped LiNiO₂ synthesised via a solid-state route, pre-calcined for 5h at 350° C and calcined for 15h at 710° C. Differential capacity plot dQ/dV comparing cycle 3 and 100. Potential window between $3-4.3\,\text{V}$ vs. Li/Li⁺ at a rate of C/20.

6.3.8. Tungsten-doped LNO

The obtained powder XRD pattern of the as-prepared W-doped LiNiO₂ sample can be seen in Figure 6.34. Compared to patterns of undoped LNO and 1% W-doped LNO derived from the ICSD, the Bragg peaks show peak broadening and a decreased intensity of the (003) peak. Yet, no side phase can be determined. From Rietveld refinements (Figure 6.35), an increased cation mixing of 12.7% is derived and the peak analysis gives a (003)/(104) ratio of 1.496, the highest in this experimental setup and not in accordance with the refined values. The peak ratio corresponding to the structural layering, exhibits the highest value in the study as well, which is an indication of poor layering within the structure due to incorporates large W⁶⁺ ions distorting the lattice. These values and observations can be ascribed to the difficulties during the precursor synthesis. The synthesis was carried out in the same way as the other doped samples, dissolving the tungsten source in the nickel sulphate solution. Removing the heat that was added to dissolve the tungsten source, lead to a precipitation of a tungsten compound in the nickel solution. Due to time restrictions, the reaction was performed nevertheless, leaving the TM solution stirring on a hot plate throughout the whole reaction. After the reaction, a tungsten

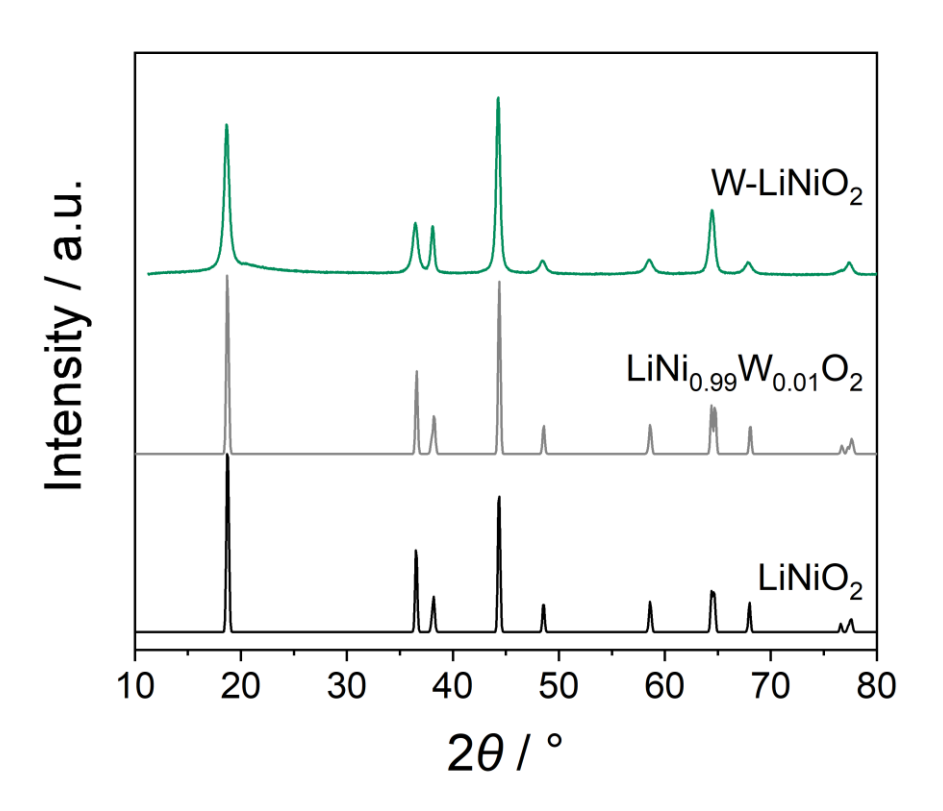


Figure 6.34: XRD pattern of W-doped LiNiO₂, pre-calcined for 5 h at 350°C and calcined for 15 h at 710°C. Calculated LiNiO₂ (black, collection code 78687 [187])) and LiNi_{0.99}W_{0.01}O₂ (grey, collection code 47982 [211]) patterns from ICSD for comparison.

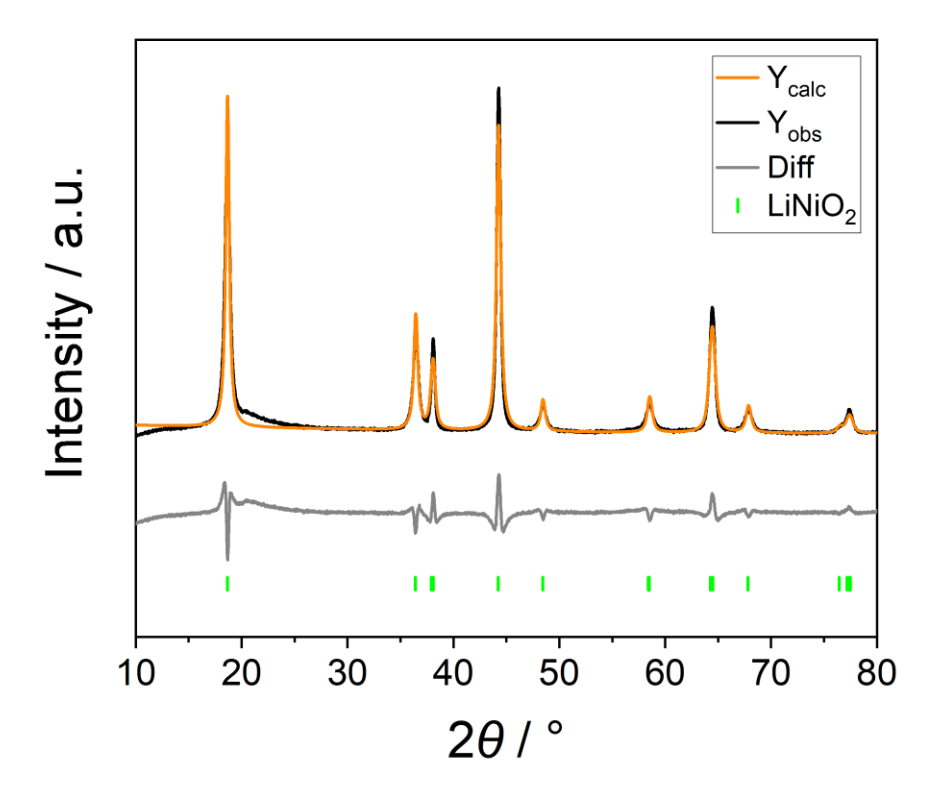


Figure 6.35: Refinement of measured Cu source XRD pattern of W-doped LiNiO₂ Measured pattern (black), calculated pattern of LiNiO₂ (orange, collection code 78687 [187]) and the difference between observed and calculated patterns (grey). Peak positions of LiNiO₂ in green.

containing precipitate remained in the TM solution bottle. Not all of the tungsten was added to the reactor and incorporated in the host structure. In accordance with that, the cell volume is increased to 102.26 Å³. The electrochemical cycling data shows a first cycle charge and discharge capacity of 186 and 170 mAh/g with the lowest 1st cycle loss of 16 mAh/g and the highest 1st cycle coulombic efficiency of 91%. Nevertheless, the capacity retention over 100 cycles indicates the worst performance of all samples in this study, with 69%.

SEM images in Figure 6.36 show very small secondary particles with a narrower particle size distribution and even smaller secondary particles, agglomerating together, for the lithiated sample than for the precursor material. The morphology can be described as cauliflower like. The primary particles can barely be distinguished in the SEM images. EDX studies of cross-sections of the particles in Figure 6.37 reveal an even distribution of the incorporated elements into the structure for the precursor as well as the lithiated LNO. All particles examined here, were hollow inside. This could explain the poor electrochemical cycling of the material. Additionally, the dQ/dV profile of the cycled cells in Figure 6.38 exhibits very sluggish

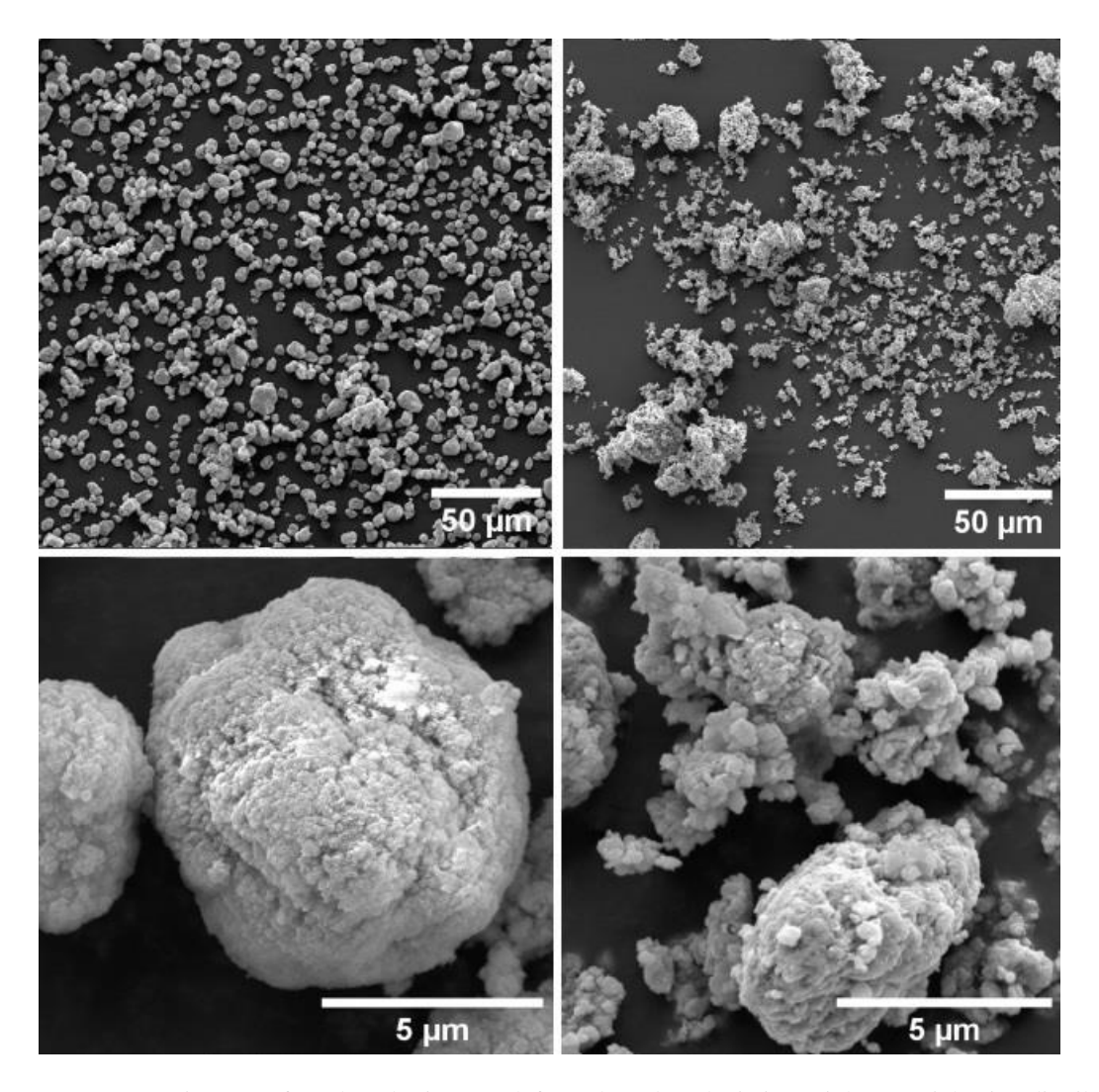


Figure 6.36: SEM images of W-doped $Ni(OH)_2$ (left) and W-doped $LiNiO_2$ (right). Particle size distribution of secondary particle assemblies using smaller magnification in the top row and primary particles at higher magnification in the bottom row.

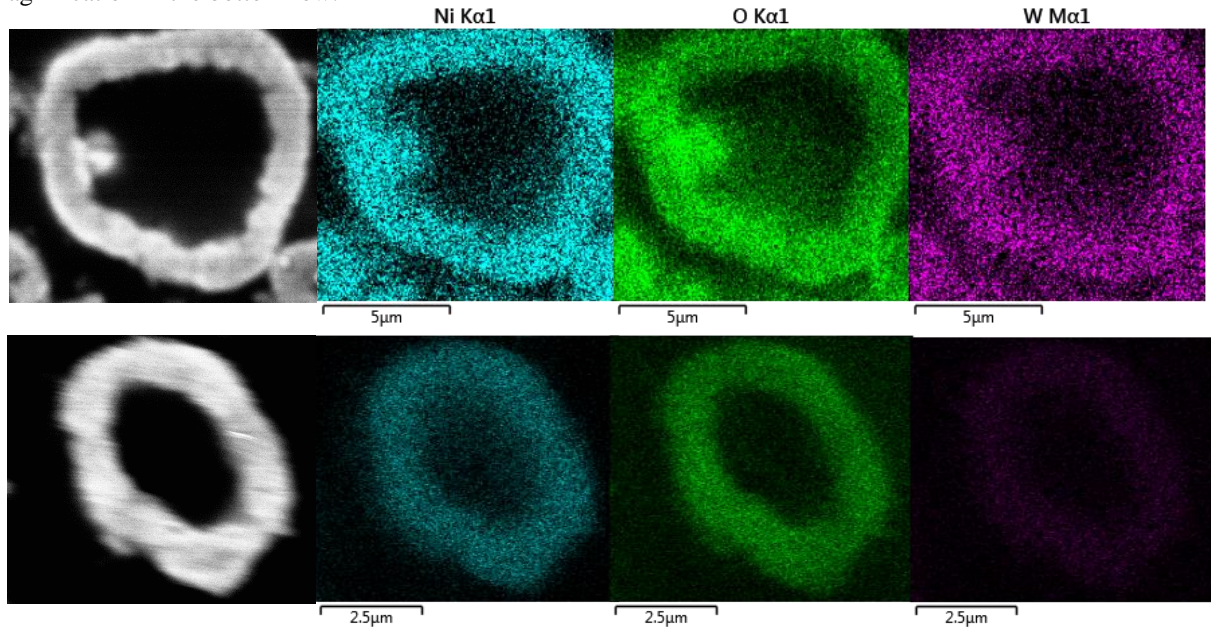


Figure 6.37: SEM image of a particles cross-section (left) and EDX analysis of the cross-section of as-prepared Ti-doped Ni(OH)₂ precursor (top row) and Ti-doped LiNiO₂ (bottom row). Elemental mapping of nickel (turquoise), oxygen (green) and titanium (pink).

transitions already in cycle three and almost no signs of phase transitions during charge and discharge in cycle 100 anymore. Post-cycling analysis was not undertaken during this work, but it would be recommended to further investigate the mechanisms occurring during cycling. Difficulties during precursor synthesis also call for further in-depth experiments on optimised synthesis conditions to ensure the desired amount of W ions is incorporated.

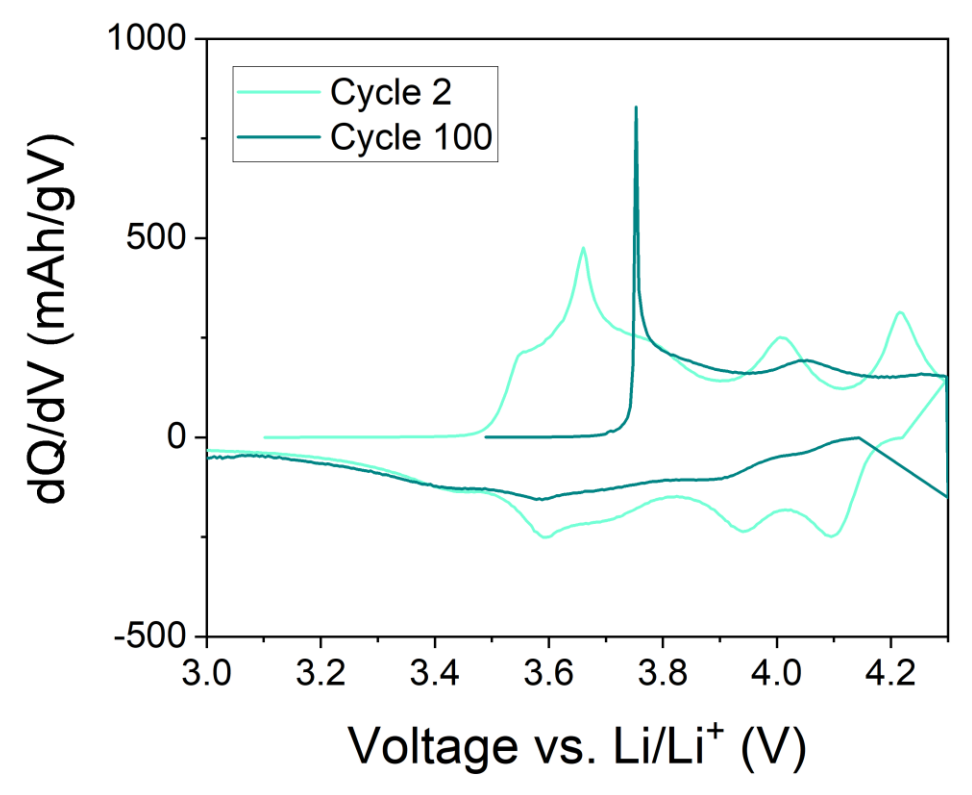


Figure 6.38: Electrochemical data obtained for W-doped LiNiO₂ synthesised via a solid-state route, pre-calcined for 5 h at 350° C and calcined for 15 h at 710° C. Differential capacity plot dQ/dV comparing cycle 3 and 100. Potential window between $3-4.3\,\text{V}$ vs. Li/Li⁺ at a rate of C/20.

6.4. Summary and Conclusion

Crystal structures and morphology of LiNiO₂ doped with various TMs differ significantly. Depending on the size of the dopant, the lattice parameters and volume change expectedly. The morphology that resembles the undoped material best, is the Sn-doped LNO. Seemingly dense packing of cuboid primary particles in secondary particle agglomerations can be seen in the SEM images for both samples whereas the Co-, Mn- and Zr-doped samples exhibit more elongated primary particles. The Cu-doped sample also shows cuboid primary particles, but the secondary particles exhibit rather big voids. This could explain the deteriorated cycling behaviour for this sample. Co-doped LNO shows the lowest 1st cycle charge and discharge capacity of 234 and 182 mAh/g and the highest cation mixing in this study of 5%, which also reflects in the Bragg peak ratios. Due to difficulties during the synthesis of the W-doped sample, these results are not taken into account here.

The Ti-doped sample stands out with the uniformity of seemingly densely packed spherical secondary particles and very narrow particle size distribution, consulting its SEM images. This is reflected in the 1st cycle capacity loss, which is the lowest in this study, also compared to the undoped sample, of 17 mAh/g. Compared to the undoped sample, the Co-doped LNO comes close to the low cation mixing in the structure of the undoped equivalent sample (1.6% for Co-doped LNO, 1.4% for undoped LNO), shows increased cycling behaviour, especially an improved capacity retention over 100 cycles of 88%. This is the highest achieved capacity retention in this study. The Sn-doped sample also reaches this capacity retention and shows superior values in charge and discharge capacity of the first cycle of 315 and 278 mAh/g, respectively.

Concluding this, doping of the LiNiO₂ cathode active material can certainly improve either morphology or the electrochemical cycling behaviour. When co-doping, dopants may influence each other, and certain qualities cannot be assigned clearly to a dopant. For that reason, examining the properties of the doped materials for each dopant on its own gives pristine, unadulterated information about its influences on the host material. This way, dopants can be chosen carefully with regards to their strengths and influences on the layered oxide material and further combined to further improve LiNiO₂ as cathode active material.

It is advisable, to further investigate these single-doped materials regarding their particle size distribution, tap density and surface area and to take a closer look at the primary particle morphology.

7. Conclusion

The aim of this thesis was to optimise the precipitation reaction of the Ni(OH)₂ precursor regarding particle size and morphology, to improve the electrochemical behaviour of the LiNiO₂ cathode as well as mitigate the cation mixing during the solid-state synthesis and structural instabilities during cycling.

To decrease the possible cation mixing in the LiNiO₂ structure, the annealing conditions were examined and optimised using an experimental design statistically varying the three main parameters pre-calcination time, pre-calcination temperature and calcination temperature within a certain range. The resulting samples were studied via TGA, XRD and its refinements, SEM, and electrochemical cycling of coin half cells. The most promising electrochemical results were observed using no pre-calcination step and a calcination at 670°C for 15 h. This leads to an initial charge and discharge capacity of 257 and 222 mAh/g and a capacity retention over 100 cycles of 81.5 % while still maintaining a low cation mixing of 2.7 %. In general, it is nearly impossible to get good values for every parameter. An exceptional charge capacity might have a capacity retention over 100 cycles of below 80 %, which is the threshold for this study. An exceptional capacity retention may be accompanied with a large 1st cycle capacity loss. Yet, it seems that the lower the calcination temperature, the longer the reaction time should be. Important is also to have an excess of Li reactant to compensate for Li loss during the reaction. A pre-calcination temperature, if used, should stay below the melting temperature of LiOH to avoid the need to regrind and air exposure.

To influence the particle growth and thus its size and morphology, the dense packing of primary particles within the secondary particle assemblies, the precursor synthesis parameters reaction time, temperature and the pH were optimised. Particle size and its distribution was examined via laser diffraction, phase purity via XRD and the morphology via SEM imaging. Best results offering a narrow particle size distribution, a visually assessed morphology showing quasispherical secondary particles with a seemingly dense packing of primary particles and phase purity. All these demands are fulfilled using a reaction time of 10 h and a dwelling time of the precipitate in the mother liquid of 9 h, a reaction temperature of 60°C and a pH of 11.

After optimising the equipment reaction parameters, the chemical ratio of Ni:NH₄OH in the reaction was optimised and the material studied via XRD, SEM, laser diffraction and tap density and BET analysis. These samples were then calcined using the optimised calcination conditions from the previous chapter and the resulting LiNiO₂ powder assessed via XRD and its

refinements, laser diffraction, tap density, SEM and BET as well as electrochemical cycling in coin half cells. Advanced characterization was applied to several samples including XANES, EXAFS, HAXPES, magnetic measurements, powder and *operando* muon spin relaxation spectroscopy and in situ XRD-CT. Some of these techniques were investigated at different beamlines in the UK, Germany, and France. Changing the Ni:NH₄OH ratio in the reaction changes the dynamics between particle nucleation and particle growth. All ratios gave quasispherical secondary Ni(OH)₂ particle assemblies with seemingly dense packing of needle-like primary particles with particle size increasing with increasing Ni:NH₄OH ratio. The lithiated samples showed very low cation mixing below 2% without exception. Secondary particle morphology deviated from the quasispherical precursor, and the primary particle changed to cuboid shapes. Electrochemical cycling again, is a trade-off between the different parameters. The sample with the Ni:NH₄OH of 1:5 was selected to be used further in these studies as its cation mixing was the lowest amongst all, with 1.5%, a capacity retention over 100 cycles of 81.8% and a first cycle charge and discharge capacity of 267 and 220 mAh/g.

Advanced methods like XANES, EXAFS, HAXPES and SQUID confirmed the structural and physical changes during cycling as well as depending on the amount of cation mixing. New insights could be gained with *operando* muon spin relaxation spectroscopy and in situ XRD-CT measurements. Here, the Li diffusion during cycling can be followed and used to optimise cycling conditions and the structure-property relationship between the crystal structure and the ongoing transitions during cycling in correlation with the Li diffusion visually and crystallographically determined using XRD-CT.

Last but not least, the optimised conditions were then used to produce doped LiNiO₂ with 3% doping of Co, Mn, Cu, Zn, Sn, Zr, Ti and W to substitute nickel in the structure and its effects on the crystal lattice via XRD, on the cation mixing using refinements of XRD patterns, its morphology via SEM as well as the distribution of the dopants in the particle using EDX analysis. Again, coin half cells were used to study the electrochemical behaviour. The resulting observations show how each dopant influences the particle morphology and electrochemical behaviour. Improvements of the structural instabilities and discharge capacities as well as capacity retention in combination with a low cation mixing provides new stimulus of implementing various new dopants like Sn in the host structure LiNiO₂.

8. Outlook

Considering the knowledge I have now compared to the beginning of this PhD, I think it is crucial, to determine the chemical composition exactly, using ICP-OES in combination with a titration method to distinguish between the Li in the LNO structure and the Li contained in side-phases. Further examining the density, surface area and potential voids in the precursor and lithiated particles will help tailor even more optimised material.

In depth studies of the Li diffusion coefficient via muon spin relaxation spectroscopy in combination with magnetic and NMR measurements to be able to explain features in the muon data will be beneficial as well as further examination of the Li diffusion pathways within the secondary particles, along the primary particles to further optimise the particle morphology.

Further combination of dopants into the host structure of LiNiO₂ needs to be implemented to merge different improvements established by the individual possible substituents. In depth analysis of the individual doped LNO is necessary to confirm the findings from this work.

Overall, the synthesis of both, precursor and lithiated material synthesis were improved and a reliable and consistent preparation of quasispherical, seemingly dense particles can be affirmed. The electrochemical data gained shows exceptional discharge capacities that have not been reported so far, especially in combination with a capacity retention over 100 cycles of above 80%, while at the same time maintaining a consistent low cation mixing below 3%. LiNiO₂ is still a promising cathode active material and worth taken to the next level of scaling up for industrial purposes.

9. References

- [1] "Europäische Komission," [Online]. Available: https://ec.europa.eu/clima/policies/international/negotiations/paris_en. [Accessed 31 March 2021].
- [2] Amnesty International, ""This is what we die for": Human Rights Abuses in the Democratic Republik of the Congo power the Global Trade in Cobalt," Amnesty International Ltd, 2016.
- [3] G. Duleep, H. van Essen, B. Kampman and M. Grünig, "Assessment of Electric Vehicle and Battery Technology," Impacts of Electric Vehicles Deliverables 2, 2011.
- [4] H. E. Melin, "The Lithium-Ion Battery End-of-Life Market A Baseline Study," www3.weforum.org, 20165.
- [5] "Birth of Electrochemistry," The Electrochemical Society, [Online]. Available: https://www.electrochem.org/birth-of-electrochemistry. [Accessed 31 March 2021].
- (6) "Battery and Fuel Cell Technology," The Electrochemical Society, [Online]. Available: https://www.electrochem.org/battery-and-fuel-cell. [Accessed 31 March 2021].
- [7] W. S. Harris, Electrochemical Studies in Cyclic Esters, California: University of California, Lawrence Radiation Laboratory, 1958.
- [8] "The Nobel Prize," [Online]. Available: https://www.nobelprize.org/prizes/chemistry/2019/press-release/. [Accessed 15 April 2021].
- [9] M. S. Whittingham, "Lithium Batteries and Cathode Materials," *Chemical Review, 104*, pp. 4271-4301, 2004.

- [10] M. S. Whittingham, "Batteries à Base de Chalcogénures". Belgium Patent 819,672, 10 March 1975.
- [11] M. S. Whittingham, "Electrical Energy Storage and Intercalation Chemistry," *Science*, 192, pp. 1126-1127, 1976.
- [12] J. B. Goodenough, K. Mizushima and P. J. Wiseman, "Electrochemical Cell and Method of Making Ion Conductors for Said Cell". Europa Patent EP0017400A1, 05 April 1979.
- [13] J. B. Goodenough and Y. Kim, "Challenges for Rechargeable Li Batteries," *Chemistry of Materials*, pp. 587-603, 2010.
- [14] A. Manthiram, "A Reflection on Lithium-Ion Battery Cathode Chemistry," *Nature Communications*, 11, p. 1150, 2020.
- [15] K. Ozawa, "Lithium-ion Recharcheable Batteries with LiCoO₂ and Carbon Electrodes: the LiCoO₂/C System," *Solid State Ionics*, 69, pp. 212-221, 1994.
- [16] B. I. J. Johnston, "High Energy Density Positive Insertion Electrodes for Next Gerenation Lithium-Ion Batteries," University of Sheffield, Sheffield, 2020.
- [17] R. D. Shannon, "Revised Effective Ionic Radii and Systematic Studies of Interatomic Distances in Halides and Chalcogenides," *Acta Crystallographica Section A*, *32*, pp. 751-767, 1976.
- [18] H.-J. Noh, S. Youn, C. S. Yoon and Y.-K. Sun, "Comparison of the Structural and Electrochemical Properties of Layered Li[Ni_xCo_yMn_z]O₂ (x = 1/3, 0.5, 0.6, 0.7, 0.8 and 0.85) Cathode Material for Lithium-Ion Batteries," *Journal of Power Sources*, vol. 233, pp. 121-130, 2013.
- [19] T. Li, X.-Z. Yuan, D. Song, K. Shi and C. Bock, "Degradation Mechanism and Mitigation Stategies of Nickel-Rich NMC-Based Lithium-Ion Batteries," *Electrochemical Energy Reviews*, vol. 3, pp. 43-80, 2020.

- [20] A. Milewska and J. Molenda, "Influence of Co Substitution and Cu Addition on Structural, Electrical, Transport and Electrochemical Properties of Li_xNi_{0.9-y}Co_yMn_{0.1}O₂ Cathode Materials," *Solid State Ionics*, vol. 225, pp. 551-555, 2012.
- [21] H.-H. Rye, N.-Y. Park, J. H. Seo, Y.-S. Yu, M. Sharma, R. Muecke, P. Kaghazchi, C. S. Yoon and Y.-K. Sun, "A Highly Stabilized Ni-Rich NCA Cathode for High-Energy Lithium-Ion Batteries," *Materials Today*, vol. 36, pp. 73-82, 2020.
- [22] D. Wang, W. Liu, X. Zhang, Y. Huang, M. Xu and W. Xiao, "Review of Modified Nickel-Cobalt Lithium Aluminate Cathode Materials for Lithium-Ion Batteries," *International Journal of Photoenergy*, 2019.
- [23] N. Zhang, X. Zhang, E. Shi, S. Zhao, K. Jiang, D. Wang, P. Wang, S. Guo, P. He and H. Zhou, "In situ X-ray Diffraction and Thermal Analysis of LiNi_{0.8}Co_{0.15}Al_{0.05}O₂ Synthesized via Co-Precipitation Method," *Journal of Energy Chemistry*, vol. 27, pp. 1655-1660, 2018.
- [24] L. D. Dyer, B. S. Borie Jr. and G. P. Smith, "Alkali Metal-Nickel Oxides of the Type MNiO₂," *Journal of the American Chemical Society*, vol. 76, pp. 1499-1503, 1954.
- [25] E. J. W. Verwey, P. W. Haaijman, F. C. Romeijn and G. W. van Oosterhout, "Controlled-Valency Semiconductors," *Philips Research Reports*, vol. 5, pp. 173-187, 1950.
- [26] J. B. Goodenough, D. G. Wickham and W. J. Croft, "Some Magnetic and Crystallographic Properties of the System Li_xNi_{2+1-2x}Ni_{3+x}O," *Hournal of Physics and Chemistry of Solids*, vol. 5, pp. 107-116, 1958.
- [27] J. B. Goodenough, D. G. Wickham and W. J. Croft, "Some Ferrimagnetic Properties of the System Li_xNi_{1-x}O," *Journal of Applied Physics*, vol. 29, no. 3, pp. 382-383, 1958.
- [28] W. Bronger, H. Bade and W. Klemm, "Zur Kenntnis der Niccolate der Alkalimetalle," *Zeitschrift fuer anorganische und allgemeine Chemie*, vol. 333, pp. 188-200, 1964.

- [29] T. Enoki and I. Tsujikawa, "Specific Heat of a quasi-two-dimensional Antiferromagnet Ni(OH)₂," *Journal of the Physical Society of Japan*, vol. 45, pp. 1515-1519, 1978.
- [30] P. Hermet, L. Gourrier, J. L. Bantignies, D. Ravot, T. Michel, S. Deabate, P. Boulet and F. Henn, "Dielectric, Magnetic and Phonon Properties of Nickel Hydroxide," *Physical Review B*, vol. 84, p. 235211, 2011.
- [31] K. Ikeda and S. Vedanand, "Optical Spectrum of Synthetic Theophrastite Ni(OH)₂," *Neues Jahrbuch fuer Mineralogie*, vol. 1, pp. 21-26, 1999.
- [32] M. C. Biesinger, B. P. Payne, L. W. M. Lau, A. Gerson and R. S. C. SMart, "X-ray Photoelectron Spectroscopic Chemical State Quantification of Mixed Nickel Metal, Oxide and Hydroxide Systems," *Surface and Interface Analysis*, vol. 41, pp. 324-332, 2009.
- [33] D. S. Hall, D. J. Lockwood, C. Bock and B. R. MacDougall, "Nickel Hydroxides and Related Materials: A Review of their Structure, Synthesis and Properties," *Proceedings of the Royal Society A*, vol. 471, p. 20140792, 2015.
- [34] J. McBreen, "Nickel Hydroxides," in *Handbook of Battery Materials*, Weinheim, Germany, Wiley-VCH Verlag GmbH & Co KGaA, 2011, pp. 149-168.
- [35] K. Lawson, S. P. Wallbridge, A. E. Catling, C. A. Kirk and S. E. Dann, "Determination of layered Nickel Hydroxide Phases in Materials disordered by Stacking Faults and Interstratification," *Journal of Materials Chemistry A*, vol. 11, pp. 789-799, 2023.
- [36] V. Kazimirov, M. B. Smirnov, L. Bourgeois, L. Guerlou-Demourgues, L. Servant, A. M. Balagurov, I. Natkaniec, N. R. Khasanova and E. V. Antipov, "Atomic Structure and Lattice Dynamics of Ni and Mg Hydroxides," *Solid State Ionics*, vol. 181, no. 39-40, pp. 1764-1770, 2010.
- [37] T. Marcopoulos and M. Economou, "Theophrastite, Ni(OH)₂, a new Mineral from northern Greece," *American Mineralogist*, vol. 66, pp. 1020-1021, 1981.

- [38] P. Oliva, J. Leonardi, J. F. Laurent, C. Delmas, J. J. Braconnier, M. Figlarz, F. Fievet and A. de Guibert, "Review of the Structure and the Electrochemistry of Nickel Hydroxides and Oxy-Hydroxides," *Journal of Power Sources*, vol. 8, pp. 229-255, 1982.
- [39] C. Delmas and C. Tessier, "Stacking Faults in the Structure of Nickel Hydroxide: a Rationale of its high Electrochemical Activity," *Journal of Materials Chemistry*, vol. 7, no. 8, pp. 1439-1443, 1997.
- [40] T. N. Ramesh and P. Vishnu Kamath, "The Effect of Stacking Faults on the Electrochemical Performance of Nickel Hydroxide Electrodes," *Materials Research Bulletin*, vol. 43, pp. 2827-2832, 2008.
- [41] R. Acharya, T. Subbaiah, S. Anand and R. P. Das, "Effect of Precipitating Agents on the Physiochemical and Electrolytic Characteristics of Nickel Hydroxide," *Materials Letters*, vol. 57, no. 20, pp. 3089-3095, 2003.
- [42] M. Bianchini, F. Fauth, P. Hartmann, T. Brezesinski and J. Janek, "An In Situ Structural Study on the Synthesis and Decomposition of LiNiO₂," *Journal of Materials Chemistry A*, 8, pp. 1808-1820, 2020.
- [43] P. Kalyani and N. Kalaiselvi, "Various Aspects of LiNiO₂ Chemistry: A Review," *Science and Technology of Advanced Materials*, vol. 6, pp. 689-703, 2005.
- [44] A. Rougier, P. Gravereau and C. Delmas, "Optimization of the Composition of the Li_{1-z}Ni_{1+z}O₂ Electrode Materials: Structural, Magnetic and Electrochemical Studies," *Journal of The Electrochemical Society*, vol. 143, no. 4, pp. 1168-1175, 1996.
- [45] M. Bianchini, M. Roca-Ayats, P. Hartmann, T. Brezesinski and J. Janek, "There and Back again The Journey of LiNiO₂ as a Cathode Active Material," *Angewandte Chemie International Edition*, vol. 58, pp. 10434-10458, 2019.
- [46] A. W. Moses, H. G. Garcia Flores, J.-G. Kim and M. A. Langell, "Surface Properties of LiCoO₂, LiNiO₂ and LiNi_{1-x}Co_xO₂," *Applied Surface Science*, 253, pp. 4781-4791, 2007.

- [47] A. Manthiram, B. Song and W. Li, "A Perspective in Nickel-Rich Layered Oxide Cathodes for Lithium-Ion Batteries," *Energy Storage Materials*, vol. 6, pp. 125-139, 2017.
- [48] Y. Kim, W. M. Seong and A. Manthiram, "Cobalt-Free, High-Nickel Layered Oxide Cathodes for Lithium-Ion Batteries: Progress, Challenges and Perspectives," *Energy Storage Materials*, vol. 34, pp. 250-259, 2021.
- [49] T. Ohzuku, A. Ueda and M. Nagayama, "Electrochemistry and Structural Chemistry of LiNiO₂ (R3m) for 4 Volt Secondary Lithium Cells," *Journal of The Electrochemical Society*, vol. 140, p. 1862, 1993.
- [50] H. Arai, S. Okada, H. Ohtsuka, M. Ichimura and J. Yamaki, "Characterization and Cathode Performance of Li_{1-x}Ni_{1+x}O₂ Prepared with the Excess Lithium Method," *Solid State Ionics*, vol. 80, pp. 261-269, 1995.
- [51] C. S. Yoon, M. H. Choi, B.-B. Lim, E.-J. Lee and Y.-K. Sun, "Review High-Capacity Li[Ni_{1-x}Co_{x/2}Mn_{x/2}]O₂ (*x*=0.1, 0.05, 0) Cathodes for Next-Generation Li-Ion Battery," *Journal of the Electrochemical Society*, *162*, pp. 2483-2489, 2015.
- [52] C. S. Yoon, D.-W. Jun, S.-T. Myung and Y.-K. Sun, "Structural Stability of LiNiO₂ Cycled above 4.2 V," *ACS Energy Letters*, vol. 2, pp. 1150-1155, 2017.
- [53] M. Okada, K. Takahashi and T. Mouri, "Synthesis and Electrochemical Characteristics of Li(Ni*M)O₂ (M=Co, Mn) Cathode for Rechargeable Lithium Batteries," *Journal of Power Sources*, vol. 68, pp. 545-548, 1997.
- [54] C. Pouillerie, E. Suard and C. Delmas, "Structural Characterization of Li_{1-z}-_xNi_{1+z}O₂ by Neutron Diffraction," *Journal of Solid State Chemistry*, vol. 158, pp. 187-197, 2001.
- [55] A. Hirano, R. Kanno, Y. Kawamoto, K. Oikawa, T. Kamiyama and F. Izumi, "Neutron Diffraction Study of layered Li_{0.5-x}Ni_{1+x}O₂," *Solid state ionics*, Vols. 86-88, pp. 791-796, 1996.

- [56] R. Kanno, H. Kubo, Y. Kawamoto, T. Kamiyama, F. Izumi, Y. Takeda and M. Takano, "Phase Relationship and Lithium Deintercalaction in Lithium Nickel Oxides," *Journal of Solid State Chemistry*, vol. 110, pp. 216-225, 1994.
- [57] J. R. Dahn, U. von Sacken and C. A. Michal, "Structure and electrochemistry of Li_{1+y}NiO₂ and a new Li₂NiO₃ Phase with the Ni(OH)₂ Structure," *Solid State Ionics*, vol. 44, pp. 87-97, 1990.
- [58] J. N. Reimers, W. Li and J. R. Dahn, "Short-Range Cation Ordering in Li_xNi_{2-x}O₂," *Physical Review B*, vol. 47, no. 14, pp. 8486-8493, 1993.
- [59] R. V. Moshtev, P. Zlatilova, V. Manev and A. Sato, "The LiNiO₂ Solid Solution as a Cathode Material for Rechargeable Lithium Batteries," *Journal of Power Sources*, vol. 54, pp. 329-333, 1995.
- [60] W. Li, J. C. Currie and J. Wolstenholme, "Influence of Morphology on the Stability of LiNiO₂," *Journal of Power Sources*, vol. 68, pp. 565-569, 1997.
- [61] C. Delmas, J. P. Peres, A. Rougier, A. Demourgues, F. Weill, A. Chadwick, M. Broussely, F. Perton, P. Biensan and P. Willmann, "On the Behaviour of Li_xNiO₂ System: An Electrochemical and Structural Overview," *Journal of Power Sources*, vol. 68, pp. 120-125, 1997.
- [62] L. de Biasi, A. Schiele, M. Roca-Ayats, G. Garcia, T. Brezensinski, P. Hartmann and J. Janek, "Phase Transformation Behaviour and Stability of LiNiO₂ Cathode Material for Li-Ion Batteries Obtained from In Situ Gas Analysis and Operando X-Ray Diffraction," *ChemSusChem*, 12, pp. 2240-2250, 2019.
- [63] J. P. Peres, C. Delmas, A. Rougier, M. Broussely, F. Perton, P. Biensan and P. Willmann, "The Relationship Between the Composition of Lithium Nickel Oxide and the Loss of Reversibility During the First Cycle," *Journal of Physics and Chemistry of Solids*, vol. 57, no. 6-8, pp. 1057-1060, 1996.
- [64] H. Arai, S. Okada, Y. Sakurai and J. Yamaki, "Reversibility of LiNiO₂ Cathode," *Solid State Ionics*, vol. 95, pp. 275-282, 1997.

- [65] M. Broussely, F. Perton, P. Biensan, J. M. Bodet, J. Labat, A. Lecerf, C. Delmas, A. Rougier and J. P. Peres, "Li_xNiO₂, a Promising Cathode for Rechargeable Lithium Batteries," *Journal of Power Sources*, vol. 54, pp. 109-114, 1995.
- [66] W. Li, J. N. Reimers and J. R. Dahn, "In Situ X-Ray Diffraction and Electrochemical Studies of Li_{1-x}NiO₂," *Solid State Ionics*, 67, pp. 123-130, 1993.
- [67] K. Kang and G. Ceder, "Factors that Affect Li Mobility in Layered Lithium Transition Metal Oxides," *Physical Review B*, vol. 74, p. 094105, 2006.
- [68] T. A. Hewston and B. L. Chamberland, "A Survey of First-Row Ternary Oxides LiMO₂ (*M*=Sc-Cu)," *Journal of Physics and Chemistry of Solids*, vol. 48, no. 2, pp. 97-108, 1987.
- [69] T. Ohzuku, A. Ueda, M. Nagayama, Y. Iwakoshi and H. Komori, "Comparative Study of LiCoO₂, LiNi_{1/2}Co_{1/2}O₂ and LiNiO₂ for 4V Secondary Lithium Cells," *Electrochimica Acta*, vol. 38, no. 9, pp. 1159-1167, 1993.
- [70] A. Rougier, C. Delmas and G. Chouteau, "Magnetism of Li_{1-z}Ni_{1+z}O₂: A Powerful Tool for Structure Determination," *Journal of Physics and Chemistry of Solids*, vol. 57, pp. 1101-1103, 1996.
- [71] I. A. Shkrob, J. A. Gilbert, P. J. Phillips, R. Klie, R. T. Haasch, J. Bareno and D. P. Abraham, "Chemical Weathering of Layered Ni-Rich Oxide Electrode Materials: Evidence for Cation Exchange," *Journal of The Electrochemical Society*, vol. 164, no. 7, pp. A1489-A1498, 2017.
- [72] R. Moshtev, P. Zlatilova, S. Vasilev, I. Bakalova and A. Kozawa, "Synthesis, XRD Characterization and Electrochemical Performance of Overlithiated LiNiO₂," *Journal of Power Sources*, Vols. 81-82, pp. 434-441, 1999.
- [73] Y. You, H. Celio, J. Li, A. Dolocan and A. Manthiram, "Stable Surface Chemistry Against Ambient Air of Modified High-Nickel Cathodes for Lithium-Ion Batteries," *Angewandte Chemie International Edition*, vol. 57, p. 6480, 2018.

- [74] H. S. Liu, Z. R. Zhang, Z. L. Gong and Y. Yang, "Origin of Deterioration for LiNiO₂ Cathode Material during Storage in Air," *Electrochemical and Solid-State Letters*, vol. 7, no. 7, p. A190, 2004.
- [75] L. Mu, Z. Yang, L. Tao, C. K. Water, Z. Xu, L. Li, S. Sainio, Y. Du, H. L. Xin, D. Nordlund and F. Lin, "The Sensitive Surface Chemistry of Co-Free, Ni-Rich Layered Oxides: Identifying Experimental Conditions that Influence Characterization Results," *Journal of Materials Chemistry*, vol. 8, pp. 17487-17497, 2020.
- [76] M. G. S. R. Thomas, W. I. F. David and J. B. Goodenough, "Synthesis and Structural Characterization of the Normal Spinel Li[Ni₂]O₄," *Materials Research Bulletin*, 20, pp. 1137-1146, 1985.
- [77] J. R. Dahn, E. W. Fuller, M. Obrovac and U. von Sacken, "Thermal Stability of Li_xCoO₂, Li_xNiO₂ and γ-MnO₂ and Consequences for the Safety of Li-Ion Cells," *Solid State Ionics*, vol. 69, pp. 265-270, 1994.
- [78] H. Arai, S. Okada, Y. Sakurai and J.-I. Yamaki, "Thermal Behaviour of Li_{1-y}NiO₂ and the Decomposition Mechanism," *Solid State Ionics*, vol. 109, pp. 295-302, 1998.
- [79] Z. Zhang, D. Fouchard and J. R. Rea, "Differential Scanning Calorimetry Material Studies: Implications for the Safety of Lithium-Ion Cells," *Journal of Power Sources*, vol. 70, pp. 16-20, 1998.
- [80] J. Li, Z. Zhou, Z. Luo, Z. He, J. Zheng, Y. Li, J. Mao and K. Dai, "Microcrack Generation and Modification of Ni-Rich Cathodes for Li-Ion Batteries: A Review," Sustainable Materials and Technologies, vol. 29, pp. 1-22, 2021.
- [81] C. Delmas, M. Menetrier, L. Croguennec, S. Levasseur, J. P. Peres, C. Pouillerie, G. Prado, L. Fournes and F. Weill, "Lithium Batteries: A new Tool in Solid State Chemistry," *International Journal of Inorganic Materials*, vol. 1, pp. 11-19, 1999.
- [82] J. P. Peres, A. Demourgues and C. Delmas, "Structural Investigations on Li_{0.65-z}Ni_{1+z}O₂ Cathode Material: XRD and EXAFS Study," *Solid State Ionics*, vol. 111, pp. 135-144, 1998.

- [83] J. P. Peres, F. Weill and C. Delmas, "Lithium/Vacancy Ordering in the Monoclinic $\text{Li}_x \text{NiO}_2$ (0.50 < x < 0.75) Solid Solution," *Solid State Ionics*, 116, pp. 19-27, 1999.
- [84] H. Li, N. Zhang, J. Li and J. R. Dahn, "Updating the Structure and Electrochemistry of $\text{Li}_x \text{NiO}_2$ for 0 < x < 1," *Journal of The Electrochemical Society*, vol. 165, no. 13, pp. A2985-A2993, 2018.
- [85] L. Croguennec, C. Pouillerie, A. N. Mansour and C. Delmas, "Structural Characterisation of the Highly Deintercalated $\text{Li}_x\text{Ni}_{1.02}\text{O}_2$ Phases (with x < 0.3)," *Journal of Materials Chemistry*, vol. 11, pp. 131-141, 2001.
- [86] J. M. Tarascon, G. Vaughan, Y. Chabre, L. Seguin, M. Anne, P. Strobel and G. Amatucci, "In Situ Structural and Electrochemical Study of Ni_{1-x}Co_xO₂ Metastable Oxides Prepared by Soft Chemistry," *Journal of Solid State Chemistry*, vol. 147, pp. 410-420, 1999.
- [87] S. W. Doo, S. Lee, H. Kim, J. H. Choi and K. T. Lee, "Hydrophobis Ni-Rich Layered Oxides as Cathode Materials for Lithium-Ion Batteries," *Applied Energy Materials*, vol. 2, pp. 6246-6253, 2019.
- [88] J. Xu, F. Lin, D. Nordlund, E. J. Crumlin, F. Wang, J. Bai, M. M. Doeff and W. Tong, "Elucidation of the Surface Characteristics and Electrochemistry of High-Performance LiNiO₂," *Chemical Communications*, vol. 52, p. 4239, 2016.
- [89] A. R. West, Solid State Chemistry and its Application, Chichester: John Wiley & Son, 2014.
- [90] M. Peng and X. Shen, "Template Growth Mechanism of Spherical Ni(OH)₂," *Journal of Central South University of Technology*, vol. 14, no. 3, pp. 310-314, 2007.
- [91] E. Weiwei, J. Cheng, C. Yang and Z. Mao, "Experimental Study by Online Measurement of the Precipitation of Nickel Hydroxide: Effects of Operating Conditions," *Chinese Journal of Chemical Engineering*, vol. 23, pp. 860-867, 2015.

- [92] J. Välikangas, P. Laine, M. Hietaniemi, T. Hu, P. Tynjaelae and U. Lassi, "Precipitation and Calcination of High-Capacity LiNiO₂ Cathode Material for Lithium-Ion Batteries," *Applied Sciences*, 10, pp. 1-11, 2020.
- [93] T. Ramesh and P. Kamath, "Synthesis of Nickel Hydroxide: Effect of Precipitation Conditions on Phase Selectivity and Structural Disorder," *Journal of Power Sources*, vol. 156, no. 2, pp. 655-661, 2006.
- [94] A. van Bommel and J. R. Dahn, "Analysis of the Growth Mechanism of Coprecipitated Spherical and Dense Nickel, Manganese and Cobalt-Containing Hydroxides in the Presence of Aqueous Ammonia," *Chemistry of Materials*, vol. 21, no. 8, pp. 1500-1503, 2009.
- [95] C. J. Brinker and G. W. Scherer, Sol-Gel Science: The Physics and Chemistry of Sol-Gel Processing, Boston: Academic Press, 1990.
- [96] W. Wen, J.-C. Yao, C.-C. Jiang and J.-M. Wu, "Solution-Combustion Synthesis of Nanomaterials for Lithium Storage," *International Journal of Self-Propagating High-Temperature Synthesis*, vol. 26, no. 3, pp. 187-198, 2017.
- [97] P. Manikandan, M. V. Ananth, T. P. Kumar, M. Raju, P. Perisamy and K. Maimaran, "Solution Combustion Synthesis of Layered LiNi_{0.5}Mn_{0.5}O₂ and its Characterization as Cathode Material for Lithium-Ion Cells," *Journal of Power Sources*, vol. 196, pp. 10148-10155, 2011.
- [98] Y. Liu, X. Wen, R. K. Lake and J. Guo, "First-Principles Study of the Doping Effect in Half Delithiated LiNiO₂ Cathodes," *Applied Energy Materials*, vol. 6, pp. 2134-2139, 2023.
- [99] S. Jouanneau and J. R. Dahn, "Preparation, Structure and Thermal Stability of New $Ni_xCo_{1-2x}Mn_x(OH)_2$ (0 < x < 1/2)," *Chemistry of Materials*, vol. 15, no. 2, pp. 495-499, 2003.

- [100] M.-H. K. Lee, S.-T. Myung and Y.-K. Sun, "Synthetic Optimization of Li[Ni_{1/3}Co_{1/3}Mn_{1/3}]O₂ via Co-Precipitation," *Electrochimica Acta*, vol. 50, pp. 939-948, 2004.
- [101] Z. Li, N. A. Chernova, M. Roppolo, S. Upreti, C. Petersburg, F. M. Alamgir and M. S. Whittingham, "Comparative Study of the Capacity and Rate Capability of LiNi_yMn_yCo_{1-2y}O₂ (y = 0.5, 0.45, 0.4, 0.33)," *Journal of the Electrochemical Society*, vol. 158, no. 5, pp. A516-A522, 2011.
- [102] S. Aryal, J. L. Durham, A. L. Lipson, K. Z. Pupek and O. Kahvecioglu, "Roles of Mn and Co in Ni-rich layered Oxide Cathodes synthesized utilizing a Taylor Vortex Reactor," *Electrochimica Acta*, vol. 391, p. 138929, 2021.
- [103] A. Rougier, I. Saadoune, P. Gravereau, P. Willmann and C. Delmas, "Effect of Cobalt Substitution on Cationic Distribution in LiNi_{1-y}Co_yO₂ Electrode Material," *Solid State ionics*, vol. 90, pp. 83-90, 1996.
- [104] E. Zhecheva and R. Stoyanova, "Stabilization of the Layered Crystal structure of LiNiO₂ by Co-Substitution," *Solid State Ionics*, vol. 66, pp. 143-149, 1993.
- [105] G. Li, L. Qi, P. Xiao, Y. Yu, X. Chen and W. Yang, "Effect of Precursor Structures on the Electrochemical Performance of Ni-rich LiNi_{0.88}Co_{0.12}O₂ Cathode Materials," *Electrochemica Acta*, vol. 270, pp. 319-329, 2018.
- [106] T. Liu, L. Yu, J. Liu, J. Lu, X. Bi, A. Dai, M. Li, M. Li, Z. Hu, L. Ma, D. Luo, J. Zheng, T. Wu, Y. Ren, J. Wen, F. Pan and K. Amine, "Understanding Co roles towards developing Co-free Ni-rich Cathodes for Rechargeable Batteries," *Nature Energy*, vol. 6, pp. 277-286, 2021.
- [107] R. Hausbrand, G. Cherkashinin, H. Ehrenberg, M. Gröting, K. Albe, C. Hess and W. Jaegermann, "Fundamental Degradation Mechanism of layered Oxide Li-Ion Battery Cathode Materials: Methodology, Insights and novel Approaches," *Materials Science and Engineering B*, vol. 192, pp. 3-25, 2015.

- [108] M. M. Thackeray, "Manganese oxides for Lithium Batteries," *Progress in Solid State Chemistry*, vol. 25, no. 1-2, pp. 1-71, 1997.
- [109] G. Vitins and K. West, "Lithium Intercalation into Layered LiMnO₂," *Journal of the Electrochemical Society*, vol. 144, no. 8, p. 2587, 1997.
- [110] T. Ohzuku and Y. Makimura, "Layered Lithium Insertion Material of LiNi_{1/2}Mn_{1/2}O₂: A Possible Alternative to LiCoO₂ for Advanced Lithium-Ion Batteries," *Chemistry Letters*, vol. 30, no. 8, pp. 744-745, 2001.
- [111] Y. Koyama, Y. Makimura, I. Tanaka, H. Adachi and T. Ohzuku, "Systematic Research on Insertion Materials based on Superlattice Models in a Phase Triangle of LiCoO₂-LiNiO₂-LiMnO₂ I. First-Principles Calculations on Electronic and Crystal Structures, Phase Stability and new LiNi_{1/2}Mn_{1/2}O₂ Material," *Journal of the Electrochemical Society*, vol. 151, no. 9, pp. A1499-A1506, 2004.
- [112] E. Rossen, C. D. Jones and J. R. Dahn, "Structure and Electrochemistry of Li_xMn_yNi₁₋ _yO₂," *Solid State Ionics*, vol. 57, pp. 311-318, 1992.
- [113] Y. Wang, Y. Zhu and P. Gao, "Synthesis and Characterization of Nickel-rich Layered LiNi_{1-x}Mn_xO₂ (x = 0.02,0.05) cathodes for Lithium-Ion Batteries," *Electrochimica Acta*, vol. 427, p. 140891, 2022.
- [114] D. Caurant, N. Baffier, V. Bianchi, G. Gregoire and S. Bach, "Preparation by a 'chimie douce' route and Characterization of LiNi_zMn_{1-z}O₂ (0.5 < z < 1) Cathode Materials," *Journal of Materials Chemistry*, vol. 6, no. 7, pp. 1149-1155, 1996.
- [115] K. Kang, Y. S. Meng, J. Breger, C. P. Grey and G. Ceder, "Electrodes with High Power and High Capacity for Rechargeable Lithium Batteries," *Science*, vol. 311, no. 5763, pp. 977-980, 2006.
- [116] X.-Z. Kong, D.-L. Li, K. Lahtinen, T. Kallio and X.-Q. Ren, "Effect of Copper-Doping on LiNiO₂ Positive Electrode for Lithium-Ion Batteries," *Journal of the Electrochemical Society*, vol. 167, p. 140545, 2020.

- [117] M. A. Martínez-Cruz, G. Ramos-Sánchez, M. Oliver-Tolentino, H. Pfeiffer and I. González, "Improving the Structural Reversibility of LiNiO₂ by Incorporation of Cu, an electrochemical and in-situ XRD Study," *Journal of Alloys and Compounds*, vol. 923, p. 166328, 2022.
- [118] N. Aquilar-Eseiza, G. Ramos-Sánchez, F. Gonzáles and I. Gonzáles, "High Voltage Improved Reversible Capacity in Ni^{+2/+3} modified Copper-based Cathodes for Lithium Ion Batteries," *Electrochemistry Communications*, vol. 96, pp. 32-36, 2018.
- [119] J. Kim and K. Amine, "A Comparative Study on the Substitution of divalent, trivalent and tetravalent Metal Ions in LiNi_{1-x} M_x O₂ ($M = Cu^{2+}$, Al³⁺ and Ti⁴⁺)," *Journal of Power Sources*, vol. 104, pp. 33-39, 2002.
- [120] L. Yang, F. Ren, Q. Feng, G. Xu, X. Li, Y. Li, E. Zhao, J. Ma and S. Fan, "Effect of Cu Doping on the Structural and Electrochemical Performance of LiNi_{1/3}Co_{1/3}Mn_{1/3}O₂ Cathode Materials," *Journal of Electrocic Materials*, vol. 47, no. 7, p. 3996, 2018.
- [121] J. Molenda, A. Milewska, M. Rybski, L. Lu, W. Zajac, S. Gerasin and J. Tobola, "High-Power and High-Energy Cu-Substituted LixNi_{0.88-y}Co_yMn_{0.1}Cu_{0.02}O₂ Cathode Material for Li-Ion Batteries," *Physica Status Solidi A*, vol. 217, p. 1900951, 2020.
- [122] L. Jie-Bin, X. You-Long, D. Xian-Feng, S. Xiao-Fei and X. Li-Long, "Improved Electrochemical Stability of Zn-Doped LiNi_{1/3}Co_{1/3}Mn_{1/3}O₂ Cathode Materials," *Acta Physico-Chimica Sinica*, vol. 28, no. 8, pp. 1899-1905, 2012.
- [123] H. Du, Y. Zheng, Z. Dou and H. Zhan, "Zn-Doped LiNi_{1/3}Co_{1/3}Mn_{1/3}O₂ Composite as Cathode Material for Lithium Ion Battery: Preparation, Characterization and Electrochemical Properties," *Journal of Nanomaterials*, vol. 2015, 2015.
- [124] G. T. Fey, J. G. Chen, V. Subramanian and T. Osaka, "Preparation and Electrochemical Properties of Zn-Doped LiNi_{0.8}Co_{0.2}O₂," *Journal of Power Sources*, vol. 112, pp. 384-394, 2002.

- [125] C. Tessier, L. Guerloc-Demourgues, C. Faure, A. Demourgues and C. Delmas, "Structural Study of Zinc-Substituted Nickel Hydroxide," *Journal of Materials Chemistry*, vol. 10, pp. 1185-1193, 1999.
- [126] C. Tessier, C. Faure, L. Guerloc-Demourgues, C. Denage, G. Nabias and C. Delmas, "Electrochemical Study of Zinc-Substituted Nickel Hydroxide," *Journal of the Electrochemical Society*, vol. 149, no. 9, pp. A1136-A1145, 2002.
- [127] L. Guerloc-Demourgues, C. Tessier, P. Bernard and C. Delmas, "Influence of Substituted Zn on Stacking Faults in Nickel Hydroxide," *Journal of Materials Chemistry*, vol. 14, pp. 2649-2654, 2004.
- [128] H. Chen, J. M. Wang, Y. L. Zhao, J. Q. Zhang and C. N. Cao, "Electrochemical Performance of Zn-Substituted Ni(OH)₂ for Alkaline Recharcheable Batteries," *Journal of Solid State Electrochemistry*, vol. 9, pp. 421-428, 2005.
- [129] M. Eilers-Rethwisch, M. Winter and F. M. Schappacher, "Synthesis, Electrochemical Investigation and Structural Analysis of Doped Li[Ni_{0.6}Mn_{0.2}Co_{0.2-x}M_x]O₂ (x = 0.005; M = Al, Fe, Sn) Cathode Materials," *Journal of Power Sources*, vol. 387, pp. 101-107, 2018.
- [130] H. Zhu, R. Shen, Y. Tang, X. Yan, J. Liu, L. Song, Z. Fan, S. Zheng and Z. Chen, "Sn-Doping and Li₂SNO₃ Nano-Coating Layer Co-Modified LiNi_{0.5}Co_{0.2}Mn_{0.3}O₂ with Improved Cycle Stability at 4.6 V Cut-off Voltage," *Nanomaterials*, vol. 10, p. 868, 2020.
- [131] T. T. Nguyen, U.-H. Kim, C. S. Yoon and Y.-K. Sun, "Enhanced Cycling Stability of Sn-doped Li[Ni_{0.90}Co_{0.05}Mn_{0.05}]O₂ via Optimization of Particle Shape and Orientation," *Chemical Engineering Journal*, vol. 405, p. 126887, 2021.
- [132] X. Ma, C. Wang, J. Cheng and J. Sun, "Effects of Sn Doping on the Structural and Electrochemical Properties of LiNi_{0.8}Co_{0.2}O₂ Cathode Materials," *Solid State Ionics*, vol. 178, pp. 125-129, 2007.

- [133] J. Wu, Y. Wen, Q. Zhou, J. Wang, L. Shen and J. Zheng, "Simultaneous Bulk Doping and Surface Coating of Sn to Boost the Electrochemical Performance of LiNiO₂," *Applied Energy Materials*, vol. 6, pp. 3010-3019, 2023.
- [134] Q. Chen, C. Du, D. Qu, X. Zhang and Z. Tang, "Synthesis and Characterization of Zr-Doped LiNi_{0.4}Co_{0.2}Mn_{0.4}O₂ Cathode Materials for Lithium-Ion Batteries," *RSC Advances*, vol. 5, p. 75248, 2015.
- [135] X. Shangguan, Q. Wang, G. Yang, G. Jia and F. Li, "New Insights into Improving Electrochemical Performance of LiNi_{0.5}Mn_{0.5}O₂ Cathode Material by Li₂ZrO₃ coating and Zr⁴⁺ doping," *Ionics*, vol. 25, pp. 4547-4556, 2019.
- [136] L. Li, Y. Han, B. Zhao, G. Zhao, W. Qiang and B. Huang, "Enhancing the Cycle Stability of Zr-doped LiNi_{0.83}Co_{0.12}Mn_{0.05}O₂ by Co-Precipitation," *Ionics*, vol. 28, pp. 1037-1046, 2022.
- [137] D. Wang, X. Li, Z. Wang, H. Guo, Y. Xu, Y. Fan and J. Ru, "Role of Zirconium Dopant on the Structure and High Voltage Electrochemical Performances of LiNi_{0.5}Co_{0.2}Mn_{0.3}O₂ Cathode Materials for Lithium-Ion Batteries," *Electrochimica Acta*, vol. 188, pp. 48-56, 2016.
- [138] C. S. Yoon, M.-J. Choi, D.-W. Jun, Q. Zhang, P. Kaghazchi, K.-H. Kim and Y.-K. Sun, "Cation Ordering of Zr-Doped LiNiO₂ Cathode for Lithium-Ion Batteries," *Chemistry of Materials*, vol. 30, pp. 1808-1814, 2018.
- [139] N.-Y. Park, S.-B. Kim, M.-C. Kim, S.-M. Han, D.-H. Kim, M.-S. Kim and Y.-K. Sun, "Mechanism of Doping with High-Valence Elements for Developing Ni-Rich Cathode Materials," *Advanced Energy Materials*, vol. 13, p. 2301530, 2023.
- [140] J. D. Steiner, H. Cheng, J. Walsh, Y. Zhang, B. Zydlewski, L. Mu, Z. Xu, M. M. Rahman, H. Sun, F. M. Michel, C.-J. Sun, D. Nordlund, W. Luo, J.-C. Zheng, H. L. Xin and F. Lin, "Targeted Surface Doping with Reversible Local Environment improves Oxygen Stability at the Electrochemical Interfaces of Nickel-Rich Cathode Materials," ACS Applied Materials & Interfaces, vol. 11, pp. 37885-37891, 2019.

- [141] K. C. Kam, A. Mehta, J. T. Heron and M. M. Doeff, "Electrochemical and Physical Properties of Ti-Substituted Layered Nickel Manganese Cobalt Oxide (NMC) Cathode Materials," *Journal of the Electrochemical Society*, vol. 159, no. 8, pp. A1383-A1392, 2012.
- [142] J. Wilcox, S. Patoux and M. Doeff, "Structure and Electrochemistry of LiNi_{1/3}Co_{1/3-yM_yMn_{1/3}O₂ (M = Ti, Al, Fe) Positive Electrode Materials," *Journal of the Electrochemical Society*, vol. 156, no. 3, pp. A192-A198, 2009.}
- [143] J. Kim and K. Amine, "The Effect of Tetravalent Titanium Substitution in LiNi_{1-x}Ti_xO₂ (0.025 < x < 0.2) System," *Electrochemistry Communications*, vol. 3, pp. 52-55, 2001.
- [144] M. Tsuda, H. Arai, M. Takahashi, H. Ohtsuka, Y. Sakurai, K. Sumitomo and H. Kageshima, "Electrode Performance of Layered LiNi_{0.5}Ti_{0.5}O₂ prepared by Ion Exchange," *Journal of Power Sources*, vol. 144, pp. 183-190, 2005.
- [145] S. N. Kwon, H. R. Park and M. Y. Song, "Electrochemical Performances of LiNiO₂ substituted by Ti for Ni via the Combustion Method," *Ceramics International*, vol. 40, pp. 11131-11137, 2014.
- [146] U. Kim, D. Jun, K. Park, Q. Zhang, P. Kaghazchi, D. Aurbach, D. T. Major, G. Goobes, M. Dixit, N. Leifer, C. M. Wang, P. Yan, D. Ahn, K.-H. Kim, C. S. Yoon and Y.-K. Sun, "Pushing the Limit of Layered Transition Metal Oxide Cathodes for High-Energy Density Rechargeable Li Ion Batteries," *Energy and Environmental Science*, vol. 11, no. 5, pp. 1271-1279, 2018.
- [147] G. Song, H. Zhong, Y. Dai, X. Zhou and J. Yang, "WO₃ Membrane-Encapsulated Layered LiNi_{0.6}Co_{0.2}Mn_{0.2}O₂ Cathode Material for advanced Li-Ion Batteries," *Ceramics International*, vol. 45, pp. 6774-6781, 2019.
- [148] H.-H. Rye, G.-T. Park, C. S. Yoon and Y.-K. Sun, "Suppressing Detrimental Phase Transitions via Tungsten Doping of LiNiO₂ Cathode for next-generation Lithium-Ion Batteries," *Journal of Materials Chemistry A*, vol. 7, p. 18580, 2019.

- [149] C. Geng, D. Rathore, D. Heino, N. Zhang, I. Hamam, N. Zaker, G. A. Botton, R. Omessi, N. Phattharasupakun, T. Bond, C. Yang and J. R. Dahn, "Mechanism of Action of the Tungsten Dopant in LiNiO₂ Positive Electrode Materials," *Advanced Energy Materials*, vol. 12, no. 6, p. 2103067, 2021.
- [150] N. Zaker, C. Geng, D. Rathore, I. Hamam, N. Chen, P. Xiao, C. Yang, J. R. Dahn and G. A. Botton, "Probing the mysterious Behaviour of Tungsten as a Dopant Inside Pristine Cobalt-Free Nickel-Rich Cathode Materials," *Advanced Functional Materials*, vol. 33, no. 16, p. 2211178, 2023.
- [151] U. Busch, "Progress in Physical X-Ray Research Until 1915," in *A Shining Life for Science*, Springer Link, 2021.
- [152] R. C. Mackenzie, "Nomenclature in Thermal Analysis, Part IV," *Thermochimica Acta*, 28, pp. 1-6, 1979.
- [153] W. Massa, Kristallstrukturbestimmung, Wiesbaden: Vieweg + Teubner, 2011.
- [154] H. Roland, Grundlagen der Lichterzeugung, Highlight-Verlag, 2009.
- [155] H. M. Rietveld, "A profile refinement method for nuclear and magnetic structures," *Journal of Applied Crystallography*, vol. 2, no. 2, pp. 65-71, 1969.
- [156] B. H. Toby and R. B. Von Dreele, "GSAS-II: the Genesis of a Modern Open-Source all Purpose Crystallography Software Package," *Journal of Applied Crystallography*, 46, pp. 544-549, 2013.
- [157] J. F. Moulder, W. F. Stickle, P. E. Sobol and K. D. Bomben, Handbook of X-ray Photoelectron Spectroscopy, Eden Prairie: Perkin-Elmer Corporation, 1992.
- [158] K. Akhtar, S. A. Khan, S. B. Khan and A. M. Asiri, "Scanning Electron Microscopy: Principle and Applications in Nanomaterials Characterization," in *Handbook of Materials Characterization*, Springer, 2018, pp. 113-145.

- [159] A. Ul-Hamid, A Beginners' Guide to Scanning Electron Microscopy, Switzerland: Springer Nature, 2018.
- [160] S. Gaisford, V. Kett and P. Haines, Principles of Thermal Analysis and Calorimetry, Cambridge: The Royal Society of Chemistry, 2016.
- [161] "Anton Paar," [Online]. Available: https://wiki.anton-paar.com/en/laser-diffraction-for-particle-sizing/. [Accessed 07 December 2023].
- [162] R. Xu, Particle Characterization: Light Scattering Methods, Springer Netherlands, 2002.
- [163] Particle size analysis Laser diffraction methods, Geneva, Switzerland: International Standard ISO 13320, 2020-01.
- [164] C. o. Europe, European Pharmacopoeia, Council of Europe, 2010.
- [165] J. P. Sousa e Silva, D. Splendor, I. M. Gonçalves, P. Costa and J. M. Sousa Lobo, "Note on the Measurement of Bulk Density and Tapped Density of Powders According to the European Pharmacopoeia," *AAPS PharmSciTech*, vol. 14, pp. 1098-1100, 2013.
- [166] "Micromeritics," [Online]. Available: https://www.micromeritics.com/particle-testing/analytical-testing/surface-area/. [Accessed 12 02 2024].
- [167] S. Lowell, Characterization of Porous Solids and Powders: Surface Area, Pore Size and Density, Springer, 2004.
- [168] J. Rouquerol, F. Rouquerol, P. Llewellyn, G. Maurin and K. Sing, Adsorption by Powders and Porous Solids: Principles, Methodology and Applications, Academic Press, 2013.
- [169] M. Newville, Fundamentals of XAFS, Chicago, IL: University of Chicago, IL, 2008.
- [170] B. Ravel, *Introduction to XAS, Athena Data Processing, XANES analysis, ARTEMIS and EXAFS fitting*, Didcot, UK: Diamond Lightsource, 2011.

- [171] C. S. Schnohr and M. C. Ridgway, X-ray Absorption Spectroscopy of Semiconductors, Berlin-Heidelberg: Springer, 2015.
- [172] "Diamond Lightsource," Diamond Lightsourse, [Online]. Available: https://www.diamond.ac.uk/Instruments/Techniques.html. [Accessed 09 12 2023].
- [173] J. Stöhr, NEXAFS Spectroscopy, Heidelberg: Springer, 1996.
- [174] L. Zhang, X-ray Absorption Spectroscopy of Metalloproteins, New York: Humana Press, 2019.
- [175] F. Lin, Y. Liu, X. Yu, L. Cheng, A. Singer, O. G. Shpyrko, H. L. Xin, N. Tamura, C. Tian, T.-C. Weng, X.-Q. Yang, S. Y. Meng, D. Nordlund, W. Yang and M. M. Doeff, "Synchrotron X-ray Analytical Techniques for Studying Materials Electrochemistry in Rechargeable Batteries," *Chemical Reviews*, vol. 117, pp. 13123-13186, 2017.
- [176] Z. W. Lebens-Higgins, H. Chung, M. J. Zuba, J. Rana, Y. Li, N. V. Faenza, N. Pereira, B. D. McCloskey, F. Rodolakis, W. Yang, M. S. Wittingham, G. G. Amatucci, Y. S. Meng, T.-L. Lee and L. F. J. Piper, "How Bulk Sensitive is Hard X-ray Photoelectron Spectroscopy: Accounting for the Cathode-Electrolyte Interface when Addressing Oxygen Redox," *The Journal of Physical Chemistry Letters*, vol. 11, no. 6, pp. 2106-2112, 2020.
- [177] S. Mugiraneza and A. M. Hallas, "Tutorial: A Beginner's Guide to Interpreting Magnetic Susceptibility Data with the Curie Weiss Law," *Communications Physics*, vol. 5, p. 95, 2022.
- [178] G. E. Pérez, J. M. Brittain, I. McClelland, S. Hull, M. O. Jones, H. Y. Playford, S. A. Cussen, P. J. Baker and E. M. Reynolds, "Neutron and Muon Characterisation Technique for Battery Materials," *Journal of Materials Chemistry A*, vol. 11, p. 10493, 2023.
- [179] J. Sugiyama, "Ion Diffusion in Solids Probed by Muon-Spin Spectroscopy," *Journal of the Physical Society Japan*, vol. 82, p. SA023, 2013.

- [180] B. I. Johnston, I. McClelland, P. J. Baker and S. A. Cussen, "Elucidating Local Diffusion Dynamics in Nickel-Rich Layered Oxide Cathodes," *Physical Chemistry Chemical Physics*, vol. 25, p. 25728, 2023.
- [181] I. McClelland, B. I. Johnston, P. J. Baker, M. Amores, E. J. Cussen and S. A. Corr, "Muon Spectroscopy for Investigating Diffusion in Energy Storage Materials," *Annual Review of Materials Research*, vol. 50, pp. 15.1-15.23, 2020.
- [182] L. Nuccio, L. Schulz and A. J. Drew, "Muon Spin Spectroscopy: Magnetism, Soft Matter and the Bridge between the two," *Journal of Physics D: Applied Physics*, vol. 47, p. 473001, 2014.
- [183] S. J. Blundell, "Spin-polarised Muons in Condensed Matter Physics," *Contemporary Physics*, vol. 40, pp. 175-192, 1999.
- [184] N. E. Omori, A. D. Bobitan, A. Vamvakeros, A. M. Beale and S. D. Jaques, "Recent Developments in X-ray Diffraction/Scattering Computed Tomography for Materials Science," *Philosophical Transactions of the Royal Society A: Mathematical, Physical and Engineering Sciences*, vol. 381, no. 2259, 2023.
- [185] N. W. Alcock, "Refinement of the Crystal Structure of Lithium Hydroxide Monohydrate," *Acta Crystallographica*, vol. B 27, pp. 1682-1683, 1971.
- [186] S. L. Mair, "The Electron Distribution of the Hydroxide Ion in Lithium Hydroxide," *Acta Crystallographica*, vol. A 34, pp. 542-547, 1978.
- [187] H. Effenberger and J. Zemann, "Verfeinerung der Kristallstruktur des Lithiumkarbonates Li₂CO₃," *Zeitschrift fuer Kristallographie Crystalline Materials*, vol. 150, no. 1, pp. 133-138, 1979.
- [188] S. Sasaki, K. Fujino and Y. Takeuchi, "X-Ray Determination of Electron-Density Destributions in Oxides, MgO, MnO, CoO and NiO and Atomic Scattering Factors of their Constituent Atoms," *Proceedings of the Japan Academy, Series B*, vol. 55, no. 2, pp. 43-48, 1979.

- [189] A. Hirano, R. Kanno, Y. Kawamoto, Y. Takeda, K. Yamaura, M. Takano, K. Ohyama, M. Ohashi and Y. Yamaguchi, "Relationship between Non-Stoichiometry and Physical Properties in LiNiO₂," *Solid State Ionics*, vol. 78, no. 1-2, pp. 123-131, 1995.
- [190] E. Zhao, L. Fang, M. Chen, D. Chen, Q. Huang, Z. Hu, Q.-b. Yan, M. Wu and X. Xiao, "New Insights into Li/Ni Disorder in layered Cathode Materials for Lithium Ion Batteries: a joint Study of Neutron Diffraction, electrochemical Kinetic Analysis and first-principles Calculations," *Journal of Materials Chamistry A*, vol. 5, p. 1679, 2017.
- [191] S. B. Schougaard, J. Breger, M. Jiang, C. P. Grey and J. B. Goodenough, "LiNi_{0.5+Δ}Mn_{0.5-Δ}O₂ - A High-Rate, High-Capacity Cathode for Lithium Rechargeable Batteries," *Advanced Materials*, vol. 18, pp. 905-909, 2006.
- [192] C. Bae, M. Dupre and B. Kang, "Further Improving Coulombic Efficiency and Discharge Capacity in LiNiO₂ Material by Activating Sluggish ~3.5 V Discharge Reaction," *ACS Applied Materials & Interfaces*, vol. 13, pp. 23760-23770, 2021.
- [193] P. Kurzhals, F. Riewald, M. Bianchini, H. Sommer, H. A. Gasteiger and J. Janek, "The LiNiO₂ Cathode Active Material: A Comprehensive Study of Calcination Conditions and their Correlation with Physicochemical Properties. Part I. Structural Chemistry," *Journal of the Electrochemical Society*, vol. 168, p. 115018, 2021.
- [194] F. Riewald, P. Kurzhals, M. Bianchini, H. Sommer, J. Janek and H. A. Gasteiger, "The LiNiO₂ Cathode Active Material: A Comprehensive Study of Calcination Conditions and their Correlation with Physicochemical Properties. Part II. Morphology," *Journal of the Electrochemical Society*, vol. 169, p. 20529, 2022.
- [195] J. Kim, H. Lee, H. Cha, M. Yoon, M. Park and J. Cho, "Prospect and Reality of Ni-Rich Cathode for Commercialization," *Advanced Ebergy Materials*, vol. 8, p. 1702028, 2018.
- [196] W. Li, E. M. Erickson and A. Manthiram, "High-Nickel Layered Oxide Cathodes for Lithium-based Automotive Batteries," *Nature Energy*, vol. 5, pp. 26-34, 2020.

- [197] C. Song, Z. Tang, H. Guo and S. L. Chan, "Structural Characteristics of Nickel Hydroxide Synthesized by a Chemical Precipitation Route under Different pH Values," *Journal of Power Sources*, vol. 112, no. 2, pp. 428-434, 2002.
- [198] R. Qiao, A. L. Wray, J.-H. Kim, N. P. W. Pieczonka, S. J. Harris and W. Yang, "Direct Experimental Probe of the Ni(II)/Ni(III)/Ni(IV) Redox Evolution in LiNi_{0.5}Mn_{1.5}O₄ Electrodes," *The Journal of Physical Chemistry C*, vol. 119, pp. 27228-27233, 2015.
- [199] F. Lin, D. Nordlund, I. M. Markus, T.-C. Weng, H. L. Xin and M. M. Doeff, "Profiling the Nanoscale Gradient in Stoichiometric Layered Cathode Particles for Li-Ion Batteries," *Energy & Environmental Science*, vol. 7, p. 3077, 2014.
- [200] F. M. F. de Groot, M. Grioni, J. C. Fuggle, J. Ghijsen, G. A. Sawatzky and H. Petersen, "Oxygen 1s X-Ray Absorption Edges of Transition-Metal Oxides," *Physical Review B*, vol. 40, no. 8, pp. 5715-5723, 1989.
- [201] J. Reimers, J. Dahn, J. Greedan, Stager C, G. Liu, Davidson I and U. Von Sacken, "Spin Glass Behaviour in the Frustrated Antiferromagnetic LiNiO₂," *Journal of Solid State Chemistry*, vol. 102, pp. 542-552, 1993.
- [202] P. Barton, Y. Premchand, P. Chater, R. Seshadri and M. Rosseinsky, "Chemical Inhomogeneity, Short-Range Order and Magnetism in the LiNiO₂-NiO Solid Solution," *Chemistry European Journal*, vol. 19, pp. 14521-14531, 2013.
- [203] V. Bianchi, D. Caurant, N. Baffier, C. Belhomme, E. Chappel, G. Chouteau, S. Bach, J. Pereira-Ramos, A. Sulpice and P. Wilmann, "Synthesis, Structural Characterization and Magnetic Properties of Quasistoichiometric LiNiO₂," *Solid State Ionics*, vol. 140, pp. 1-17, 2001.
- [204] M. Nùñez-Regueiro, E. Chappel, G. Chouteau and C. Delmas, "Magnetic Structure of Li_{1-z}Ni_{1+z}O₂," *The European Physical Journal B*, vol. 16, pp. 37-41, 2000.
- [205] D. Goonetilleke, B. Schwarz, H. Li, F. Fauth, E. Suard, S. Mangold, S. Indris, T. Brezesinski, M. Bianchini and D. Weber, "Stoichiometry Matters: Correlation between

- Antisite Defects, Microstructure and Magnetic Behaviour in the Cathode Material Li_{1-z}Ni_{1+z}O₂," *Journal of Materials Chemistry A*, vol. 11, p. 13468, 2023.
- [206] J. Sugiyama, Y. Ikedo, K. Mukai, H. Nozaki, M. Mansson, O. Oder, M. Harada, K. Kamazawa, Y. Miyake, J. Brewer, E. Ansaldo, K. Chow, I. Watanabe and T. Ohzuku, "Low-Temperature Magnetic Properties and High-Temperature Diffusive Behaviour of LiNiO₂ investigated by Muon-Spin Spectroscopy," *Physical Review B*, vol. 82, p. 224412, 2010.
- [207] W. Yang and T. P. Devereaux, "Anionic and cationic redox and interfaces in batteries. Advances from soft X-ray absorption spectroscopy to resonant inelastic scattering," *Journal of Power Sources*, vol. 389, pp. 188-197, 2018.
- [208] "Panasonic," [Online]. Available: https://industrial.panasonic.com/ww/products/batteries/secondary-batteries/lithium-ion. [Accessed 15 April 2021].
- [209] P. Roy and S. K. Srivastava, "Nanostructured Anode Materials for Lithium Ion Batteries," *Journal of Materials Chemistry A*, *3*, pp. 2454-2484, 2015.
- [210] Y. S. Meng, G. Ceder, C. P. Grey, W.-S. Yoon, M. Jiang, J. Breger and Y. Shao-Horn, "Cation Ordering in Layered O3 ($Ni_xLi_{0.33-2x/3}Mn_{0.67-x/3}$)O₂ ($0 \le x \le 1/2$) Compounds," *Chemistry of Materials*, vol. 17, pp. 2386-2394, 2005.
- [211] Z. K. Heiba and K. El-Sayed, "Structural and Anisotropic Thermal Expansion Correlation of Li₂ZrO₃ at different Temperatures," *Journal of Applied Crystallography*, vol. 35, pp. 634-636, 2002.
- [212] C. S. Ho, S.-G. Kang, S.-W. Song, J.-B. Yoon and J.-H. Choy, "Crystal Structure and Spectroscopic Properties of Li_xNi_{1-y}Ti_yO₂ and their Electrochemical Behaviour," *Solid State Ionics*, vol. 86, pp. 171-175, 1996.
- [213] D. Goonetilleke, A. Mazilkin, D. Weber, Y. Ma, F. Fauth, J. Janek, T. Brezesinski and M. Bianchini, "Single Step Synthesis of W-modified LiNiO₂ using an Ammonium

Tungstate Flux," *Journal of Materials Chemistry A: Materials for Energy and Sustainability*, vol. 10, no. 14, pp. 7841-7855, 2022.

[214] J. Longsworth, N. Schillings and M. Sha, "Dissolved Oxygen Control Tuning for Cell Culture Applications," *BioProcess International*, vol. online, 2022.

10. Appendix

Chapter 4

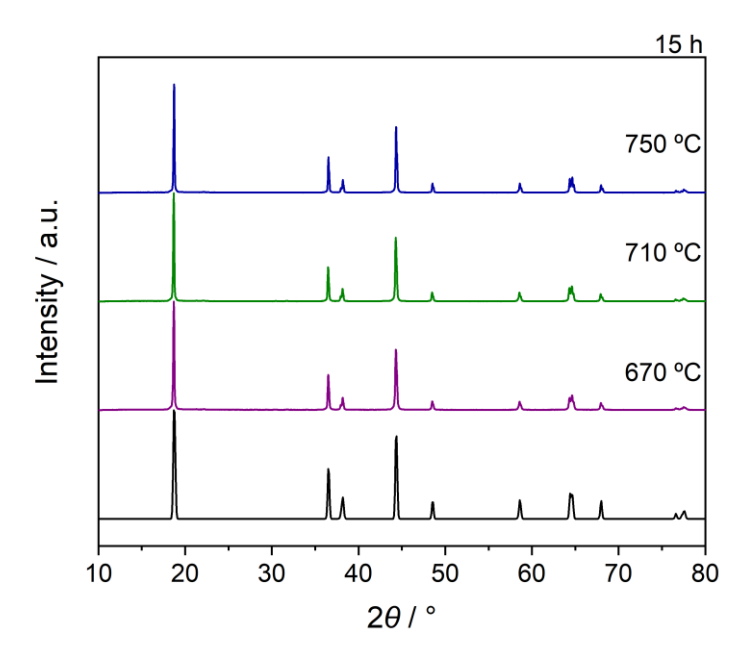


Figure 10.1: XRD pattern of LiNiO₂ samples calcined for 15 h at 670° C (purple), 710° C (green) and 750° C (blue) without any pre-calcination procedure. Calculated LiNiO₂ pattern from ICSD (black, collection code 78687 [187]) as comparison.

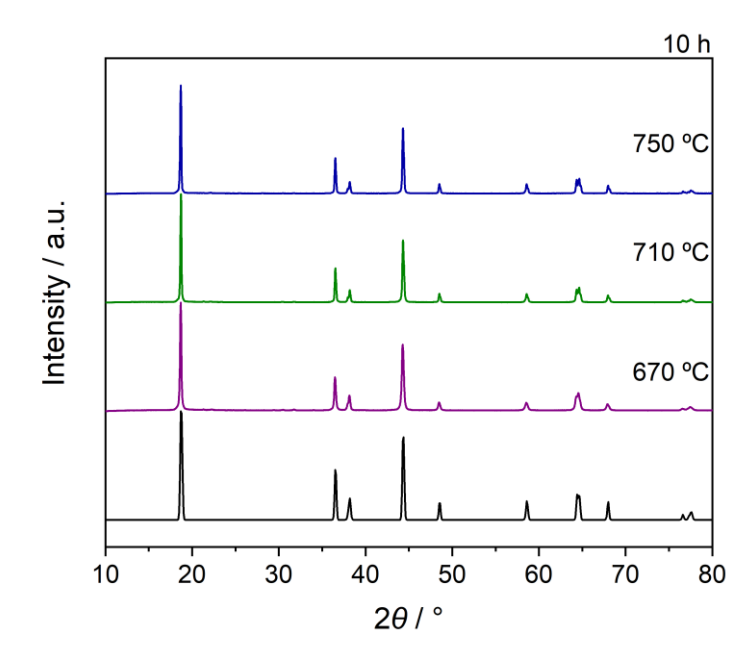


Figure 10.2: XRD pattern of LiNiO₂ samples calcined for 10 h at 670° C (purple), 710° C (green) and 750° C (blue) without any pre-calcination procedure. Calculated LiNiO₂ pattern from ICSD (black, collection code 78687 [187]) as comparison.

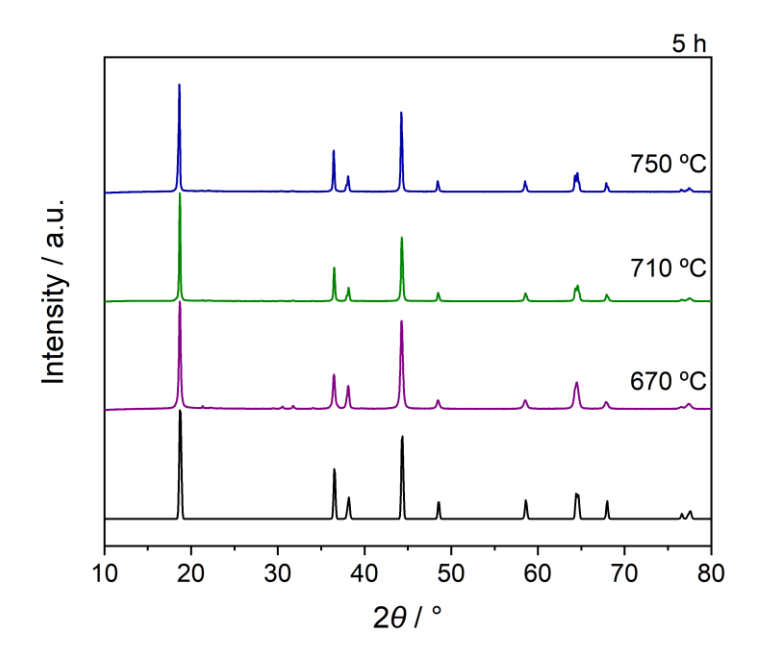


Figure 10.3: XRD pattern of LiNiO₂ samples calcined for 5 h at 670°C (purple), 710°C (green) and 750°C (blue) without any pre-calcination procedure. Calculated LiNiO₂ pattern from ICSD (black, collection code 78687 [187]) as comparison.

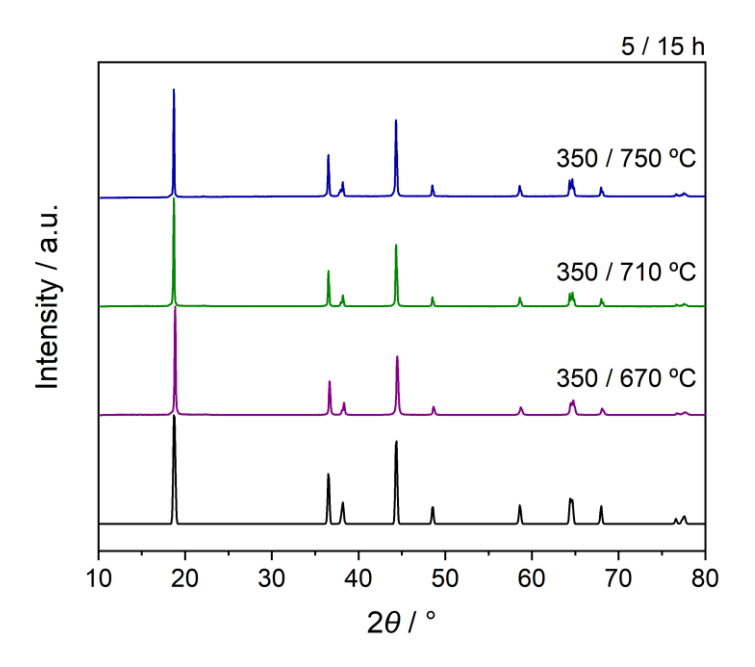


Figure 10.4: XRD pattern of selected as prepared LiNiO $_2$ samples. These samples are all pre-calcined for 5 h at 350°C and calcined for 15 h at 670°C (purple), 710°C (green) and 750°C (blue). Calculated LiNiO $_2$ pattern from ICSD (black, collection code 78687 [187]) as comparison including Bragg peak labels.

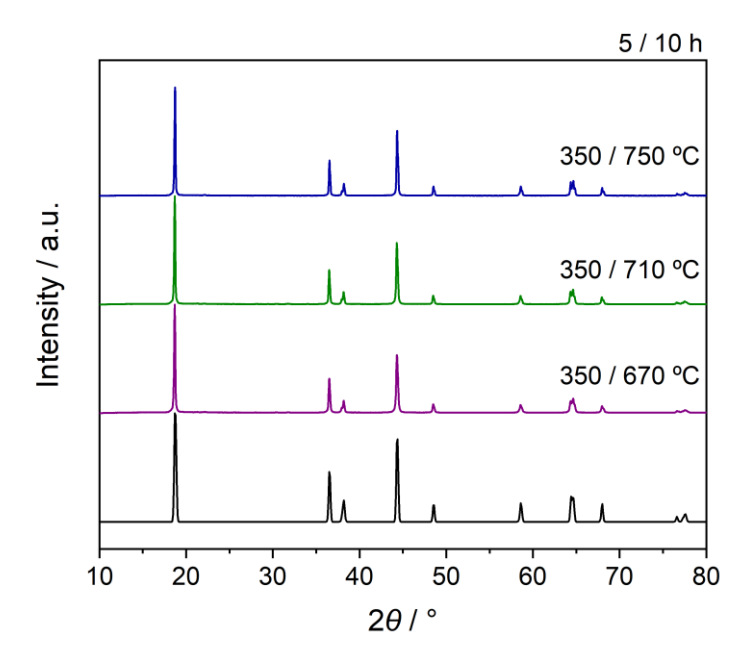


Figure 10.5: XRD pattern of selected as prepared LiNiO₂ samples. These samples are all pre-calcined for 5 h at 350° C and calcined for 10 h at 670° C (purple), 710° C (green) and 750° C (blue). Calculated LiNiO₂ pattern from ICSD (black, collection code 78687 [187]) as comparison including Bragg peak labels.

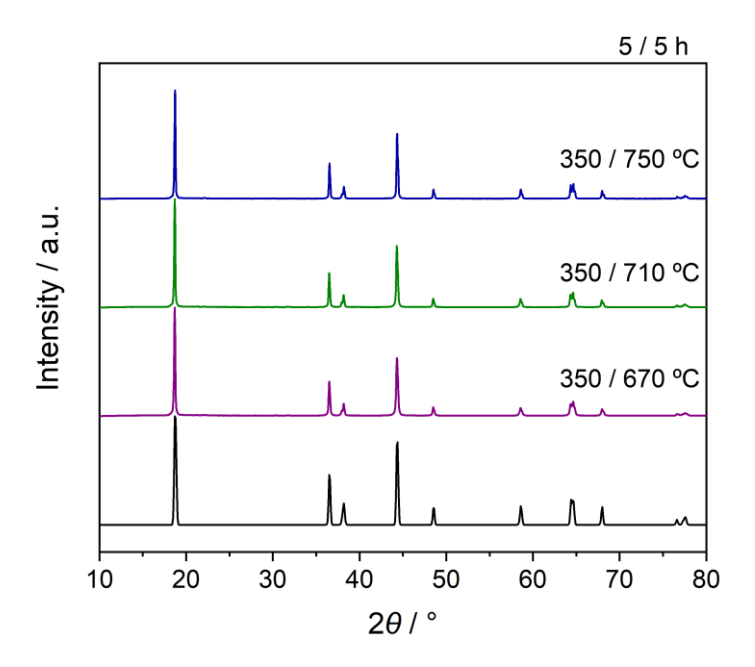


Figure 10.6: XRD pattern of selected as prepared LiNiO $_2$ samples. These samples are all pre-calcined for 5 h at 350°C and calcined for 5 h at 670°C (purple), 710°C (green) and 750°C (blue). Calculated LiNiO $_2$ pattern from ICSD (black, collection code 78687 [187]) as comparison including Bragg peak labels.

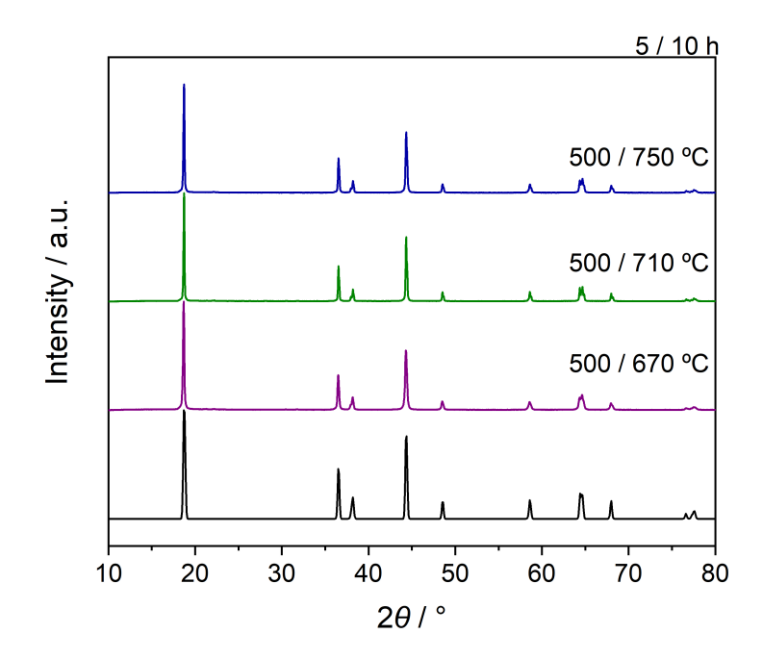


Figure 10.7: XRD pattern of selected as prepared LiNiO₂ samples. These samples are all pre-calcined for 5 h at 500° C and calcined for 10 h at 670° C (purple), 710° C (green) and 750° C (blue). Calculated LiNiO₂ pattern from ICSD (black, collection code 78687 [187]) as comparison including Bragg peak labels.

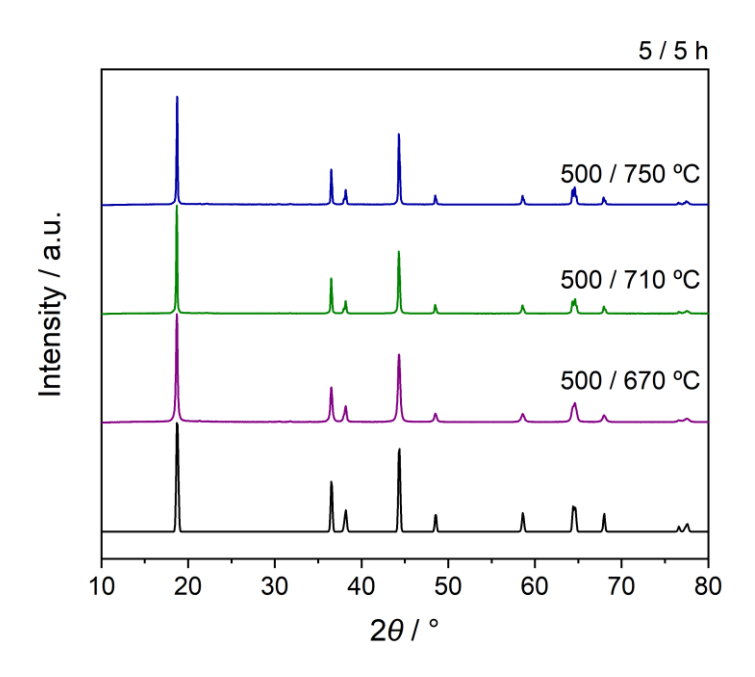


Figure 10.8: XRD pattern of selected as prepared LiNiO₂ samples. These samples are all pre-calcined for 5 h at 500° C and calcined for 10 h at 670° C (purple), 710° C (green) and 750° C (blue). Calculated LiNiO₂ pattern from ICSD (black, collection code 78687 [187]) as comparison including Bragg peak labels.

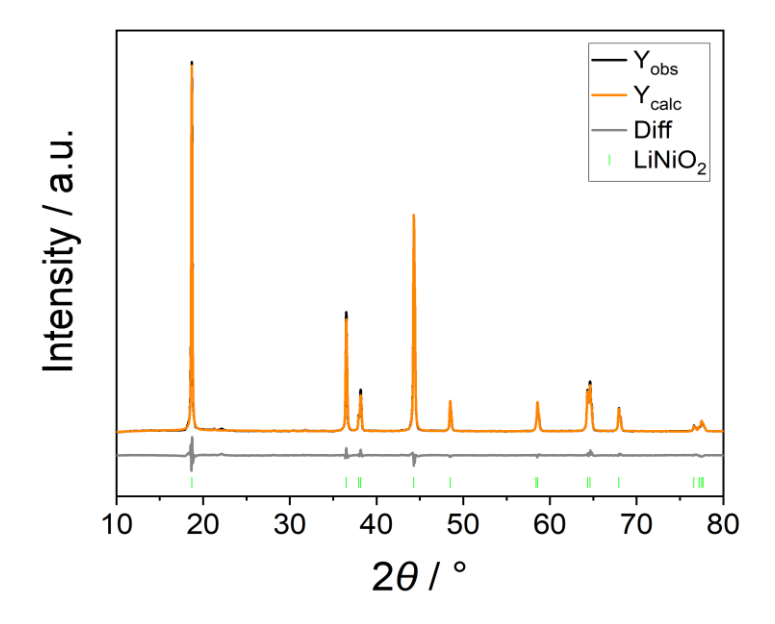


Figure 10.9: Refinement of measured Cu source XRD pattern of LiNiO₂ calcined for 15 h at 670°C without pre-calcination. Measured pattern (black), calculated LiNiO₂ pattern (orange, collection code 78687 [187]) and the difference between observed and calculated pattern (grey). Peak positions of LiNiO₂ in green.

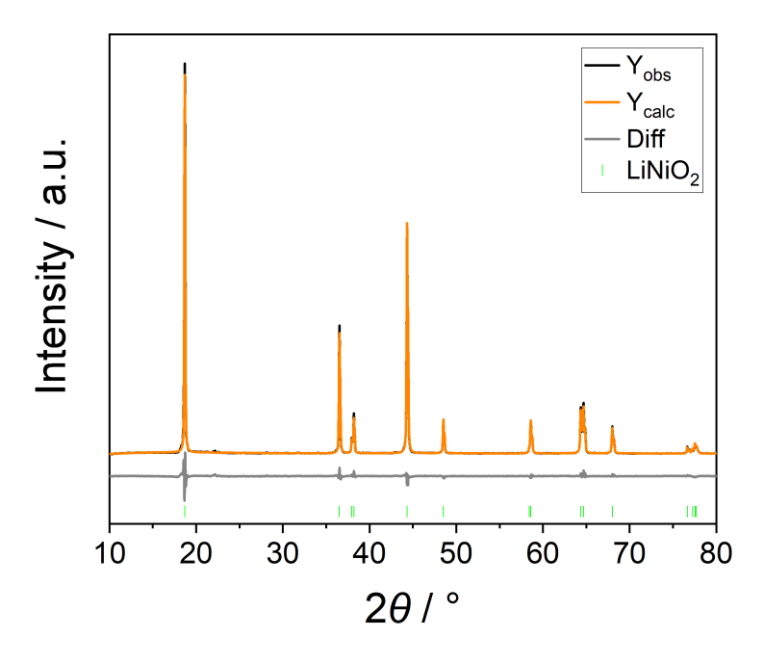


Figure 10.10: Refinement of measured Cu source XRD pattern of LiNiO₂ pre-calcined for 5 h at 350°C and calcined for 15 h at 710°C. Measured pattern (black), calculated LiNiO₂ pattern (orange, collection code 78687 [187]) and the difference between observed and calculated pattern (grey). Peak positions of LiNiO₂ in green.

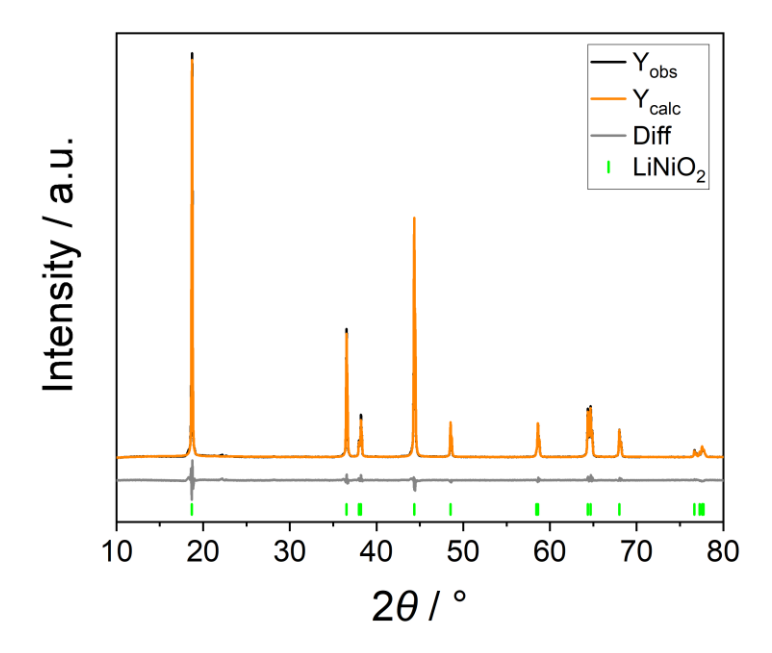


Figure 10.11: Refinement of measured Cu source XRD pattern of LiNiO₂ pre-calcined for 5 h at 500°C and calcined for 15 h at 750°. Measured pattern (black), calculated LiNiO₂ pattern (orange, collection code 78687 [187]) and the difference between observed and calculated pattern (grey). Peak positions of LiNiO₂ in green.

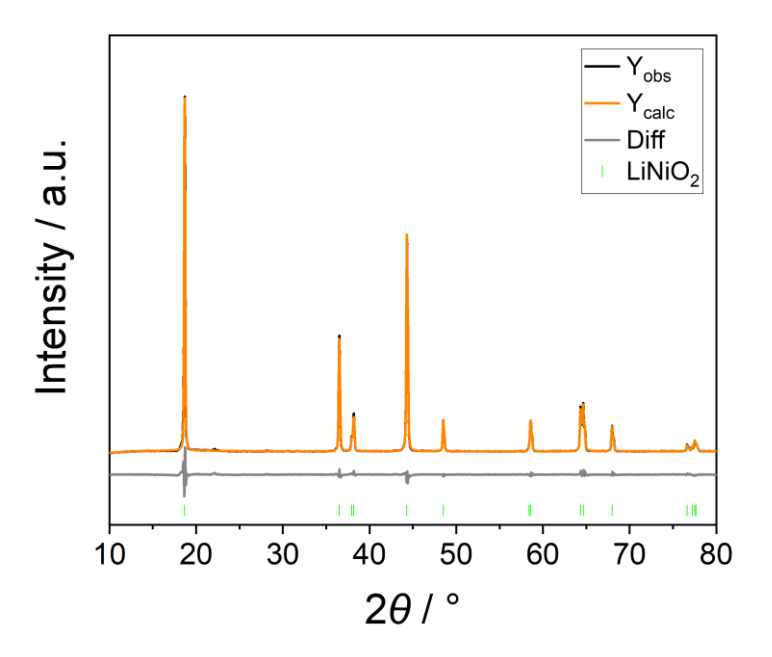


Figure 10.12: Refinement of measured Cu source XRD pattern of LiNiO₂ calcined for 10 h at 750° C with no pre-calcination. Measured pattern (black), calculated LiNiO₂ pattern (orange, collection code 78687 [187]) and the difference between observed and calculated pattern (grey). Peak positions of LiNiO₂ in green.

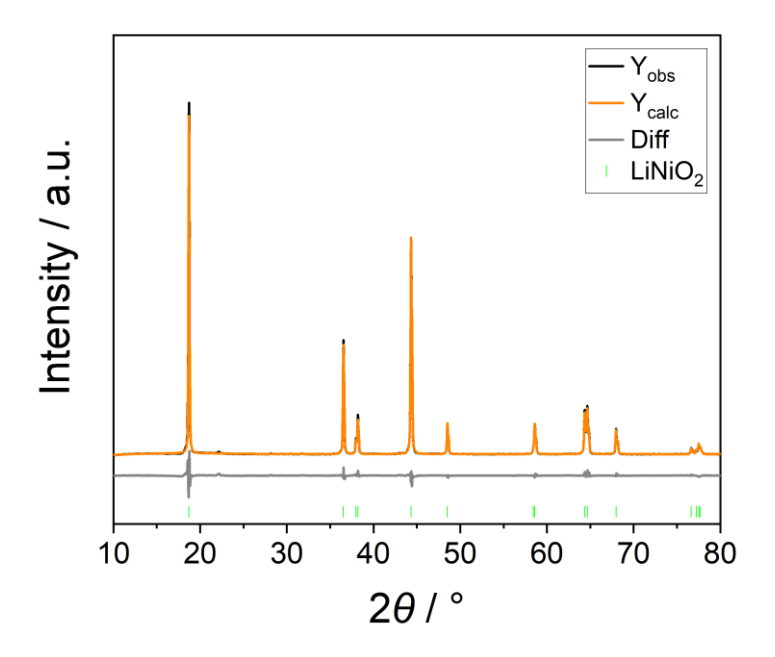


Figure 10.13: Refinement of measured Cu source XRD pattern of LiNiO₂ pre-calcined for 5 h at 350°C and calcined for 10 h at 750°C. Measured pattern (black), calculated LiNiO₂ pattern (orange, collection code 78687 [187]) and the difference between observed and calculated pattern (grey). Peak positions of LiNiO₂ in green.

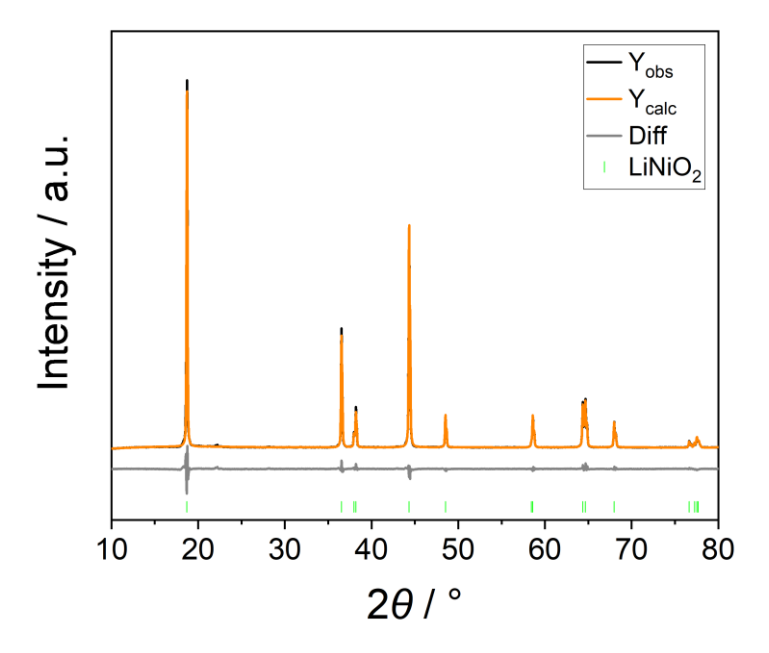


Figure 10.14: Refinement of measured Cu source XRD pattern of LiNiO₂ pre-calcined for 5 h at 500° C and calcined for 10 h at 710° C. Measured pattern (black), calculated LiNiO₂ pattern (orange, collection code 78687 [187]) and the difference between observed and calculated pattern (grey). Peak positions of LiNiO₂ in green.

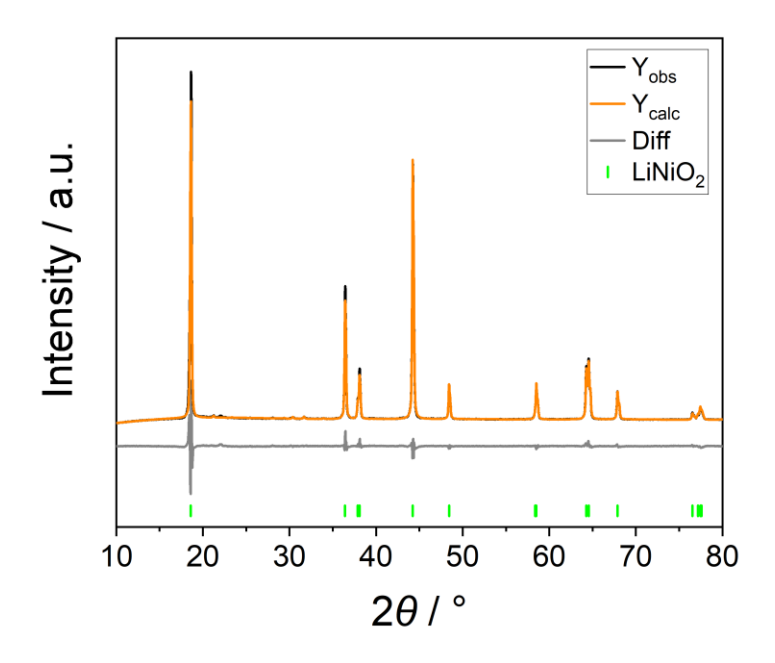


Figure 10.15: Refinement of measured Cu source XRD pattern of LiNiO₂ calcined for 5 h at 750°C without pre-calcination step. Measured pattern (black), calculated LiNiO₂ pattern (orange, collection code 78687 [187]) and the difference between observed and calculated pattern (grey). Peak positions of LiNiO₂ in green.

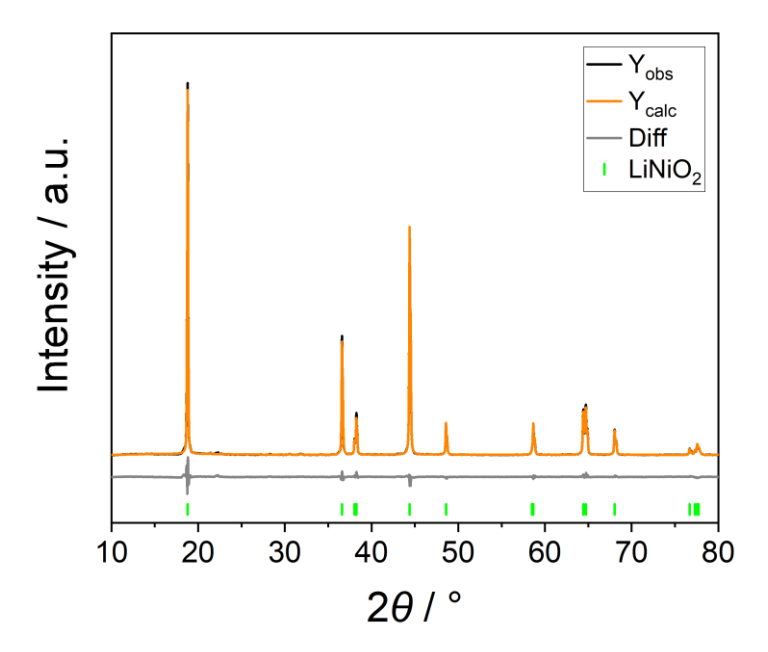


Figure 10.16: Refinement of measured Cu source XRD pattern of LiNiO₂ pre-calcined for 5 h at 350°C and calcined for 5 h at 750°C. Measured pattern (black), calculated LiNiO₂ pattern (orange, collection code 78687 [187]) and the difference between observed and calculated pattern (grey). Peak positions of LiNiO₂ in green.

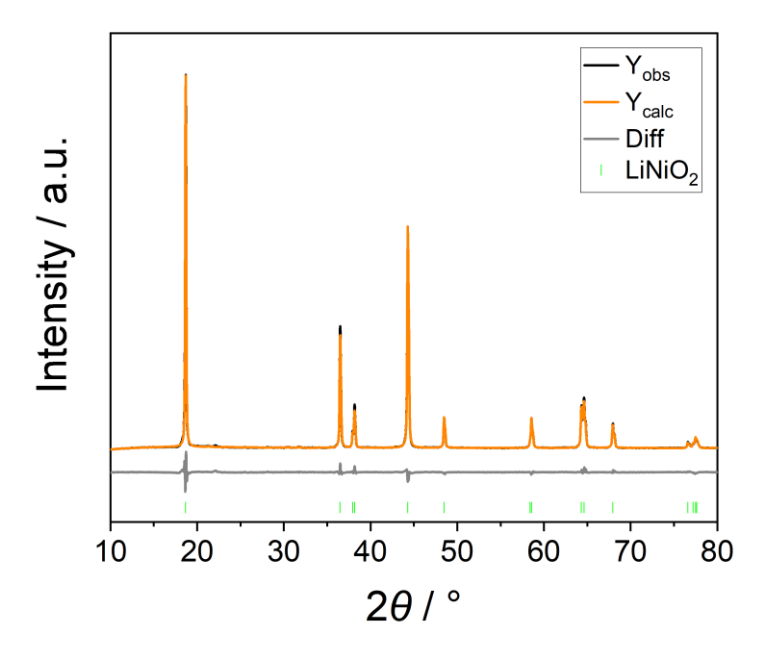


Figure 10.17: Refinement of measured Cu source XRD pattern of LiNiO₂ pre-calcined for 5 h at 500°C and calcined for 5 h at 710°. Measured pattern (black), calculated LiNiO₂ pattern (orange, collection code 78687 [187]) and the difference between observed and calculated pattern (grey). Peak positions of LiNiO₂ in green.

Chapter 5

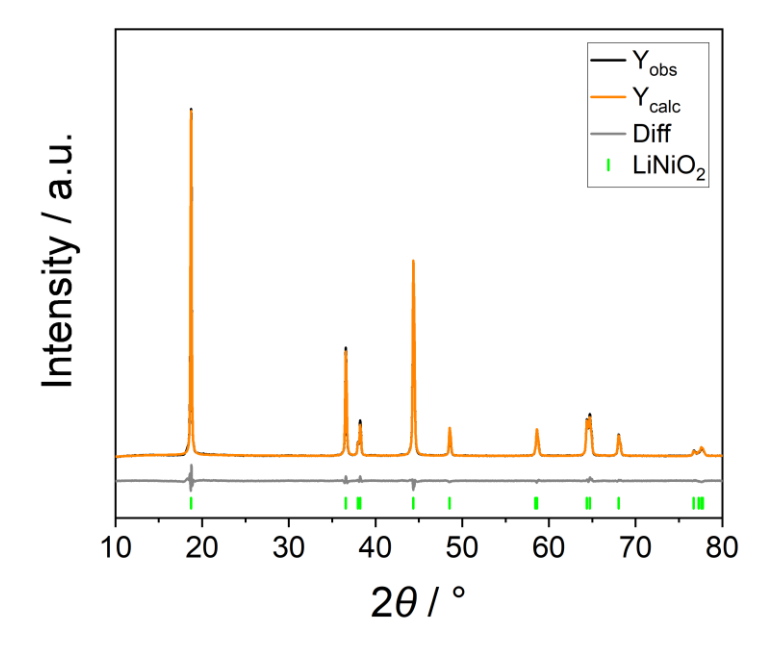


Figure 10.18: Refinement of measured Cu source XRD pattern of LiNiO₂ pre-calcined for 5 h at 350°C and calcined for 15 h at 710°C using a Ni(OH)₂ precursor synthesised at a Ni:NH₄OH ratio of 1:1.2. Measured pattern (black), calculated LiNiO₂ pattern (orange, collection code 78687 [187]) and the difference between observed and calculated pattern (grey). Peak positions of LiNiO₂ in green.

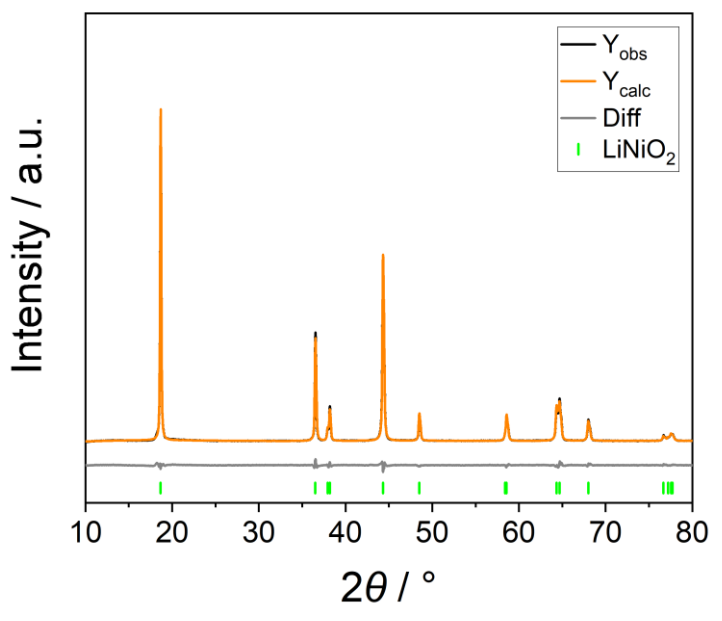


Figure 10.19: Refinement of measured Cu source XRD pattern of LiNiO₂ pre-calcined for 5 h at 350°C and calcined for 15 h at 710°C using a Ni(OH)₂ precursor synthesised at a Ni:NH₄OH ratio of 1:2.5. Measured pattern (black), calculated LiNiO₂ pattern (orange, collection code 78687 [187]) and the difference between observed and calculated pattern (grey). Peak positions of LiNiO₂ in green.

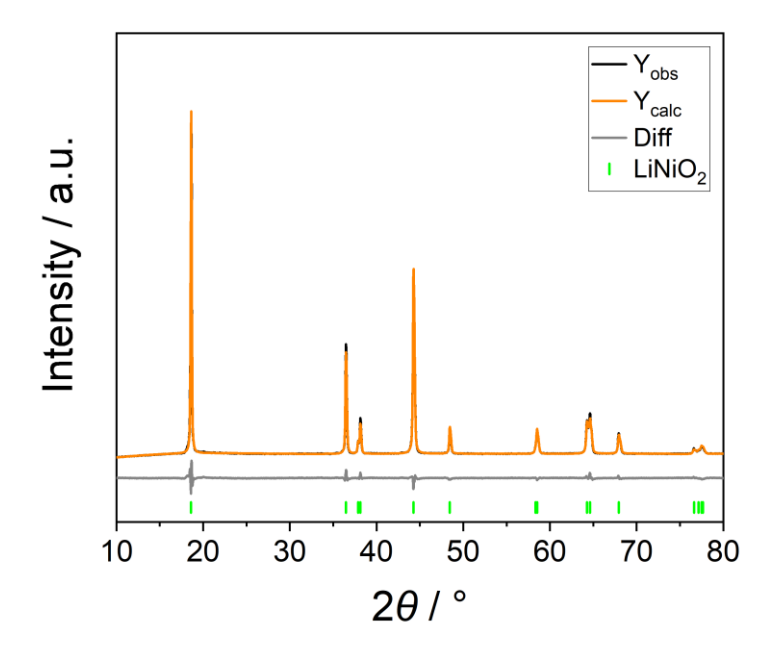


Figure 10.20: Refinement of measured Cu source XRD pattern of LiNiO₂ pre-calcined for 5 h at 350°C and calcined for 15 h at 710°C using a Ni(OH)₂ precursor synthesised at a Ni:NH₄OH ratio of 1:3.75. Measured pattern (black), calculated LiNiO₂ pattern (orange, collection code 78687 [187]) and the difference between observed and calculated pattern (grey). Peak positions of LiNiO₂ in green.

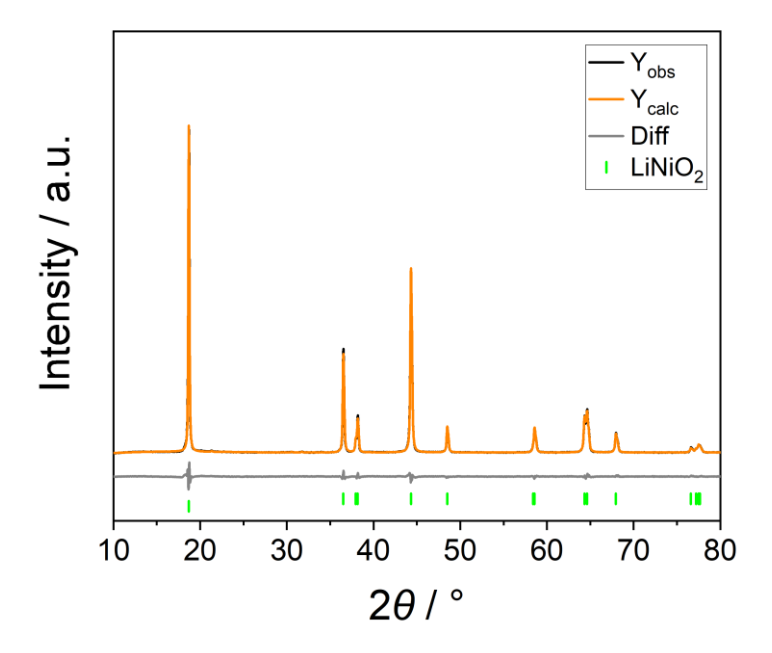


Figure 10.21: Refinement of measured Cu source XRD pattern of LiNiO₂ pre-calcined for 5 h at 350°C and calcined for 15 h at 710°C using a Ni(OH)₂ precursor synthesised at a Ni:NH₄OH ratio of 1:5. Measured pattern (black), calculated LiNiO₂ pattern (orange, collection code 78687 [187]) and the difference between observed and calculated pattern (grey). Peak positions of LiNiO₂ in green.

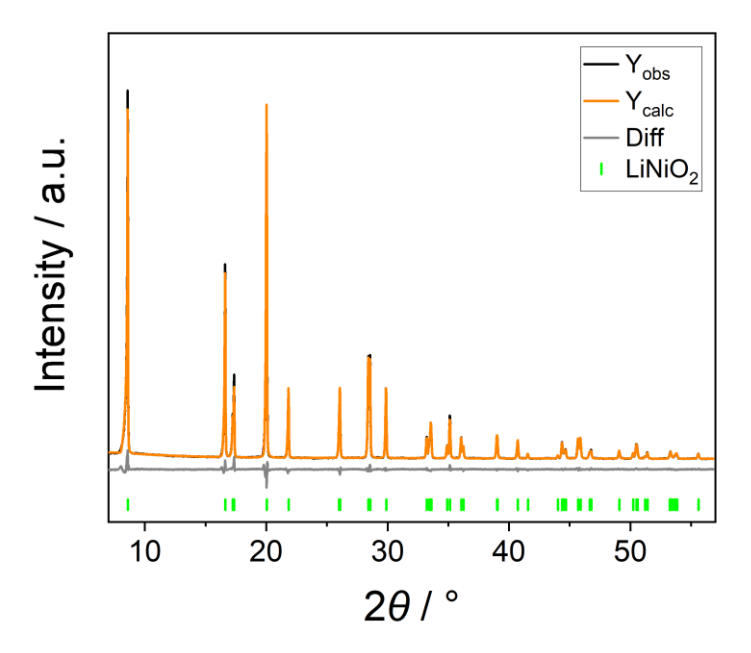


Figure 10.22: Refinement of measured Mo source XRD pattern of LiNiO₂ pre-calcined for 5 h at 350°C and calcined for 15 h at 710°C using a Ni(OH)₂ precursor synthesised at a Ni:NH₄OH ratio of 1:1.2. Measured pattern (black), calculated LiNiO₂ pattern (orange, collection code 78687 [187]) and the difference between observed and calculated pattern (grey). Peak positions of LiNiO₂ in green.

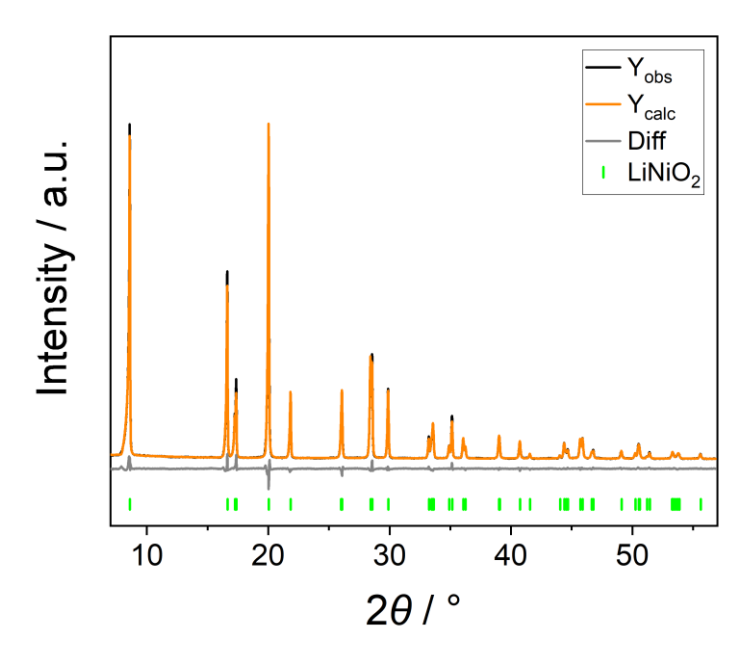


Figure 10.23: Refinement of measured Mo source XRD pattern of $LiNiO_2$ pre-calcined for 5 h at 350°C and calcined for 15 h at 710°C using a $Ni(OH)_2$ precursor synthesised at a $Ni:NH_4OH$ ratio of 1:2.5. Measured pattern (black), calculated $LiNiO_2$ pattern (orange, collection code 78687 [187]) and the difference between observed and calculated pattern (grey). Peak positions of $LiNiO_2$ in green.

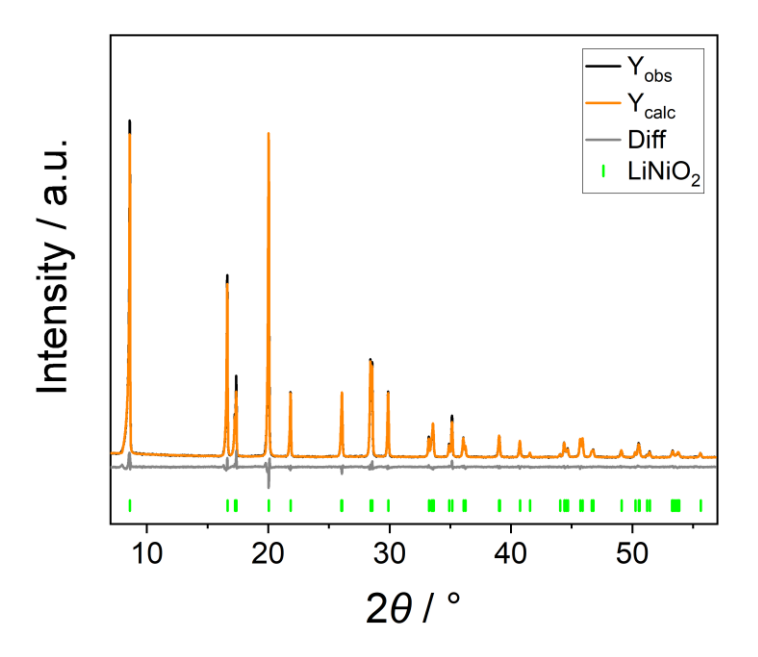


Figure 10.24: Refinement of measured Mo source XRD pattern of LiNiO₂ pre-calcined for 5 h at 350°C and calcined for 15 h at 710°C using a Ni(OH)₂ precursor synthesised at a Ni:NH₄OH ratio of 1:3.75. Measured pattern (black), calculated LiNiO₂ pattern (orange, collection code 78687 [187]) and the difference between observed and calculated pattern (grey). Peak positions of LiNiO₂ in green.

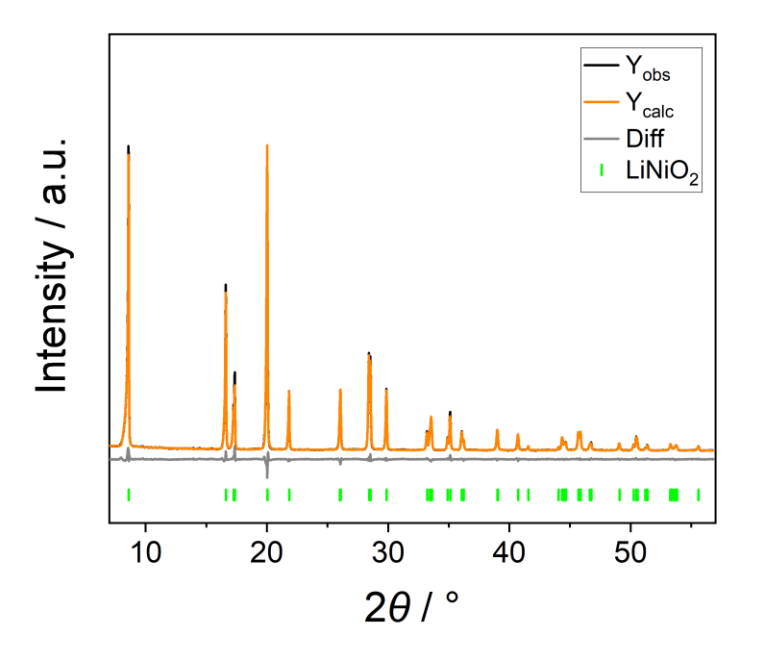


Figure 10.25: Refinement of measured Mo source XRD pattern of LiNiO $_2$ pre-calcined for 5 h at 350°C and calcined for 15 h at 710°C using a Ni(OH) $_2$ precursor synthesised at a Ni:NH $_4$ OH ratio of 1:5. Measured pattern (black), calculated LiNiO $_2$ pattern (orange, collection code 78687 [187]) and the difference between observed and calculated pattern (grey). Peak positions of LiNiO $_2$ in green.

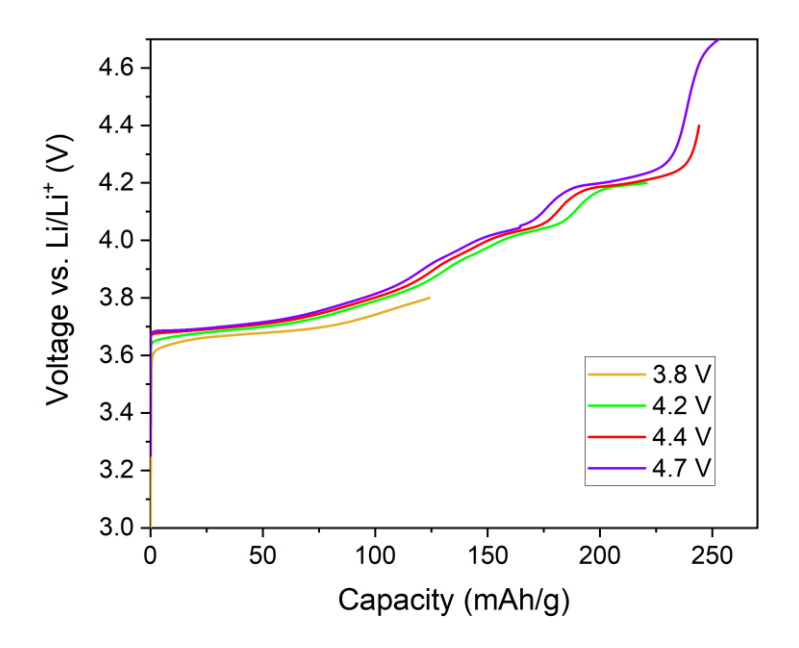


Figure 10.26: Electrochemical data obtained for LiNiO $_2$ using a precursor synthesised at a Ni:NH $_4$ OH ratio of 1:5. LNO cathodes cycled to 3.8 V (yellow), 4.2 V (green), 4.4 V (red) and 4.7 V (purple), decrimped and used for sXAS measurements.

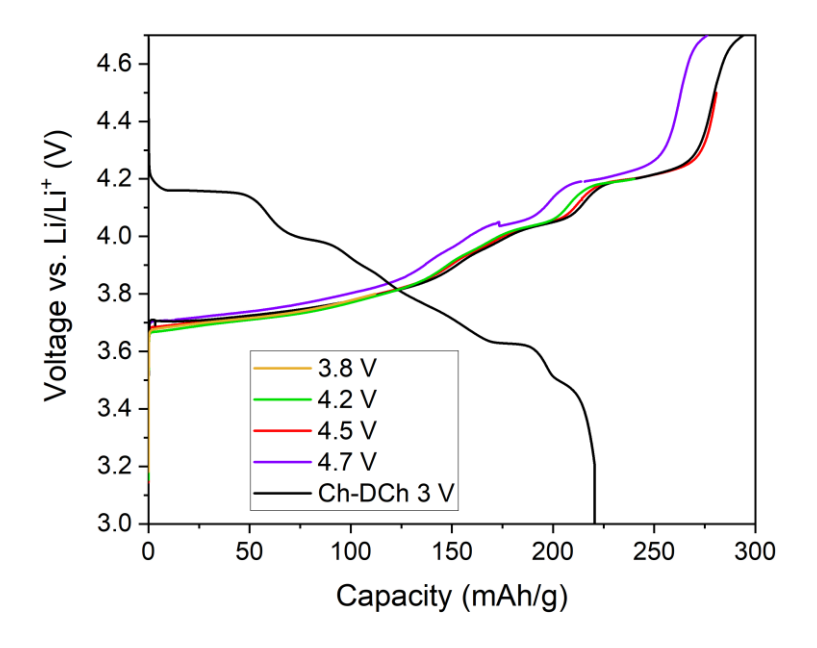


Figure 10.27: Electrochemical data obtained for LiNiO₂ using a precursor synthesised at a Ni:NH₄OH ratio of 1:5. LNO cathodes cycled to 3.8 V (yellow), 4.2 V (green), 4.4 V (red), 4.7 V (purple) and charged and discharged (4.7 V - 3 V, black), decrimped and used for HAXPES measurements.

Chapter 6

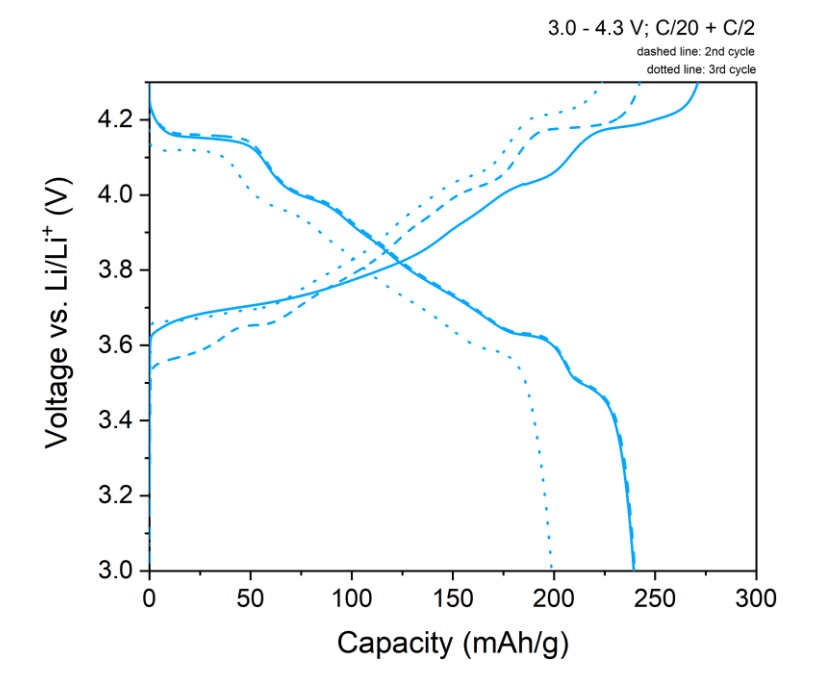


Figure 10.28: Electrochemical data obtained for Co-doped LiNiO₂ synthesised via a solid-state route, pre-calcined for 5 h at 350°C and calcined for 15 h at 710°C. Charge/discharge plot between $3-4.3\,V$ vs. Li/Li⁺ at a rate of C/20 for two cycles and C/2 for the third cycle. Solid line shows 1st cycle, dashed line depicts 2nd cycle and dotted line represents the 3rd cycle.

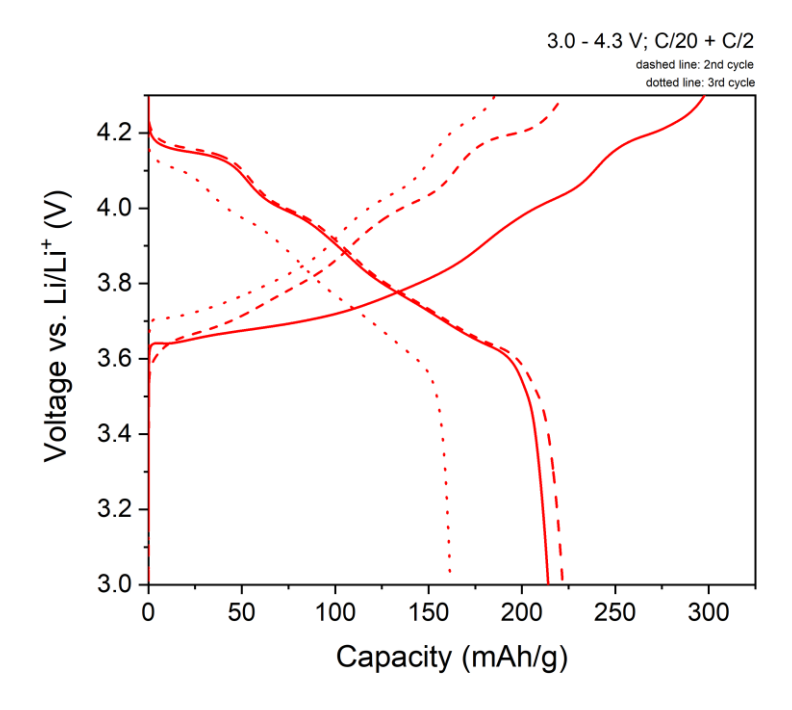


Figure 10.29: Electrochemical data obtained for Mn-doped LiNiO $_2$ synthesised via a solid-state route, pre-calcined for 5 h at 350°C and calcined for 15 h at 710°C. Charge/discharge plot between 3 – 4.3 V vs. Li/Li $^+$ at a rate of C/20 for two cycles and C/2 for the third cycle. Solid line shows 1st cycle, dashed line depicts 2nd cycle and dotted line represents the 3rd cycle.

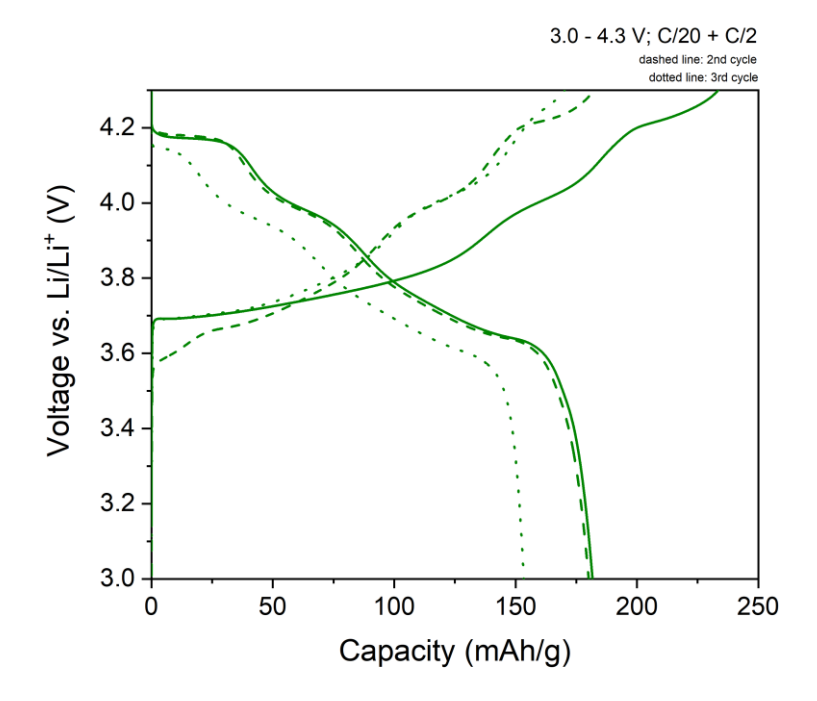


Figure 10.30: Electrochemical data obtained for Cu-doped LiNiO₂ synthesised via a solid-state route, pre-calcined for 5 h at 350°C and calcined for 15 h at 710°C. Charge/discharge plot between $3 - 4.3 \,\mathrm{V}$ vs. Li/Li⁺ at a rate of C/20 for two cycles and C/2 for the third cycle. Solid line shows 1st cycle, dashed line depicts 2nd cycle and dotted line represents the 3rd cycle.

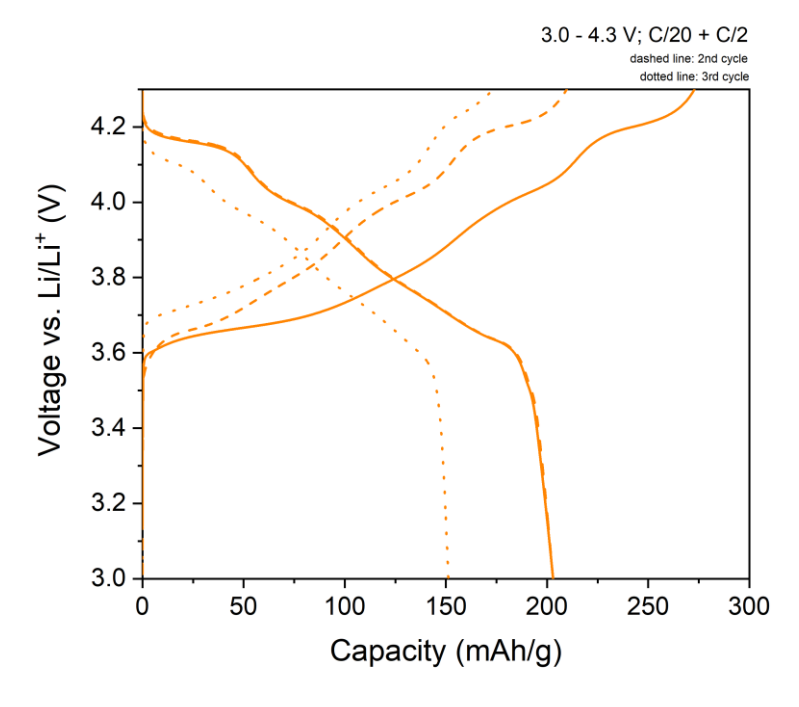


Figure 10.31: Electrochemical data obtained for Zn-doped LiNiO $_2$ synthesised via a solid-state route, pre-calcined for 5 h at 350°C and calcined for 15 h at 710°C. Charge/discharge plot between 3 – 4.3 V vs. Li/Li⁺ at a rate of C/20 for two cycles and C/2 for the third cycle. Solid line shows 1st cycle, dashed line depicts 2nd cycle and dotted line represents the 3rd cycle.

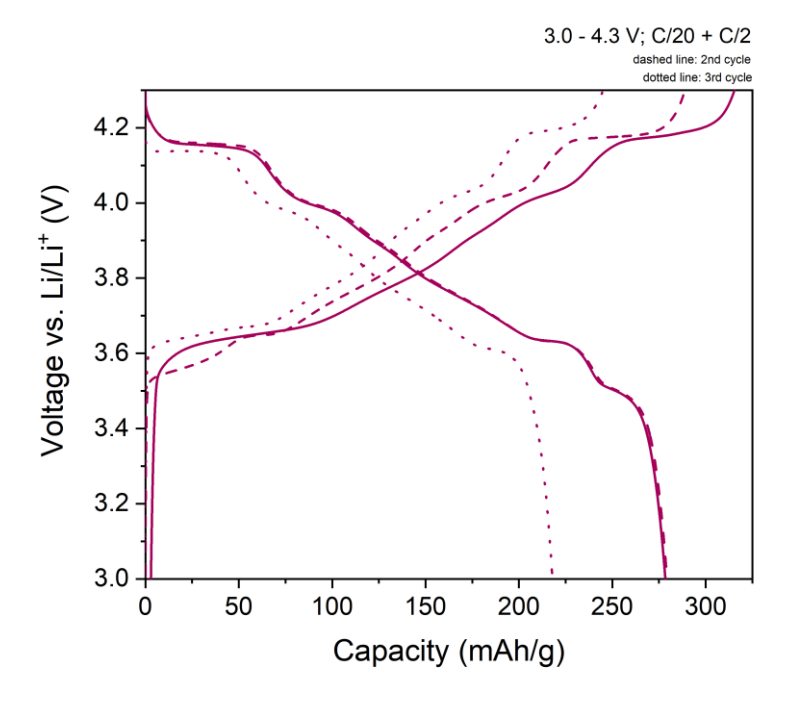


Figure 10.32: Electrochemical data obtained for Sn-doped LiNiO₂ synthesised via a solid-state route, pre-calcined for 5 h at 350°C and calcined for 15 h at 710°C. Charge/discharge plot between $3-4.3\,\mathrm{V}$ vs. Li/Li⁺ at a rate of C/20 for two cycles and C/2 for the third cycle. Solid line shows 1st cycle, dashed line depicts 2nd cycle and dotted line represents the 3rd cycle.

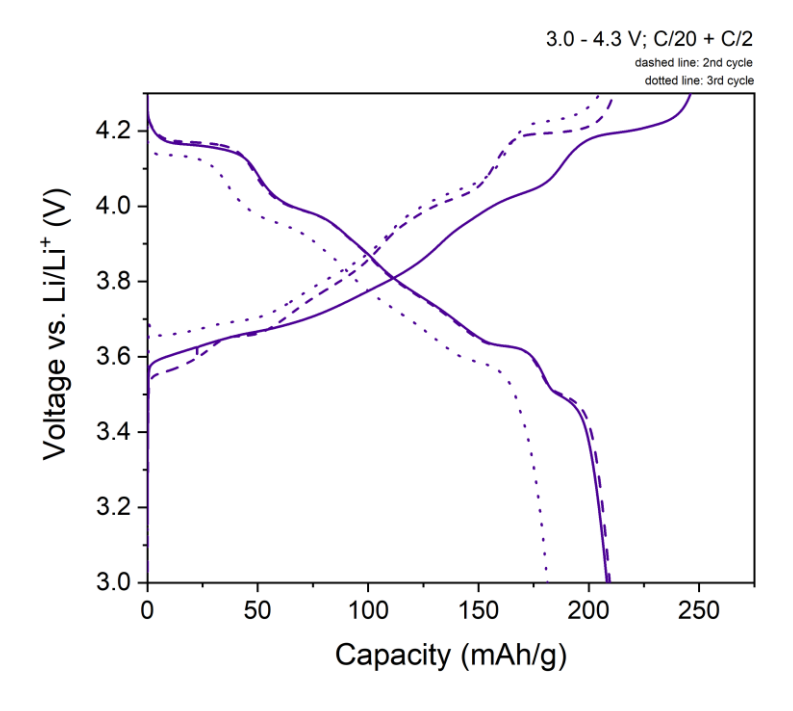


Figure 10.33: Electrochemical data obtained for Zr-doped LiNiO₂ synthesised via a solid-state route, pre-calcined for 5 h at 350°C and calcined for 15 h at 710°C. Charge/discharge plot between $3 - 4.3 \,\mathrm{V}$ vs. Li/Li⁺ at a rate of C/20 for two cycles and C/2 for the third cycle. Solid line shows 1st cycle, dashed line depicts 2nd cycle and dotted line represents the 3rd cycle.

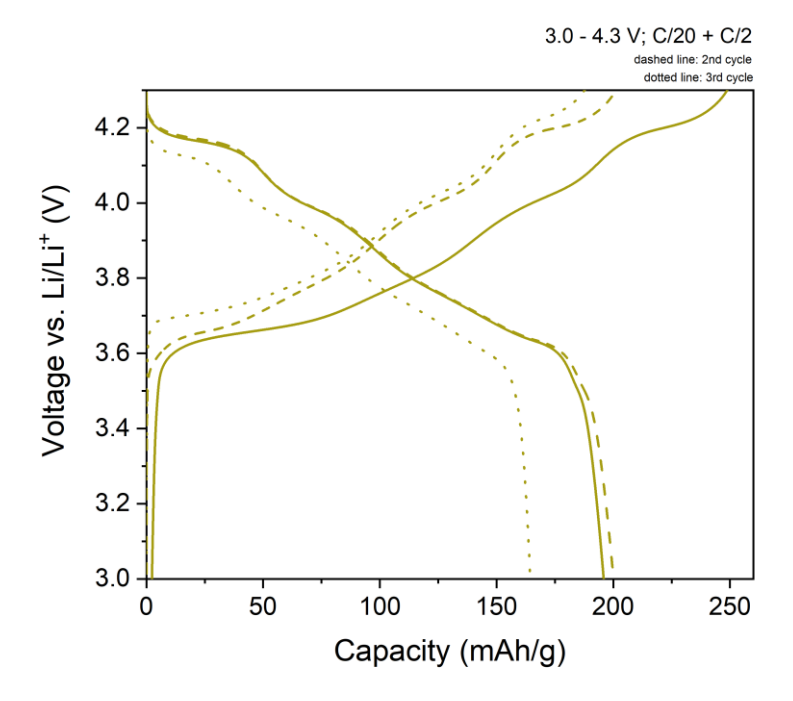


Figure 10.34: Electrochemical data obtained for Ti-doped LiNiO₂ synthesised via a solid-state route, pre-calcined for 5 h at 350°C and calcined for 15 h at 710°C. Charge/discharge plot between $3 - 4.3 \,\mathrm{V}$ vs. Li/Li⁺ at a rate of C/20 for two cycles and C/2 for the third cycle. Solid line shows 1st cycle, dashed line depicts 2nd cycle and dotted line represents the 3rd cycle.

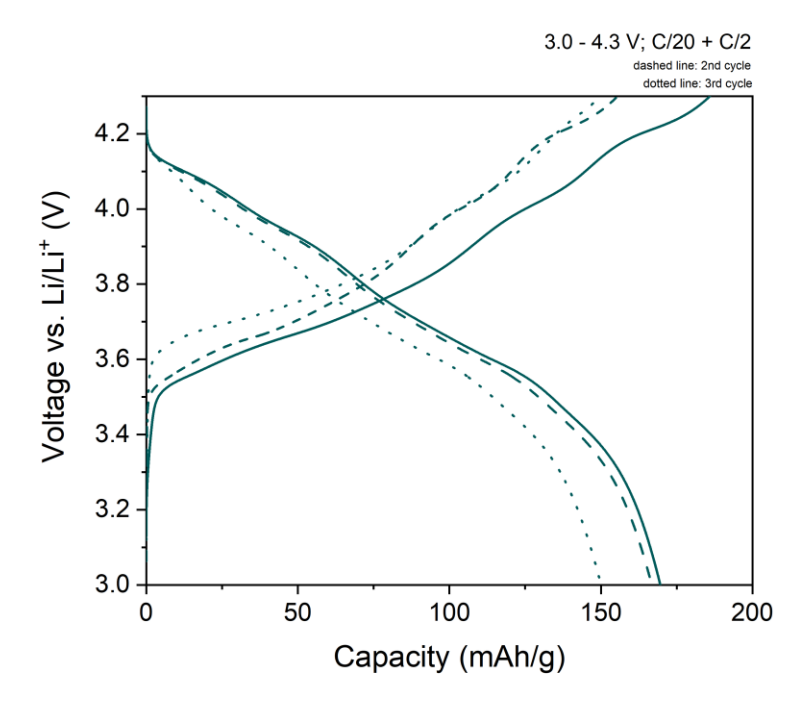


Figure 10.35: Electrochemical data obtained for W-doped LiNiO $_2$ synthesised via a solid-state route, pre-calcined for 5 h at 350°C and calcined for 15 h at 710°C. Charge/discharge plot between 3 – 4.3 V vs. Li/Li⁺ at a rate of C/20 for two cycles and C/2 for the third cycle. Solid line shows 1st cycle, dashed line depicts 2nd cycle and dotted line represents the 3rd cycle.

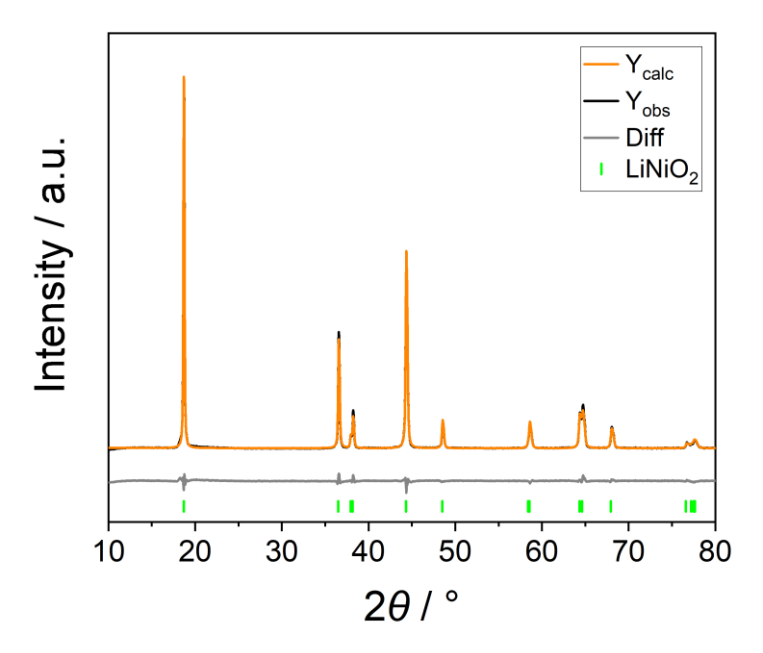


Figure 10.36: Refinement of measured Cu source XRD pattern of Co-doped LiNiO₂ calcined for 5 h at 350°C and calcined for 15 h at 710°C using a 3% Co-doped Ni(OH)₂ precursor synthesised at a Ni:NH₄OH ratio of 1:5. Measured pattern (black), calculated LiNiO₂ pattern (orange, collection code 78687 [187]) and the difference between observed and calculated pattern (grey). Peak positions of LiNiO₂ in green.

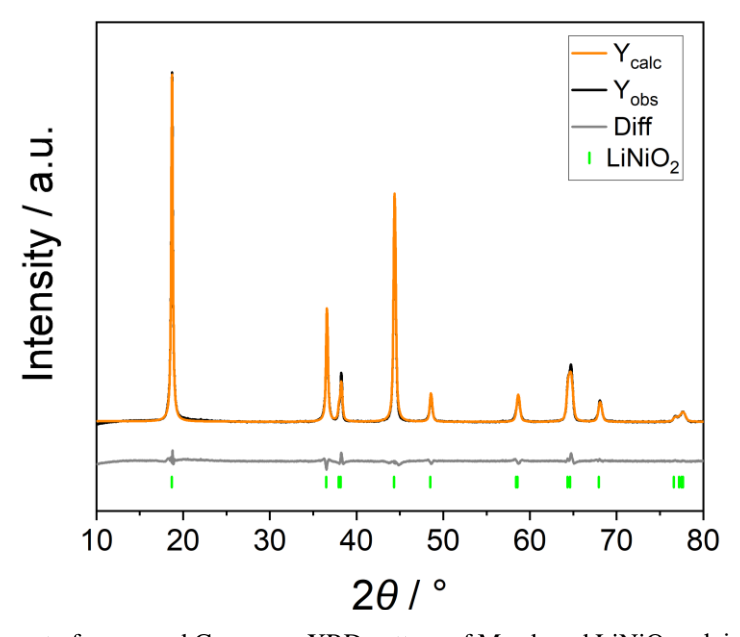


Figure 10.37: Refinement of measured Cu source XRD pattern of Mn-doped LiNiO $_2$ calcined for 5 h at 350°C and calcined for 15 h at 710°C using a 3% Mn-doped Ni(OH) $_2$ precursor synthesised at a Ni:NH4OH ratio of 1:5. Measured pattern (black), calculated LiNiO $_2$ pattern (orange, collection code 78687 [187]) and the difference between observed and calculated pattern (grey). Peak positions of LiNiO $_2$ in green.

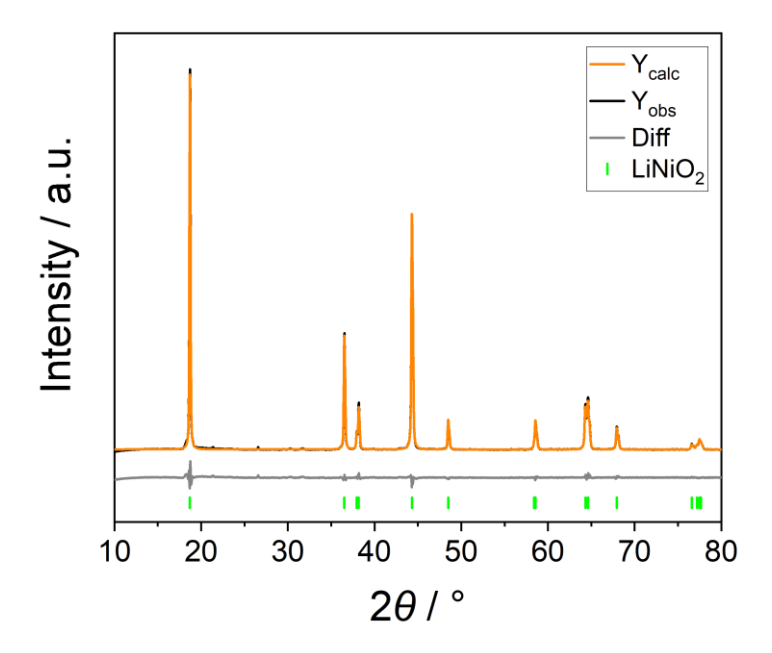


Figure 10.38: Refinement of measured Cu source XRD pattern of Cu-doped LiNiO₂ calcined for 5 h at 350° C and calcined for 15 h at 710° C using a 3 % Cu-doped Ni(OH)₂ precursor synthesised at a Ni:NH₄OH ratio of 1:5. Measured pattern (black), calculated LiNiO₂ pattern (orange, collection code 78687 [187]) and the difference between observed and calculated pattern (grey). Peak positions of LiNiO₂ in green.

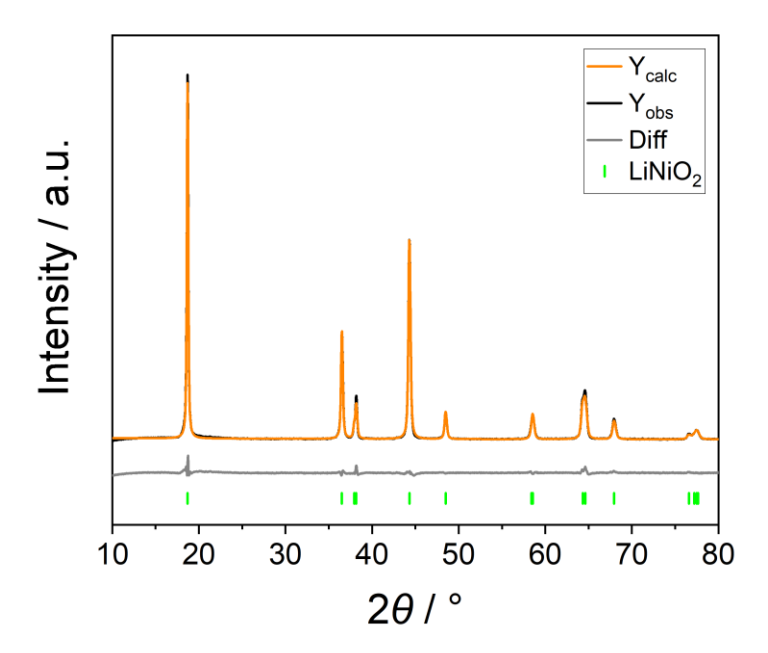


Figure 10.39: Refinement of measured Cu source XRD pattern of Zn-doped LiNiO $_2$ calcined for 5 h at 350°C and calcined for 15 h at 710°C using a 3% Zn-doped Ni(OH) $_2$ precursor synthesised at a Ni:NH $_4$ OH ratio of 1:5. Measured pattern (black), calculated LiNiO $_2$ pattern (orange, collection code 78687 [187]) and the difference between observed and calculated pattern (grey). Peak positions of LiNiO $_2$ in green.

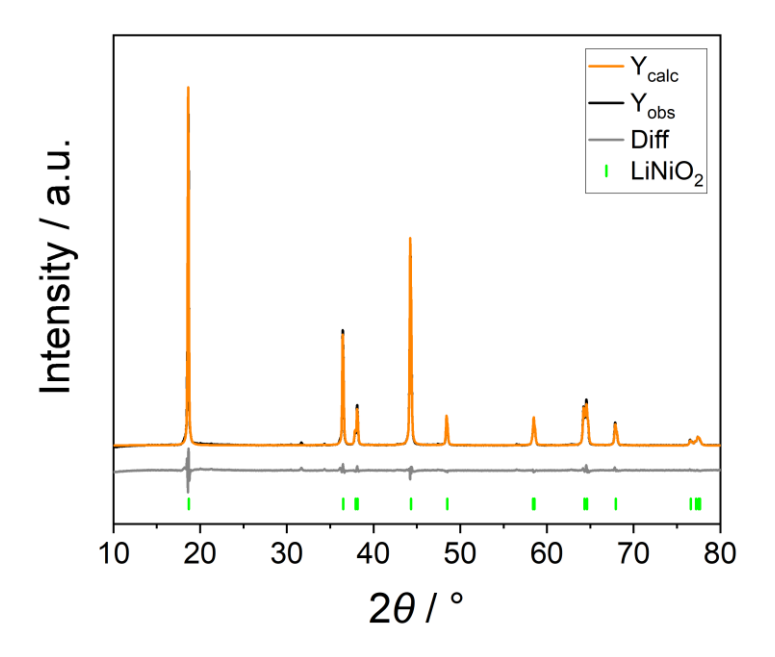


Figure 10.40: Refinement of measured Cu source XRD pattern of Sn-doped LiNiO₂ calcined for 5 h at 350°C and calcined for 15 h at 710°C using a 3 % Sn-doped Ni(OH)₂ precursor synthesised at a Ni:NH₄OH ratio of 1:5. Measured pattern (black), calculated LiNiO₂ pattern (orange, collection code 78687 [187]) and the difference between observed and calculated pattern (grey). Peak positions of LiNiO₂ in green.

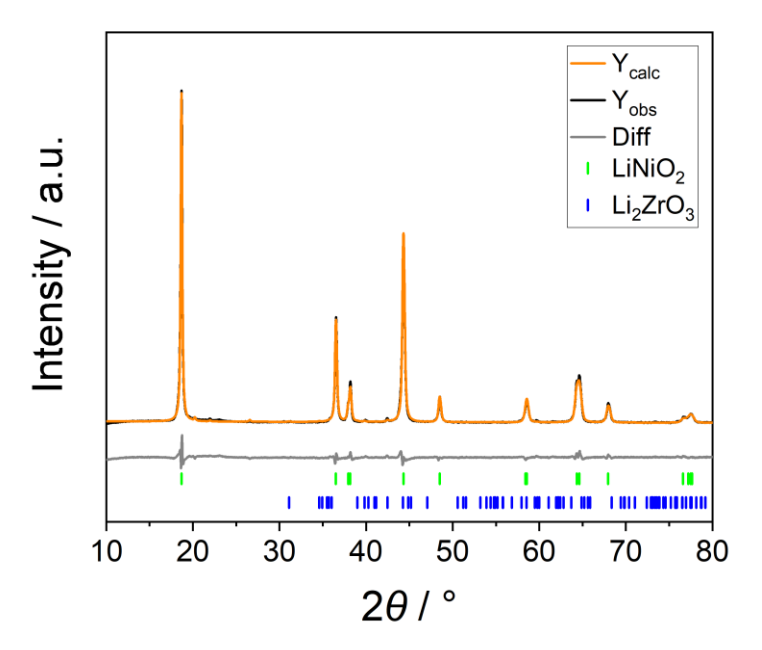


Figure 10.41: Refinement of measured Cu source XRD pattern of Zr-doped LiNiO₂ calcined for 5 h at 350°C and calcined for 15 h at 710°C using a 3 % Zr-doped Ni(OH)₂ precursor synthesised at a Ni:NH₄OH ratio of 1:5. Measured pattern (black), calculated LiNiO₂ pattern (orange, collection code 78687 [187]) and the difference between observed and calculated pattern (grey). Peak positions of LiNiO₂ in green and of the Li₂ZrO₃ side phase in blue.

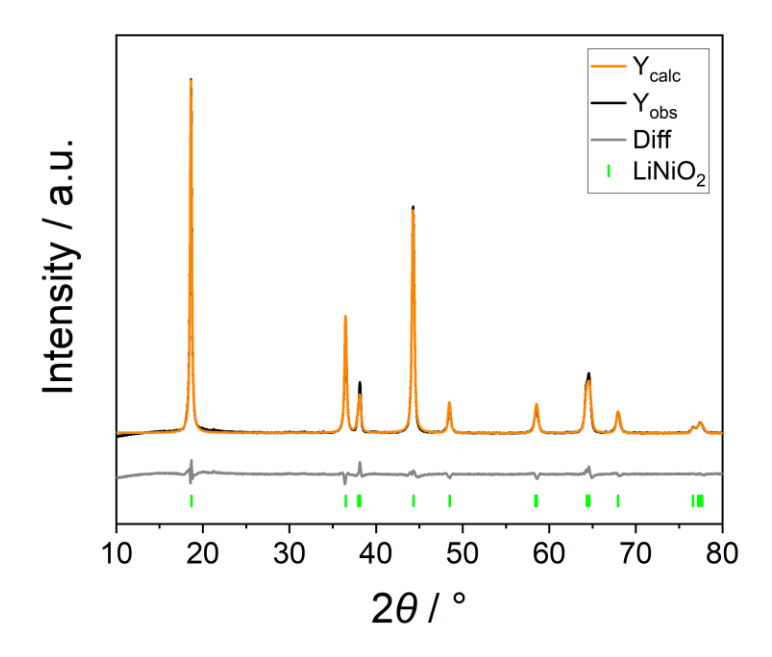


Figure 10.42: Refinement of measured Cu source XRD pattern of Ti-doped LiNiO₂ calcined for 5 h at 350°C and calcined for 15 h at 710°C using a 3% Ti-doped Ni(OH)₂ precursor synthesised at a Ni:NH₄OH ratio of 1:5. Measured pattern (black), calculated LiNiO₂ pattern (orange, collection code 78687 [187]) and the difference between observed and calculated pattern (grey). Peak positions of LiNiO₂ in green.